




Universitat Autònoma de Barcelona

ADVERTIMENT. L'accés als continguts d'aquesta tesi queda condicionat a l'acceptació de les condicions d'ús establertes per la següent llicència Creative Commons:  http://cat.creativecommons.org/?page_id=184

ADVERTENCIA. El acceso a los contenidos de esta tesis queda condicionado a la aceptación de las condiciones de uso establecidas por la siguiente licencia Creative Commons:  <http://es.creativecommons.org/blog/licencias/>

WARNING. The access to the contents of this doctoral thesis it is limited to the acceptance of the use conditions set by the following Creative Commons license:  <https://creativecommons.org/licenses/?lang=en>

Design and Synthesis of Submicron Diagnostic Systems Based on Coordination Polymers

Javier Aríñez Soriano

Tesi Doctoral
Doctorat en Química

Directors de la Tesi:

Prof. Dr. Daniel Maspoch
Dr. Inhar Imaz

Tutor de la Tesi:

Dr. Jordi Hernando

Institut Català de Nanociència i Nanotecnologia (ICN2)
Departament de Química. Facultat de Ciències.

2016

Memòria presentada per a aspirar al Grau de Doctor per Javier Aríñez Soriano.

Vist-i-plau.

Prof. Dr. Daniel Maspoch.

Investigador ICREA.

Supramolecular Nanochemistry and Materials Group.

Institut Català de Nanociència i Nanotecnologia (ICN2).

Dr. Inhar Imaz.

Investigador Ramón y Cajal.

Supramolecular Nanochemistry and Materials Group.

Institut Català de Nanociència i Nanotecnologia (ICN2).

Dr. Jordi Hernando.

Professor Agregat.

Departament de Química.

Universitat Autònoma de Barcelona (UAB)

Bellaterra, 16 de setembre de 2016

Table of contents

<i>Table of contents</i>	v
<i>Abstract</i>	ix
<i>Resum</i>	xi
<i>Acknowledgements</i>	xiii
<i>Glossary of acronyms</i>	xv
Chapter 1. General Introduction	1
1.1. A brief history of coordination polymers (CPs).....	3
1.2. What is a coordination polymer?.....	4
1.3. Crystal engineering and applications of CPs.....	5
1.4. Coordination polymers for biomedicine.....	7
1.4.1. CP particles for therapeutics. Drug Delivery.....	7
1.4.1.1. Incorporation of therapeutic organic molecules in the pores of CP particles..	7
1.4.1.2. Incorporation of therapeutic gases in the pores of the CP particles	9
1.4.1.3. Incorporation of therapeutic organic molecules as linkers.....	9
1.4.1.4. Incorporation of therapeutic metal complexes as linkers.....	10
1.4.2. CP particles for diagnostics. Medical imaging.....	11
1.4.2.1. Incorporation of organic molecules-based CA as linkers.....	11
1.4.2.2. Incorporation of metal-based CAs as connecting nodes.....	12
1.5. Toxicity of leached toxic metal ions in CPs.....	14
1.6. References.....	17
Chapter 2. Objectives	21
Chapter 3. Publication 1	25
3.1. Metal Polyazamacrocyclic complexes as building blocks for the design of CPs.....	27
3.1.1. Introduction to polyazamacrocyclic ligands.....	27
3.1.2. Functionalization of polyazamacrocyclic ligands.....	27
3.2. Classification of CPs containing polyazamacrocyclic ligands.....	30
3.2.1. Group (I): Primary metal centre (M_1) as connecting node.....	30
3.2.1.1. Group (I-a): Connection through auxiliary ligands.....	30
3.2.1.2. Group (I-b): Connection through pendant arms.....	31
3.2.2. Group (II): Secondary metal centre (M_2) as connecting node.....	31
3.2.2.1. Group (II-a): Homometallic CPs of group (II).....	32
3.2.2.2. Group (II-b): Heterometallic CPs of group (II).....	32
3.2.2.3. Group (II-c): Members of group (II) with an empty macrocyclic cavity	33
3.2.3. Group (III): Primary (M_1) and secondary (M_2) metal centres as connecting nodes.....	33
3.2.3.1. Subgroup (III-a): Homometallic members of group (III).....	34

3.2.4. Summary of the reported CPs containing polyazamacrocyclic ligands.....	34
3.3. Design of a new macrocyclic ligand to avoid the release of free M_1 ions.....	34
3.4. Results and discussion.....	36
3.4.1. Design of the new ligand H_4L1	36
3.4.2. Two-step synthesis strategy.....	36
3.4.3. Synthesis and characterization of ligand H_4L1	38
3.4.4. First step: Synthesis and characterization of M_1-L1 complexes.....	38
3.4.4.1. General synthesis and characterization of M_1-L1 complexes.....	39
3.4.4.2. Structure of $[Mn(H_1L1)] \cdot [Na(H_2O)_6] \cdot 4H_2O$ (3).....	39
3.4.4.3. Structure of $[Ni(H_2L1)] \cdot 2H_2O$ (4).....	39
3.4.5. Second step: Synthesis and characterization of CPs.....	40
3.4.5.1. Synthesis and structure of $[Zn(ZnL1)H_2O] \cdot 3H_2O$ (5).....	40
3.4.5.2. Synthesis and structure of $[Zn(NiL1)H_2O] \cdot 8H_2O$ (6).....	41
3.4.5.3. Synthesis and structure of $[Zn(MnL1)H_2O] \cdot 9H_2O$ (7).....	41
3.5. Conclusions.....	42
3.6. References.....	44
Chapter 4. Publication 2	47
4.1. A new ligand for the design of Gd-containing CPs: DOTA-4AmP.....	49
4.2. Metal phosphonates.....	49
4.2.1. Layered hybrid organic-inorganic compounds. Monotopic ligands.....	50
4.2.2. Phosphonate-based CPs. Polytopic ligands.....	52
4.2.3. Phosphonate functionalised polyazamacrocyclic ligands.....	53
4.3. Flexible coordination polymers.....	56
4.3.1. Guest induced flexibility.....	56
4.3.2. Breathing modes of flexible CPs.....	57
4.4. Ours results.....	58
4.4.1. Synthesis of Gd-DOTA-4AmP.....	59
4.4.2. Synthesis and characterization of the structure of $[Mn_2(Gd-H-DOTA-4AmP)(H_2O)_7] \cdot 21H_2O$ (1-op).....	59
4.4.3. Transformation between $[Mn_2(Gd-H-DOTA-4AmP)(H_2O)_7] \cdot 21H_2O$ (1-op) and $[Mn_2(Gd-H-DOTA-4AmP)(H_2O)_7] \cdot 5H_2O$ (1-cp).....	61
4.4.4. Water sorption and humidity-controlled PXRD measurements.....	63
4.4.4.1. Water vapour sorption isotherm.....	64
4.4.4.2. Humidity-controlled PXRD measurements.....	64
4.5. Conclusions.....	66
4.6. References.....	67
Chapter 5. Publication 3	69
5.1. A CP based on Gd-DOTA-4AmP and Zn(II) for MRI CA.....	71

5.2. Fundamentals of Magnetic Resonance Imaging (MRI).....	71
5.2.1. Total magnetization.....	71
5.2.2. Relaxation time.....	72
5.2.3. Contrast Agents (CA). Relaxivity r_i and parameters controlling it.....	72
5.2.4 Methods for improving longitudinal relaxivity r_1	74
5.2.4.1. Increase of the hydration state, q	75
5.2.4.2. Optimization of residence lifetime, τ_M	75
5.2.4.3. Increase of rotational correlation time, τ_R	75
5.2.5. Strategies to slow down tumbling motion.....	76
5.3. Our results.....	77
5.3.1. Synthesis and characterization of $Zn_{6.5}[Gd_3(H-DOTA-4AmP)_2(DOTA-4AmP)(H_2O)_3] \cdot 18H_2O$ (1).....	77
5.3.2. Miniaturisation of 1 in amorphous Zn-Gd-DOTA-4AmP nanoparticles and their characterisation.....	79
5.3.3. X-Ray Total Scattering PDF analysis of crystalline 1 and amorphous Zn-Gd-DOTA-4AmP nanoparticles.....	81
5.3.4. Relaxometric studies.....	82
5.3.4.1. Stability studies.....	82
5.3.4.2. Relaxometric measurements.....	83
5.3.4.3. Relaxivity r_1 pH-dependence study.....	83
5.4. Conclusions.....	85
5.5. References.....	86
Conclusions	89
Appendix	91
Publication 1	93
Publication 1: Supporting Information	105
Publication 2	125
Publication 2: Supporting Information	131
Publication 3	145
Publication 3: Supporting Information	157

Abstract

The present Thesis is dedicated to the design and synthesis of new diagnostic systems for Magnetic Resonance Imaging (MRI) based on metal-organic coordination networks. The work has been focused on the synthesis of new Coordination Polymers (CPs) containing polyazamacrocyclic ligands to avoid the release of toxic metals during their use as Contrast Agents (CAs) for MRI.

In Chapter 1, the evolution of the field of CPs is reviewed, from the precedents that made their discovery possible to their current applications and prospects. Special attention is paid to their applications in biomedicine and particularly in the field of bioimaging.

In Chapter 2, the general and specific objectives of this Thesis are introduced.

In Chapter 3, the reported examples of CPs containing polyazamacrocyclic ligands as linkers are reviewed and classified. The use of these ligands as a general strategy for obtaining heterometallic CPs is proposed, and the synthesis of a new carboxylic-based polyazamacrocyclic ligand for such purpose is done. Then, the CPs obtained using this ligand are presented and described. And finally, the limitations of the synthesised ligand to produce Gd(III)-based CPs are exposed.

In Chapter 4, the use of phosphonate-based ligands is proposed as an alternative to overcome the limitations encountered in the synthesis of Gd(III)-based CPs. The phosphonate-based CPs are reviewed and their tendency to show flexibility is analysed. Then, the use of the Gd(III)-DOTA-4AmP phosphonate-based complex as the linker for the construction of CPs is presented. Finally, the study of the flexible behaviour of the synthesised CP upon water vapour sorption is carried out thanks to humidity-controlled X-ray diffraction measurements.

In Chapter 5, MRI is introduced and the principal parameters controlling relaxivity r_1 are analysed. Then, the main strategies used by researchers to increase r_1 are shown and special attention is paid to those strategies based on the use of nanostructured platforms. The synthesis of a new CP containing the Gd(III)-DOTA-4AmP unit is done and miniaturised, yielding CP nanoparticles that form stable colloids appropriate for their use in the study of the MRI relaxometric properties. Finally, the results of this study are presented and analysed.

Resum

La present Tesi està dedicada al disseny i la síntesi de nous sistemes de diagnòstic per a Ressonància Magnètica (MRI) basats en xarxes de coordinació metal-orgàniques. El treball s'ha centrat en la síntesi de nous Polímers de Coordinació (CPs) que contenen lligands poliazamacrocíclics per evitar l'alliberament de metalls tòxics durant el seu ús com Agents de Contrast (CAs) en MRI.

En el Capítol 1, es revisa l'evolució en el camp dels CPs, des dels precedents que van fer possible el seu descobriment fins a les seves actuals aplicacions i perspectives. Es presta especial atenció a les seves aplicacions en biomedicina i en particular en el camp del "Bioimaging".

En el Capítol 2, s'introdueixen els objectius generals i específics de la Tesi.

En el Capítol 3, es revisen i classifiquen els exemples reportats de CPs que contenen lligands poliazamacrocíclics. Es proposa l'ús d'aquests lligands com una estratègia general per a l'obtenció de CPs heterometàl·lics i es duu a terme la síntesi d'un nou lligand poliazamacrocíclic basat en la funció carboxílica. A continuació, es presenten i descriuen els CPs obtinguts fent ús d'aquest lligand. Finalment, s'exposen les limitacions del lligand sintetitzat per a produir CPs basat en Gd(III).

En el Capítol 4, es proposa l'ús de lligands basats en la funció fosfònica com alternativa per superar les limitacions trobades en la síntesi de CPs basats en Gd(III). Es revisen els CPs basats en la funció fosfònica i s'analitza la seva tendència a la flexibilitat. A continuació, es presenta l'ús del complex fosfonat Gd(III)-DOTA-4AmP com a connector per a la construcció de CPs. Finalment, es duu a terme l'estudi de la flexibilitat del CP sintetitzat, durant l'adsorció/desorció de vapors d'aigua, gràcies a mesures de difracció de raigs X en situació d'humitat controlada.

En el Capítol 5, es presenta la MRI i s'analitzen els principals paràmetres que controlen la relaxativitat r_1 . A continuació, es mostren les principals estratègies usades pels investigadors per augmentar r_1 , amb especial atenció en aquelles estratègies basades en l'ús de plataformes nanoestructurades. Es duu a terme la síntesi d'un nou CP que conté l'unitat Gd(III)-DOTA-4AmP i es miniaturitza donant lloc a nanopartícules que formen col·loides estables apropiats per l'ús en l'estudi de les propietats relaxomètriques de MRI. Finalment, els resultats d'aquest estudi es presenten i s'analitzen.

Acknowledgements

En primer lugar quiero agradecer al “Institut Català de Nanociència i Nanotecnologia”, a la “Universitat Autònoma de Barcelona y al “Programa de Doctorat en Química” per haberme dado la posibilidad de desarrollar esta Tesis en las mejores condiciones. Así mismo, quiero agradecer al “Ministerio de Educación, Cultura y Deporte” del “Gobierno de España” por su programa de ayudas predoctorales FPU por haberme concedido la beca que me ha permitido realizar la presente Tesis Doctoral.

Sin duda, este trabajo no hubiera sido posible sin la guía de mis dos excelentes directores Prof. Dr. Daniel MasPOCH y Dr. Inhar Imaz, de los cuales he aprendido muchísimo. También quiero expresar mi gratitud a mi tutor Dr. Jordi Hernando así como al Dr. Félix Busqué por su guía en la síntesis orgánica de los ligandos diseñados.

La resolución de las estructuras cristalinas no hubiera sido posible sin la infraestructura facilitada por el sincrotrón ALBA-CELLS, y el soporte técnico del Dr. Jordi Juanhuix. Las medidas de PDF han sido realizadas gracias a las instalaciones de “Brookhaven National Laboratory” y el soporte técnico del Sr. Maxwell W. Terban. Las medidas de relaxometría han sido posibles gracias a una estancia doctoral realizada en el “Centre de Biophysique Moléculaire” en el grupo de la Dra. Éva Tóth, y bajo la supervisión de la Dra. Célia S. Bonnet i la Sra. Agnès Pallier. Las medidas de PXRD bajo humedad controlada han sido realizadas por el Prof. Dr. Aurelio Cabeza en el “Departamento de Química Inorgánica” de la “Universidad de Málaga”. Las medidas de citotoxicidad han sido llevadas a cabo por la Dra. Julia Lorenzo en el “Institut de Biotecnologia i Biomedicina” de la UAB.

Quiero agradecer especialmente a mis compañeros de aventuras Iván Burneo y Arnau Carné por su compañía en este arduo camino, les debo a los dos una buena cena como las de nuestro piso. A mis compañeros y excompañeros de oficina: Marta Rubio, Carlos Carbonell, Jordi Espín. Claudia Vignatti, Civan Avci y Heng Xu, por su compañía, por todos los cafés, comidas y salidas montaÑeras compartidas. A los vecinos del final del pasillo: Abraham Ayala y Luis Carlos Garzón por su amistad y su futura hospitalidad en el continente americano. A Jorge Albalad, quien en la última etapa de esta Tesis me ha ayudado tantísimo en el laboratorio y en la escritura de los artículos y a quien estoy seguro que aguarda un futuro prometedor. A todos y cada uno de los miembros de NanoUp que han hecho de esta experiencia una de las más enriquecedoras de mi vida.

A mis amigos, por no preguntar demasiadas veces cuando acabaría la Tesis.

A Dúnia por su paciencia y comprensión en la parte más dura del recorrido.

Y por último, y con especial énfasis, a mis padres quienes me han enseñado a no arrojar la toalla aunque las cosas sean difíciles y no salgan a la primera, ni a la segunda, ni a la tercera...Y a mi hermano por preguntar demasiadas veces cuándo acabaría la Tesis y cuánto tiempo más iba a necesitar el coche. Es por ello que esta Tesis es también suya.

Glossary of acronyms

ATMP	Aminotris(methylenephosphonic acid
BDC	Benzene-1,4-dicarboxylic acid
BET	Brunauer–Emmett–Teller theory
BHC	Benzenehexacarboxylic acid
BTC	Benzene-1,3,5-tricarboxylic acid
CA	Contrast Agent
CEST	Chemical Exchange Saturation Transfer
CN	Coordination Number
CP	Coordination Polymer
<i>cp</i>	closed pore
CT	Computed Tomography
Cyclam	1,4,8,11-tetraazacyclotetradecane
Cyclen	1,4,7,10-tetraazacyclododecane
DEF	Diethylformamide
DMF	Dimethylformamide
DOTA	1,4,7,10-tetraazacyclododecane-1,4,7,10-tetraacetic acid
DOTA-4AMP	1,4,7,10-tetraazacyclododecane-1,4,7,10-tetraacetamidomethylene phosphonic acid
DOTP	1,4,7,10-tetraazacyclododecane-1,4,7,10-tetramethylene phosphonic acid
EDTA	Ethylenediaminetetraacetic acid
EMA	European Medicines Agency
EPR effect	Enhanced Permeability Retention effect
ESI-TOF	Electrospray Ionization-Time-of-Flight
FT-IR	Fourier Transform Infrared
HEPES buffer	4-(2-hydroxyethyl)-1-piperazineethanesulfonic acid buffer
ICP	Inductively Coupled Plasma
ICP-MS	Inductively Coupled Plasma-Mass Spectrometry
IUPAC	International Union of Pure and Applied Chemistry
MAS NMR	Magic Angle Spinning Nuclear Magnetic Resonance
MOF	Metal-Organic Framework
MRI	Magnetic Resonance Imaging
MRI-CA	Magnetic Resonance Imaging-Contrast Agent
MS	Mass Spectrometry
NMOF	Nanoscale Metal-Organic Framework
NMR	Nuclear Magnetic Resonance
NMRD	Nuclear Magnetic Relaxation Dispersion
NOTP	1,4,7-triazacyclononane-1,4,7-trismethylenephosphonic acid
NSF	Nephrogenic Systemic Fibrosis
<i>op</i>	open pore
ParaCEST	Paramagnetic Chemical Exchange Saturation Transfer
PBS	Phosphate Buffered Saline
PCP	Porous Coordination Polymer
PDF	Pair Distribution Function
PVP	Polyvinylpyrrolidone
PXRD / PXD	Powder X-Ray Diffraction

RAFT	Reversible Addition-Fragmentation Chain Transfer
RF	Radiofrequency
RH	Relative Humidity
SBM equation	Solomon-Bloembergen-Morgan equation
SC	Single Crystal
SC-SC	Single Crystal-to-Single Crystal
SCXRD	Single Crystal X-Ray Diffraction
SEM	Scanning Electron Microscopy
TACN	1,4,7-Triazacyclononane
TEM	Transmission Electron Microscopy
TEOS	Tetraethyl orthosilicate
TGA	Thermogravimetric Analysis
XRD	X-Ray Diffraction

Chapter 1

General Introduction

1.1. A brief history of Coordination Polymers (CPs).

At the beginning of the 18th century, the first Coordination Polymer (CP), Prussian Blue, was discovered. As so many times it has occurred in the history of science, its discovery was a combination of chance and observation, sometimes called serendipity. The conventional story of the invention of this CP of formula $\text{Fe}_4[\text{Fe}(\text{CN})_6]_3$ was first told in a book published in 1731, about 25 years after its discovery.¹ This episode took place in Berlin in Dippel's laboratory. Dippel was preparing the so-called animal oil by distillation of animal blood to which potash (potassium carbonate) was added. Concurrently, a colour maker named Diesbach was working in the same laboratory trying to produce Florentine lake, a red pigment based on cochineal red. For this, he needed to add potash to an extract of cochineal (produced by boiling dried cochineal insects with water). However, having no more potash, he borrowed some from Dippel. That potash was contaminated with hexacyanoferrate, and so, the addition of contaminated potash to a solution that already contained iron sulphate resulted in a blue precipitate, the Prussian Blue, instead of the expected red product.² This new pigment was less expensive and more easily produced as compared to other blue pigments that were in use at that time. Today, Prussian Blue is still used as a pigment, but it also has other applications ranging from electrochromics and sensors to poison antidotes (it is included in the "World Health Organization's List of Essential Medicines")³. Despite being used all over the world, it was not until 1977 that its crystalline structure was solved.⁴ Today, it is known that Prussian Blue is a CP with a 3D cubic structure built up from the combination of Fe(II) and Fe(III) centres connected between them through cyanide organic ligands, resulting in a mixed valence polycyanide compound with a characteristic strong colour blue.

In the intervening years, between Prussian's blue discovery and its crystalline structure solving in 1977, little attention was paid to CPs compared to purely organic or inorganic solids, and only a few structural studies were reported. At the end of the 1940s, Powell and Rayner determined the structure of the Hofmann clathrate⁵, a coordination polymer of formula $\text{Ni}(\text{CN})_4\text{Ni}(\text{NH}_3)_2 \cdot 2\text{C}_6\text{H}_6$ that contained two benzene guest molecules. Few years later, in 1968, Iwamoto and co-workers extended those studies to other clathrate compounds of general formula $\text{M}(\text{NH}_3)_2\text{M}'(\text{CN})_4 \cdot 2\text{G}$ (G=guest).⁶ In 1959, Saito *et al.* determined the structure of Bis(adiponitrilo)copper(I) nitrate.⁷ The 1D chain structures of $\text{Ag}(\text{PZ})(\text{NO}_3)$ and $\text{Cu}(\text{PZ})(\text{NO}_3)_2$ (PZ=pyrazine) were reported in 1966⁸ and 1970,⁹ respectively.

At that point, new CP structures might have been accumulated without any judgement. However, in 1977 Prof. A. F. Wells published a very careful work entitled "Three-dimensional nets and polyhedra", in which he introduced the concept that crystal structures could be seen as networks by reducing them to well-defined nodes and connections.¹⁰ Later on, in a short communication published in 1989¹¹ and a subsequent full paper in 1990¹², Prof. Robson applied Well's approach to describe a family of CPs as *"solid polymeric materials (...) afforded by linking together centers with either a tetrahedral or an octahedral array of valencies by rod-like connecting units"*. Remarkably, he already predicted some of the most interesting properties of CPs: *"When models of 3D networks based on tetrahedral centers are constructed, a very striking feature is the relatively large size of the cavities and windows produced even by rods of only modest length. Lattices of this general type (...) may show interesting molecular sieve and ion exchange properties, they may have unusual mechanical and electrical properties, and they may, after*

*appropriate functionalization of the rods, provide tailor-made materials for heterogeneous catalysis (...)*¹¹. Properties predicted by Prof. Robson has become today some of the most distinctive traits of CPs such as their tunability, potential porosity, guest exchange or catalytical capacity. Six years later, in 1995 Prof. Yaghi confirmed the potential of Robson's thesis by reporting the synthesis of a crystalline, metal-organic, open-framework CP of formula $\text{Cu}(\text{4,4'-bpy})_{1.5}\text{NO}_3(\text{H}_2\text{O})_{1.25}$. They showed that the structure contained large rectangular channels filled by nitrate ions and that these nitrates could be exchanged by other anions, demonstrating for the first time that channels in CPs could be accessible. Yaghi referred to such porous CPs as Metal-Organic Frameworks (MOFs).

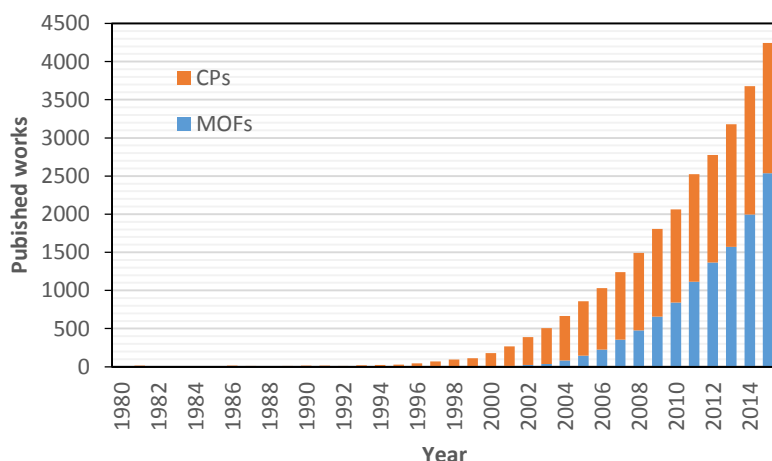


Figure 1.1. The bar chart shows the evolution of published works about CP and/or MOFs in the last decades.

Since the publication of the first CPs structures until today, the research in the field has experienced an unstoppable growth as the exponential increase of publications evidences (Figure 1.1).

1.2. What is a coordination polymer?

Coordination polymers (CPs) are metal-ligand assemblies that extend infinitely into one, two or three dimensions (1D, 2D or 3D) *via* metal-ligand bonding (*a.k.a.* dative covalent bond or coordinate bond). The ligand must be a bridging organic molecule. This requires the use of multidentate ligands with at least two or more donor atoms. At least in one dimension, the metal atoms must be exclusively bridged by the organic ligand. Furthermore, at least one carbon atom must lie between the donor atoms. This definition proposed by Prof. Janiak in 2002¹³ is schematically represented in Figure 1.2.

Prof. Janiak's definition excludes from being classified as CPs those organyloxides (RO^-), organophosphonates (RPO_3^{2-}) or organosulphonates (RSO_3^-) which bridge with their one inorganic end group only. It also does not include metal-ligand assemblies where the metal-organic connectivity is interrupted by inorganic bridges or where an extended inorganic metal-ligand network is lined by only terminal organic ligands. All these should be called "organic-inorganic hybrid-materials" (Figure 1.3). On the other hand, the supramolecular architectures of metal complexes created by purely hydrogen bonding should neither be considered as CPs.

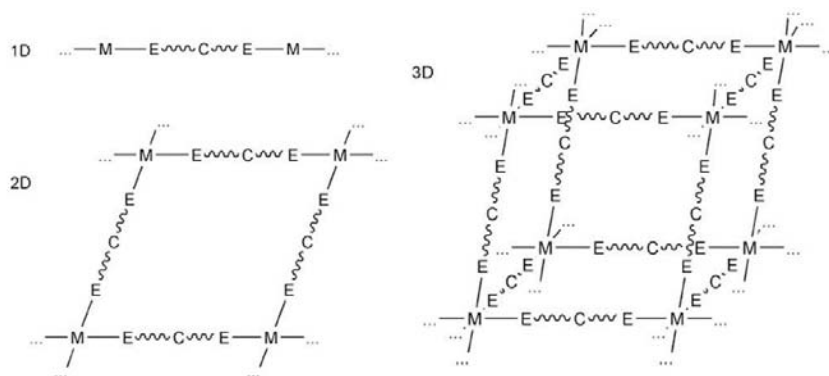


Figure 1.2. Schematic representation of the definition of 1D, 2D or 3D coordination polymers having organic bridging ligands with at least one carbon atom in-between the donor atoms (E).¹³

In this respect, IUPAC define a metal-organic framework, abbreviated to MOF as a coordination network with organic ligands containing potential voids.¹⁴ Furthermore, in its recommendations, IUPAC also explicitly discourage the use of the term “hybrid organic-inorganic materials” to refer to CPs or MOFs.

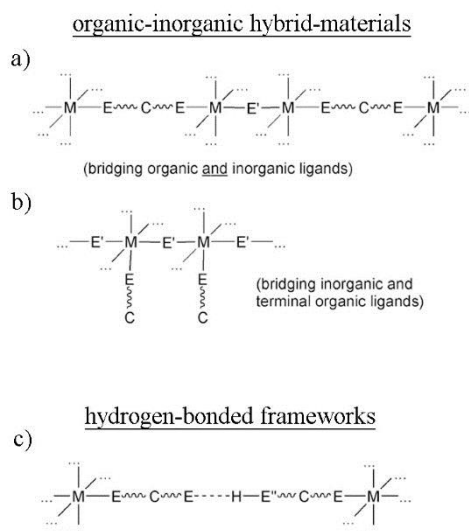


Figure 1.3. Schematic representations of materials that should not be mistaken as CP: (a) Metal-ligand assemblies where the metal-organic connectivity is interrupted by inorganic bridges (b) Inorganic metal-ligand networks lined by only terminal organic ligands and (c) supramolecular architectures of metal complexes created by purely hydrogen bonding.¹³

1.3. Crystal engineering and applications of CPs.

The term “Crystal engineering” was defined in 1988 by Gautam Desiraju as “*the understanding of intermolecular interactions in the context of crystal packing and the utilization of such understanding in the design of new solids with desired physical and chemical properties*”. CPs as metal-ligands assemblies held up by coordinative bonds are part of the field of study of crystal engineering. They are solid materials formed by infinite arrays of organic molecules (*a.k.a.* bridging ligands or linkers) and metals/metal clusters. Furthermore, they are often crystalline materials and as such can be characterized by X-ray diffraction (XRD) techniques.

CPs are held up by coordinative bonds established between metals and organic ligand's donor atoms. Coordinative bonds are stronger than other weak interactions and have high directionality. It is this directionality, indeed, which plays a crucial role in the ability to predict topology and structure of CPs. Directionality of coordinative bonds gives rise to coordination molecular geometry; that is, the geometrical pattern formed by the donor atoms around a central metal ion. Coordination molecular geometry depends mainly on the nature of the central metal ion but also on the hardness of the donor atoms. Therefore, a judicious choice of the metal ion and the ligand can help to predict the coordination geometry of the metals inside the CPs. On the other hand, organic ligands play also an important role on controlling the final architecture of CPs. They have to bridge between metal ions, and this requires using multidentate ligands with two or more donor atoms. Such bridging ligands are called di-, tri- tetratopic, etc., depending on the number of donor atoms. The diversity of organic molecules is also the basis for the variety in structural topologies. Furthermore, by selecting the organic ligand, one also aims to tune the physicochemical properties and, thus, realize various applications such as catalysis, electrical conductivity, luminescence, magnetism, gas sorption, etc. Control of topology and physicochemical properties of CPs by the judicious choice of the ligand constitutes the basis of the "linker design" approach,¹⁵ to which many effort in the last decades have been dedicated. The myriad of applications that CPs can have is consequence of the unlimited combinations in terms of metal nodes and organic linkers, together with the possibility of modifying the organic linkers. Thereby, offering infinite possibilities for the formation of new networks with novel architectures and advanced applications. Offering a detailed index of all the applications to which CPs haven been postulated is out of the scope of this introduction. Nevertheless, it is worthy to mention gas storage/gas separation and catalysis as the most relevant applications:

- Gas storage and gas separation: Potential porosity of some CPs/MOFs enables them to be used as adsorbents for gases. The first example of reversible gas adsorption was provided by Kitagawa *et al.* in 1997, in a 1D CP of general formula $M_2(4,4'\text{-BPY})_3(\text{NO}_3)_4$ ($M=\text{Co, Ni, Zn}$ and $\text{BPY}=4,4'\text{-bipyridine}$). They proved that this CP could adsorb gas molecules (O_2 , CH_4 and N_2) at high pressure.¹⁶ This storage capacity early attracted researchers' attention to the increase of the porosity reaching today unprecedented surface areas that exceed $7,000 \text{ m}^2\cdot\text{g}^{-1}$, as in NU-110.¹⁷ The interest expanded to other gases, being the most important H_2 ¹⁸⁻²¹ and CH_4 ²²⁻²⁵ for their applications as alternative fuel, and CO_2 for being responsible of the anthropogenic greenhouse effect.^{26,27} Furthermore, the different affinity of CPs to different gases can also be used to separate mixtures of gases.²⁸

- Catalysis: CPs have several properties that make them attractive for catalysis. These properties are an ordered arrangement of the active metals centres along with a potential porosity and chirality. Nonetheless, their use suffers also from drawbacks such as low thermal or chemical stability, especially compared to zeolites. Excellent reviews have been published summarizing the catalytical properties of porous^{29,30} and non-porous CPs.¹³

Furthermore, CPs encounter applications in many other fields such as conductivity,^{13,31} luminescence,^{13,32,33} magnetism,^{13,34} spin-transition behaviour,¹³ non-linear optics,^{13,35} etc.

1.4. Coordination polymers for biomedicine.

Apart from the above mentioned applications, in the last years, CPs have appeared as good candidates to respond some of the challenges raised in the field of biomedicine. These challenges are the administration of poor soluble drugs, the administration of species with low blood circulation half-life, the selective targeting to specific tissues, and reducing the systemic toxicity of certain therapeutic/diagnostic systems, among others.

In this context, CP particles offer interesting properties as vehicles for the delivery of therapeutic and diagnostic substances. First of all, CPs can have regular porous systems. These pores can also be tuned in size and hydrophilicity/hydrophobicity by the judicious choice of the ligand and thereby, a wide range of substances can be encapsulated. Second, the infinite number of combinations of metals and ligands opens up the use of bioactive species as building blocks for the construction of new CPs (Figure 1.4). Third, the medium to high strength of the metal-ligand coordinative bond facilitate the production of more biodegradable particles (especially when compared to inorganic materials such as silica or zeolites). Last but not least, CPs have been successfully down-scaled in the form of CP particles (*a.k.a.* Nanoscale MOFs or NMOFs) by diverse technologies ranging from emulsion-based methods,^{36–38} use of hard templates,^{39,40} fast precipitation,^{41,42} microwave radiation,⁴³ to spray-drying.⁴⁴ Miniaturisation of CPs at the nanoscale is important since nanoparticles have demonstrated to be preferentially accumulated in tumours due to the Enhanced Permeability Retention (EPR) effect.^{45,46}



Figure 1.4. The use of biomedically active species as building blocks for the formation of new CP is a highly efficient way of incorporating these substances in high yields.⁶¹

The most relevant uses of CP particles in biomedicine have been for therapeutics (esp. drug delivery) and diagnostics (esp. medical imaging). Moreover, there is recently the tendency of incorporating therapeutical substances together with diagnostic systems. This combination of diagnostics and therapy has been named *theranostics*.

1.4.1. CP particles for therapeutics. Drug delivery.

Therapeutics is the attempted remediation of a disease. Very often, medical therapies consist on the administration of drugs. Different strategies to incorporate therapeutic species in CPs have been used. Henceforth we show some relevant examples.

1.4.1.1. Incorporation of therapeutic organic molecules in the pores of CP particles.

This strategy to incorporate drugs into the CP's pore system is carried out by immersing the activated CP particles in a concentrated solution of the target molecule. This strategy is highly versatile as

the same CP can be used to adsorb a wide range of molecules, with the limitation of the relative size between the target molecule and the pore aperture. However, as the interactions between the adsorbant and the adsorbate are only of the weak supramolecular type, the encapsulation becomes a reversible process that can lead to low yields of encapsulation and fast cargo releases.

For instance, Horcajada *et al.* have widely used this strategy to encapsulate various drugs using different members of the MIL family. In 2006, the authors used the rigid MIL-100 and MIL-101, two CPs built up by Cr(III) and BTC or BDC, respectively, to encapsulate Ibuprofen.⁴⁷ Ibuprofen was adsorbed by the dehydrated powdered materials from a solution in hexane. Interestingly, PXD measurements showed that both materials retained their structures after drug adsorption. MIL-100 adsorbed 0.35 g of Ibuprofen/g of dehydrated MIL-100, whereas MIL-101 adsorbed 1.4 g of Ibuprofen/g of dehydrated MIL-101. Differences in adsorption could be presumably explained by structural reasons as MIL-100 has smaller apertures than MIL-101. Authors also studied kinetics of release of the encapsulated Ibuprofen in simulated body fluid, which took three days in the case of MIL-100 and six days in MIL-101. Even though authors used a Cr(III)-containing material for the study, which is a well-known toxic metals, it can be considered that this was the first time where the remarkable capacity for drug encapsulating and controlled delivery of CP particles was reported.

In 2008, Horcajada and co-workers used the flexible MIL-53(Cr) and its non-toxic counterpart MIL-53(Fe) to study the encapsulation of controlled release of Ibuprofen as a model drug.⁴⁸ Adsorption of Ibuprofen was carried out by immersing previously dehydrated MIL-53(Cr, Fe) solids in hexane solutions containing Ibuprofen. Interestingly, PXRD measurements showed that Ibuprofen containing solids MIL-53(Cr,Fe) structures were in between those of the open and closed structures, indicating a partial pore opening due to encapsulation of Ibuprofen into the pores. The delivery of Ibuprofen in simulated body fluid was studied. Surprisingly, a very slow delivery that was complete only after 3 weeks was observed. Summarizing, this study showed that no substantial differences in the total drug uptake were observed depending on the metal as both MILs showed around 0.21-0.22 g Ibuprofen/g of dehydrated materials. Moreover, authors postulated that the materials might be useful for the design of unique administration therapeutic systems that lead to a stable blood concentration and a minimization of the toxic effects.

More recently, in 2010, Horcajada *et al.* reported a very complete study in which they used some non-toxic iron(III) carboxylate-based CPs (MIL-53, MIL-88A, MIL-88Bt, MIL-89, MIL-100 and MIL-101-NH₂) to test their efficiency as drug carriers of four challenging anticancer or antiviral drugs (busulfan (Bu), azidothymidine triphosphate (AZT-TP), cidofovir (CDV) and doxorubicin (Dox)) in addition to other model drugs (Ibuprofen, caffeine, urea, etc. see Figure 1.5).⁴¹ Authors also adapted the synthetic conditions to obtain these materials as nanoparticles. Interestingly, there was a high diversity of encapsulation yields depending on the combination of drug and carrier, ranging from the lowest of 2.8 g AZT-TP/g MIL-53 to the highest value of 90.4 g AZT-TP/g MIL-101-NH₂.

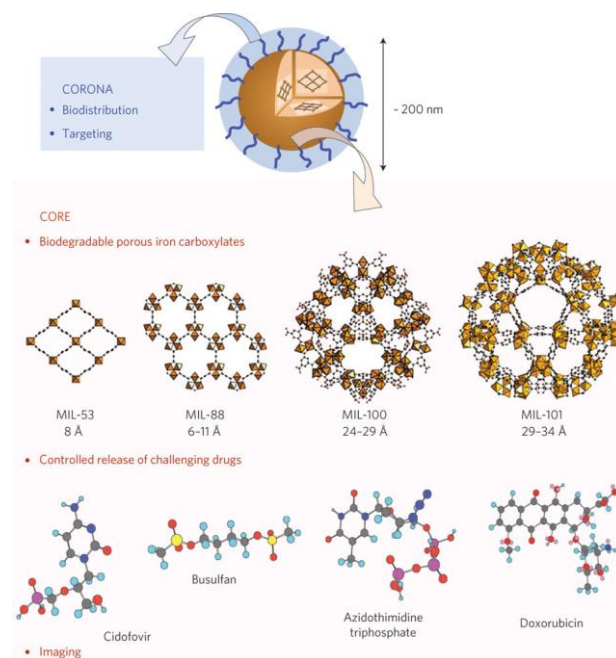


Figure 1.5. Horcajada *et al.* used different iron(III) carboxylate-based CP to test the encapsulation of some challenging anticancer and antiviral drugs.⁴¹

1.4.1.2. Incorporation of therapeutic gases in the pores of the CP particles.

The well-studied capacities of porous CPs to capture and storage gases can be used also with therapeutic purposes as it is known that some gases play important biological roles as signalling molecules (NO, H₂S, CO, etc.). For instance, NO is a key vertebrate biological messenger, contributing to vessel homeostasis by inhibiting vascular smooth muscle contraction, among others. In this respect, Morris *et al.* studied the capacity of HKUST-1 and Ni/Co-CPO-27 for the storage and delivery of NO. The strategy relies on the strong interaction between NO and the mentioned materials to store the gas for long periods (up to 2 years) but with easy and controllable triggered release on exposure to moisture.^{49–52}

1.4.1.3. Incorporation of therapeutic organic molecules as linkers.

This strategy to incorporate relevant therapeutic molecules takes advantage of the versatility of composition in CPs. This strategy has as the main advantage the high loading yields achieved. On the other hand, therapeutic molecules are not specifically designed for CP synthesis, and consequently its use as bridging ligands can result challenging.

For instance, in 2010, Serre *et al.* described for the first time the direct coupling of a bioactive molecule to a metal to build a MOF, in which the bioactive molecule acted as the bridging ligand of the structure.⁵³ They announced that this new approach would avoid the necessity of large pores and volumes required to achieve high loadings of a drug. In this new approach, the release of the biomolecule is achieved through the biodegradation of the CP particles. They used nicotinic acid (*a.k.a.* niacin) as bridging ligand and the non-toxic iron as the connecting node of the framework. Nicotinic acid is a drug that has demonstrated pellagra-curative, vasodilating and antilipemic properties. They named the new CP based on Fe(III)/Fe(II) and nicotinic acid as BioMIL-1. Its structure consisted on a three-

dimensionally connected framework built up from trimeric $\text{Fe}_3\text{N}_3\text{O}_{13}$ units linked together via nicotinate molecules (Figure 1.6).

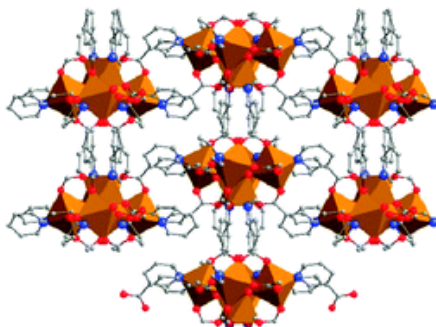


Figure 1.6. Crystal structure of BioMIL-1 showing the 3-D framework built up from trimeric $\text{Fe}_3\text{N}_3\text{O}_{13}$ units linked together via nicotinate molecules.⁵³

The biodegradable character of the as-prepared materials was studied under physiological conditions (PBS buffer, pH=7.4, 37°C). The degradation of the materials occurred in about one hour. Although the degradation of the CPs took place very fast under physiological conditions, these authors demonstrated that with their approach is possible to incorporate biomedically active ligands in very high yields (75% wt.)

1.4.1.4. Incorporation of therapeutic metal complexes as linkers.

Although there are not so many examples of metals used as active ingredients compared to organic molecules, there exists a handful of examples of metals being used for therapeutic purposes. Particularly well-known is the case of platinum-based antineoplastic drugs. They are coordination complexes of platinum used to treat cancer. Although this kind of drugs are used to treat nearly the half of cancer patients, they are also affected by serious side effects. Nanotechnology has been proposed to deliver these drugs in a more efficient and targeted way and, in this sense, CP particles might be a good strategy of delivery. In 2008, Lin *et al.* used a Pt-based drug (disuccinatocisplatin or DSCP, see figure 1.7) as the linker and Tb(III) as the connecting node for the design of a new CP particles.⁵⁴

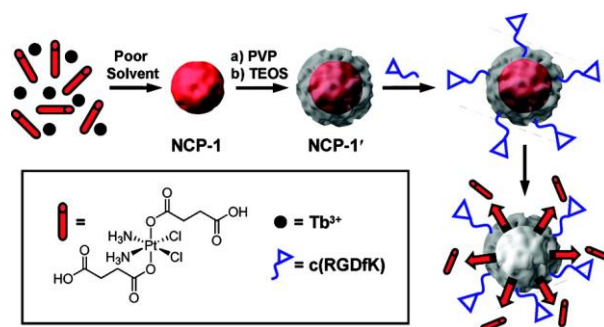


Figure 1.7. Strategy for the construction of a new CP particles based on disuccinatocisplatin (DSCP) as bridging ligand and Tb(III) as connecting node.⁵⁴

As Figure 1.7 shows, these CP particles (named **NCP-1**), were precipitated from an aqueous solutions of the components via the addition of a poor solvent. The as-synthesised CP particles exhibited spherical

morphology (Figure 1.8) and they were amorphous. Induced Coupled Plasma-Mass Spectrometry (ICP-MS) and Thermogravimetric analysis (TGA) confirmed the empirical formula $\text{Tb}_2(\text{DSCP})_3(\text{H}_2\text{O})_{12}$. In order to stabilize the CP particles against dissolution in water, the authors encapsulated them in shells of amorphous silica. In the coating procedure, PVP-functionalized particles were treated with tetraethyl orthosilicate (TEOS). The authors investigated the controlled release of the silica-coated particles against HEPES buffer (pH 7.4, 37°C), demonstrating that the release of the Pt drug can be controlled by varying the silica shell thickness. The half-lives of dissolution were 5.5 h for 2 nm thick particles and 9 h for 7 nm thick ones, whereas non-coated particles had a half-life of 1 h. Finally, the authors grafted silica coated nanoparticles with the cyclic peptide c(RGDfK) to enhance the cellular uptake of the CP particles.

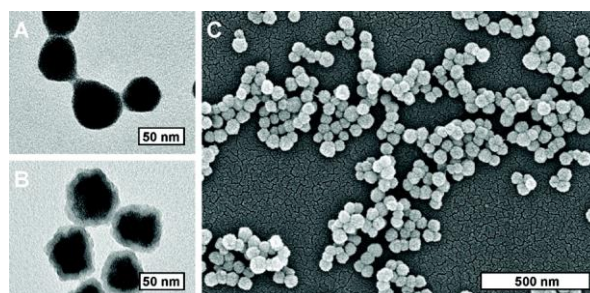


Figure 1.8. Electron microscopy images of NCP-1 showing their spherical morphology.

1.4.2. CP particles for diagnostics. Medical imaging.

Medical diagnosis is the analysis of the cause of a health problem or disease. Very often a correct diagnostic can only be achieved with the help of medical imaging. Medical imaging is defined as the collection of techniques and processes for creating visual representation of the interior of the body as well as the function of some organs and tissues. Computed tomography (CT) or Magnetic Resonance Imaging (MRI) are among the most spread medical imaging techniques. On the other hand, techniques such as fluorescence imaging or ParaCEST MRI are emerging technologies with promising applications. Interestingly, techniques such as CT or MRI do not need the use of any active ingredient to form images. However, it is very common the use of specific substances to enhance the contrast between healthy and diseased tissues. These substances are called Contrast Agents (CAs). Conversely, techniques such as fluorescence imaging or ParaCEST MRI necessarily need the use of CAs to form images. CAs can be very varied, ranging from iodinated organic molecules used in CT to gadolinium chelates for MRI. However, in general terms and depending on the nature of the active substance, we can classify them as organic molecules or metal ions. Henceforth, different strategies to incorporate CAs in CPs are shown.

1.4.2.1. Incorporation of organic molecules-based CA as linkers.

Computed tomography (CT) is an imaging technique based on X-ray attenuation by a specimen, and it is used to provide 3D images with excellent spatial resolution. Materials containing high Z number, such as iodine, barium, etc., can be used to increase the contrast of such images. To date, the only CT-CAs approved for clinical uses are iodinated aromatic molecules and barium sulphate for gastrointestinal tract. However, large doses of iodinated aromatic molecules are needed to provide adequate contrast, which can cause adverse reactions in some patients. Thereby, the use of iodinated aromatic molecules in

CP particles has been postulated as a way to overcome these drawbacks by providing high payloads and accumulation at diseased sites.

Therefore, in 2009, Lin and co-workers synthesised five new CPs using 2,3,5,6-tetraiodo-1,4-benzenedicarboxylic (I_4 -BDC- H_2) (Figure 1.9) and Cu(II) or Zn(II) as connecting nodes.⁵⁵ Reaction of I_4 -BDC- H_2 with $Cu(NO_3)_2$ or $Zn(NO_3)_2$ in *N,N*-dimethylformamide (DMF), *N,N*-diethylformamide (DEF), water, and ethanol, or mixtures of them, yielded five different CPs as it is shown in Figure 1.9.

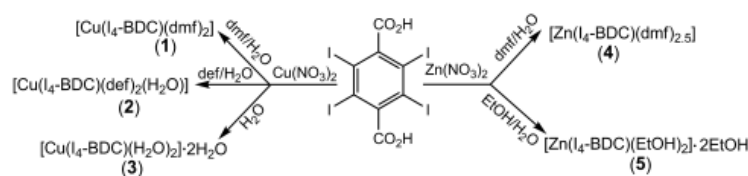


Figure 1.9. The scheme shows conditions for the synthesis of five CP (**1-5**) by reaction of I_4 -BDC- H_2 with $Cu(NO_3)_2$ and $Zn(NO_3)_2$.⁵⁵

SCXRD studies of **1-5** (Figure 1.9.) revealed that all formed one-dimensional (1D) polymeric structures, as it is shown in Figure 1.10.

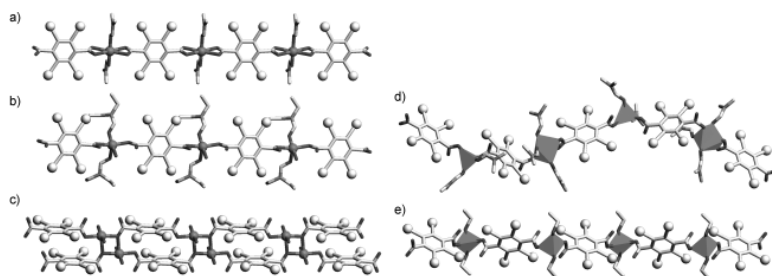


Figure 1.10. Crystal structures of 1-D CP of: (a) $[Cu(I_4-BDC)(dmf)_2]$ (**1**), (b) $[Cu(I_4-BDC)(def)_2(H_2O)]$ (**2**), (c) $[Cu(I_4-BDC)(H_2O)_2] \cdot 2H_2O$ (**3**), (d) $[Zn(I_4-BDC)(dmf)_{2.5}]$ (**4**) and (e) $[Zn(I_4-BDC)(EtOH)_2] \cdot 2EtOH$ (**5**).⁵⁵

Lin *et al.* also produced nanoparticles of **3** and **5**. They were chosen to be down-scaled since they did not contain toxic DMF/DEF coordinated molecules. Nanoparticles of **3** with different morphologies were obtained by using microemulsions, whereas those of **5** were obtained by a rapid precipitation procedure. They also demonstrated that the as-synthesized CP nanoparticles presented the same PXRD patterns that the bulk phases. Then, they used CP nanoparticles of **3** and **5** to conduct phantom studies to evaluate their potential for CT contrast agents. Nanoparticles showed X-ray attenuation coefficients comparable to those of molecular CAs. Finally, the authors also studied their biodegradability dialyzing nanoparticles of **3** against a phosphate buffer (PBS, pH 7.4) at 37°C. The particles were completely dissolved after 46 hours, with a half-life of about 1.5 h, demonstrating their biodegradable nature that is still longer as compared to molecular iodinated contrast agents (<10 min).

1.4.2.2. Incorporation of metal-based CAs as connecting nodes.

Metals have been widely used as CAs for diverse medical imaging techniques. For instance, gadolinium chelates are the most extended CAs for MRI, but also other paramagnetic metal ions, such as Mn(II), Fe(II), etc., are known to have MRI-CA properties. On the other hand, lanthanide ions such as

Eu(III) and Tb(III) are known to be fluorescent with applications in fluorescence imaging. Furthermore, Eu(III) complexes have been used as CA in the emerging ParaCEST MRI. Therefore, there has been a big interest in producing new CP particles containing such imaging active metals in their frameworks. The next examples show that most of the attempts to incorporate active metals consisted on using them as connecting nodes.

In 2006, Lin and co-workers used a water-in-oil microemulsion-based methodology for the synthesis of two nanoscale CPs.³⁷ The combination of GdCl_3 and 1,4-benzenedicarboxylate (BDC) yielded a CP of formula $\text{Gd}(\text{BDC})_{1.5}(\text{H}_2\text{O})_2$. In parallel, they also used the ligand 1,2,4-benzenetricarboxylate to produce a CP of formula $[\text{Gd}(1,2,4\text{-BTC})(\text{H}_2\text{O})_3]\cdot\text{H}_2\text{O}$. Then, they used a suspension of $\text{Gd}(\text{BDC})_{1.5}(\text{H}_2\text{O})_2$ in water (0.1% xanthan gum) to study its potential for MRI, obtaining unprecedented values of r_1 ($35.8 \text{ s}^{-1}\text{mM}^{-1}$). They also found an inverse size dependence for r_1 , consistent with the decreasing surface-to-volume ratio for larger CP particles. Furthermore, the same authors successfully produced luminescent nanorods of $\text{Gd}(\text{BDC})_{1.5}(\text{H}_2\text{O})_2$ by using Eu(III) or Tb(III) as dopants by mixing 5% mol of EuNO_3 or TbNO_3 during the synthesis. Using this strategy, they obtained CP particles that can be potentially used as dual CAs in MRI and fluorescence imaging.

In 2008, Prof. Lin reported the synthesis of CP obtained from the combination of Gd(III) with the bridging ligand benzenehexacarboxylic (BHC).⁵⁶ In this case, they used a surfactant-assisted microemulsion method at 120°C for 18 h to obtain nanocrystals of formula $[\text{Gd}_2(\text{BHC})(\text{H}_2\text{O})_6]$. The crystal structure (Figure 1.11) shows that Gd(III) centres are nine-coordinated, binding to four different BHC ligands, with three water molecules occupying three coordination sites. On the other hand, each BHC ligand binds a total of eight Gd(III) centres. The four-connected Gd(III) centres and eight-connected BHC ligands link to each other to form a 3D CP.

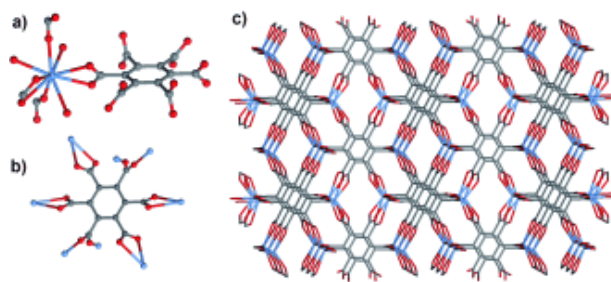


Figure 1.11. (a) Coordination environment of Gd(III), (b) BHC connecting a total of eight Gd(III) centres, and (c) Crystal structure of $[\text{Gd}_2(\text{BHC})(\text{H}_2\text{O})_6]$.⁵⁶

The same year, in 2008, Prof. Lin reported the synthesis of a Mn(II)-based CP for MRI.⁵⁷ Although the good relaxivity values obtained in the previous reported examples of $\text{Gd}(\text{BDC})_{1.5}(\text{H}_2\text{O})_2$ ³⁷ and $\text{Gd}_2(\text{BHC})(\text{H}_2\text{O})_6$,⁵⁶ the toxicity of leached Gd(III) free ions precludes any clinical application of these CP particles. Thereby, the authors proposed the use of Mn(II) centres, which are supposedly less toxic than Gd(III). Combination of Mn(II) ions with BDC and BTC in reverse-phase microemulsions yielded CP particles of the previously reported phase $\text{Mn}(\text{BDC})(\text{H}_2\text{O})_2$, in addition to nanoparticles of formula $\text{Mn}_3(\text{BTC})_2(\text{H}_2\text{O})_6$ that do not correspond to any known phase. Silica coated nanoparticles of

$\text{Mn}_3(\text{BTC})_2(\text{H}_2\text{O})_6$ were prepared by base-catalyzed condensation of TEOS on PVP-modified particles. Although r_1 of the CP particles was modest, authors hypothesised that they can become an efficient vehicle for delivery of large doses of Mn(II) ions, which exhibit very high r_1 values inside cells. Thereby, they also evaluated leaching of $\text{Mn}_3(\text{BTC})_2(\text{H}_2\text{O})_6$ and its silica-coated counterpart. Leaching studies indicated that the silica coated $\text{Mn}_3(\text{BTC})_2(\text{H}_2\text{O})_6$ particles and uncoated had half-lives of 7.5 h and 3.5 h in H_2O , respectively (Figure 1.12), whereas half-lives were reduced to 1.44 h and 18 min in PBS buffer.

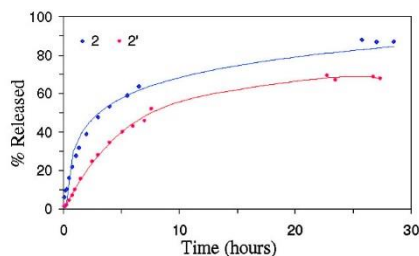


Figure 1.12. Dissolution curves of uncoated (blue) and silica-coated (red) $\text{Mn}_3(\text{BTC})_2(\text{H}_2\text{O})_6$ nanoparticles in water at 37°C (% released vs. time).

In 2010, Horcajada *et al.*, in a previously commented example, synthesised some non-toxic Fe (III) carboxylate MOFs and adapted their synthesis conditions to obtain these materials as nanoparticles.⁴¹ They studied their efficiency to encapsulate anticancer and antiviral drugs. Interestingly, they also evaluated the potential of one of them, MIL-88A nanoparticles, as MRI-CAs on Wistar female rats. Acquired images show that the treated organs were darker than the normal ones (Figure 1.13). Relaxivity r_2 values were measured, being of the order of $50 \text{ s}^{-1}\text{mM}^{-1}$.

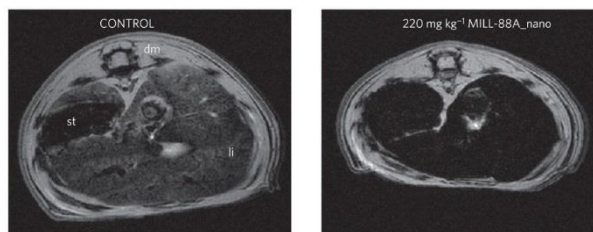


Figure 1.13. Acquired MRI images show that organs treated with MIL-88A nanoparticles were darker than normal ones.

1.5 Toxicity of leached toxic metal ions in CPs.

In the previous section, several examples of CPs incorporating lanthanide ions as connecting nodes have been shown. We have seen that this approach constitutes an interesting strategy for the fabrication of CP particles for applications in medical imaging. However, those examples also showed that as-synthesised CPs were unstable to dissolution in different media (water, PBS buffer, simulated body fluid, etc.) with half-lives that can range from minutes to hours. Such instability is a major issue that prevents any clinical use of CP particles. Indeed, very recently, in 2006, reports of a rare systemic fibrosing condition called nephrogenic systemic fibrosis (NSF) were linked to exposure of patients with advanced kidney disease to Gd(III) ions⁵⁸.

In order to overcome toxicity problems in gadolinium-based CP particles, different approaches have been proposed. First approach consists on substituting Gd(III) by other paramagnetic metals less toxic such as manganese⁵⁷ or iron⁴¹. However this strategy is not completely satisfactory since these metals are not such efficient r_1 CAs as Gd(III). Second approach relies on coating the CP particles with polymers to increase their half-lives, and consequently, reducing Gd(III) leaching. In this respect, silica coatings^{54,57} and RAFT polymerizations^{59,60} have been used. Unfortunately, although half-lives could be increased, Gd(III) leaching was not been totally avoided. **The third approach was proposed in our group and it is unprecedented to date. It consists on using gadolinium complexes as linkers for the design of new CPs.** In this way, if the CP particles are dissolved in the body, safe gadolinium complexes will be released, instead of free Gd(III) ions, which are the actual toxic species.

Actually, when one examines the current gadolinium-based MRI-CAs approved for clinical uses, it is seen that all of them consist on chelates formed between Gd(III) ions and aminopolycarboxylic acids (Figure 1.14). Aminopolycarboxylic acids are a group of organic molecules related with ethylenediaminetetraacetic acid (EDTA), which are well-known for its chelating ability. Aminopolycarboxylic acids of Figure 1.14 can be classified as acyclic or cyclic. The latter are also named as polyazamacrocyclic ligands. Taking into account the toxicity of free Gd(III) and its probable association with NSF disease, the European Medicines Agency (EMA) classified gadolinium-based agents into three risk groups, depending on their likelihood of releasing Gd(III) inside the body (Figure 1.14). Interestingly, acyclic complexes having neutral charge are more likely to release Gd(III), acyclic complexes negatively charged have an intermediate likelihood, whereas polyazamacrocyclic complexes have the lowest probability and are considered to be the safest.

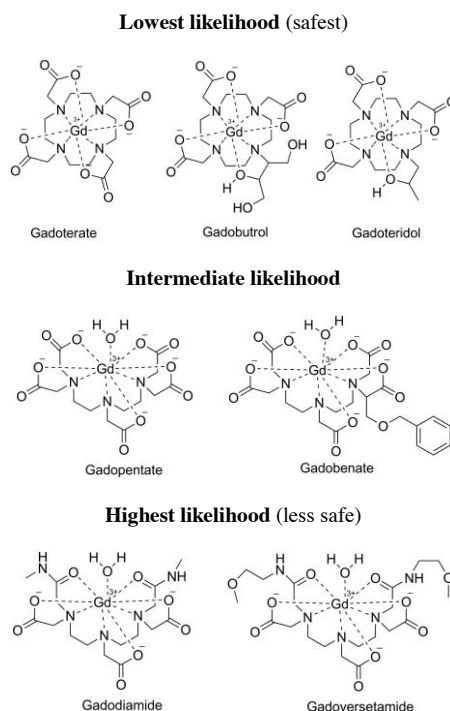


Figure 1.14. Clinical approved MRI CA classified by their likelihood of releasing free Gd(III).

Taking into account EMA classification, cyclic complexes (or polyazamacrocyclic complexes) have been chosen to be used as linkers for the design of new CPs for CA applications, following the above-mentioned **third approach**. This constitutes one of the main objectives of this Thesis and will be explained more in detail in the next **Chapter 2**.

1.6. References.

1. Stahl, G. E. Experimenta, observationes, animadversiones, CCC Numero Chymicae et Physicae. (1731).
2. Kraft, A. On the discovery and history of Prussian Blue. *Bull. Hist. Chem.* **33**, 61–67 (2008).
3. WHO Model List of Essential Medicines, 19th List. *WHO Model List Essent. Med. 19th List* (2015).
4. Buser, H. J., Schwarzenbach, D., Petter, W. & Ludi, A. The crystal structure of Prussian Blue: $\text{Fe}_4[\text{Fe}(\text{CN})_6]_3 \cdot x\text{H}_2\text{O}$. *Inorg. Chem.* **16**, 2704–2710 (1977).
5. Powell, H. M. & Rayner, J. H. Clathrate compound formed by benzene with an ammonia–nickel cyanide complex. *Nature* **163**, 566–567 (1949).
6. Iwamoto, T. *et al.* The Hofman-type clathrate: $\text{M}(\text{NH}_3)_2\text{M}'(\text{CN})_4 \cdot 2\text{G}$. *Inorganica Chim. Acta* **2**, 313–316 (1968).
7. Kinoshita, Y., Matsubara, I., Higuchi, T. & Saito, Y. The crystal structure of bis(adiponitrilo)copper(I) nitrate. *Bull. Chem. Soc. Jpn.* **32**, 1221–1226 (1959).
8. Vranka, R. G. & Amma, E. L. Metal ion–aromatic complexes. II. The crystal structure of the 1:1 silver nitrate–pyrazine complex. *Inorg. Chem.* **5**, 1020–1025 (1966).
9. Santoro, A., Mighell, A. D. & Reimann, C. W. The crystal structure of a 1:1 cupric nitrate–pyrazine complex $\text{Cu}(\text{NO}_3)_2 \cdot (\text{C}_4\text{N}_2\text{H}_4)$. *Acta Crystallogr. Sect. B Struct. Crystallogr. Cryst. Chem.* **26**, 979–984 (1970).
10. Wells, A. F. Three-dimensional nets and polyhedra. (John Wiley & Sons, Ltd., 1977).
11. Hoskins, B. F. & Robson, R. Infinite polymeric frameworks consisting of three dimensionally linked rod-like segments. *J. Am. Chem. Soc.* **111**, 5962–5964 (1989).
12. Hoskins, B. F. & Robson, R. Design and construction of a new class of scaffolding-like materials comprising infinite polymeric frameworks of 3D-linked molecular rods. *J. Am. Chem. Soc.* **112**, 1546–1554 (1990).
13. Janiak, C. Engineering coordination polymers towards applications. *Dalt. Trans.* 2781–2804 (2003). at <<http://pubs.rsc.org/en/content/articlehtml/2003/dt/b305705b>>
14. Batten, S. R. *et al.* Terminology of metal–organic frameworks and coordination polymers (IUPAC Recommendations 2013). *Pure Appl. Chem.* **85**, 1715–1724 (2013).
15. Lu, W. *et al.* Tuning the structure and function of metal–organic frameworks via linker design. *Chem. Soc. Rev.* **43**, 5561–5593 (2014).
16. Kondo, M., Yoshitomi, T., Matsuzaka, H., Kitagawa, S. & Seki, K. three-dimensional framework with channeling cavities for small molecules: $\{[\text{M}_2(4, 4'\text{-bpy})_3(\text{NO}_3)_4] \cdot x\text{H}_2\text{O}\}_n$ (M= Co, Ni, Zn).

- Angew. Chemie Int. Ed.* **36**, 1725–1727 (1997).
17. Farha, O. K. *et al.* Metal-organic framework materials with ultrahigh surface areas: is the sky the limit? *J. Am. Chem. Soc.* **134**, 15016–15021 (2012).
 18. Rosi, N. L. *et al.* Hydrogen storage in microporous metal-organic frameworks. *Science* **300**, 1127–1129 (2003).
 19. Rowsell, J. L. C. & Yaghi, O. M. Strategies for hydrogen storage in Metal-Organic Frameworks. *Angew. Chemie Int. Ed.* **44**, 4670–4679 (2005).
 20. Murray, L. J., Dincă, M. & Long, J. R. Hydrogen storage in metal–organic frameworks. *Chem. Soc. Rev.* **38**, 1294–1314 (2009).
 21. Suh, M. P., Park, H. J., Prasad, T. K. & Lim, D.-W. Hydrogen storage in Metal–Organic Frameworks. *Chem. Rev.* **112**, 782–835 (2012).
 22. Eddaoudi, M. *et al.* Systematic design of pore size and functionality in isoreticular MOFs and their application in methane storage. *Science* (80-.). **295**, 469–472 (2002).
 23. Guo, Z. *et al.* A Metal-Organic Framework with optimized open metal sites and pore spaces for high methane storage at room temperature. *Angew. Chemie Int. Ed.* **50**, 3178–3181 (2011).
 24. Dören, T., Sarkisov, L., Yaghi, O. M. & Snurr, R. Q. Design of new materials for methane storage. *Langmuir* **20**, 2683–2689 (2004).
 25. Konstas, K. *et al.* Methane storage in metal organic frameworks. *J. Mater. Chem.* **22**, 16698–16708 (2012).
 26. Sumida, K. *et al.* Carbon dioxide capture in Metal–Organic Frameworks. *Chem. Rev.* **112**, 724–781 (2012).
 27. Millward, A. R. & Yaghi, O. M. Metal–Organic Frameworks with exceptionally high capacity for storage of carbon dioxide at room temperature. *J. Am. Chem. Soc.* **127**, 17998–17999 (2005).
 28. Li, J.-R., Sculley, J. & Zhou, H.-C. Metal–Organic Frameworks for separations. *Chem. Rev.* **112**, 869–932 (2012).
 29. García-García, P., Müller, M. & Corma, A. MOF catalysis in relation to their homogeneous counterparts and conventional solid catalysts. *Chem. Sci.* **5**, 2979–3007 (2014).
 30. Lee, J. *et al.* Metal–organic framework materials as catalysts. *Chem. Soc. Rev.* **38**, 1450–1459 (2009).
 31. Givaja, G., Amo-Ochoa, P., Gómez-García, C. J. & Zamora, F. Electrical conductive coordination polymers. *Chem. Soc. Rev.* **41**, 115–147 (2012).
 32. Heine, J. & Müller-Buschbaum, K. Engineering metal-based luminescence in coordination polymers and metal–organic frameworks. *Chem. Soc. Rev.* **42**, 9232–9242 (2013).

33. Allendorf, M. D., Bauer, C. A., Bhakta, R. K. & Houk, R. J. T. Luminescent metal–organic frameworks. *Chem. Soc. Rev.* **38**, 1330–1352 (2009).
34. Batten, S. R. & Murray, K. S. Structure and magnetism of coordination polymers containing dicyanamide and tricyanomethanide. *Coord. Chem. Rev.* **246**, 103–130 (2003).
35. Wang, C., Zhang, T. & Lin, W. Rational synthesis of noncentrosymmetric Metal–Organic Frameworks for second-order nonlinear optics. *Chem. Rev.* **112**, 1084–1104 (2012).
36. Vaucher, S., Li, M. & Mann, S. Synthesis of prussian blue nanoparticles and nanocrystal superlattices in reverse microemulsions. *Angew. Chemie Int. Ed.* **39**, 1793–1796 (2000).
37. Rieter, W. J., Taylor, K. M. L., An, H., Lin, W. & Lin, W. Nanoscale metal-organic frameworks as potential multimodal contrast enhancing agents. *J. Am. Chem. Soc.* **128**, 9024–9025 (2006).
38. Liang, G., Xu, J. & Wang, X. Synthesis and characterization of organometallic coordination polymer nanoshells of prussian blue using miniemulsion periphery polymerization (MEPP). *J. Am. Chem. Soc.* **131**, 5378–5379 (2009).
39. Hou, S., Harrell, C. C., Trofin, L., Kohli, P. & Martin, C. R. Layer-by-layer nanotube template synthesis. *J. Am. Chem. Soc.* **126**, 5674–5675 (2004).
40. Lee, H. J. *et al.* Advanced fabrication of metal–organic frameworks: template-directed formation of polystyrene@ZIF-8 core–shell and hollow ZIF-8 microspheres. *Chem. Commun.* **48**, 221–223 (2012).
41. Horcajada, P. *et al.* Porous metal-organic-framework nanoscale carriers as a potential platform for drug delivery and imaging. *Nat. Mater.* **9**, 172–178 (2010).
42. Chalati, T. *et al.* Optimisation of the synthesis of MOF nanoparticles made of flexible porous iron fumarate MIL-88A. *J. Mater. Chem.* **21**, 2220–2227 (2011).
43. Ni, Z. & Masel, R. I. Rapid Production of Metal–Organic Frameworks via microwave-assisted solvothermal synthesis. *J. Am. Chem. Soc.* **128**, 12394–12395 (2006).
44. Carné-Sánchez, A., Imaz, I., Cano-Sarabia, M. & Maspoch, D. A spray-drying strategy for synthesis of nanoscale metal–organic frameworks and their assembly into hollow superstructures. *Nat. Chem.* **5**, 203–211 (2013).
45. Matsumura, Y. & Maeda, H. A new concept for macromolecular therapeutics in cancer chemotherapy: mechanism of tumoritropic accumulation of proteins and the antitumor agent smancs. *Cancer Res.* **46**, 6387–6392 (1986).
46. Dreher, M. R. *et al.* Tumor vascular permeability, accumulation, and penetration of macromolecular drug carriers. *J. Natl. Cancer Inst.* **98**, 335–344 (2006).
47. Horcajada, P. *et al.* Metal–Organic Frameworks as efficient materials for drug delivery. *Angew. Chemie* **118**, 6120–6124 (2006).

48. Horcajada, P. *et al.* Flexible porous Metal-Organic Frameworks for a controlled drug delivery. *J. Am. Chem. Soc.* **130**, 6774–6780 (2008).
49. Hinks, N. J., McKinlay, A. C., Xiao, B., Wheatley, P. S. & Morris, R. E. Metal-Organic Frameworks as NO delivery materials for biological applications. *Microporous Mesoporous Mater.* **129**, 330–334 (2010).
50. McKinlay, A. C. *et al.* Exceptional behavior over the whole adsorption–storage–delivery cycle for NO in porous Metal Organic Frameworks. *J. Am. Chem. Soc.* **130**, 10440–10444 (2008).
51. Xiao, B. *et al.* High-capacity hydrogen and nitric oxide adsorption and storage in a Metal–Organic Framework. *J. Am. Chem. Soc.* **129**, 1203–1209 (2007).
52. Bordiga, S. *et al.* Adsorption properties of HKUST-1 toward hydrogen and other small molecules monitored by IR. *Phys. Chem. Chem. Phys.* **9**, 2676–2685 (2007).
53. Miller, S. R. *et al.* Biodegradable therapeutic MOFs for the delivery of bioactive molecules. *Chem. Commun.* **46**, 4526–4528 (2010).
54. Rieter, W. J., Pott, K. M., Taylor, K. M. L. & Lin, W. Nanoscale coordination polymers for platinum-based anticancer drug delivery. *J. Am. Chem. Soc.* **130**, 11584–11585 (2008).
55. DeKrafft, K. *et al.* Iodinated nanoscale coordination polymers as potential contrast agents for computed tomography. *Angew. Chemie Int. Ed.* **48**, 9901–9904 (2009).
56. Taylor, K. M. L., Jin, A. & Lin, W. Surfactant-assisted synthesis of nanoscale gadolinium metal-organic frameworks for potential multimodal imaging. *Angew. Chem. Int. Ed.* **47**, 7722–7725 (2008).
57. Taylor, K. M. L., Rieter, W. J. & Lin, W. Manganese-based nanoscale metal-organic frameworks for magnetic resonance imaging. *J. Am. Chem. Soc.* **130**, 14358–14359 (2008).
58. Perazella, M. A. Current status of gadolinium toxicity in patients with kidney disease. *Clin. J. Am. Soc. Nephrol.* **4**, 461–469 (2009).
59. Rowe, M. D. *et al.* Tuning the magnetic resonance imaging properties of positive contrast agent nanoparticles by surface modification with RAFT polymers. *Langmuir* **25**, 9487–9499 (2009).
60. Rowe, M. D., Thamm, D. H., Kraft, S. L. & Boyes, S. G. Polymer-modified gadolinium metal-organic framework nanoparticles used as multifunctional nanomedicines for the targeted imaging and treatment of cancer. *Biomacromolecules* **10**, 983–993 (2009).
61. Della Rocca, J., Liu, D. & Lin, W. Nanoscale metal-organic frameworks for biomedical imaging and drug delivery. *Acc. Chem. Res.* **44**, 957–968 (2011).

Chapter 2

Objectives

In **Chapter 1**, the different existing strategies to incorporate bioactive species in CPs were introduced. It has been seen that bioactive species can be broadly classified in therapeutic or diagnostic species. Thanks to the versatility of the CPs, both therapeutic and diagnostic species can be incorporated in CP systems either by adsorption in their pore systems or by using active species as building blocks of the structure. In this **Thesis**, we are particularly interested in the design of new CPs for diagnostic purposes, especially as CAs for MRI. It has been postulated that the use of CP particles would help to overcome some of the limitations that the current MRI-CAs encounter. Among these limitations, CP particles might help to achieve a more targeted delivery, reducing at the same time side effects and contributing to lengthen half-lives of CAs.

Also in **Chapter 1** also several examples of CP systems for diagnostic purposes were introduced. Some of them relied on the incorporation of active species as bridging ligands (e.g. iodinated organic molecules for CT), but the vast majority were based on the use of metals as connecting nodes of CP structures. However, as it was also mentioned in the previous Chapter, most of the metals used for diagnostic purposes (e.g. Gd(III), Eu(III), etc.) are toxic when released as free ion metals in the body. Thereby, as the low stability of the CPs obtained to date precludes their use in clinical situations, strategies to reduce the leaching of free metal ions are being searched. Among these strategies are: (i) the use of less toxic metal ions (e.g. Mn(II) instead of Gd(III)); and (ii) the use of coatings for CP particles. However, both strategies reduce the performance of the systems and do not avoid completely the risk of leaching of free toxic metal ions. For this reason, we propose an alternative strategy that constitutes the **main objective of this Thesis**. This strategy consists on: **producing CPs that incorporate diagnostic active metals in the form of metal complexes to avoid the leaching of toxic free metal ions**.

In order to reach this objective, at the end of **Chapter 1**, we proposed the use of polyazamacrocyclic metal complexes as bridging ligands for the design of new CPs (see Figure 2.1.). Gadolinium-based agents containing polyazamacrocyclic ligands have been classified by the European Medicines Agency (EMA) as the safest and less likely of releasing free Gd(III) ions among all the gadolinium-based agents approved for clinical uses. Inspired by this fact, we propose the use of polyazamacrocyclic-metal complexes as bridging ligands for the construction of CPs as a useful strategy to avoid the leaching of imaging active metals in the form of their toxic free metal ions. On the other hand, by following our strategy, in the case of the eventual degradation of the CP particles inside the body, the active metal in the form of safe polyazamacrocyclic complexes would be released.

For the sake of simplicity, this Thesis's main objective:

- **Producing CPs that incorporate diagnostic active metals in the form of metal complexes (polyazamacrocyclic-metal complexes) to avoid the leaching of toxic free metal ions.**

has been divided into sub-goals as follows:

1. Designing and synthesising or choosing polyazamacrocyclic ligands with the ability of forming complexes with imaging active metals. Those metal complexes will be further used as bridging ligands for the formation of new CPs by reaction with additional non-toxic metal centres (Figure 2.1.)
2. Expanding the scope of our strategy by synthesizing metal complexes containing different imaging active metals and combining them with different metal connecting nodes. Especially focusing on obtaining gadolinium-based CPs for MRI.
3. Miniaturising designed CP systems to the nanoscale and obtaining stable CP particles suspensions appropriate to the study of their properties as MRI-CAs.
4. Studying the MRI-CA properties of CP particles suspensions at variable magnetic fields, Nuclear Magnetic Resonance Dispersion (NMRD) profiles, and their dependence with pH.

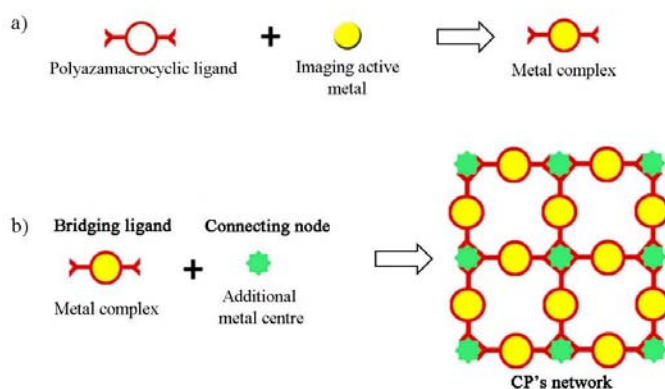


Figure 2.1. Summary of the strategy followed to fabricate CPs that avoid the leaching of toxic free metal ions: (a) Formation of the metal complex between the polyazamacrocyclic ligand and the imaging active metal. (b) Use of this metal complex as a bridging ligand for the formation of new CPs.

Chapter 3.

Publication 1: “Two-step synthesis of heterometallic coordination polymers using polyazamacrocyclic linker.”

3.1. Metal Polyazamacrocyclic complexes as building blocks for the design of CPs.

In **Chapter 2**, the fabrication of new CPs that avoid the leaching of toxic free metal ions has been set as the main objective of this **Thesis**. Our proposed strategy to reach such objective consists on the use of polyazamacrocyclic metal complexes as linkers for the fabrication of new coordination networks. In the present chapter, the use of polyazamacrocyclic ligands and complexes as building blocks in the synthesis of new CPs is explored. Moreover, examples reported to date of CPs containing polyazamacrocyclic ligands are introduced and their utility to meet our objectives is analysed.

3.1.1. Introduction to polyazamacrocyclic ligands.

Polyazamacrocyclic ligands are a family of cyclic chelating agents that form strong complexes with a wide variety of metal ions due to the preorganization of their binding sites and their kinetic and thermodynamic stability induced by the macrocyclic effect.^{1,2} These polyazamacrocyclic ligands are usually based on the cores of 1,4,7-Triazacyclononane (TACN), 1,4,7,10-tetraazacyclododecane (cyclen) and 1,4,8,11-tetraazacyclotetradecane (cyclam) (Figure 3.1).

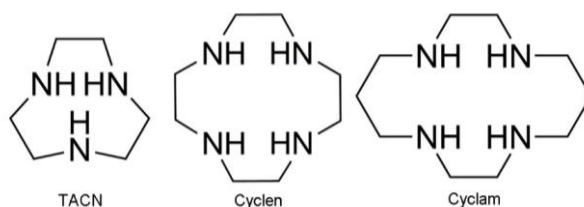


Figure 3.1. The most common cores of polyazamacrocyclic ligands.

These kinetic and thermodynamic stabilities make polyazamacrocyclic ligands particularly useful for catalytical,^{3,4} environmental,^{5,6} and medical applications.^{7–11} Regarding to diagnostic uses, which is the scope of this Thesis, polyazamacrocycles proved useful for various imaging techniques such as Magnetic Resonance Imaging (MRI),^{7,12} PARACEST MRI,^{8,13,14} Computerized Tomography (CT),⁹ and Fluorescence imaging as potential fluorescent probes.^{10,11} The use of macrocyclic ligands ensures the chelation of the imaging active metal (e.g. Gd(III), Eu(III), Tb(III), Mn(II), Ni(II), etc.), reducing or eliminating the toxicity of the free metal ion. Thereby, metal-polyazamacrocyclic complexes has been chosen as the preferred building blocks for the construction of CP particles endowed with medical imaging activity.

3.1.2 Functionalization of polyazamacrocyclic ligands.

Functionalization of polyazamacrocyclic ligands refers to the process of introducing pendant arms to the macrocyclic cores. Functionalization of the polyazamacrocyclic cores can be carried out for a variety of reasons. First of all, the introduction of additional coordinating donor atoms in the pendant arms can increase the kinetic and thermodynamic stability of the metal chelates. For instance, in the case of the Gd(III)-chelates, octacoordinated complexes are preferred due to its higher stability and lower toxicity.¹⁵ Secondly, the nature of the macrocyclic pendant arms can have a strong influence in controlling the residence lifetime (τ_M) of the metal-bound water molecule. This parameter has a strong influence in controlling the MRI-CA properties of Gd(III)-complexes, and will be analysed in detail in **Chapter 5**. Finally, functionalization with pendant arms is a way of

introducing additional coordinating functional groups to bind the metals that act as connecting nodes of the new CP structure.

Functionalization of polyazamacrocyclic cores normally takes place at the reactive amine positions of the macrocyclic ring following the general scheme shown in Figure 3.2.

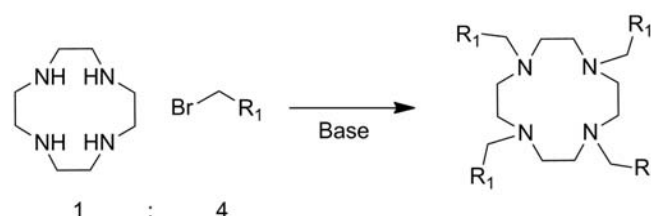


Figure 3.2. General scheme for the functionalization of polyazamacrocyclic cores.

As it is shown in the Figure 3.2, functionalization takes place through the nucleophilic attack of the ring N-atoms to the electrophilic C-atom of the future pendant arm (usually bromide is preferred as leaving group). The reaction typically takes place in presence of a base that deprotonates the N-atom. By controlling the number of moles of the pendant arm in the reaction, it is possible to obtain mono-, di- tri- and tetrafunctionalized macrocycles.

For instance, Chang *et al.*¹⁶ synthesised a monosubstituted macrocycle, by reacting a fivefold excess of cyclen with *p*-bromotoluic acid in presence of lithium hydroxide with a yield of 24% (Figure 3.3).

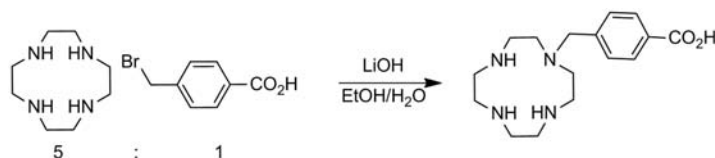


Figure 3.3. Synthetic route followed by Chang *et al.*¹⁶ for the obtaining of the monosubstituted macrocycle.

In another example Sherry *et al.* described the synthesis of a series of asymmetrically tetrasubstituted ligands following the general synthetic route shown in Figure 3.4.¹⁷ In a first step, a threefold excess of ethyl-2-bromoacetamido acetate was mixed with cyclen. After that, a purification over silica gel yielded the trifunctionalized macrocycle. In a second step, the three-armed macrocycle was coupled with a range of different *N*-aryl-bromoacetamides.

As above-mentioned, functionalization of polyazamacrocyclic ligands with pendant arms can pursue different applications. In the present Chapter, we are interested on it as a way of introducing additional functional groups necessary for coordinating metal nodes. Table 3.1 shows some examples of functionalised macrocycles that have been used as building blocks for the construction of CPs. Most of them used carboxylic acid functionalities, but examples based on phosphonate groups have also been reported.

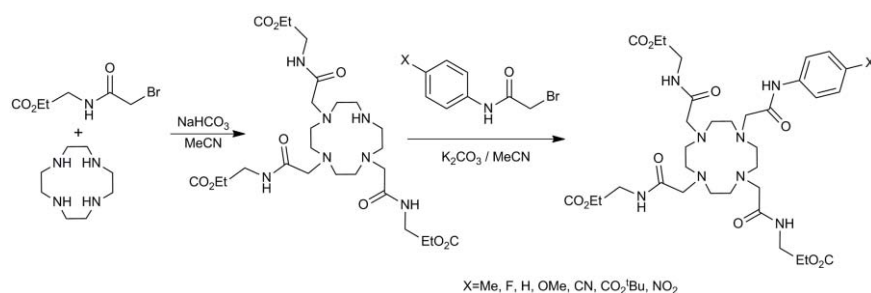


Figure 3.4. Synthetic route followed by Sherry *et al.*¹⁷ for the synthesis of asymmetrically tetrasubstituted polyazamacrocyclic ligands.

Table 3.1. This table summarizes some interesting examples of functionalised ligands used as building blocks in the formation of CPs.

Ligand	Precursors	Ligand code	Ref.
		H ₃ L2	23
		H ₄ L3	20,24,25
		H ₄ L4	19
		H ₈ DOTP	21,22

3.2. Classification of CPs containing polyazamacrocyclic ligands.

Additional coordinating functional groups can be easily introduced in macrocyclic ligands through the addition of pendant arms. This fact, together with the multiple applications that these ligands encounter in fields such as catalysis,^{3,4} environment^{5,6} and medicine^{7–11}, make them good candidates to be used as building blocks for the construction of functional CPs. Surprisingly, examples of CPs based on polyazamacrocycles are still limited. In the present section these examples are classified in three broad categories depending on their topological features. Before introducing this classification, it is important to highlight that polyazamacrocyclic-based CPs usually contain two types of crystalline unique metal centres in their structure. Attending to the position that these centres occupy in the structure, we will refer to the metal centre placed in the interior of the macrocyclic cavity as the “**primary metal centre**” or M_1 , whereas the centre placed out of the macrocycle will be referred to as “**secondary metal centre**” or M_2 . When both types of unique metal centres are formed by the same element ($M_1=M_2$), we say that the CP is *homometallic*, on the other hand, when the two centres correspond to different elements ($M_1\neq M_2$), we refer to as *heterometallic*. Depending on which metal centres act as connecting nodes of the framework, CPs can be classified in the categories shown in Figure 3.5.

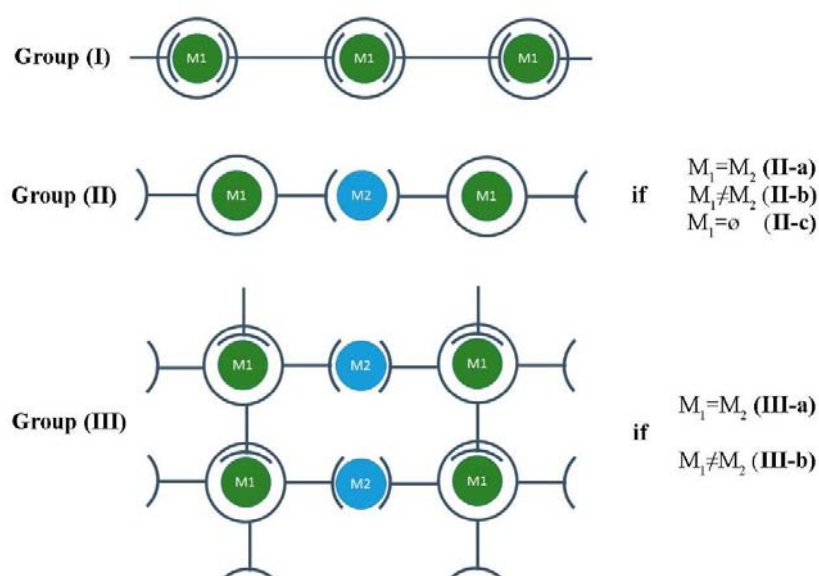


Figure 3.5. (I) M_1 is the only metal centre and acts as connecting node. (II) M_1 and M_2 are present but only M_2 acts as connecting node. (III) M_1 and M_2 are present and both act as connecting nodes.

3.2.1. Group (I): Primary metal centre (M_1) as connecting node.

This category is formed by those CPs that have only M_1 centres. Consequently, M_1 centres are the only connecting nodes of the coordination network. If the connection between the different macrocyclic units is done through the use of auxiliary ligands, they are classified as (I-a). On the other hand, if the macrocyclic units are connected through their pendant arms, they are classified as (I-b).

3.2.1.1. Group (I-a): Connection through auxiliary ligands.

This situation is illustrated by the example developed by Suh *et al.*¹⁸ where they synthesized a CP with the formula $[\text{Ni}(\text{cyclam})(\text{bpydc})]\cdot 5\text{H}_2\text{O}$ (cyclam = 1,4,8,11-tetraazacyclotetradecane, and bpydc=2,2'-bipyridyl-

5,5'-dicarboxylate). $[\text{Ni}(\text{cyclam})(\text{bpydc})]\cdot 5\text{H}_2\text{O}$ formed monodimensional chains, where Ni(II) is the M_1 centre and presents a coordination number of 6, in a octahedral molecular geometry, formed by the four ring N-atoms and completed with two carboxylic O-atoms of two auxiliary bpydc ligands. As it is shown in Figure 3.6, every macrocyclic unit is connected to two bpydc ligands, while at the same time, every bpydc ligand connects two Ni-cyclam units yielding infinite chains. Using a non-functionalised polyazamacrocyclic ligand such as cyclam makes essential the use of an auxiliary ligand (bpydc) to interconnect the different Ni-cyclam units. In addition, since Ni(II) is the only metal ion present in the structure it should necessarily act as the connecting node.

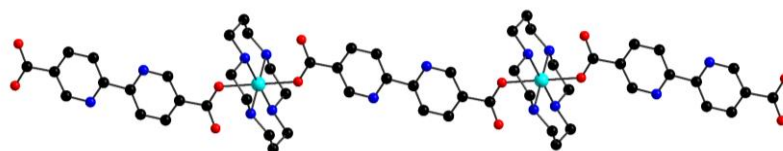


Figure 3.6. Structure of the monodimensional chains of $[\text{Ni}(\text{cyclam})(\text{bpydc})]\cdot 5\text{H}_2\text{O}$ synthesised by Suh *et al.*¹⁸ Colour code: Cu, cyan; C, black; N, blue; O, red.

3.2.1.2. Group (I-b): Connection through pendant arms.

Ma *et al.*¹⁹ produced an example that illustrates this subgroup by using the two-armed ligand ($\text{H}_4\text{L4}$, Table 3.1). When the authors heated a mixture of $\text{CuCl}_2\cdot 2\text{H}_2\text{O}$ and $\text{H}_4\text{L4}$ in DMF and water at 100°C for 3 days, a CP of formula $\text{Cu}(\text{H}_2\text{L4})\cdot \text{DMF}\cdot 2\text{H}_2\text{O}$ was obtained. As the structure reveals, each Cu(II) lies in the interior of the macrocyclic cavity. The Cu(II) ion shows an octahedral molecular geometry formed by the four ring N-atoms defining the equatorial plane, whereas the axial positions are occupied by two carboxylate oxygen atoms from two other ($\text{H}_2\text{L4}$)²⁻ ligands. The only metal ion present in the structure is the Cu1 that defines 2D layers composed of hexagonal and triangular rings (Figure 3.7).

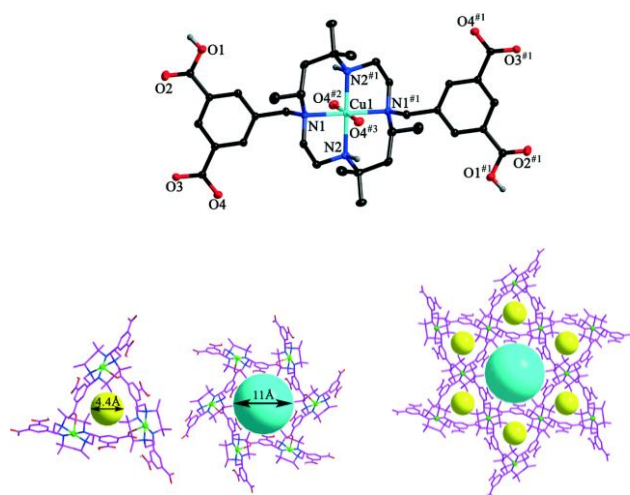


Figure 3.7. Coordination sphere surrounding the Cu1 in $\text{Cu}(\text{H}_2\text{L4})\cdot \text{DMF}\cdot 2\text{H}_2\text{O}$ (Top) View of the small and large channels (bottom left). View of the large channel surrounded by six small channels (bottom right). Colour code: Cu, cyan; C, black; N, blue; O, red.

3.2.2. Group (II): Secondary metal centre (M_2) as connecting node.

Group (II) is formed by those CPs where M_2 act as the connecting node of the network. Depending on the relation between M_1 and M_2 , three situations are possible: **(II-a)** it corresponds to those examples where

both metal centres are formed by the same element ($M_1=M_2$), members of this subgroup are *homometallic*; (**II-b**) it corresponds to examples where the two metal centres are formed by different elements ($M_1\neq M_2$), members of this subgroup are *heterometallic*; (**II-c**) it corresponds to those cases where the M_1 centre is absent ($M_1=\emptyset$), meaning that the macrocyclic ligand is empty.

3.2.2.1. Group (**II-a**): Homometallic CPs of group (**II**).

Situation (**II-a**) is illustrated by the example of Turner *et al.*,²⁰ where they reacted the ligand H_4L3 (Table 3.1) with copper (II) chloride dihydrate in a mixture of water/ethanol (2:3) to yield a CP of formula $[Cu_4Cl_2(H_2L3)_2(HOEt)_2]\cdot CuCl_4\cdot 5H_2O$. This CP presents Cu(II) ions in three different coordination environments (Figure 3.8). Cu1 constitutes the M_1 centre, occupying the macrocyclic cavity, and exhibiting a coordination number of five in a square pyramidal geometry, with four equatorial positions occupied by the four ring N-atoms and the axial position occupied by a chloride anion. Cu2 are the M_2 centres. Two Cu2 ions are bridged by four carboxylate groups forming a paddle wheel that acts as the connecting node of the network. Finally, one Cu3 placed in the cavities of the framework acts as counterion. Cu3 shows a tetrahedral molecular geometry with a coordination environment formed by four chloride anions.

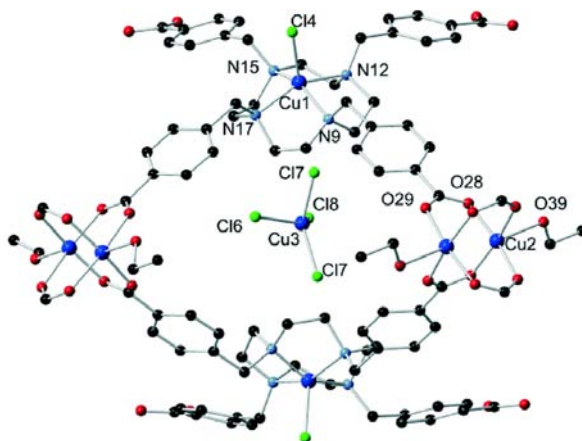


Figure 3.8. The structure of $[Cu_4Cl_2(H_2L3)_2(HOEt)_2]\cdot CuCl_4\cdot 5H_2O$ shows Cu(II) in three different environments. Cu1 is acting as M_1 , Cu2 correspond to M_2 acting as the connecting nodes, and finally, Cu3 occupies the cavities to balance the charges. Colour code: Cu, blue; C, black; N, cyan; Cl, green; O, red.

3.2.2.2. Group (**II-b**): Heterometallic CPs of group (**II**).

A good example to illustrate situation (**II-b**) was developed in our group by Carné *et al.*²¹ In this example, the authors made react the ligand H_8DOTP (Table 3.1) with copper (II) chloride and Gd(III) nitrate to yield the three-dimensional infinite CP of formula $[GdCu(DOTP)Cl]\cdot 4.5H_2O$ (Figure 3.9) Cu(II) is the M_1 metal centre. This metal ion is chelated inside the macrocyclic cavity in a square pyramidal geometry with the four ring N-atoms occupying the equatorial plane and one chloride anion in the axial position. On the other hand, Gd(III) constitutes the M_2 centre that acts as the connecting node of the framework. Gd(III) shows an octahedral coordination environment, in which all the positions are occupied by O-atoms of the pendant arm phosphonate groups.

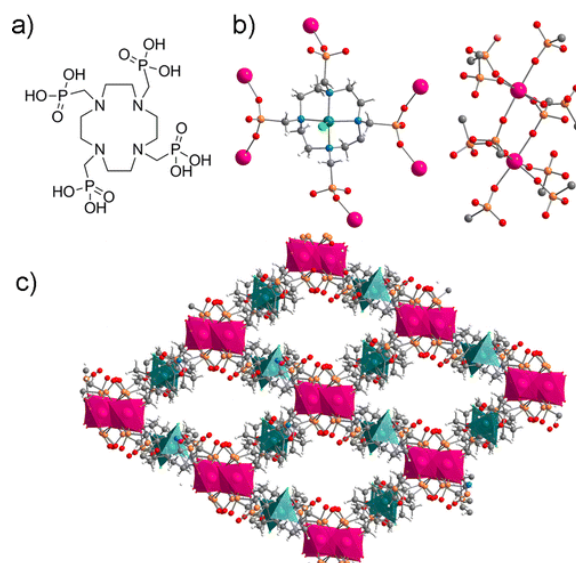


Figure 3.9. (a) H₈DOTP formula. (b) Coordination sphere of the primary metal centre Cu(II) (left) and the secondary metal centre Gd(III) (right). (c) Three-dimensional structure of the CP [GdCu(DOTP)Cl]·4.5H₂O showing the presence of 1-D channels. Color code: Gd, pink; C, gray; N, blue; Cu, dark green; Cl, light green; O, red.

3.2.2.3. Group (II-c): Members of group (II) with an empty macrocyclic cavity.

This situation is illustrated by the example developed by Clearfield *et al.*²² In this case the authors synthesised a new CP of formula $\text{Mn}[\text{C}_3\text{NH}_7(\text{PO}_3\text{H}_{0.5})]_4$ using the ligand H₈DOTP and MnCl₂. As illustrated in Figure 3.10, the structure revealed the lack of the M₁ centres, as the interior of the DOTP macrocyclic cavity is empty. On the other hand, Mn(II) constitute the M₂ centres acting as the connecting nodes of the structure, showing a tetrahedral coordination environment formed by four O-atoms of the pendant arms phosphonate groups.

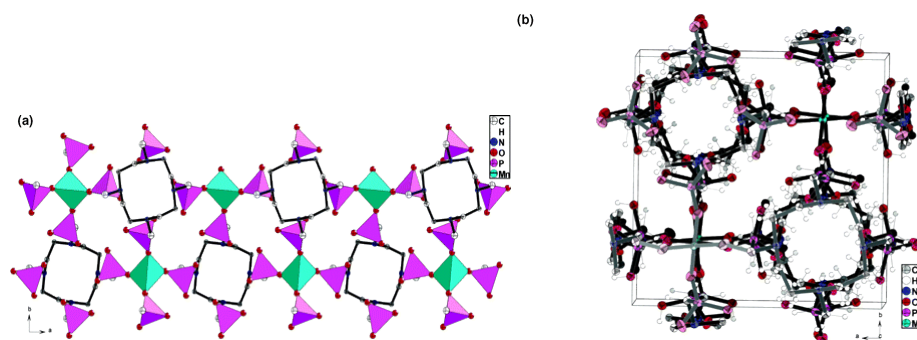


Figure 3.10. (a) Polyhedral representation of the CP $\text{Mn}[\text{C}_3\text{NH}_7(\text{PO}_3\text{H}_{0.5})]_4$. (b) Unit cell packing diagram in the *ab* plane viewed down the *c* axis.

3.2.3. Group (III): Primary (M₁) and secondary (M₂) metal centres as connecting nodes.

Members of this group have both types of metal centres (M₁ and M₂), and both act as connecting nodes of the network. Depending on the relation between M₁ and M₂, two different situations are possible: **(III-a)** corresponding to those examples where both metal centres are formed by the same element (M₁=M₂), members of this subgroup are *homometallic*; **(III-b)** it is formed by those cases where the two metal centres correspond to

different elements ($M_1 \neq M_2$), members of this subgroup are *heterometallic*. To our knowledge, there are not still reported CPs corresponding to the subgroup (III-b).

3.2.3.1. Subgroup (III-a): Homometallic members of group (III).

An example of the subgroup (III-a) was published by Guillard *et al.*²³ In this case, the authors mixed the ligand H_3L2 (Table 3.1) with zinc nitrate hexahydrate to obtain a CP of formula $[Zn_2(L2)(H_2O)]Cl \cdot DMF$. Such structure is depicted in Figure 3.11, and shows Zn(II) ions in two different coordination environments. Zn1, which is placed in the centre of the triazacyclononane (TACN) cavity, represents the M_1 centre. Zn1 is hexacoordinated and its coordination sphere is formed by the three N-atoms of the TACN and completed with three O-atoms of the pendant arms carboxylic groups of three different macrocyclic units. On the other hand, Zn2 is the M_2 centre and shows a tetrahedral coordination environment formed by four O-atoms of four carboxylate groups. As the coordination sphere of Zn1 is completed with O-atoms of other pendant arm carboxylate groups, Zn1 acts also as connecting node of the network.

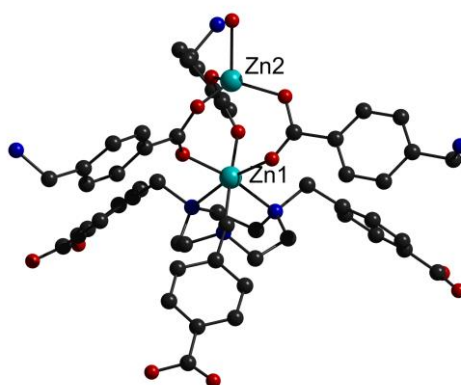


Figure 3.11. Coordination sphere of the primary metal centre Zn1 and the secondary metal centre Zn2, showing that both metal centres act as connecting nodes of the network. Color code: Zn, cyan; C, black gray; N, blue; O, red.

3.2.4 Summary of the reported CPs containing polyazamacrocyclic ligands.

Table 3.2 summarizes the polyazamacrocyclic-based CPs reported to date classified in the groups and subgroups explained before together with their ligands (see Table 3.1), and some of their most representative structural features and properties.

3.3. Design of a new macrocyclic ligand to avoid the release of free M_1 ions.

In the previous section, different examples of metal-containing polyazamacrocyclic-based CPs have been introduced and classified into three broad groups depending on their topological features. From the above-mentioned examples, it becomes clear that, in the case of an eventual degradation of the framework, the different examples do not have the same likelihood of releasing the encapsulated primary metal centre (M_1).

Table 3.2. Summarizing table of the polyazamacrocyclic-based CPs reported to date.

Type	Ligand	M ₂	M ₁	Structural features	Properties	Ref.
I-a	Cyclam	-	Ni(II)	1D chains	Permanent porosity; Hydrogen storage; SC-SC transformation	18
I-b	H₄L4	-	Cu(II)	2D layers	Gas adsorption(N ₂ , CO ₂); Reversible I ₂ adsorption.	19
II-a	H₄L3	Cu(II)	Cu(II)	1D chains	-	20
II-b	H₈DOTP	Gd(III)	Cu(II)	3D	MRI contrast agent	21
II-c	H₈DOTP	Mn(II)	-	2D layers	Capture of Cs ⁺ from solution.	22
III-a	H₃L2	Zn(II)	Zn(II)	3D	Rigid, microporous BET: 1350 m ² g ⁻¹ ; Selectivity for CO ₂ over CO, CH ₄ , O ₂ and N ₂ .	23
III-a	H₄L3	Cd(II)	Cd(II)	3D Doubly interpenetrated, kdd related net	Separation of polycyclic aromatic hydrocarbons and polar analyte mixtures.	24
III-a	H₄L3	Cd(II)	Cd(II)	3D Doubly interpenetrated ins related net	Langmuir surface area: 600 m ² g ⁻¹ ; selectivity for CO ₂ over N ₂	25

In order to avoid the release of free M₁ ions in the medium, the metal complex (M₁-L), product of the CP disassembly, should be kinetically and thermodynamically stable in solution. For CPs of group (I) and group (III), M₁ is stabilised inside the macrocyclic cavity through bonds with donor atoms of neighbouring ligands. In such cases, when the coordination network is disassembled, the bonds between M₁ and the neighbouring ligands' donor atoms are broken, leaving open metal sites in M₁-L in solution. Therefore, the complex is more prone to dissociation or transmetallation. On the other hand, in CPs of group (II), M₁ does not form bonds with neighbouring ligands, and consequently, the disassembly of the coordination network affects less to the stability of the M₁-L unit. Thus, we postulate that type-(II) CPs are more suitable to avoid the release of free M₁ ions after disassembly of their networks.

From the analysis of the examples reported in the previous section, it is possible to formulate a series of conclusions. Firstly, it is clear that the use of non-functionalised ligands, such as cyclam, forces the use of auxiliary ligands and the consequent formation of type-(I-a) CPs, as it occurred in the case reported by Suh *et al.*¹⁸ Secondly, M₁ ions that require high coordination numbers (CN>5) to fill up their coordination spheres tend to establish bonds with neighbouring ligands' donor atoms, consequently forming type-(I-b)¹⁹ and type-(III) CPs.^{23–25} Thirdly, M₁ ions with low coordination numbers (CN≤5) can be stabilised through forming bonds with

ring N-atoms and additional anions, such as chloride, and do not need to establish bonds with neighbouring ligands, leading to type-(**II**) CPs.^{20,21}

From these conclusions, it appears that the formation of type-(**II**) CPs for M_1 ions with high CN is not possible, at least, with the polyazamacrocyclic ligands used to date. However, metals required for medical imaging (e.g. Gd(III), Eu(III), Mn(II), etc.) usually present high CN. Therefore, the objective of this Chapter has been the design of a new polyazamacrocyclic ligand that allows the formation of type-**II** CPs for M_1 ions with high CN.

3.4. Results and discussion.

In the present section, our investigations to develop a new polyazamacrocyclic ligand (**H₄L1**) with ability to form metal complexes with imaging active metals with high CN, and the attempts to use such complexes in the formation of type-(**II**) CPs are presented. These works led to the **Publication 1**, entitled: “Two-step synthesis of heterometallic coordination polymers using a polyazamacrocyclic linker”.

3.4.1. Design of the new ligand **H₄L1**.

Our strategy consisted on designing the new ligand **H₄L1** shown in Figure 3.12. **H₄L1** has four O-atoms placed in the nearby of the macrocyclic cavity that act as donor atoms together with the four ring N-atoms. Two O-atoms correspond to amide functionalities, whereas the other two O-atoms correspond to carboxylic groups. Thanks to these four O-atoms and the four ring N-atoms, M_1 ions with CN as high as eight or nine can be chelated inside the macrocyclic cavity. Furthermore, the presence of two benzene carboxylic acids assure the availability of free donor groups to bond M_2 ions that act as the connecting nodes of the network (see Figure 3.12)

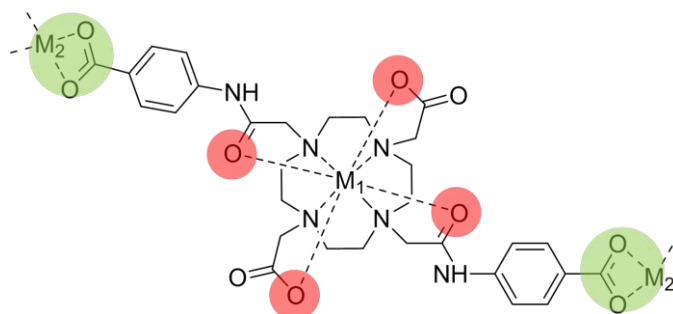


Figure 3.12. Scheme of $M_2[M_1-L1]$ showing the four O-atoms placed in the nearby of the aza-ring to stabilise M_1 inside the macrocyclic cavity (red), and the two benzene carboxylic acids placed to coordinate M_2 connecting nodes.

3.4.2. Two-step synthesis strategy.

Our strategy consists on using the ligand **H₄L1** to obtain heterometallic type-(**II**) CPs with the imaging active metal inside the macrocyclic cavity (M_1) and a second non-toxic metal ion (M_2) connecting the different M_1 -**L1** units through the coordination with the benzene carboxylic groups. However, such a precise control of metals position in the coordination network is not easy to achieve since many metals may show very similar stability constants. For instance, Table 3.3 shows a list of stability constants for some common transition metal ions with DOTA ligand,²⁶ showing that they have similar stability constants and also similar to lanthanides (Gd(III), $K_d=24.7$, $K_{eff,pH\ 7.4}=17.2$).^{27,28}

Table 3.3. List of stability constants observed for common transition metals with DOTA.²⁶

Metal ion	Stability constant, log K_d
Fe(III)	29.40 ²⁹
	24.48 ³⁰
Cu(II)	22.72 ³¹
	22.25 ²⁹
Ga(III)	21.33 ²⁹
Ni(II)	20.50 ³¹
	20.03 ³⁰
Co(II)	19.30 ³¹
	20.27 ³⁰
Zn(II)	18.70 ³¹
	21.09 ³⁰

Similarity between stability constants might explain why most of the CPs reported to date (Table 3.2) are homometallic. Actually, the only heterometallic reported example has been developed in our group by Carné *et al.* by combining DOTP ligand, Cu(II) and Gd(III) in one-pot synthesis.²¹ Unfortunately, the obtained CP presented Cu(II) as M_1 and Gd(III) as M_2 coordinated through the pendant arm's phosphonate groups (see Section 3.2.2.2).

To achieve a better control over metal position, we introduce in this chapter a “two-step synthesis” strategy. This strategy (Figure 3.13. and Scheme 1 of Publication 1) consisted on: (a) preforming the M_1 -**L1** complex; and secondly (b) adding M_2 to connect the preformed M_1 -**L1** units.

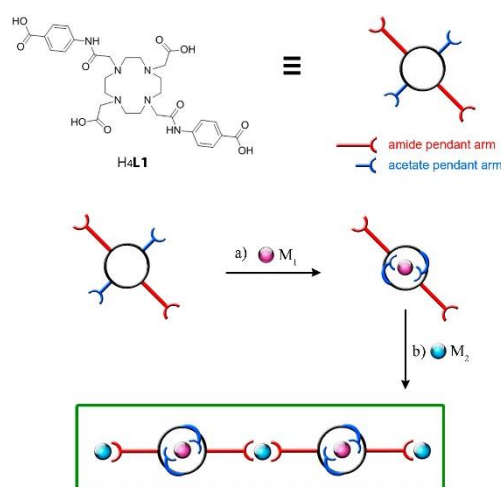


Figure 3.13. Scheme of the “two-step synthesis” strategy. (a) Preformation of the M_1 -**L1** complex. (b) Addition of M_2 to connect M_1 -**L1** units.

This “two-step” strategy offers finer control over metal position than “one-pot” synthesis does. By preforming kinetically stable M_1 -**L1** complexes, transmetalation with other metals is avoided, even if both metals show similar stability constants. Furthermore, the preformation of M_1 -**L1** complexes offers the opportunity to characterize such complexes by SCXRD in order to obtain further structural information of the isolated linkers of the CPs and might allow predictions of its topology.

3.4.3. Synthesis and characterization of ligand H₄L1.

Synthesis of ligand H₄L1 (1,4,7,10-tetraazacyclododecane-1,7-bis(4-acetamidobenzoic)-4,10-diacetic acid) was carried out following the synthetic route showed in Figure 3.14 (or Scheme 2 of Publication 1). Synthesis was started from the commercial precursors *tert*-butyl-4-aminobenzoate, bromoacetyl bromide and the polyazamacrocycle DO2AtBu. Intermediate species **1**, **2** and the final product H₄L1 were characterized by elemental analysis, ¹H NMR, ¹³C NMR, FT-IR and mass spectrometry, confirming the purity of all of them (see Experimental details of Publication 1).

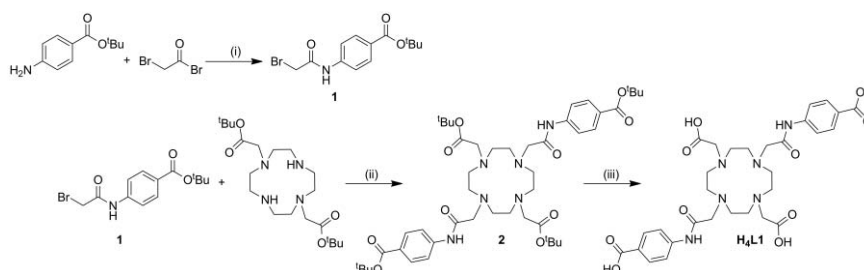


Figure 3.14: Synthetic route for the synthesis of H₄L1. Reagents and conditions: (i) K₂CO₃, CH₂Cl₂, 0°C to RT, 12 h; (ii) K₂CO₃, CH₃CN, reflux 85°C, 72h + column chromatography, 13% MeOH in CH₂Cl₂; (iii) trifluoroacetic acid, CH₂Cl₂, 16 h.

Furthermore, crystals of H₄L1 suitable for SCXRD were obtained by diffusion in acidic vapours. The crystalline structure was solved and refined in the monoclinic space group C2/c. The asymmetric unit was found to contain one half of the macrocyclic H₄L1 lying about a twofold axis, one half of a water molecule (O1W) on another twofold axis and three water molecules in general positions, resulting in the overall formula H₄L1·7H₂O (Figure 3.15 and Figure 1a of Publication 1). H₄L1 is protonated on two of the four ring N-atoms (N2 and N2#) and on two of the four benzene carboxylic moieties (O2 and O2#). Further structural details can be found in Results and Discussion section of Publication 1.

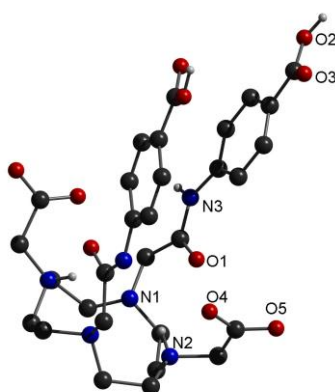


Figure 3.15. Structure of H₄L1·7H₂O with unique heteroatom labelling. Hydrogen atoms describing protonation state have been included, and the rest have been omitted for clarity. Color code: C, black; N, blue; O, red.

3.4.4. First step: Synthesis and characterization of M₁-L1 complexes.

As it has been said, the first step of the “two-step synthesis” strategy (Figure 3.13) consisted on preforming M₁-L1 complexes.

3.4.4.1. General synthesis and characterization of M_1 -**L1** complexes.

After many attempts, metal complexes for M_1 =Mn(II) and Ni(II), named **3** and **4** respectively, were successfully obtained and crystallised. The general route followed to obtain such metal complexes consisted on: (i) A certain amount of ligand H_4L1 was dissolved in water by careful addition of 1M NaOH until pH=8; (ii) a stoichiometric amount of M_1 salt was added into ligand solution; (iii) pH was readjusted to pH 8 by addition of 1M NaOH; (iv) the mixture was left under stirring for 18 h and after that filtered; and finally, (v) pH was lowered to pH=3 by careful addition of 1 M HCl in order to precipitate M_1 -**L1** in the form of powder. Complexes **3** and **4** were characterized by elemental analysis, mass spectrometry (ESI-TOF) and FT-IR (see Experimental details of Publication 1).

3.4.4.2. Structure of $[Mn(H_1L1)] \cdot [Na(H_2O)_6] \cdot 4H_2O$ (**3**).

Crystals of **3** suitable for SCXRD were obtained by slow diffusion of acid vapours into a basic solution of **3** in water ($5 \text{ mg} \cdot \text{mL}^{-1}$, pH=8.5) at 5°C for one week. Analysis of the crystals gave a structural model in the monoclinic space group $P2_1/c$, where the asymmetric unit was found to contain the formula unit $[Mn(H_1L1)] \cdot [Na(H_2O)_6] \cdot 4H_2O$ (Figure 3.16 and Figure 1b of Publication 1). Mn(II) ion is placed within the macrocyclic cavity in a square antiprismatic molecular geometry. The square antiprism has one plane defined by the four ring N-atoms and the other plane defined by O1 and O6 of the amide groups and O4 and O9 of the acetate pendant arms.

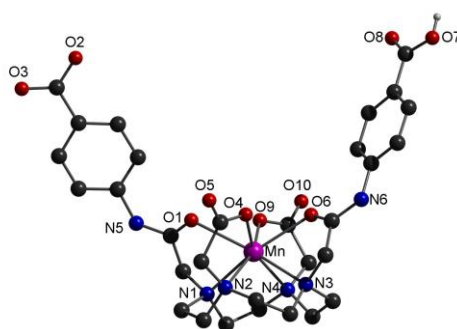


Figure 3.16. Structure of **3** with unique heteroatom labelling showing Mn(II) in the macrocyclic cavity in a square antiprismatic molecular geometry. Color code: Mn, violet; C, black; N, blue; O, red.

3.4.4.3. Structure of $[Ni(H_2L1)] \cdot 2H_2O$ (**4**)

Crystals of **4** suitable for SCXRD were obtained by slow diffusion of acid vapours into a basic solution of **4** in water ($5 \text{ mg} \cdot \text{mL}^{-1}$, pH=8.5) at 5°C for one week. Analysis of the crystals gave a structural model in the monoclinic space group $C2/c$, where the asymmetric unit was found to contain one half of the formula unit $[Ni(H_2L1)] \cdot 2H_2O$ (Figure 3.17 and Figure 1c of Publication 1). Ni(II) ion lies on a twofold axis within the macrocyclic cavity in a highly distorted octahedral geometry, coordination sphere of Ni(II) is formed by four ring N-atoms and two equivalent O4 atoms of the acetate pendant arms. Conversely to **3**, O-atoms of the amide groups are not involved in any coordination bond, leaving both arms free to rotate.

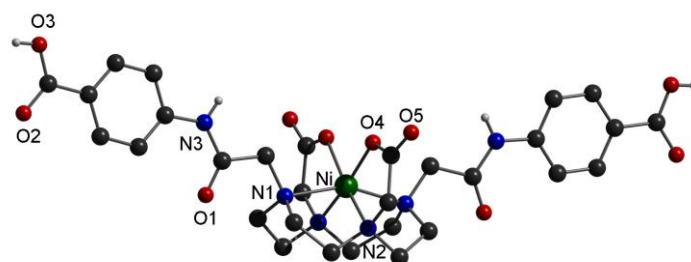


Figure 3.17. Structure of **4** with unique heteroatom labelling showing Ni(II) in the macrocyclic cavity in a distorted octahedral molecular geometry. Color code: Ni, green; C, black; N, blue; O, red.

3.4.5. Second step: Synthesis and characterization of CPs by reaction of M_2 with M_1-L1 .

According to our “two-step synthesis” strategy (Figure 3.13), after obtaining M_1-L1 complexes, the second step consisted on combining them with M_2 ions to produce CPs. For that purpose, complexes **3** and **4** were reacted with Zn(II) ions to yield $[Zn(NiL1)H_2O] \cdot 8H_2O$ (**6**) and $[Zn(MnL1)H_2O] \cdot 9H_2O$ (**7**). Additionally, H_4L1 reacted with zinc acetate to yield the homometallic $[Zn(ZnL1)H_2O] \cdot 3H_2O$ (**5**).

3.4.5.1. Synthesis and structure of $[Zn(ZnL1)H_2O] \cdot 3H_2O$ (**5**)

An aqueous solution of zinc acetate was added dropwise into a solution of H_4L1 adjusted at pH=6.7 to yield white crystalline powder of **5** (see Experimental details in Publication 1). As-synthesised crystals of **5** were analysed by SCXRD and solved in the space group $P2_1/n$. The crystal structure revealed the formation of homometallic 1D chains (Figure 3.17 and Figure 2 of Publication 1). The asymmetric unit contained Zn(II) ions in two different coordination environments.

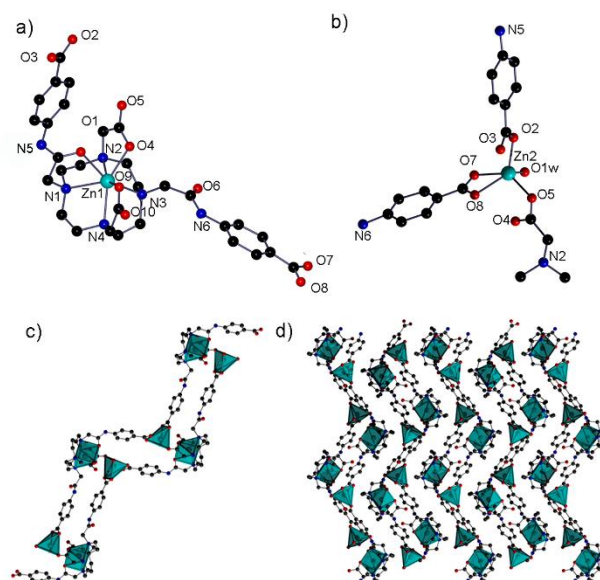


Figure 3.18. Ball and stick representation of the crystal structure of **5**. (a) Zn1-L1 unit. (b) Zn2 unit. (c) Double strand chain extending along the b axis. (d) Packing of the double strand chains viewed along the b axis. The sky blue capped trigonal prisms and square pyramids represent the coordination environment of Zn(II) in (c,d). H atoms have been omitted for clarity. Atom colour code: Zn: sky blue; C: black-grey; N: blue; O: red.

CP **5** showed Zn1 acting as primary metal centre (M_1) in a capped trigonal prism geometry (Figure 3.18a) with a coordination sphere formed by the four ring N-atoms, two O-atoms of the acetate pendants arms (O4 and O9) and one O-atom of one amide arm (O1). On the other hand, Zn2 acted as secondary metal centre (M_2) in a square pyramidal geometry (Figure 3.18b) coordinated to benzene carboxylate groups in a bidentate (O7 and O8) and monodentate (O2) fashion, one acetate group (O5), and one water molecule (O1W).

3.4.5.2. Synthesis and structure of $[Zn(NiL1)H_2O] \cdot 8H_2O$ (**6**):

A mixture of **4** and zinc acetate in pure distilled water was basified to pH=6.5 with 1M NaOH. The solution was allowed to react for 12 h at 85°C. After this period, plate-shaped crystals of **6** were obtained and solved in the monoclinic space group $P2_1/n$, revealing the formation of one-dimensional chains (Figure 3.19 and Figure 3 of Publication 1). Interestingly, the asymmetric unit of **6** contained a slightly modified building unit of **4** with the benzene rings slightly rotated.

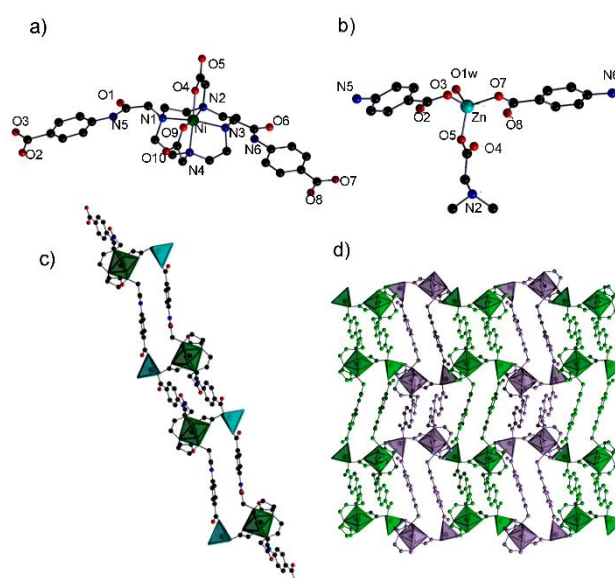


Figure 3.19. Ball and stick representation of the crystal structure of **6**. (a) Ni-L1 unit. (b) Zn unit. (c) Double strand chain extending along the [110] or [-110] direction. (d) Neighbouring double strand chains viewed along the a axis. The green octahedra and sky blue tetrahedra represent the coordination environment of Ni(II) and Zn(II), respectively, in (c). Different chains have been differently coloured in (d). H atoms have been omitted for clarity. Atom colour code: Zn: sky blue; Ni: green; C: black-grey; N: blue; O: red.

Compound **6** showed Ni acting as primary metal centre (M_1) in a distorted octahedral geometry (Figure 3.19a) with a coordination sphere formed by the four ring N-atoms, and the two O-atoms of the acetate pendants arms (O4 and O9). On the other hand, Zn acts as the secondary metal centre (M_2) in a tetrahedral geometry (Figure 3.19b) coordinated to two benzene carboxylate groups in a monodentate fashion (O3 and O7), one acetate group (O5), and one water molecule (O1W).

3.4.5.3. Synthesis and structure of $[Zn(MnL1)H_2O] \cdot 9H_2O$ (**7**):

A solution of zinc acetate in distilled water was added dropwise to a solution of **3** in water at room temperature and pH=8.5. After ten minutes, white crystals of **7** appeared. Crystals of **7** were solved and refined in the monoclinic space group $C2/c$, revealing 2D layers. The structural model shows a modified building unit **3** and Zn(II) ions connecting these units. When comparing the initial conformation of **3** to that found in **7**, it is

observed that the Mn(II) ion has changed its coordination number from eight to seven, leaving one amide pendant arm free to be accommodated in an extended position and, thus, facilitating the coordination of Zn(II) ions with the two benzene carboxylic acid groups.

In **7**, Mn(II) ions act as primary metal centres (M_1) in a capped trigonal prismatic geometry coordinated to the four ring N-atoms, two O-atoms of the acetate groups (O4 and O9) and one O-atom of the amide pendant arm (O1). Similarly to **6**, Zn(II) ions act as secondary metal centres (M_2), being tetrahedrally coordinated to two benzene carboxylic groups acting in monodentate fashion (O2 and O7), one O-atom of the acetate pendant arm (O5) and one water molecule (O1w). The 2D layers are built up by connecting each Mn(II)-**L1** unit through three Zn(II) ions, forming corrugated layers that grow along the (-101) plane. Different layers are packed in an ABAB sequence.

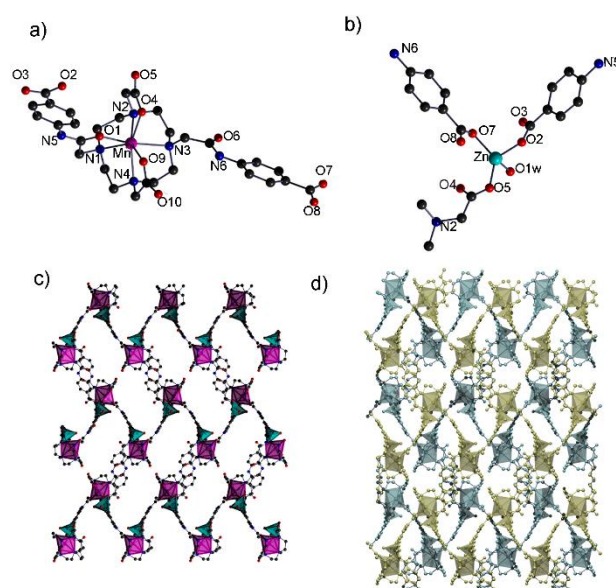


Figure 3.20. Ball and stick representation of the crystal structure of **7**. (a) Mn-**L1** unit. (b) Zn unit. (c) Single coordination layer viewed along the c axis. (d) Two neighbouring layers viewed along the c axis. The violet capped trigonal prisms and the sky blue tetrahedral represent the coordination environments of Mn(II) and Zn(II) in (c). The two layers in (d) have been differently coloured. H-atoms have been omitted for clarity. Atom colour code: Zn, sky blue; Mn, violet; C, black-grey; N blue; O, red.

3.5. Conclusions.

In conclusion, in the present Chapter we have introduced the study that led to **Publication 1**. The study consisted in the synthesis of the ligand **H4L1**, which has demonstrated its versatility to form discrete metal complexes Mn-**L1** (**3**) and Ni-**L1** (**4**), which have been further used as linkers to create two heterometallic type-(II) CPs: Zn(II)-Ni(II) (**6**) and Zn(II)-Mn(II) (**7**), by using a “two-step synthesis” strategy.

H4L1 has been designed to be used as a general ligand for the construction of CPs containing primary metals centres (M_1) that require high coordination numbers ($CN > 5$). We successfully achieved the production of CPs containing Ni(II) and Mn(II) as M_1 , with CN 6 and 7, respectively. However, all the attempts to use Gd(III) as M_1 failed. Moreover, crystals of the complex Gd-**L1** suitable for SCXRD could not be obtained, and hence, the conformation of the complex remains unknown. Nevertheless, conformation of Mn(II) complex **3** could help to shed light. In **3**, Mn(II) shows a $CN=8$ and thereby, the distances between Mn(II) and the O-atoms of the amide

groups are short, being 2.50 and 2.43 Å (Figure 3.16). These short distances force amide pendant arms upwards, forming a closed angle (87.6°) between the Mn centre and the two benzene carboxylic groups (Figure 3.21a). This closed angle is not favourable for the formation of extended networks, as it has been confirmed in the synthesis of **7**. Indeed, in **7**, Mn(II) ion changed from a CN 8 in **3** to a CN 7 in **7**. This change allowed one pendant amide arm to move downwards, in an extended position facilitating the coordination of the Zn(II) connecting nodes (Figure 3.21b).

However, Gd(III) has a higher tendency to form complexes with CN=8-9⁷ than Mn(II) does, due to the strength of the coordinative Gd-O bonds. Thus, Gd-**L1** complex would presumably not allow a change of conformation to lower CN, as it occurred in Mn(II) complex, and therefore preventing the formation of any CP with this Gd(III) complex.

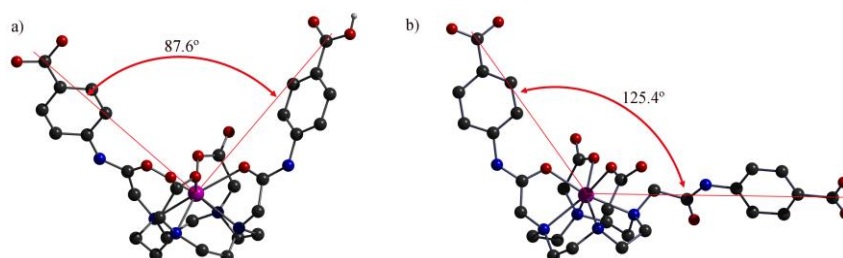


Figure 3.21. Scheme showing the change of CN in Mn-**L1** building block. (a) Conformation of Mn-**L1** in **3**. (b) Conformation of Mn-**L1** in **7**.

3.6. References.

1. Busch, D. H. Distinctive coordination chemistry and biological significance of complexes with macrocyclic ligands. *Acc. Chem. Res.* **11**, 392–400 (1978).
2. Hubin, T. Synthesis and coordination chemistry of topologically constrained azamacrocycles. *Coord. Chem. Rev.* **241**, 27–46 (2003).
3. Kim, M., Jeon, J. W. & Suh, J. Angiotensin-cleaving catalysts: conversion of N-terminal aspartate to pyruvate through oxidative decarboxylation catalyzed by Co(III)cyclen. *J. Biol. Inorg. Chem.* **10**, 364–372 (2005).
4. Jeung, C.-S., Song, J. B., Kim, Y.-H. & Suh, J. Hydrolysis of linear DNA duplex catalyzed by Co(III) complex of cyclen attached to polystyrene. *Bioorg. Med. Chem. Lett.* **11**, 3061–3064 (2001).
5. Zhou, R. *et al.* Cyclen-functionalized perylenebisimides as sensitive and selective fluorescent sensors for Pb²⁺ in aqueous solution. *Chem. Commun.* **47**, 6668–6670 (2011).
6. Hancock, R. D. & Martell, A. E. Ligand design for selective complexation of metal ions in aqueous solution. *Chem. Rev.* **89**, 1875–1914 (1989).
7. Caravan, P., Ellison, J. J., McMurry, T. J. & Lauffer, R. B. Gadolinium(III) chelates as MRI contrast agents: structure, dynamics, and applications. *Chem. Rev.* **99**, 2293–2352 (1999).
8. Zhang, S., Merritt, M., Woessner, D. E., Lenkinski, R. E. & Sherry, A. D. PARACEST agents: modulating MRI contrast via water proton exchange. *Acc. Chem. Res.* **36**, 783–790 (2003).
9. Esteban, J. M., Alonso, A., Cervera, V. & Martínez, V. One-molar gadolinium chelate (gadobutrol) as a contrast agent for CT angiography of the thoracic and abdominal aorta. *Eur. Radiol.* **17**, 2394–2400 (2007).
10. Leonard, J. P. & Gunnlaugsson, T. Luminescent Eu(III) and Tb(III) complexes: developing lanthanide luminescent-based devices. *J. Fluoresc.* **15**, 585–595 (2005).
11. Gunnlaugsson, T., Mac Dónaill, D. A. & Parker, D. Lanthanide macrocyclic quinolyl conjugates as luminescent molecular-level devices. *J. Am. Chem. Soc.* **123**, 12866–12876 (2001).
12. Caravan, P., Farrar, C. T., Frullano, L. & Uppal, R. Influence of molecular parameters and increasing magnetic field strength on relaxivity of gadolinium- and manganese-based T₁ contrast agents. *Contrast Media Mol. Imaging* **4**, 89–100 (2009).
13. Olatunde, A. O., Dorazio, S. J., Sperryak, J. A. & Morrow, J. R. The NiCEST approach: nickel(II) paraCEST MRI contrast agents. *J. Am. Chem. Soc.* **134**, 18503–18505 (2012).
14. Dorazio, S. J., Tsitovich, P. B., Sifers, K. E., Sperryak, J. A. & Morrow, J. R. Iron(II) PARACEST MRI contrast agents. *J. Am. Chem. Soc.* **133**, 14154–14156 (2011).
15. Caravan, P. Strategies for increasing the sensitivity of gadolinium based MRI contrast agents. *Chem.*

- Soc. Rev.* **35**, 512–523 (2006).
16. Knight, D. A. *et al.* Carboxylic acid functionalized cobalt(III) cyclen complexes for catalytic hydrolysis of phosphodiester bonds. *Dalt. Trans.* 2006–2011 (2004). doi:10.1039/b405307a
 17. Ratnakar, S. J., Woods, M., Lubag, A. J. M., Kovacs, Z. & Sherry, A. D. Modulation of water exchange in europium(III) DOTA-tetraamide complexes via electronic substituent effects. *J. Am. Chem. Soc.* **130**, 6–7 (2008).
 18. Lee, E. Y. & Suh, M. P. A robust porous material constructed of linear coordination polymer chains: reversible single-crystal to single-crystal transformations upon dehydration and rehydration. *Angew. Chem. Int. Ed. Engl.* **43**, 2798–2801 (2004).
 19. Zhang, H.-M. *et al.* Syntheses, structures, gas adsorption and reversible iodine adsorption of two porous Cu(II) MOFs. *CrystEngComm* **17**, 1583–1590 (2015).
 20. Hawes, C. S., Batten, S. R. & Turner, D. R. Self-assembly of discrete and polymeric metallosupramolecular architectures from cyclen-derived ligands. *CrystEngComm* **16**, 3737–3748 (2014).
 21. Carné-Sánchez, A. *et al.* Relaxometry studies of a highly stable nanoscale metal-organic framework made of Cu(II), Gd(III), and the macrocyclic DOTP. *J. Am. Chem. Soc.* **135**, 17711–17714 (2013).
 22. Kong, D., Medvedev, D. G. & Clearfield, A. DOTP-manganese and -nickel complexes: from a tetrahedral network with 12-membered rings to an ionic phosphonate. *Inorg. Chem.* **43**, 7308–7314 (2004).
 23. Ortiz, G., Brandès, S., Rousselin, Y. & Guillard, R. Selective CO₂ adsorption by a triazacyclononane-bridged microporous metal-organic framework. *Chem. - A Eur. J.* **17**, 6689–6695 (2011).
 24. Hawes, C. S. *et al.* Metal-organic frameworks as stationary phases for mixed-mode separation applications. *Chem. Commun.* **50**, 3735–3737 (2014).
 25. Gao, W.-Y. *et al.* Porous metal-organic framework based on a macrocyclic tetracarboxylate ligand exhibiting selective CO₂ uptake. *CrystEngComm* **14**, 6115–6117 (2012).
 26. Viola-Villegas, N. & Doyle, R. P. The coordination chemistry of 1,4,7,10-tetraazacyclododecane-N,N',N'',N'''-tetraacetic acid (H₄DOTA): Structural overview and analyses on structure–stability relationships. *Coord. Chem. Rev.* **253**, 1906–1925 (2009).
 27. Sherry, A. D., Caravan, P. & Lenkinski, R. E. Primer on gadolinium chemistry. *J. Magn. Reson. Imaging* **30**, 1240–1248 (2009).
 28. Pasha, A., Tircsó, G., Benyó, E. T., Brücher, E. & Sherry, A. D. Synthesis and characterization of DOTA-(amide)(4) derivatives: equilibrium and kinetic behavior of their lanthanide(III) complexes. *Eur. J. Inorg. Chem.* **2007**, 4340–4349 (2007).
 29. Clarke, E. T. & Martell, A. E. Stabilities of trivalent metal ion complexes of the tetraacetate derivatives

- of 12-, 13- and 14-membered tetraazamacrocycles. *Inorganica Chim. Acta* **190**, 37–46 (1991).
30. Chaves, S., Delgado, R. & Da Silva, J. J. R. F. The stability of the metal complexes of cyclic tetra-aza tetra-acetic acids. *Talanta* **39**, 249–254 (1992).
31. Clarke, E. T. & Martell, A. E. Stabilities of the alkaline earth and divalent transition metal complexes of the tetraazamacrocyclic tetraacetic acid ligands. *Inorganica Chim. Acta* **190**, 27–36 (1991).

Chapter 4.

Publication 2: “Single-crystal and humidity-controlled powder diffraction study of the breathing effect in a metal-organic framework upon water adsorption /desorption.”

4.1. A new ligand for the design of Gd-containing CPs: DOTA-4AmP

In the previous **Chapter 3**, the ligand **H₄L1** has been proposed as a general polyazamacrocyclic ligand for the formation of heterometallic type-II CPs containing imaging active M_1 centres that require high coordination numbers. Although two heterometallic CPs, Zn(II)-Ni(II) (**6**) and Zn(II)-Mn(II) (**7**), were successfully formed, the ligand **H₄L1** failed to obtain CPs with Gd(III) as M_1 . We speculate that the inability to obtain Gd-containing CPs with **H₄L1** was due to the high CN required by Gd(III) (8-9), which leads to a closed angle conformation. This fact together with the rigidity of the benzene rings of the pendant arms and the high directionality of the free carboxylic acid groups hinder the formation of extended CP networks. On the other hand, it is worthy to say that the introduction of donor atoms in the nearby of M_1 was a successful strategy to stabilise this metal ion in the macrocyclic cavity without the intervention of donor atoms of neighbouring ligands. To overcome the limitations of **H₄L1**, we proposed the use of ligand DOTA-4AmP (Figure 4.1) for the construction of Gd(III)-containing CPs.

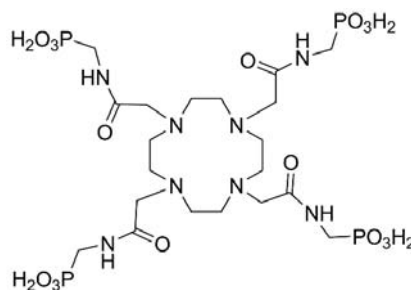


Figure 4.1. Formula of DOTA-4AmP

As it occurred in **H₄L1**, DOTA-4AmP has also four oxygen donor atoms placed near the macrocyclic cavity to stabilise M_1 within. Differently from **H₄L1**, the spacer between the N-atom of the amide and the free coordinative group has been changed from a benzene ring to an aliphatic C-atom in DOTA-4AmP. Now, rotation around the N-C bond allows different orientations for the free coordinative group. Finally, in DOTA-4AmP the carboxylic groups have been substituted by phosphonate groups, which offer a number of coordination modes higher than carboxylic groups.

4.2. Metal phosphonates.

To date, CP/MOFs based on carboxylate ligands have been foremost investigated since these ligands are easily produced and, in many cases, they are commercially available. In addition, CPs made of carboxylate ligands can often be obtained as single crystals, making their characterization an easier process. Also, the coordination chemistry of carboxylate ligands is rather simple, allowing the use of “isorecticular synthesis”. Isorecticular synthesis consists on the use of new ligands to tune the pore size or the functionality, on the basis of known structures, without affecting the overall structural features of the parent framework, such as topology and connectivity.¹ Thanks to these reasons, thousands of carboxylate-based CPs with new architectures, growing pore sizes, and innumerable functionalities have been reported so far. However, carboxylate-based CPs usually have low chemical stability, especially towards hydrolysis, which limits their practical employment.²

In parallel, some critical factors have hindered the progress on phosphonate-based CPs. Some of these factors have already been pointed out in two recent reviews by Prof. Shimizu³ and Prof. Clearfield.⁴ Firstly, metal phosphonates have a pronounced tendency to form dense layered phases with extended inorganic connectivity, so that the formation of porous open-framework compounds is generally considered a hard challenge. Secondly, they are highly insoluble. Therefore, obtaining single crystals is usually very difficult, and they are often obtained as microcrystalline powders, making their characterization more difficult. Thirdly, as phosphonates offer more coordination modes than carboxylates (they can act as mono-, di- or tridentate), their coordination chemistry becomes less predictable. On the other hand, the robustness of metal phosphonates represent an alternative to overcome the weaknesses that the typical carboxylate-based CPs offer.

Phosphonic acids -RP(O)(OH)_2 contain two exchangeable protons, the dianionic phosphonate -RPO_3^{2-} is tripodal, and the three coordinating O-atoms occupy the relative spatial disposition of the three vertices of a tetrahedron with the phosphorus in the centre. A large number of coordination modes are possible for the phosphonate group, having a maximum coordination number of nine.

4.2.1. Layered hybrid organic-inorganic compounds. Monotopic ligands.

In 1976, Yamanaka *et al.*⁵ carried out for the first time the synthesis of a zirconium ethyl phosphonate. He treated the γ -ZrP, an inorganic phase, with ethylene oxide. Through a series of techniques that included PXRD measurements, thermogravimetric analysis and infrared spectra, he could confirm the formation of P-O-C ester bonds on the interlamellar surfaces of the phosphate layer, he called the newly formed material a glycol ester of γ -ZrP, or just γ -ZrP·2EO. Interestingly, thermogravimetric analysis of γ -ZrP·2EO revealed that it contained adsorbed water, the amount of which varied with the drying conditions. Unlike the initial phase γ -ZrP, γ -ZrP·EO swelled in water, showing various X-ray reflection peaks during drying: 23.9, 21.5, 20.8 and finally 18.4 Å (Figure 4.2). When 18.4 Å phase was dried at 150°C for 1 h it changed into a new phase with basal spacing of 17.2 Å, reverting rapidly to the 18.4 Å phase by readsorbing environmental moisture. The author also carried out an isothermal adsorption-desorption curve for water. Remarkably, Yamanaka announced that the new compound was not neither an inorganic compound nor an organic one, instead it should be considered as a sort of hybrid inorganic-organic material.

The first example of zirconium phenylphosphonates and alkylphosphonates were reported by Alberti *et al.*⁶ in 1978. The structures were solved from PXRD patterns after a long reflux time in HF acid. In principle, phosphonates of tetravalent metals are highly insoluble and the precipitation in cold or at room temperature conditions leads to amorphous materials. However, the authors developed a procedure to obtain microcrystalline powder. The procedure consisted on heating with HF above 60°C. Under these conditions, the tetravalent metals form a soluble complex $[\text{ZrF}_6^{2-}]$ that establishes an equilibrium with free Zr^{4+} , that slowly precipitates as microcrystals.

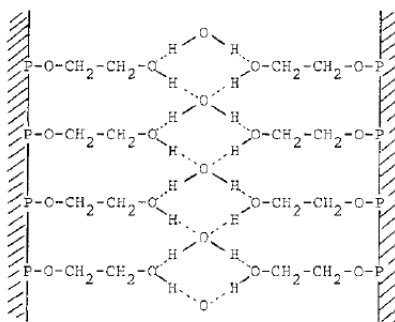


Figure 4.2. Schematic illustration of the arrangement of the glycol chains and water in the interlayer region of 18.4 Å phase with a composition $\text{Zr}(\text{HOCH}_2\text{CH}_2\text{OPO}_3) \cdot \text{H}_2\text{O}$.

Some years later, in 1985, Clearfield⁷ introduced an alternative method to produce zirconium polyether phosphonates consisting on first synthesising the polyether phosphonate ligand, and subsequently adding soluble zirconium species to precipitate the polyether phosphonate layered compounds (Figure 4.3). Actually, this strategy resembles much more the solvothermal methods used for the synthesis of CPs/MOFs. Presumably, these works paved the way of the phosphonate-based CPs.

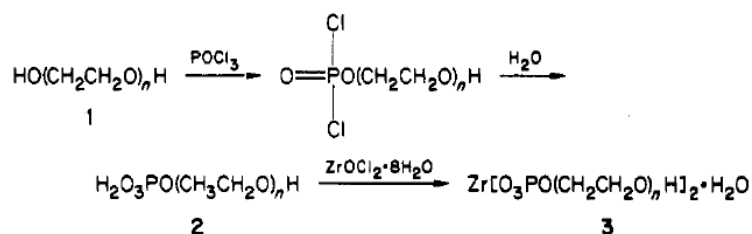


Figure 4.3. Synthetic route followed by Clearfield *et al.*⁷ for the synthesis of zirconium polyether phosphonates.

A common feature of layered phosphonates is the segregation of the hydrophobic groups from the hydrophilic groups. This is evident in the formation of the staged compounds resulting from the reaction of ZrF_6^{2-} at 60-70°C and phenylphosphonic acid that resulted in the staged compound shown in Figure 4.4.

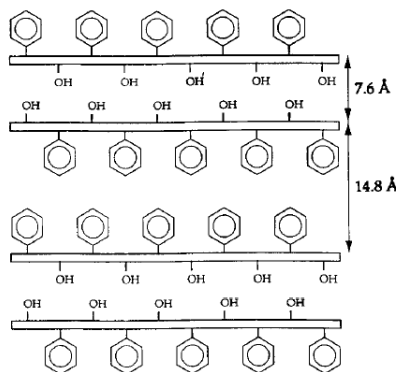


Figure 4.4. Schematic representation of the segregation of hydrophobic groups in staged structures formed by reaction of phenylphosphonic acids and soluble zirconium species.

4.2.2. Phosphonate-based CPs. Polytopic ligands.

As it has been shown in the previous section, all the staged/layered phosphonate compounds are based on monotopic ligands such as phenyl phosphonate, polyether, alkylphosphonates, etc. It is important to highlight that the structures shown in the previous section should not be classified as CPs but as hybrid organic-inorganic compounds. On the other hand, the introduction of multitopic phosphonate ligands paved the way for the synthesis of actual CPs based on the phosphonate functionality.

Interestingly, in 2001, Prof. Clearfield combined the tritopic ligand aminotris(methylenephosphonic acid) (**H₆-ATMP**) (Figure 4.5) with several M^{2+} cations to yield a family of CPs in the form of 1D helical chains⁸, where **H₄-ATMP** anions are connected through the motif shown in Figure 4.6. These CPs were synthesised by reacting the ligand **H₆-ATMP** with the metal salts under mild hydrothermal conditions by using layering techniques. By combining different mixtures of M^{2+} metal salts (Mn^{2+} , Ni^{2+} , Co^{2+} , etc.), ten isomorphous compounds were obtained. The monodimensional helical chains were held together by hydrogen bonds, as it is shown in Figure 4.6.

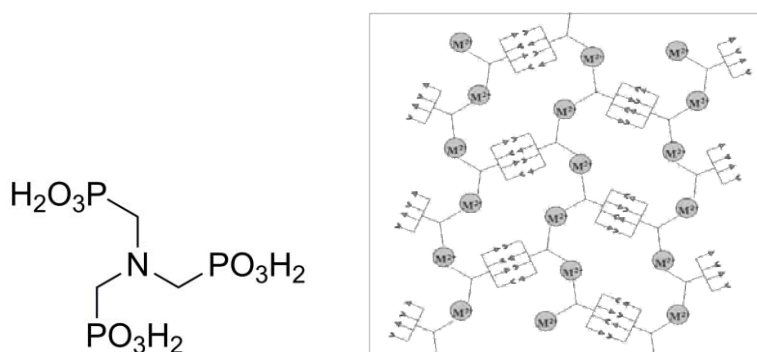


Figure 4.5. (Left) Aminotris(methylenephosphonic acid) (**H₆-ATMP**) and (Right) Schematic representation of the monodimensional helical chains held together through hydrogen bonds.

In the following years 2006^{9,10} and 2010,^{11,12} open-framework structures using *N,N'*-bis(phosphonomethyl)piperazine and *N,N'*-bis(phosphonomethyl)-4,4'-bipiperidine (Figure 4.6) were synthesised. Attempts to perform isorecticular synthesis with similar ligands have also been made. Remarkably, in 2011, Wharmby and co-workers used *N,N'*-bis(phosphonomethyl)bipiperidine to form an isorecticular structure (STA-16) with respect to STA-12, based on *N,N'*-bis(phosphonomethyl)piperazine.¹³

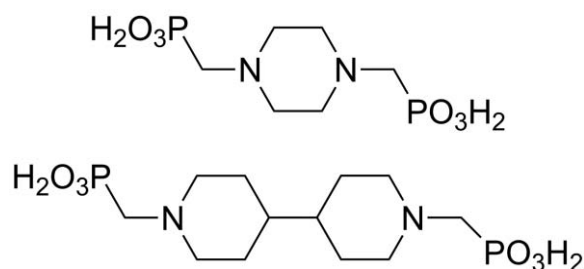


Figure 4.6. Representation of *N,N'*-bis(phosphonomethyl)piperazine (up) and *N,N'*-bis(phosphonomethyl)-4,4'-bipiperidine (down).

As above-mentioned, isorecticular synthesis and rational structure predictions in phosphonates becomes particularly challenging due to the multiple coordination modes that they can adopt. Thereby, the use of rigid ligands constitutes an interesting strategy to reduce the number of possible conformations, and in this sense, the use of aromatic cores is a good way to introduce rigidity and robustness in structures. Very recently, it has appeared a review about open-framework CPs based on a series of tritopic phosphonoaromatic ligands (Figure 4.7)¹⁴ that illustrate this approach.

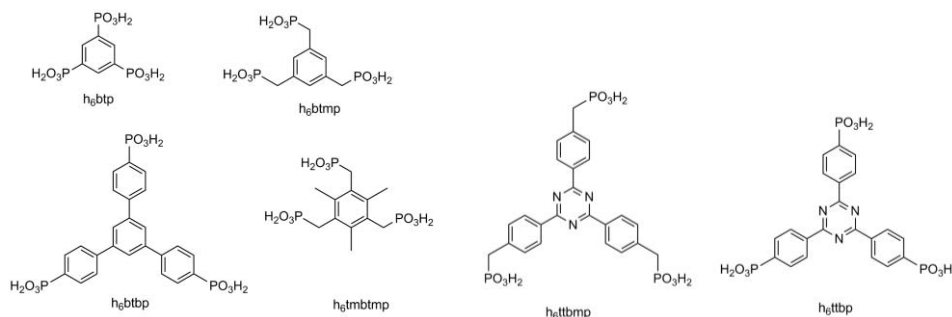


Figure 4.7. Structural formulas of phosphonoaromatic ligands used for the synthesis of open-framework CPs.¹⁴

4.2.3. Phosphonate functionalised polyazamacrocyclic ligands.

However, in this Thesis, we are interested in the design of CPs by using polyazamacrocyclic ligands. Conversely to the rigid phosphonoaromatic ligands, polyazamacrocyclic ligands are flexible molecules that can adopt multiple conformations. This high degree of flexibility leads to obtaining CPs with flexible structures that may present multistable phase equilibrium and usually prevent permanent porosity. The lack of permanent porosity and the difficulties of characterizing multistable phase systems are responsible for the scarcity of examples of CPs containing phosphonate-functionalized polyazamacrocyclic ligands. To the best of our knowledge, there are only three examples reported to date of CPs containing this type of ligands.

The first example was reported in the year 2004 by Prof. Clearfield,¹⁵ and it has been already introduced in Chapter 3. In this example, the authors combined the phosphonate-functionalised H₈**DOTP** ligand with manganese chloride to obtain a CP formed by infinite 2-D layers extending along the *ab* plane (Figure 4.8).

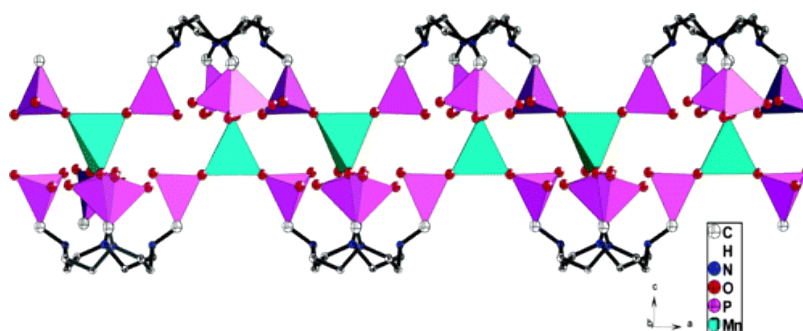


Figure 4.8. Polyhedral diagram of the 2-D layers viewed along the *b* axis. (purple tetrahedral represent CPO₃, and cyan tetrahedra MnO₄).¹⁵

The second example was reported in our group in 2013 by Carné *et al.*,¹⁶ and it has also been introduced in Chapter 3. Herein, the authors also used the H₈DOTP ligand, which in combination with Gd(NO₃)₃·6H₂O and CuCl₂ in water at 85°C for 12 h, yielded crystals suitable for SCXRD. The structure revealed the formation of a 3D CP that was porous to CO₂ (Figure 4.9).

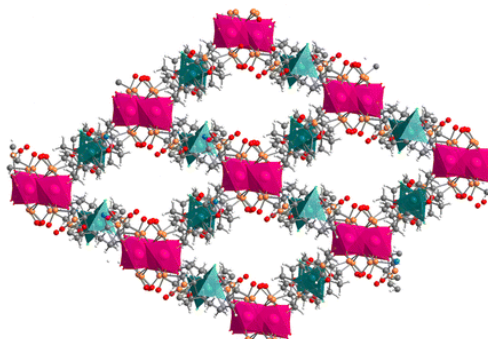


Figure 4.9. Three-dimensional structure of the CP [GdCu(DOTP)Cl]·4.5H₂O showing the presence of 1-D channels.¹⁶ Color code: Gd, pink; C, gray; N, blue; Cu, dark green; Cl, light green; O, red.

The third and last example was reported in 2015 by Li-Min Zheng *et al.*¹⁷ This structure is particularly interesting since it has many similarities with the example that will be described in this Chapter. In this third example, the authors reported the synthesis of a new 2D CP based on the H₆NOTP ligand (Figure 4.10)

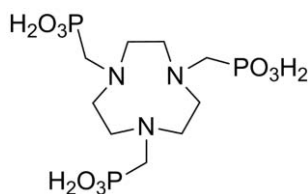


Figure 4.10. Structural formula of H₆NOTP ligand.

This CP had the general formula of [CoCa(H₂NOTP)(H₂O)₂](ClO₄)_n·nH₂O, abridged as **CoCa·nH₂O**. Interestingly, **CoCa·nH₂O** showed a multistable equilibrium between phases of different hydration states. In this study, the authors were able to characterize the different phase transformations depending on the relative humidity (RH) by using different techniques (SCXRD, PXRD, and water vapour sorption isotherms). They first synthesised the compound Co(H₃NOTP)·3H₂O, and then Ca(OH)₂ was added into a solution of Co(H₃NOTP) in water. The suspension was stirred overnight at 100°C and then filtered. The filtrate was adjusted by addition of 1M HClO₄ to pH 1.9 and left at room temperature for 3 days to afford violet crystals of **CoCa·4H₂O**. Co(III) shows an octahedral molecular geometry with the six sites occupied by three ring N-atoms and three O-atoms from the same H₂NOTP⁴⁻ ligand, whereas Ca(II) atoms also has a distorted octahedral geometry, formed by four phosphonate O-atoms and two water molecules (Figure 4.11)

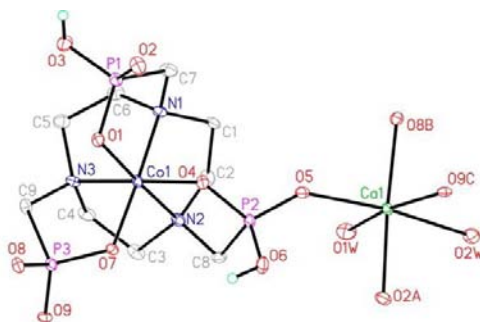


Figure 4.11. Coordination environments of Co(III) and Ca(II) in **CoCa·4H₂O**.¹⁷

When **CoCa·4H₂O** was exposed to dry ambient conditions, this led to the new phase **CoCa·2H₂O**. This new phase crystallized in the same monoclinic P2₁/n space group to that **CoCa·4H₂O**. The layer topology of this new phase was identical to **CoCa·4H₂O**. However, the phase transition produced a rearrangement of the cell parameters. By heating **CoCa·2H₂O** up to 220°C, a new dehydrated phase called **CoCa-de** appeared. Although temperature-dependent PXRD measurements were useful to characterize the progressive phase transformation between **CoCa·2H₂O** and **CoCa-de**, they were not appropriate to follow the transformation between **CoCa·2H₂O** and **CoCa·4H₂O**. Hence, a droplet of water had to be added to the sample (Figure 4.12) to see this transformation.

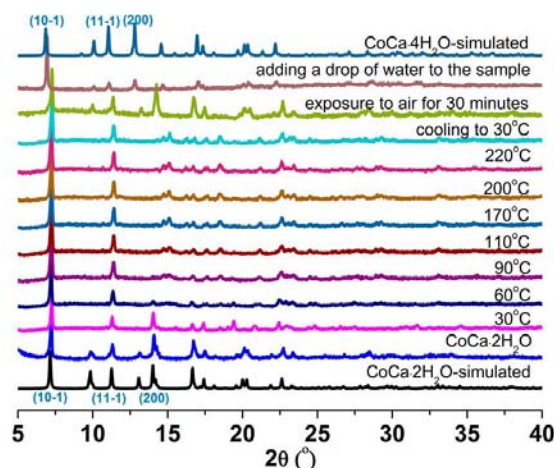


Figure 4.12. Temperature-dependent PXRD measurements showing the progressive transformation between **CoCa·2H₂O** and **CoCa-de**, the recovering of **CoCa·2H₂O** after the “exposure to air for 30 min” and the transformation to **CoCa·4H₂O** after “adding a drop of water to the sample”.

Furthermore, the authors also measured a water adsorption-desorption isotherm to obtain more information about the different phase transformations (Figure 4.13). To perform the isotherm, the sample was previously activated at 120°C under vacuum for 2 h to obtain the fully dehydrate **CoCa-de** phase. As the isotherm shows, **CoCa-de** experienced a five-step adsorption process in the RH range of 0-97 %. They attributed each step to a different phase: **CoCa-de**, **CoCa·2H₂O**, **CoCa·3H₂O** and **CoCa·4H₂O**. Unfortunately the authors were not able to isolate a pure phase of **CoCa·3H₂O** due to the difficulty for controlling the humidity during the XRD measurements.

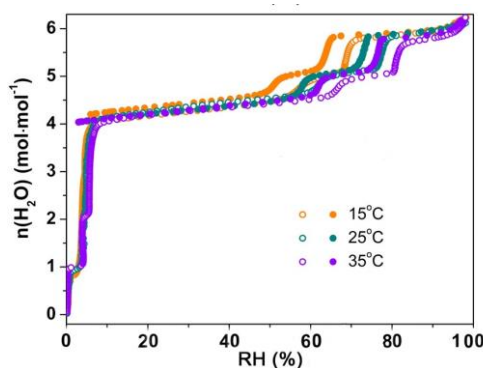


Figure 4.13. Water adsorption-desorption isotherm of **CoCa-de** showing the five-step adsorption process.¹⁷

4.3. Flexible coordination polymers.

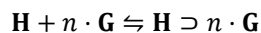
Phenomena of phase transformation as the one reported for **CoCa·nH₂O** in the previous section, or the one reported by us in the Publication 2 of this Thesis, are not rare in the field of CPs. These phenomena are related to the structural flexibility of CPs, which can be induced by different stimuli, including temperature, light, pressure and guest effects. Among them, structural transformations induced by guest effects, and particularly, guest solvent effects constitute by far the most known and studied cases.

4.3.1. Guest induced flexibility.

CPs are usually synthesised in the presence of solvent and thereby, they usually crystallise accommodating solvent molecules in their frameworks. These solvent guest molecules are bonded through weak supramolecular interactions (e.g. hydrogen bonding, π -interactions, etc.) with the framework and are responsible of achieving an optimal packing. However, due to the weakness of these interactions, very often guest molecules can be easily removed from the host framework inducing changes in the CP structure. In 1998, Prof. Kitagawa classified the CPs in three categories depending on their response to the removal of guest molecules.¹⁸ The **first generation** corresponds to CPs that show irreversible framework collapse upon removal of guest molecules. The **second generation** includes those CPs having stable and robust porous frameworks that showed permanent porosity after the removal of guest molecules. Finally, the **third generation** refers to CPs having flexible and dynamic frameworks that upon removal of guest molecules respond with reversible changes in their porosity.

Since the raise of the field of CPs/MOFs, most of the attention in research has been devoted to the second generation whereas members of the third generation have been overlooked. This fact can be explained because of the enormous interest for obtaining porous coordination polymers (PCPs) for gas-related applications, such as capture, storage or separation of H₂, CO₂, CH₄, etc. However, in the last years, the interest for the flexible third generation CPs has been recovered thanks to their promising stimuli-responsive behaviour and selectivity for guest adsorption, which is beyond the scope of rigid frameworks.

Prof. Kitagawa classified transformations of this **third generation** of CPs in three different types.¹⁹ According to the following scheme, a guest induced transformation can be seen as an exchange between two equilibrium states:



Where \mathbf{H} refers to the host without guests (also called apohost), \mathbf{G} is the guest molecule, n is the stoichiometry of guest vs. apohost, and state $\mathbf{H} \supset n \cdot \mathbf{G}$ corresponds to the host framework containing the guest molecules.

The three different types of structural transformations are (Figure 4.14):

- Type I of “recoverable collapsing” corresponds to the transformation between a crystalline state $\mathbf{H} \supset n \cdot \mathbf{G}$ that leads to an amorphous state \mathbf{H} by removal of the guest molecules \mathbf{G} . It is a reversible process, that is, the crystalline state should be recovered under exposure of \mathbf{H} to the initial conditions. It is also referred to as a “crystal-to-amorphous transformation.”
- Type II of “guest-induced transformation” takes place when the simultaneous exchange of \mathbf{G} molecules with another guest \mathbf{G}' is accompanied with structural changes between the two crystalline states $\mathbf{H} \supset n \cdot \mathbf{G}$ and $\mathbf{H} \supset n \cdot \mathbf{G}'$. Type II is considered also as a type of “crystal-to-crystal transformation”.
- Type III of “guest-induced reformation” refers to the transformation between a crystalline state $\mathbf{H} \supset n \cdot \mathbf{G}$ that leads to a crystalline state \mathbf{H} by removal of guest molecules \mathbf{G} . It is also reversible, so crystalline state $\mathbf{H} \supset n \cdot \mathbf{G}$ can be recovered under the initial conditions. It is also a type of “crystal-to-crystal transformation”.

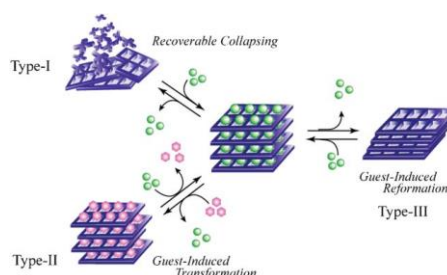


Figure 4.14. Schematically representation of the three types of transformations experienced by the third generation of CPs.¹⁹

4.3.2. Breathing modes of flexible CPs.

A first classification for the different mechanisms of flexibility in third generations CPs was given in 2004 by Kitagawa and Uemura.¹⁹ They categorized the variety of breathing mechanisms as a function of the dimension. This initial insight has been later review by other authors such Ferey and Serre²⁰ and Jenkins *et al*²¹. The six modes of flexibility proposed are as follows:

- I. 1-D Chains: Guest molecules occupy the voids between chains yielding a compact packing. Upon guest removal or exchange, 1D chains change their conformation to obtain a more favourable packing.
- II. 2-D stacked layers: Guest molecules occupy the interlayer space and their interaction with the 2D layers determines the manner in which the layers stack up. This manner can be either superimposed or shifted.

- III. 2-D interdigitated layers: Interdigitated 2D layers stack up forming 1-D channels, which are occupied by guest molecules. Removal of guest molecules causes the closure of the 1-D channels, thus approaching these layers. This transformation is reflected in the shortening of the stacking parameter.
- IV. 3-D Pillared layers: For those 3D frameworks formed by pillared layers, the reversible elongation/shortening of the stacking parameter upon inclusion/removal of guest molecules is realized by flexible pillar ligands.
- V. 3-D expanding and shrinking grids: In these frameworks, the drastic volume change is induced by strong host-guest interactions. The volume decrease can be associated either with removal or evacuation of the guests.
- VI. 3-D Interpenetrated grids: In this case, interpenetrated grids are densely packed in the absence of guests, whereas their inclusion generates a sliding of one network.

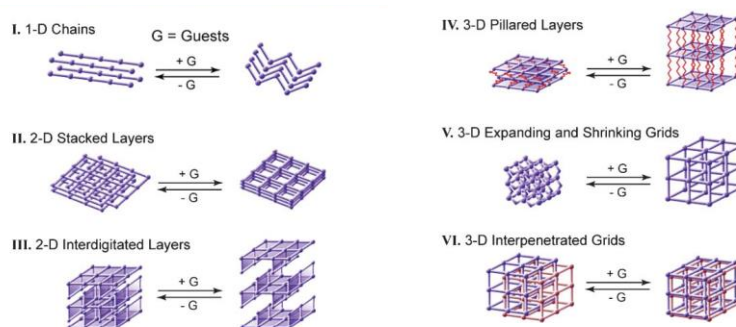


Figure 4.15. Schematic representation of the six modes of flexibility proposed by Prof. Kitagawa and Uemura.¹⁹

4.4. Our results.

At this stage of the Thesis, our main objective was the formation of heterometallic CPs containing the Gd(III)-DOTA-4AmP unit. For this purpose, we used the “two-step synthesis” strategy introduced in Chapter 3, by first synthesising the metal complex Gd(III)-DOTA-4AmP, and subsequently, using it as the bridging ligand for the construction of new CPs. Various transition metals in a great variety of conditions of reaction (e.g. concentration, pH, temperature, solvent composition, etc.) were tried in combination with the ligand Gd(III)-DOTA-4AmP. However, only in two cases, crystals suitable for SCXRD analysis were obtained. These cases corresponded to the systems formed with Mn(II) and Zn(II) ions.

For Mn(II), a 2-D CP of formula $[\text{Mn}_2(\text{Gd-H-DOTA-4AmP})(\text{H}_2\text{O})_7] \cdot n\text{H}_2\text{O}$ was obtained, whereas a 3-D CP of formula $\text{Zn}_{6.5}[\text{Gd}_3(\text{H-DOTA-4AmP})_2(\text{DOTA-4AmP})(\text{H}_2\text{O})_3] \cdot 18\text{H}_2\text{O}$ was formed when Zn(II) was used. The Mn(II)-based CP presented flexibility upon gain/loss of guest solvent molecules. This transformation was thoroughly studied in the Publication 2 of this Thesis, and will be reviewed in detail in the present section. On the other hand, the Zn(II)-based CP is the object of study of the Third publication, and it will be reviewed in the next Chapter 5 along with the study of its relaxometric properties as contrast agents for MRI.

4.4.1. Synthesis of Gd-DOTA-4AmP.

The ligand 1,4,7,10-tetraazacyclododecane-1,4,7,10-tetraacetamidomethylene phosphonic acid (known as DOTA-4AmP, Figure 4.1) was first reported by Sherry and co-workers in 1999.²² In this early work, the authors described the formation of the Gd(III)-DOTA-4AmP unit as well as its unique relaxivity properties. Indeed, they found a dependence of the relaxivity to the pH, which proved useful to monitor changes in pH. In 2007,²³ Sherry and co-workers published a more detailed relaxometric and potentiometric study of the pH dependence properties of the Gd(III)-DOTA-4AmP complex and speculated that this behaviour can be related with the exchangeable protons of the pendant arms of the phosphonate groups.

In our work, the synthesis of DOTA-4AmP was done following the synthetic route proposed by Sherry in 2007,²³ starting from the commercially available diethyl phthalimidomethylphosphonate (Figure 4.16).

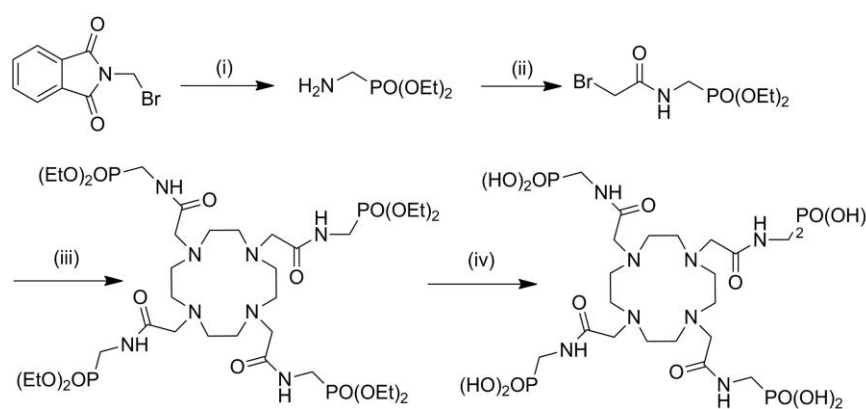


Figure 4.16. Synthetic route of DOTA-4AmP based on the procedure reported by Sherry *et al.*²³ (i) $\text{N}_2\text{H}_4/\text{EtOH}$; (ii) $\text{BrCH}_2\text{COBr}/\text{K}_2\text{CO}_3/\text{CH}_2\text{Cl}_2$; (iii) cyclen/ $\text{K}_2\text{CO}_3/\text{CH}_3\text{CN}$, 70°C ; (iv) 30% HBr/AcOH , RT.

Once DOTA-4AmP was synthesised, the metal macrocyclic complex Gd-DOTA-4AmP was formed. This formation took place by adding an aqueous solution of gadolinium chloride hexahydrate into an aqueous solution of DOTA-4AmP (pH 10; adjusted using 1M NaOH) under stirring at 70°C . The pH of the mixture was kept at 10 using 1M NaOH throughout the addition. Then, the mixture was left at 70°C under stirring for 18 h. Finally, the pH was adjusted to pH=8 by the addition of concentrated HCl. The exact concentration of Gd(III) ions was determined by ICP-MS, and the final concentration of the Gd-DOTA-4AmP was adjusted to 20 mM by the addition of water (see Experimental Section of the Publication 2's Supporting Information). For solubility reasons, the complexation reaction should be exclusively carried out in aqueous medium. In addition, as already pointed out by Sherry *et al.*²³ and conversely to what occurred in other complexation reactions of DOTA-tetraamide ligands in water, which are performed in acidic conditions to avoid the formation of the insoluble gadolinium hydroxide, complexation reaction between DOTA-4AmP and Gd(III) should be carried out at basic pH ($\text{pH} > 8$) in order to form the desired highly symmetrical complex.

4.4.2. Synthesis and characterization of the structure of $[\text{Mn}_2(\text{Gd-H-DOTA-4AmP})(\text{H}_2\text{O})_7] \cdot 21\text{H}_2\text{O}$ (1-op).

An aqueous solution of manganese acetate tetrahydrate (0.8 mmol) was mixed with a solution of Gd-DOTA-4AmP (0.4 mmol) previously adjusted to pH=6. Immediately after mixing, a white precipitate

appeared. Then, the pH of the mixture was adjusted to pH=5.4 by cautious addition of concentrated HCl (1M), at which point the precipitate disappeared. Then, the mixture was left undisturbed in a conical flask for 10 days. After that, transparent needle-like crystals appeared at the bottom of the flask (see Experimental Section of the Publication 2's Supporting Information).

In this reaction, it is important to point out the necessity to assure a pH=6 through all the addition of manganese acetate over Gd-DOTA-4AmP to avoid the formation of Mn(II) hydroxide, which is faster than the formation of the CP. Furthermore, Mn(II) hydroxide is irreversibly oxidized by atmospheric oxygen to Mn(III) oxide. Also it is very important to adjust the pH to 5.4 once the white precipitate appears. Evolution of this amorphous precipitate led to the formation of the crystalline material. Interestingly, it was observed that, by lowering the pH of the mixture, the formation of the crystals became slower but better crystals were obtained. By successive trials, we determined that the pH of dissolution of the amorphous precipitate (pH=5.4) was the lowest possible pH to obtain any crystalline precipitate. At lower pH values, the precipitation of any solid material is precluded.

The needle-like crystals obtained at pH=5.4 were washed three times with deionized water and analysed by SCXRD. The analysis of the structure revealed the formation of a 2-D CP of formula $[\text{Mn}_2(\text{Gd-H-DOTA-4AmP})(\text{H}_2\text{O})_7] \cdot 21\text{H}_2\text{O}$ (**1-op**). **1-op** was solved and refined in the monoclinic space group $P2_1/c$. The asymmetric unit contains one Gd-H-DOTA-4AmP unit, two Mn(II) ions and 28 water molecules. Connecting nodes in **1-op** are formed by binuclear Mn(II) units of formula $[\text{Mn}(\text{PO}_3\text{R})_4(\text{H}_2\text{O})_6]$, in which the two Mn(II) ions are bridged by two O-atoms of two phosphonate groups (Figure 4.17 and Figure 1b of the Publication 2). Both Mn(II) centres adopt a distorted octahedral geometry coordinated to three O-atoms of phosphonate groups, one acting as monodentate and two bridging O-atoms acting as bidentate, and three water molecules. On the other hand, Gd(III) ions are within the macrocyclic cavity of DOTA-4AmP, with a coordination sphere formed by four ring N-atoms, four O-atoms of the amide pendant arms and one water molecule in the apical position (Figure 4.17 and Figure 1a of the Publication 2).

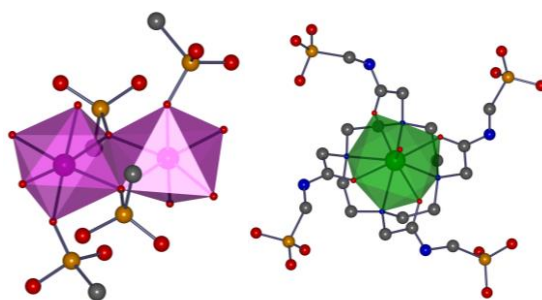


Figure 4.17. Coordination environments of Mn(II) (Left) and Gd(III) (Right). Colour code: Mn, violet; Gd, green; C, black grey; N, blue; O, red.

Each binuclear unit is connected to four Gd-H-DOTA-4AmP linkers and vice versa, creating layers that extend along the *ac* plane (Figure 4.18 and Figure 1c of the Publication 2).

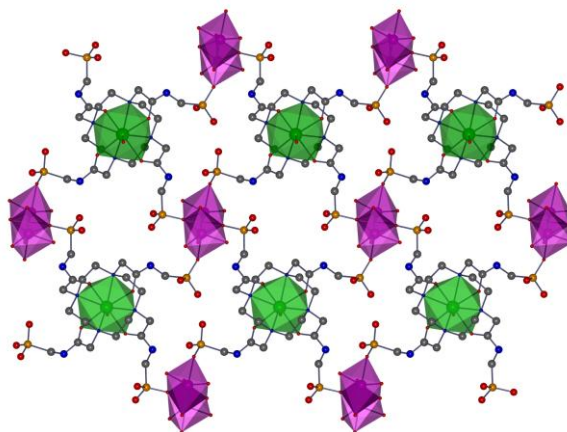


Figure 4.18. 2-D layers extending along *ac* plane. Colour code: Mn, violet; Gd, green; C, black grey; N, blue; O, red.

These layers show a corrugated conformation that stack up along the *b*-axis forming 1-D channels along the *a*-axis. These channels are filled with 21 guest water molecules per formula unit (Figure 4.19), as confirmed by elemental analysis and thermogravimetric analysis (Table S2 and Figure S1 in the Publication 2's Supporting Information). The 1-D channels have approximately dimensions of 14.8×9.5 Å, affording an estimated solvent-accessible void volume of 2657 Å^3 , representing the 45% of the total cell volume (5958 Å^3).

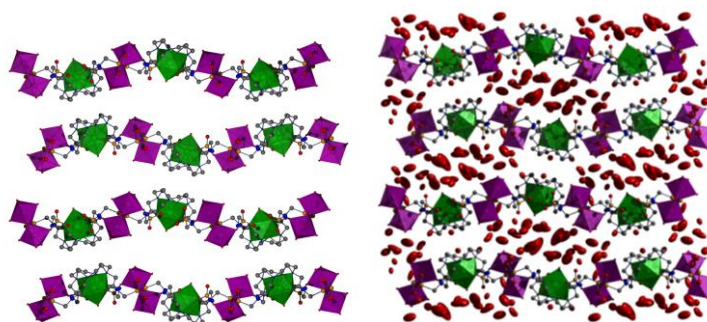


Figure 4.19. Corrugated 2-D layers viewed along the *a*-axis, showing empty 1-D channels along the *a*-axis (Left), and 1-D channels showing the contained guest water molecules (Right).

4.4.3. Transformation between $[\text{Mn}_2(\text{Gd-H-DOTA-4AmP})(\text{H}_2\text{O})_7] \cdot 21\text{H}_2\text{O}$ (**1-open pore**) and $[\text{Mn}_2(\text{Gd-H-DOTA-4AmP})(\text{H}_2\text{O})_7] \cdot 5\text{H}_2\text{O}$ (**1-closed pore**).

When single crystals of **1-op** were exposed to a dry environment ($\text{RH} < 40\%$), a new phase was formed as confirmed by the PXRD measurements (Figure S5 of the Publication 2's Supporting Information). The crystalline structure of this new phase was determined by SCXRD. The new phase was solved and refined in the monoclinic space group *C2/c*, revealing the formation of a 2-D CP very similar to **1-op** in its topology and connectivity with a formula unit $[\text{Mn}_2(\text{Gd-H-DOTA-4AmP})(\text{H}_2\text{O})_7] \cdot 5\text{H}_2\text{O}$ (**1-cp**); that is, with 16 guest water molecules less in its structure. When comparing **1-op** with **1-cp** structures, a drastic reduction in the cell volume was observed (5958 Å^3 (**1-op**) compared to 4335 Å^3 (**1-cp**); 27% reduction) and, in particular, in the solvent-accessible volume (from 2657 Å^3 (**1-op**) to 682 Å^3 (**1-cp**); 27% reduction).

(**1-cp**); 74% reduction). This reduction is a consequence of the change of conformation in the 2-D layers from a corrugated disposition in **1-op** to a flatter conformation in **1-cp**. This change led to a closer packing between the 2D-layers along the *b*-axis. Indeed, the *b*-axis is reduced from 19.8 Å (**1-op**) to 14.5 Å (**1-cp**), thereby closing the 1-D channels with the consequent loss of 16 water molecules during the transformation (Figure 4.20).

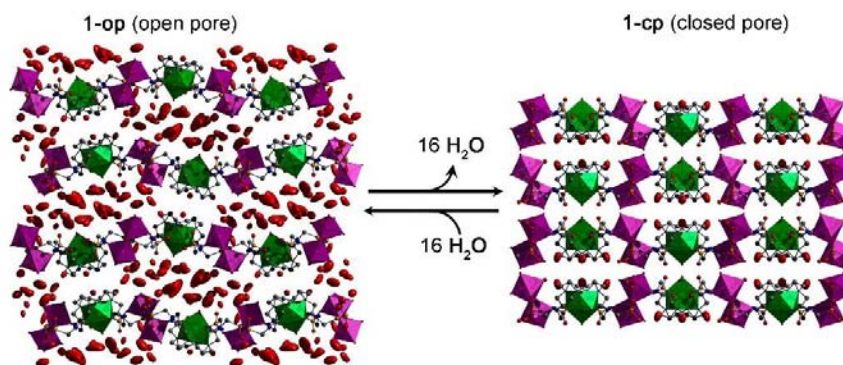


Figure 4.20. Representation of **1-op** ↔ **1-cp** transformation upon guest water removal.

Interestingly, the single crystal-to-single crystal (SC-SC) transformation allows understanding the atomistic details that take place during transition. Thanks to the rearrangement of the 2-D layers in the **1-cp** phase, two new interlayer H-bonds appeared (Figure 4.21), one double H-bond formed between the gadolinium-bound water molecule and the O7 atom of one phosphonate group (O1W⋯O7, 2.65 Å), and one simple H-bond between the non-coordinated O3 atom of one phosphonate group and one manganese-bound water molecule (O3W⋯O3, 2.83 Å). On the contrary, there were no direct H-contacts between the 2-D layers in the **1-op** phase.

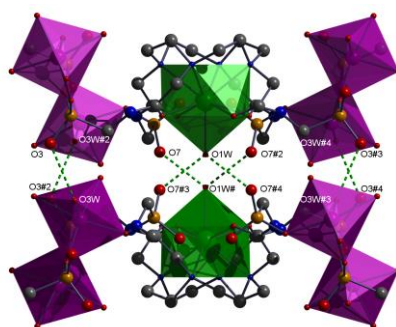


Figure 4.21. Representation of direct H-bond contacts between 2-D layers in **1-cp** phase.

Furthermore, a more detailed analysis of the **1-op**→**1-cp** transformation shows that the transition from corrugated layers (**1-op**) to flatter layers (**1-cp**) is promoted by the rotation of the Mn-based binuclear units about the *a* axis. As it is seen in Figure 4.22, this rotation implies the cleavage and formation of two phosphonate-Mn(II) and two water-Mn(II) coordination bonds per Mn(II) binuclear unit.

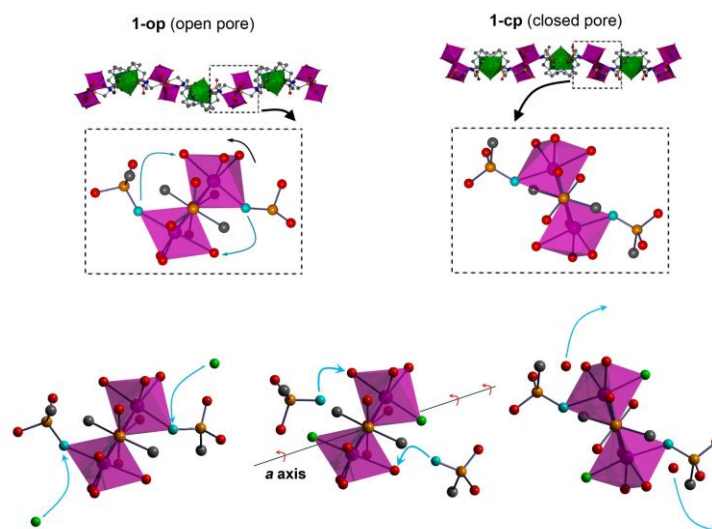


Figure 4.22. (Top) Transformation between **1-op** and **1-cp** implies the rotation of the Mn(II) binuclear unit about *a*-axis. (Bottom) This rotation presumably takes place *via* a ligand exchange mechanism in which two water molecules (green) displace two O-atoms of the phosphonate (blue) forming an intermediate that can freely rotate around the *a*-axis, in the final step of the mechanism, the O-atoms (blue) displace two coordinated water molecules (red) to form two new $\text{-PO}_2\text{O-Mn}$ bonds.

We hypothesised that water molecules may participate in the rotation of the Mn(II)-based binuclear subunit *via* a ligand exchange mechanism illustrated in Figure 4.22. As In a first step, two water molecules (depicted in green) per Mn-binuclear unit substitute two O-atoms (depicted in cyan) of two phosphonate groups in the axial positions of the Mn(II) coordination sphere. Thanks to this substitution, the Mn(II) binuclear unit is free to rotate about *a* axis, and by rotating, the previous O-atoms of the phosphonate groups (cyan) can approach to the leaving waters (depicted in red) positions and substitute them.

The reversibility of the SC-SC transformation was confirmed by incubating crystals of **1-cp** in water overnight. PXRD analysis of the resulting sample revealed that **1-op** phase is recovered (see Figure S5 of the Publication 2's Supporting Information), demonstrating that the transition **1-op**↔**1-cp** is reversible. Therefore, this transformation can be classified as a Type-III "Guest-induced reformation" according to Kitagawa's classification (see section 4.3.1.) since refers to the transformation between to crystalline states promoted by the removal of guest molecules. Furthermore, the transformation is reversible and the initial state can be recovered by exposing the material under the initial conditions.

4.4.4. Water sorption and humidity-controlled PXRD measurements.

Since this phase transformation involves loss/gain of water, we were particularly interested in understanding the water sorption behaviour of **1** and its relationship with **1-op**↔**1-cp** phase transformation. To better understand how this relationship was, we combined the data from a water vapour isotherm with humidity-controlled PXRD measurements.

4.4.4.1. Water vapour sorption isotherm.

Previously to measuring water vapour sorption isotherm, a certain amount of as-made **1-op** was exposed to high vacuum during 16 h to assure the full conversion to the **1-cp** phase. Later on, water vapour adsorption-desorption isotherm was measured using a gravimetric instrument DVS Advantage-1 (Surface Measurement Systems Ltd.) (see Publication 2's Supporting Information). The collected isotherm showed different paths between the adsorption and desorption branches (Figure 4.23). The adsorption branch follows a representative type-II trend up to RH of 85%, in which the water uptake is $0.28 \text{ g}_{\text{water}} \cdot \text{g}_1^{-1}$ or 19 H_2O molecules per formula unit. Above this RH, a step appears, changing the trend of the isotherm. This step in the adsorption branch, reflected in an abrupt increase in the water uptake, might be attributed to a **gate-opening** effect, which is a characteristic effect of flexible CPs. The pressure (or RH) at which the step appears is referred to as **gate-opening pressure** and represents the onset pressure at which a structure changes from a closed-pore to an open-pore state.²⁴ This event raised the water uptake up to $0.40 \text{ g}_{\text{water}} \cdot \text{g}_1^{-1}$ or 28 H_2O per formula unit at RH of 95%. On the other hand, the desorption branch, which had a hysteretic behaviour, presented also a step. This step might be attributed to a **gate-closing** effect and occurs in the RH range from 70% to 55%.

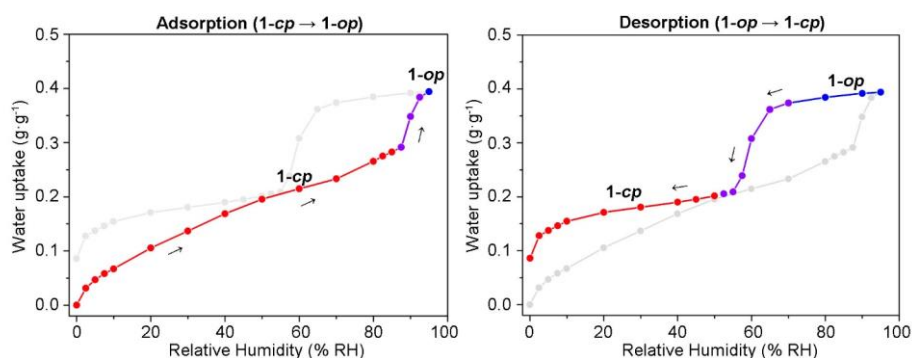


Figure 4.23. (Left) Adsorption branch showing a step at 95% RH (Right) Desorption branch shows hysteretic behaviour and a step between 70 and 55% RH.

4.4.4.2. Humidity-controlled PXRD measurements.

As we have seen in the previous section 4.4.2.1 the presence of steps in the adsorption-desorption isotherm is usually attributed to flexibility in CPs.²⁴ However, other phenomena such as capillary condensation or the formation of multilayers may also produce multi-step sorption isotherms.²⁵ Therefore, it is necessary to conduct XRD measurements to confirm that these steps actually coincide with **1-op** ↔ **1-cp** phase transformations.

At this point, it is worthy to highlight that there are few examples reported in the literature of phase transformation in CPs induced by water vapour adsorption-desorption fully characterized by XRD measurements. This scarcity of examples is likely consequence of the difficulty in performing XRD studies in humidity-controlled environments.

For instance, in 2010, Morris *et al.*²⁶ reported a very interesting study of the flexible CP Cu-SIP-3 having a phase transition between a hydrated and a dehydrated phase. The authors followed the phase transition by

SCXRD. At $T < 370$ K, the structure was confirmed as being hydrated. Interestingly, in the temperature range where the dehydration takes place $370 \text{ K} < T < 405 \text{ K}$, no discrete sharp Bragg peaks were observed in the SCXRD pattern, indicating a significant loss of long-range order during the transformation. Finally, at $T > 405$ K, the Bragg peaks returned and a new structure corresponding to the dehydrate Cu-SIP-3 was solved. This study was particularly interesting since due to the continuous SCXRD data acquired during the measurement, atomistic details of the guest water molecules (e.g. site occupancy factor, U_{eq}) could be monitored during all the transition. On the other hand, the authors did not perform any study about water vapour sorption and its relationship with phase transformation.

In 2011, Hiroshi Kitagawa and co-workers²⁷ studied proton conductivity properties of a series of MIL-53(M) frameworks. As a part of their study, they calculated the cell parameters of all the compounds by powder pattern fitting, before and after heating them. Then, they measured water vapour sorption isotherms of all the candidates, and very interestingly, the two cases where a gate-opening effect was observed [MIL-53(Al) and MIL-53(Al)-OH] coincided with those cases where more significant differences in the cell parameters of hydrated and dehydrated phases were observed. However, the main objective of the work was not the characterization of the relationship between the phase transformation and the water sorption behaviour and therefore, the authors did not perform any humidity-controlled PXRD measurements.

In 2013 and 2015, Li-Min Zheng and co-workers^{17,28} reported two cases of cobalt phosphonate flexible CPs showing a phase transformation upon gain/loss of guest water molecules. However, in both cases, the authors followed the phase transformation by continuous PXRD measurements by heating the sample. Interestingly, in the more recent work, which has been already commented in Section 4.2.3., the authors also observed steps in the water adsorption-desorption isotherms that they tentatively attributed to different hydration states, although some of them could not be detected by XRD measurements due to the difficulties that they have by doing these measurements in humidity-controlled environments.

In 2015, Cheetham *et al.* reported an interesting study about the transition in a CP, showing one partially hydrated phase ($\text{H}_2\text{O}/\text{Zr}=0.5$) and one fully hydrated phase ($\text{H}_2\text{O}/\text{Zr}=4$). An abrupt increase in water uptake was observed at an onset pressure $P/P_0 \approx 0.6$, most likely corresponding to the transition between phases. Very interestingly, the authors confirmed their presumption by collecting PXRD measurements under humidity controlled environment. They observed a change in the PXRD pattern at a $P/P_0=0.62$, agreeing with the step observed in the adsorption-desorption isotherm. To the best of our knowledge, this is the only reported example where the authors could make agree the onset pressure observed in a water vapour sorption isotherm with PXRD measurements carried out in a humidity controlled environment. However, it is important to highlight that the PXRD measurements were not done in continuous mode, but just at certain values of relative humidity. Furthermore, not PXRD measurements were carried out for the desorption branch even though it would have been interesting since the transformation showed a hysteretic behaviour.

In our case, we wanted to fully characterize the transition between **1-op** ↔ **1-cp** by continuous PXRD measurements under a humidity controlled environment. To this end, PXRD patterns were collected at 25 °C and at relative humidity (RH) values ranged between 5% and 95%. Samples were held at each relative humidity at least for 30 min (see S1.5. on the Publication 2's Supporting Information). Figure 4.24 shows the PXRD patterns at different RH values for the adsorption and desorption processes.

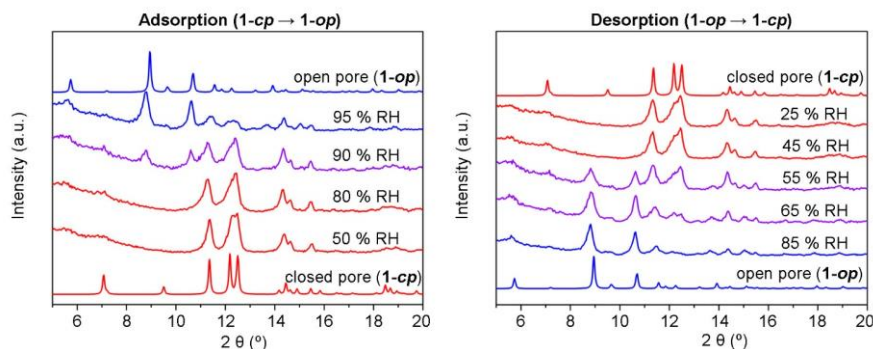


Figure 4.24. Humidity-controlled PXRD measurements of **1-cp**→**1-op** (left) and **1-op**→**1-cp** (right) transitions.

The careful analysis of Figure 4.24 reveals that the presence of a step around RH 90% in the adsorption branch (Figure 4.23) is in good agreement with the transition phase **1-cp**→**1-op** recorded using humidity-controlled PXRD. Indeed, while the corresponding patterns of **1-cp** were observed up to a RH of 80%, the PXRD pattern showed the coexistence of peaks characteristic of both phases at a RH of 90%. Finally, the transition was completed at a RH of 95 %, in which the PXRD pattern showed the characteristic pattern of **1-op**.

On the other hand, the step in the desorption branch, corresponding to the **gate-closing** effect was observed in the RH range from 70% to 55%. Interestingly, this range agreed well with the humidity-controlled PXRD measurements of the transition **1-op**→**1-cp**. Thereby, the PXRD pattern at a RH of 85 % corresponded to the pure phase **1-op**, whereas those patterns collected at RH's between 65% and 55% showed the coexistence of characteristic peaks of both phases. For RH values below 45%, the PXRD pattern is characteristic of **1-cp**.

4.5. Conclusions

To summarize, we have successfully synthesised a flexible CP using a Gd-containing phosphonate-based polyazamacrocyclic complex as the bridging ligand. Interestingly, the obtained CP presented a flexible behaviour upon water adsorption/desorption. Its flexible behaviour consisted in a phase transformation between an open-pore (**1-op**) and a closed-pore phase (**1-cp**). Such transformation was fully characterized by SCXRD of both phases, water vapour adsorption-desorption isotherm and humidity controlled PXRD measurements.

Unfortunately, **1** had some drawbacks that precluded the study of its relaxometric properties and any potential uses as MRI-CA. First, its synthesis yielded microcrystalline powder and any attempt to scale-down the size of the material led to amorphous material. Second, the use of Mn(II) ions as connecting nodes complicate any easy analysis of the relaxometric data, since the material has two sources of relaxation; that is Mn(II) and Gd(III) ions. And third, the stability of the CP under acidic media was low, and its exposure to pH<7 cause the disassembly of the framework. For all these reasons, the study of the relaxometric properties was carried out with the Zn(II)-based CP, and its results are presented in the next Chapter 5.

4.6. References.

1. Eddaoudi, M. *et al.* Systematic design of pore size and functionality in isorecticular MOFs and their application in methane storage. *Science* **295**, 469–472 (2002).
2. Burch, N. C., Jasuja, H. & Walton, K. S. Water stability and adsorption in Metal–Organic Frameworks. *Chem. Rev.* **114**, 10575–10612 (2014).
3. Shimizu, G. K. H., Vaidhyanathan, R. & Taylor, J. M. Phosphonate and sulfonate metal organic frameworks. *Chem. Soc. Rev.* **38**, 1430–1449 (2009).
4. Gagnon, K. J., Perry, H. P. & Clearfield, A. Conventional and unconventional Metal–Organic Frameworks based on phosphonate ligands: MOFs and UMOFs. *Chem. Rev.* **112**, 1034–1054 (2012).
5. Yamanaka, S. Synthesis and characterization of the organic derivatives of zirconium phosphate. *Inorg. Chem.* **15**, 2811–2817 (1976).
6. Alberti, G., Costantino, U., Allulli, S. & Tomassini, N. Crystalline $\text{Zr}(\text{R-PO}_3)_2$ and $\text{Zr}(\text{R-OPO}_3)_2$ compounds (R = organic radical). *J. Inorg. Nucl. Chem.* **40**, 1113–1117 (1978).
7. Ortiz-Avila, C. Y. & Clearfield, A. Polyether derivatives of zirconium phosphate. *Inorg. Chem.* **24**, 1773–1778 (1985).
8. and, C. V. K. S., Clearfield*, A., Aurelio Cabeza, Miguel A. G. Aranda, A. & Bruque, S. Deprotonation of phosphonic acids with M^{2+} cations for the design of neutral isostructural organic–inorganic hybrids. *J. Am. Chem. Soc.* **123**, 2885–2886 (2001).
9. Serre, C. *et al.* Synthesis, structure and properties of related microporous N , N' -piperazinebismethylenephosphonates of aluminum and titanium. *Chem. Mater.* **18**, 1451–1457 (2006).
10. Groves, J. A. *et al.* The first route to large pore metal phosphonates. *Chem. Commun.* **34**, 3305–3307 (2006).
11. Wharmby, M. T. *et al.* Yttrium bisphosphonate STA-13: A racemic phosphonate metal organic framework with permanent microporosity. *Dalt. Trans.* **39**, 6389–6391 (2010).
12. Taddei, M., Costantino, F. & Vivani, R. Synthesis and crystal structure from X-ray powder diffraction data of two zirconium diphosphonates containing piperazine groups. *Inorg. Chem.* **49**, 9664–9670 (2010).
13. Wharmby, M. T., Mowat, J. P. S., Thompson, S. P. & Wright, P. A. Extending the pore size of crystalline metal phosphonates toward the mesoporous regime by isorecticular synthesis. *J. Am. Chem. Soc.* **133**, 1266–1269 (2011).
14. Taddei, M., Costantino, F. & Vivani, R. Robust Metal–Organic Frameworks based on tritopic phosphonoaromatic ligands. *Eur. J. Inorg. Chem.* (2016). doi:10.1002/ejic.201600207
15. Kong, D., Medvedev, D. G. & Clearfield, A. DOTP-manganese and -nickel complexes: from a tetrahedral network with 12-membered rings to an ionic phosphonate. *Inorg. Chem.* **43**, 7308–

- 7314 (2004).
16. Carné-Sánchez, A. *et al.* Relaxometry studies of a highly stable nanoscale metal-organic framework made of Cu(II), Gd(III), and the macrocyclic DOTP. *J. Am. Chem. Soc.* **135**, 17711–17714 (2013).
 17. Bao, S.-S. *et al.* Co–Ca Phosphonate showing humidity-sensitive single crystal to single crystal structural transformation and tunable proton conduction properties. *Chem. Mater.* **27**, 8116–8125 (2015).
 18. Kitagawa, S. & Kondo, M. Functional micropore chemistry of crystalline metal complex-assembled compounds. *Bull. Chem. Soc. Jpn.* **71**, 1739–1753 (1998).
 19. Kitagawa, S. & Uemura, K. Dynamic porous properties of coordination polymers inspired by hydrogen bonds. *Chem. Soc. Rev.* **34**, 109–119 (2005).
 20. Férey, G. & Serre, C. Large breathing effects in three-dimensional porous hybrid matter: facts, analyses, rules and consequences. *Chem. Soc. Rev.* **38**, 1380 (2009).
 21. Murdock, C. R., Hughes, B. C., Lu, Z. & Jenkins, D. M. Approaches for synthesizing breathing MOFs by exploiting dimensional rigidity. *Coord. Chem. Rev.* **258**, 119–136 (2014).
 22. Zhang, S., Wu, K. & Sherry, A. D. A Novel pH-sensitive MRI contrast agent. *Angew. Chemie Int. Ed.* **38**, 3192–3194 (1999).
 23. Kalman, F. K. *et al.* Potentiometric and relaxometric properties of a gadolinium-based MRI contrast agent for sensing tissue pH. *Inorg. Chem.* **46**, 5260–5270 (2007).
 24. Kitaura, R., Seki, K., Akiyama, G. & Kitagawa, S. Porous coordination-polymer crystals with gated channels specific for supercritical gases. *Angew. Chemie Int. Ed.* **42**, 428–431 (2003).
 25. Brunauer, S. *The adsorption of gases and vapors Vol I - Physical Adsorption*. (Princeton University Press, 1943).
 26. Allan, P. K., Xiao, B., Teat, S. J., Knight, J. W. & Morris, R. E. In situ single-crystal diffraction studies of the structural transition of metal-organic framework copper 5-sulfoisophthalate, Cu-SIP-3. *J. Am. Chem. Soc.* **132**, 3605–3611 (2010).
 27. Shigematsu, A., Yamada, T. & Kitagawa, H. Wide control of proton conductivity in porous coordination polymers. *J. Am. Chem. Soc.* **133**, 2034–2036 (2011).
 28. Zheng, T. *et al.* Breathing effect in a cobalt phosphonate upon dehydration/rehydration: a single-crystal-to-single-crystal study. *Chem. Eur. J.* **19**, 16394–16402 (2013).

Chapter 5.

Publication 3: “pH-Responsive relaxometric behaviour of coordination polymer nanoparticles made of a stable macrocyclic gadolinium chelate”.

5.1. A CP based on Gd-DOTA-4AmP and Zn(II) for MRI CA.

In **Chapter 4**, the metal complex Gd-DOTA-4AmP was successfully synthesised and used as the bridging ligand for the synthesis of a new CP. Reaction of Gd-DOTA-4AmP with Mn(II) led to the formation of a flexible 2-D CP of formula $[\text{Mn}_2(\text{Gd-H-DOTA-4AmP})(\text{H}_2\text{O})_7] \cdot n\text{H}_2\text{O}$. Unfortunately, due to a series of reasons explained in Section 4.5, this Gd(III)-Mn(II) heterometallic CP was not suitable to be studied as MRI-CA. In our search to construct more CPs, we combined Gd-DOTA-4AmP with Zn(II) ions to yield a 3-D CP of formula $\text{Zn}_{6.5}[\text{Gd}_3(\text{H-DOTA-4AmP})_2(\text{DOTA-4AmP})(\text{H}_2\text{O})_3] \cdot 18\text{H}_2\text{O}$ (**1**). This CP could be miniaturised to the nanoscale to form a colloidal suspension that was stable in a wide range of pH=4-6. This allowed us to study the relaxometric properties of **1** and its potential applications as a MRI CA.

5.2. Fundamentals of Magnetic Resonance Imaging (MRI).

Magnetic resonance imaging (MRI) is currently one of the most powerful biomedical imaging techniques in medicine due to its non-invasive character and sub-millimetric spatial resolution. It allows obtaining 3-D images of the soft tissue, which is of great interest in the diagnosis of cancer and brain diseases.

5.2.1. Total magnetization.

Magnetic Resonance Imaging (MRI) derives directly from the phenomenon of Nuclear Magnetic Resonance (NMR), which is widely used by chemists to determine molecular structures. MRI focuses on ^1H proton nuclei of water. Like a spinning top precessing in the Earth's gravitational field, the ^1H nuclei precess in the static magnetic field B_0 of a spectrometer magnet. This precession occurs at a frequency (ν_0) dictated by the nature of the nucleus and the strength of the magnetic field of the magnet:

Equation 1:
$$\nu_0 = \frac{-\gamma}{2\pi} B_0$$

Where ν_0 is the Larmor frequency, γ is the gyromagnetic ratio, and B_0 is the static magnetic field of the spectrometer magnet. As shown in Figure 5.1, ^1H nuclei can precess parallel ($m=+1/2$) or antiparallel ($m=-1/2$) to B_0 , corresponding to two energy states in the presence of the static magnetic field B_0 . According to Boltzmann equation, there are more ^1H nuclei in the lower level (parallel to B_0) than in the upper level. Therefore, there will be total magnetization (M_0) of the sample, parallel to B_0 (by definition, the z axis).

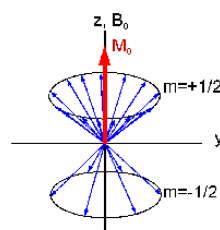


Figure 5.1. Schematic representation showing the ^1H nuclei precessing parallel ($m=+1/2$) or antiparallel ($m=-1/2$) to B_0 , and the resulting magnetization M_0 , parallel to z axis.

5.2.2. Relaxation time.

In a typical NMR experiment, the sample is exposed to an oscillating electromagnetic field B_1 (frequency ν_1) perpendicular to B_0 . For an observer placed within a rotating frame around the z axis at frequency ν_1 , it is as if the magnetization M_0 precesses around the magnetic field B_1 , which is stationary in this frame. The duration of the B_1 (radiofrequency (RF) pulse) can be calculated for tilting M_0 a flip angle α . At the end of this RF pulse, the system returns to equilibrium, the magnetization in the xy plane decreases exponentially with a time constant T_2 , and the magnetization rises exponentially on axis z with a time constant T_1 .

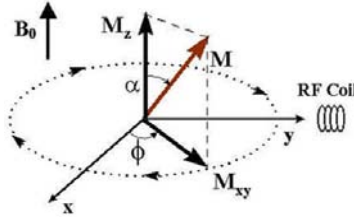


Figure 5.2. Representation of how the magnetization M_0 is tilted a flip angle α , after exposed to a radiofrequency pulse ν_1 , and how the new magnetization M can be decomposed in the magnetization M_z and the magnetization M_{xy} in the xy plane.

The longitudinal relaxation time T_1 is characteristic of the return to equilibrium of the magnetization along z (M_z) or longitudinal magnetization, as shown in Equation 2. This relaxation is due to the interaction of the excited nuclei with their environment; particularly with the magnetic active agents of this environment (^1H nuclei, unpaired electrons). For this mechanism to work, there must be a movement of the molecules (Brownian motion). T_1 relaxation time will depend on the mobility and therefore, on the viscosity of the environment.

Equation 2:

$$M_z = M_0(1 - e^{-\frac{t}{T_1}})$$

The T_2 transversal relaxation time is characteristic of the disappearance of the signal in the xy plane. This is an entropy phenomenon that corresponds to spin dephasing in the xy plane. T_2 is always below T_1 .

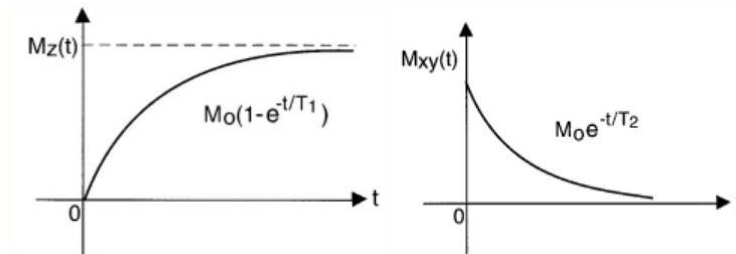


Figure 5.3. Relaxation processes of longitudinal M_z (left) and transversal M_{xy} (right) magnetization.

5.2.3 Contrast Agents (CA). Relaxivity r_i and parameters controlling it.

Contrary to other techniques such as fluorescence imaging, where the CA is visible by itself, and no images can be acquired without the use of CAs, MRI does not require the use of CAs for acquiring

images. However, many times they are used to enhance the intrinsic contrast of images and thereby, allowing the visualization of disease states that otherwise can go unnoticed.

MRI-CAs are substances that modify the relaxation of water ^1H nuclei in their surroundings, usually shortening it (Figure 5.4). This objective is achieved with paramagnetic substances through a dipole-dipole mechanism that accelerate the recovery of the equilibrium state of the ^1H nuclei after the radiofrequency pulse. In 1948, Bloch *et al.* reported, for the first time, the use of the paramagnetic ferric nitrate salt to enhance relaxation rates of water. Some 30 years later, Lauterbur *et al.* applied a Mn(II) salt to distinguish between different tissues based on the differential relaxation times. Nowadays, Gd(III) complexes are the most widely used MRI-CAs in the clinical practice due to its seven unpaired electrons, which makes it the most paramagnetic stable metal ion.

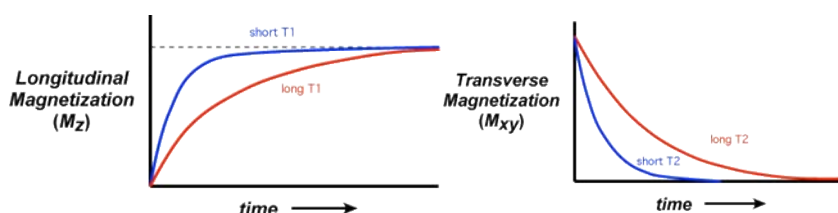


Figure 5.4. Relaxation processes for longitudinal (left) and transversal (right) magnetization without (red) and with (blue) the use of CAs.

Relaxation enhancement of hydrogen water nuclei by Gd(III) -complexes is a catalytic process in which water molecules in the proximity of the Gd(III) ion are relaxed faster and subsequently, exchanged with the bulk solvent (see Figure 5.5). Water molecules in the nearby of Gd(III) can be classified in three categories: (i) inner-sphere water, this correspond to water molecules directly coordinated to Gd(III) ; (ii) second-sphere water, this describes water molecules in the immediate proximity of the complex (for example, forming hydrogen bonds); and (iii) outer-sphere water, this term corresponds to the water molecules in the bulk and its interaction is only governed by random translational diffusion. Relaxation of water hydrogen atoms occurs via a dipolar mechanism; fluctuating magnetic dipoles cause spin relaxation.

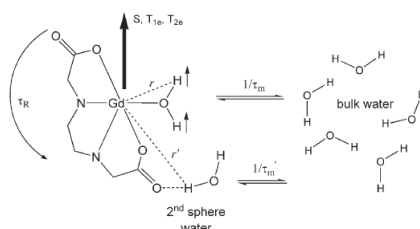


Figure 5.5 Schematic representation of the relaxation enhancement of hydrogen water nuclei by Gd(III) complexes. The main parameters controlling the process are represented: rotational correlation time, τ_R ; residence time, τ_M ; Gd-H distance, r ; spin number S and dipole relaxation times, T_{1e} and T_{2e} .

Figure 5.5. tries to summarize the parameters controlling relaxation of water hydrogen atoms mediated by Gd(III) -based CAs. The hydrogen nuclei magnetic dipoles are denoted by small vectors. In this Figure,

there is one water molecule in the inner-sphere ($q=1$) with a Gd-H distance r and a residence time τ_m . The Gd(III) ion has a much larger dipole characterized by the spin number S . This dipole undergoes a relaxation described by T_{1e} and T_{2e} . The complex has rotational motion. Sometimes this motion is known as tumbling, and it is described by a rotational correlation time, τ_R .

The efficiency of a CA is expressed by relaxivity r_i , which is defined by Equation 3.

Equation 3:

$$r_i = \frac{\Delta T_i^{-1}}{[CA]}$$

Those CAs that produce big changes in relaxation time T_i with small concentration of CA will show higher values of r_i , being more efficient CAs. One can define longitudinal relaxivity r_l and transversal relaxivity r_2 . In this Thesis, we will pay attention only to r_l . Longitudinal relaxivity r_l can be divided in its contributions coming from the inner and the outer sphere (Equation 4).

Equation 4:

$$r_l = r_l^{IS} + r_l^{OS}$$

Parameters controlling the outer-sphere relaxivity r_l^{OS} are complex and will not be explained in this Thesis (the interested reader is addressed to other sources).¹ However, for the currently used Gd(III)-based CAs under the usual clinical conditions, is considered that the terms of the inner- and the outer-sphere are comparable. Moreover, for common situations in which the inner-sphere water is labile and the exchange between the Gd(III)-bound water and the bulk solvent represents the main source of relaxation enhancement, it can be considered that r_l^{IS} can be given by the Equation 5.

Equation 5:

$$r_l^{IS} = \frac{q [CA]}{55.6 (T_{1M} + \tau_M)}$$

Where q is the number of water molecules coordinated in the inner-sphere, $[CA]$ is the concentration of the CA, τ_M is the residence lifetime of the Gd(III)-bound water molecule, and T_{1M} is the longitudinal nuclear magnetic relaxation time of the bound water molecules. In Figure 5.5, we have introduced the terms q and τ_M . On the other hand, the term T_{1M} is a complex term that describes the time fluctuation of the water proton-Gd(III) dipolar coupling and depends of parameters such as the Gd-H distance, the residence lifetime (τ_M), the rotational correlation time (τ_R) and the electric paramagnetic relaxation T_{1e} and T_{2e} . The value of T_{1e} is given by the Solomon-Bloembergen-Morgan (SBM) equations. Explaining the SBM equations is far beyond the scope of this Thesis. The interested reader can find more information in specialized sources.¹

5.2.4. Methods for improving longitudinal relaxivity r_l .

Use of CAs having high relaxivity (r_l) values has been the preferred way of overcoming the sensitivity problems of the MRI technique. It has been pointed out in the previous section that the relaxivity of a CA is controlled by a complex interplay of parameters, which at the same time can also differ according to the magnetic field strength, temperature, pH, etc. However, in this section, we want to

introduce the main strategies followed by the researchers to pursue higher relaxivities, to later focusing on the strategy of lengthening the rotational correlation time (τ_R).

5.2.4.1. Increase of the hydration state, q .

According to Equation 5, an increase in the relaxivity might be simply obtained by increasing the number of water protons in the coordination sphere of the Gd(III) ion. All the Gd(III)-based CAs currently used in clinical protocols possess only one water molecule coordinated to the gadolinium centre ($q=1$) due to the presence of eight donor atoms in their ligands. However, the use of hepta- or hexacoordinating ligands would allow the design of CAs with $q>1$. Unfortunately, this approach is limited by two main drawbacks related with the higher solvent accessibility to the metal centre: (i) the reduced kinetic and thermodynamical stability of the metal complex; and (ii) the possibility that anionic species replace water in the inner coordination sphere of Gd(III). Even though these aspects, some efforts have been dedicated to achieve Gd(III)-complexes with $q>1$, which are stable enough for *in vivo* applications.^{2,3}

5.2.4.2. Optimization of residence lifetime, τ_M .

Residence lifetime τ_M of coordinate water protons is one of the most important parameters that control the relaxivity in Gd(III)-complexes. For low molecular weight anionic Gd(III) chelates, τ_M values are about 100-500 ns and the contribution of τ_M to T_{1M} is negligible. These situations are known as fast exchange regime. On the other hand, in neutral or cationic complexes, τ_M is comparable to T_{1M} , and T_{1M} strongly depends on τ_M . These situations are called of intermediate or low exchange regime. Intermediate/low exchange regime situations are also found when dealing with high molecular weight gadolinium platforms, since the increased molecular size results in shorter values of T_{1M} . Due to this complex interplay between τ_M and T_{1M} , the design of high relaxivity CAs requires a fine tuning of residence lifetime. Thereby, much efforts have been dedicated to understand the factors controlling τ_M . In general, it has been observed that the overall electric charge of the complex affect τ_M , which is short for anionic complexes and long for cationic ones.⁴ Other parameters such as the coordination geometry of the Gd(III) coordination sphere^{5,6} and the hydrophobicity of the macrocyclic pendant arms⁷ are also important.

5.2.4.3. Increase of rotational correlation time, τ_R .

Rotational correlation time τ_R tends to be the term that dominates T_{1M} in situations of fast exchange regime. The effect of increasing τ_R was understood early on and, consequently, the attempts at increasing relaxivity were mainly focused on slowing down the rotation of Gd(III)-based agents. Figure 5.6 illustrates very nicely the effect of lengthening τ_R . It shows how relaxivity is significantly enhanced following the increase in τ_R . Interestingly, at $\tau_R=0.42$ ns, the characteristic peak of slow-rotating complexes appears, increasing in intensity and sharpening at $\tau_R=29$ ns.

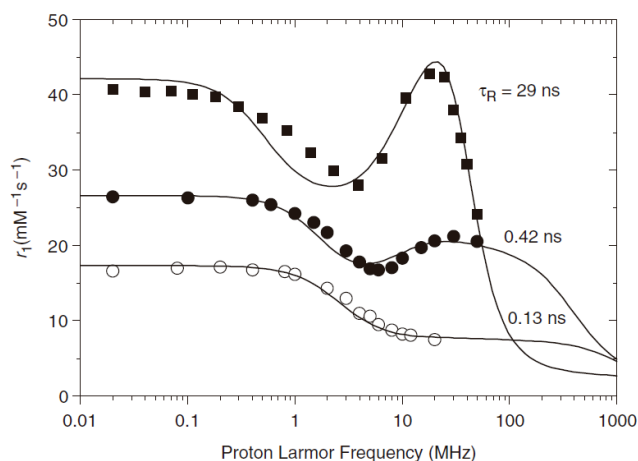


Figure 5.6. ^1H NMRD profiles (25°C) of $[\text{GdDOTA}(\text{BOM})_3(\text{H}_2\text{O})]^-$ (open circles), its inclusion complex with β -cyclodextrin (filled circles) and of $[\text{GdDOTA}(\text{BOM})_3(\text{H}_2\text{O})]^-$ HAS adduct (squares). The different shapes and amplitudes of the profiles are primarily due to the different rotational correlation τ_R of the paramagnetic complexes.¹

The task of increasing τ_R can be achieved in general by slowing down the tumbling motion of Gd(III)-based complexes. In the next section, we will devote more attention to the different strategies followed to attain this objective.

5.2.5. Strategies to slow down tumbling motion.

Basically, all the strategies for slowing down tumbling motion have been based on using high molecular weight entities as CAs. To achieve this objective, we can differentiate two broad strategies: (i) Grafting Gd(III)-agents to high molecular weight platforms; and (ii) using Gd(III) ions as building blocks to construct new high molecular weight platforms.

Regarding the first strategy, there exist a wide variety of high molecular weight platforms in which Gd(III) ions can be incorporated. These platforms include inorganic nanoparticles,⁸ viral capsids,⁹ proteins,¹⁰ mesoporous silica,¹¹ colloidal self-assembled nanoparticles,¹² zeolites,¹³ nanotubes,¹⁴ fullerenes,¹⁵ etc. An illustrative example of this first strategy was developed by Mirkin *et al.*⁸ In this work, the authors grafted Gd(III)-based agents on the surface of DNA-gold nanoparticles through a click chemistry reaction (Figure 5.7).

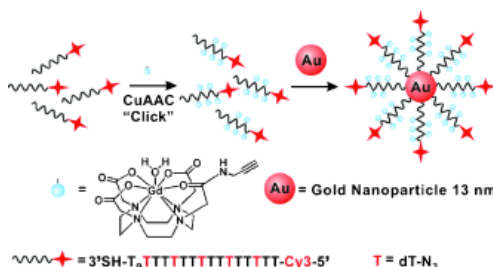


Figure 5.7. Schematic illustration of the synthesis of Cy3-DNA-Gd(III)@AuNP conjugates.⁸

On the other hand, in the second strategy, Gd(III) ions are usually part of crystal lattices and the rotational motion of Gd(III) is more hindered than in the first strategy, where gadolinium ions can undergo internal

motion about the linkages with the high molecular weight platform.¹⁶ First reported examples consisted on using Gd(III) ions as building blocks of inorganic crystal lattices. In the first example, reported in 2006 by Suzuki and co-workers,¹⁷ the authors synthesised dextran coated GdPO₄ nanoparticles from Gd(III) nitrate hexahydrate and ammonium hydrogen-phosphate. One year later, in 2007, Bridot *et al.*¹⁸ synthesised colloidal Gd₂O₃ nanoparticles by addition of sodium hydroxide into a solution of gadolinium chloride salt in diethylene glycol. Later on, in 2012, Xueyuan Chen *et al.*¹⁹ designed amine-functionalized lanthanide-doped KGdF₄ nanocrystals *via* a facile one-step solvothermal route by employing polyethylenimine as surfactant and capping ligand. Interestingly, in all these cases, the authors proved the performance of the materials as MRI-CAs with high relaxivity. Moreover, such type of densely packed structures allow for high densities of Gd(III) ions per CA particle.

In this context, CPs appeared as a good strategy to organise Gd(III) ions in crystal networks. In the Section 1.4.2.2 of Chapter 1, we have already introduced the most relevant examples of crystalline CPs containing Gd(III) as building blocks of their networks.^{20,21} In all the cases, Gd(III) ions acted as metal connecting nodes to yield CPs of formulas [Gd(1,2,4-BTC)(H₂O)₃]·H₂O, [Gd(BDC)_{1.5}(H₂O)₂] or [Gd₂(BHC)(H₂O)₆]. These CPs offered values of relaxivity as high as 35.8 s⁻¹mM⁻¹. Unfortunately, these CPs offered poor stabilities in water and high releases of free toxic Gd(III) ions. Thereby, in our group, we proposed the unprecedented strategy of using Gd(III)-based complexes as bridging ligands for the constructions of new CPs (Section 1.5 of Chapter 1).

5.3. Our Results.

In Chapter 4, we demonstrated for the first time the ability to produce CPs from the metal complex Gd-DOTA-4AmP by the synthesis of a new 2-D CP of formula [Mn₂(Gd-H-DOTA-4AmP)(H₂O)₇]·*n*H₂O. In the present section, the synthesis of the 3-D CP of formula Zn_{6.5}[Gd₃(H-DOTA-4AmP)₂(DOTA-4AmP)(H₂O)₃]·18H₂O (**1**) containing Zn(II) ions as connecting nodes is presented. This new CP is stable in a wide range of pHs, pH=4-6.5, and could be successfully miniaturised at the nanoscale, forming colloidal suspensions. These characteristics were beneficial for the study of **1** as a MRI-CA, including its Nuclear Magnetic Relaxation Dispersion (NMRD) profile and the dependence of relaxivity *r*₁ with pH.

5.3.1. Synthesis and characterization of Zn_{6.5}[Gd₃(H-DOTA-4AmP)₂(DOTA-4AmP)(H₂O)₃]·18H₂O (**1**).

The synthesis of the bridging ligand Gd-DOTA-4AmP was carried out following the same procedure reported before (Section 4.4.2. or Experimental Section of the Publication 3). Then, the Gd-DOTA-4AmP chelate was slowly diffused with Zn(II) ions. To that end, an ethanolic solution of zinc acetate dihydrate (4 mL, 11.3 mM) was carefully layered onto a Gd-DOTA-4AmP aqueous solution (4mL, 5.2 mM) in a glass vial (see Experimental Section of the Publication 3). The glass vial containing the liquid diffusion was capped and left undisturbed at room temperature for two weeks. After that, transparent octahedral crystals of **1** appeared on the walls and at the bottom of the vial. Crystal structure of **1** was solved and refined in the tetragonal P4₂/n group (see Table S1 of the Publication 3's Supporting Information). The asymmetric unit was found to contain three Gd-DOTA-4AmP units, in which, importantly, Gd(III) was confirmed to be chelated inside the macrocyclic cavity, as it can be seen in

Figure 5.8. Gd(III) ion adopts a capped square antiprismatic geometry with a coordination sphere formed by the four ring N-atoms, the four O-atoms of the amide pendant arms and one water molecule at the capping position.

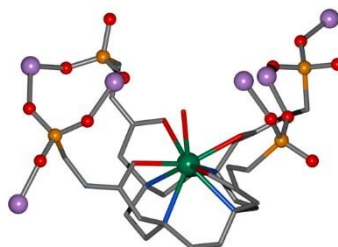


Figure 5.8. Molecular geometry of the Gd-DOTA-4AmP unit in **1**. Colour code: Gd, green; Zn, purple; C, grey; P, orange; N, blue; O, red.

The three Gd-DOTA-4AmP units appearing in the asymmetric unit of **1** have slight differences in the coordination modes of their pendant arms. According to the notation introduced by Harris *et al.*,²² the different coordination modes can be described as shown in Figure 5.9 (or Figure S1 of the Publication 3's Supporting Information). Gd1 and Gd2 units show the tridentate binding mode [3.111] in one arm and the bidentate mode [2.110] in three arms, whereas Gd3 unit shows the monodentate mode [1.100] in one arm, the bidentate mode [2.110] in two arms and the [3.111] in one arm.

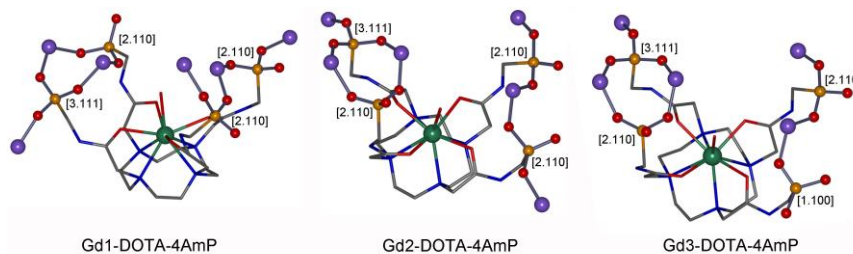


Figure 5.9. Different coordination modes of the three Gd-DOTA-4AmP units of **1**. Colour code: Gd, green; Zn, purple; C, grey; P, orange; N, blue; O, red.

On the other hand, Zn(II) ions adopt a tetrahedral geometry with a coordination environment formed by four O-atoms of four different phosphonate groups. Also, it is very interesting to note that Zn(II) ions are associated forming binuclear units called tri-winged paddle-wheel units (Figure 5.10). In this tri-winged paddle-wheels, two Zn(II) ions are linked *via* three bridging phosphonate groups with two O-atoms of two phosphonate groups at the capping positions.

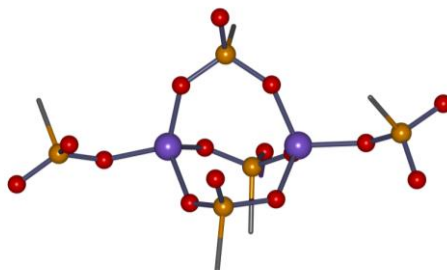


Figure 5.10. Molecular geometry of tri-winged paddle wheels units found in **1**. Colour code: Gd, green; Zn, purple; C, grey; P, orange; N, blue; O, red.

Alternatively, the 3-D structure of **1** can be analysed only in terms of an inorganic framework formed by the $\cdots\text{Zn(II)}\text{-PO}_3\text{-Zn(II)}\text{-PO}_3\cdots$ linkages. These linkages form two different types of $\text{Zn}_x\text{P}_x\text{O}_{2x}$ rings (Figure 5.11), one circular 24-membered ring ($\text{Zn}_6\text{P}_6\text{O}_{12}$, 10.9×10.3 Å) and one egg-shaped 32-membered ring ($\text{Zn}_8\text{P}_8\text{O}_{16}$, 16.3×5.6 Å). This kind of rings are common features in the chemistry of metal phosphonates.^{23,24} Interestingly, the size of these rings is relatively larger than other rings previously reported.²⁵

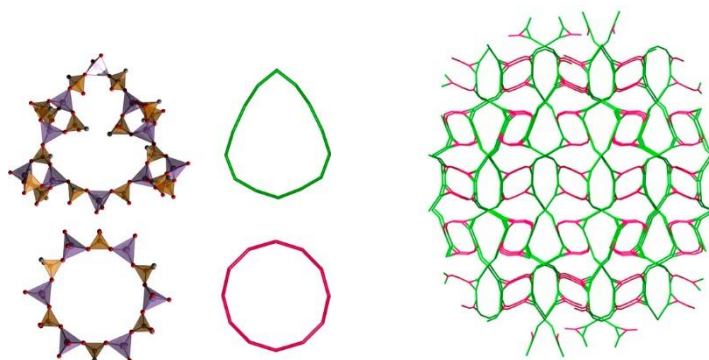


Figure 5.11. Two types of $\text{Zn}_x\text{P}_x\text{O}_{2x}$ rings present in **1**. The 3-D framework of **1** can be seen as the assembly of circular 24- (pink) and 32-membered rings (green).

5.3.2. Miniaturisation of **1** in amorphous Zn-Gd-DOTA-4AmP nanoparticles and their characterisation.

All the attempts to miniaturise **1** and form colloidal crystalline nanoparticles by means of different techniques (hydrothermal synthesis, fast mixing of reactants, emulsions, etc.) failed. All the trials led to the formation of amorphous Zn-Gd-DOTA-4AmP nanoparticles. Actually, by reproducing the same synthesis of Section 5.3.1, but instead of using a slow diffusion, both reactants were rapidly mixed, amorphous Zn-Gd-DOTA-4AmP nanoparticles in the form of a colloidal suspension were immediately formed. The resulting white colloid (Figure 5.12a) showed good stability with flocculation traces appearing only after one day. SEM and TEM images of the colloid demonstrated the formation of rounded nanoparticles (Figure 5.12b-d) with an average size of $90(\pm 30)$ nm).

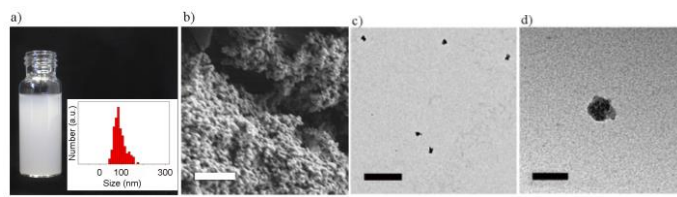


Figure 5.12. a) Photograph of the colloidal suspension of Zn-Gd-DOTA-4AmP nanoparticles and the size distribution (inset). b) SEM, and c, d) TEM images of Zn-Gd-DOTA-4AmP nanoparticles. Scale bars: b) 1 μm , c) 500 nm, and d) 100 nm.

Characterization of amorphous CPs is always challenging, since it cannot be done using Bragg diffraction-based techniques as SCXRD or PXRD. However, and even though the lack of Bragg diffraction peaks from the amorphous nanoparticles, we had the suspicion that the chemical composition and connectivity in Zn-Gd-DOTA-4AmP nanoparticles was not very different from **1**. Thereby, to prove our hypothesis and gain more information about the structural-chemical correspondence between Zn-Gd-DOTA-4AmP nanoparticles and **1**, we carried out a series of analysis using different techniques.

First, we used ICP-MS and Elemental Microanalysis CHNS to deduct the empirical formula of nanoparticles and **1**. Interestingly, Table 5.1 (or Table S2 of the Publication 3's Supporting Information) showed good correspondence for both.

Table 5.1. The table shows the correspondence between the elemental analysis of Zn-Gd-DOTA-4AmP nanoparticles and **1**. C, H and N content have been obtained from CHN elemental microanalysis, whereas Zn and Gd content have been obtained from ICP-MS analysis.

	Calculated from 1 (wt. %)	Zn-Gd-DOTA-4AmP nanoparticles (wt. %)
C	20.1	21.8 ± 1.2
N	9.4	9.8 ± 1.1
H	4.2	4.0 ± 1.4
Zn	11.9	12.2 ± 1.0
Gd	13.2	14.2 ± 1.0

Infrared (FT-IR) measurements confirmed that the phosphonate groups of Gd-DOTA-4AmP were coordinated (Figure 5.13 or Figure S5 of the Publication 3's Supporting Information), as evidenced in both spectra by the presence of two strong peaks at 1070 and 992 cm^{-1} .²⁶

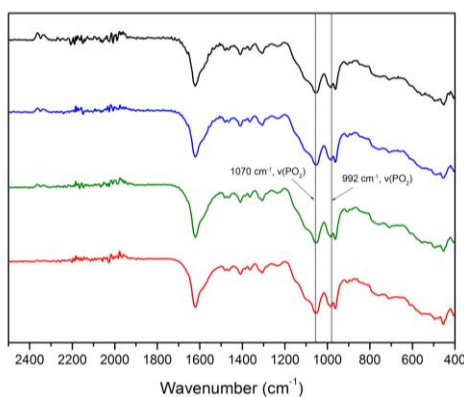


Figure 5.13. FT-IR spectra of **1** (red), Zn-Gd-DOTA-4AmP Nanoparticles (green), **1**-Eu (blue) and Zn-Eu-DOTA-4AmP

^{31}P MAS NMR solid state measurements were also performed. However, Gd(III) is highly paramagnetic and would disturb any NMR measurement. For this reason, we prepared analogous material to **1** and nanoparticles, but instead of using Gd(III)-DOTA-4AmP, we used Eu(III)-DOTA-4AmP. Eu(III) has a very similar chemical behaviour to Gd(III), but it is diamagnetic and thereby does not disturb NMR measurements. Eu(III)-DOTA-4AmP was synthesised following the same procedure as for Gd(III)-DOTA-4AmP, but using europium chloride instead of gadolinium chloride. The synthesis of the **1**-Eu analogue was done by slow diffusion of the reactants (see Section 5.3.1.). PXRD measurements confirmed that **1** and **1**-Eu were isostructural (Figure S3 of the Publication 3's Supporting Information). After confirming isostructurality of **1** and **1**-Eu, the synthesis of Zn-Eu-DOTA-4AmP nanoparticles was carried out following the same procedure as for Zn-Gd-DOTA-4AmP nanoparticles. ^{31}P MAS NMR measurements (Figure 5.14 or Figure S7 of the Publication 3's Supporting Information) confirmed that the lanthanide was placed inside the macrocyclic cavity in both crystalline and amorphous samples as it is shown by the change to chemical shifts of the $-\text{PO}_2\text{O}-$ phosphorus (17.3 ppm for Eu-DOTA-4AmP complex compared to 13.8 ppm for DOTA-4AmP ligand), similar shifts to high values were observed for **1**-Eu (17.6 ppm) and Zn-Eu-DOTA-4AmP nanoparticles (18.6 ppm).

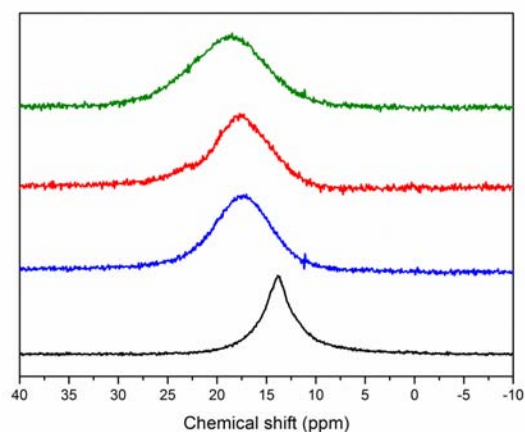


Figure 5.14. ^{31}P MAS NMR measurements for DOTA-4AmP ligand (black), Eu-DOTA-4AmP complex (blue), **1**-Eu crystals (red), and Zn-Eu-DOTA-4AmP Nanoparticles.

5.3.3. X-Ray Total Scattering PDF analysis of crystalline **1** and amorphous Zn-Gd-DOTA-4AmP nanoparticles.

Pair Distribution Function (PDF) analysis is an excellent technique to access structural information about materials in which disorder or crystallite size broadening effects limit the use of conventional Bragg crystallographic techniques. Because of this, PDF has recently been applied in CP/MOFs to study conformational changes²⁷ or to identify certain structural features in CP nanocrystals²⁸.

The results of PDF measurements for **1** and Zn-Gd-DOTA-4AmP nanoparticles are shown in Figure 5.15a in the form of $G(r)$ function. $G(r)$ provides the real-space probability of finding a pair of atoms at a distance r , relative to the average atomic density in an isotropic sample; that is, it is a weighted histogram of atom-atom distances in a structure. Each peak in $G(r)$ can be assigned to a contribution of one or more pairs of atoms, agreeing well with the distances extracted from the crystalline structure of **1**. On the other

hand, the presence of peaks in the case of **1** at $r > 5\text{\AA}$ indicates long-range order, and agrees with the Bragg diffraction observed in the XRD studies. For Zn-Gd-DOTA-4AmP nanoparticles peaks do not appear for $r > 5\text{\AA}$, demonstrating the loss of long-range order as a consequence of the miniaturisation process. However, the analysis of peaks positions reveals that **1** and Zn-Gd-DOTA-4AmP nanoparticles present a very similar pattern. Figure 5.15c shows the correlation between peaks of $G(r)$ with the average atomic distances extracted from the crystalline structure of **1**, proving that the main building blocks of **1** are also present in the amorphous nanoparticles.

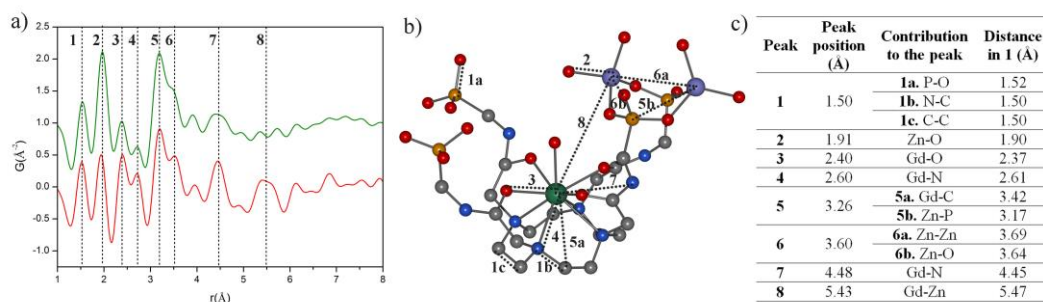


Figure 5.15. a) Pair distribution function $G(r)$ of **1** (red) and Zn-Gd-DOTA-4AmP nanoparticles (green). b) Characteristic distances indicated in the PDF. c) Pair atom correlations contributing to the peaks in the PDF with their corresponding average crystallographic distance in **1**.

5.3.4. Relaxometric studies.

Any reliable studies of relaxometric properties should be done in a stable nanoparticle colloid. Thus, we first studied the stability of nanoparticles in a physiological saline solution.

5.3.4.1. Stability studies.

Exposure of a colloid of Zn-Gd-DOTA-4AmP nanoparticles to saline solutions at pH 5.5, 7.4, and 8.5 and at $T=37.5^\circ\text{C}$ led to negligible leaching of total Gd(III): 1.7, 1.2 and 1.8% in the first 10 min, and 3.6, 1.3, and 1.8% after 10 h, as determined by ICP-MS (Figure 5.16 or Figure S10 of the Publication 3's Supporting Information)

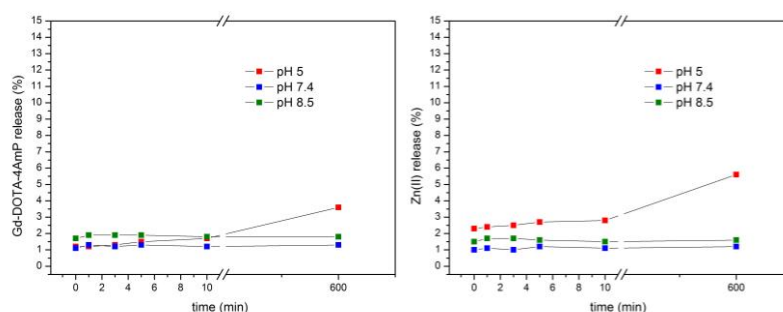


Figure 5.16. Leaching of Gd-DOTA-4AmP (Left) and Zn(II) (Right) of colloidal suspensions of Zn-Gd-DOTA-4AmP nanoparticles incubated in saline solutions at different pHs.

We also carried out Mass Spectrometry (MS) measurements (Figure S11 of the Publication 3's Supporting Information) of the leached products to prove that Gd(III) was actually released in the form of Gd-DOTA-4AMP instead of the free Gd(III) ion. MS patterns showed the presence of the species: $[^{158}\text{Gd-4H-DOTA-4AmP}] = 930.1$, $[^{160}\text{Gd-4H-DOTA-4AmP}] = 932.1$, $[^{157}\text{Gd-4H-DOTA-4AmP}] = 929.1$, $[^{156}\text{Gd-4H-DOTA-4AmP}] = 928.1$ and $[^{155}\text{Gd-4H-DOTA-4AmP}] = 927.1$.

5.3.4.2. Relaxometric measurements.

MRI-CA properties were investigated by doing ^1H Nuclear Magnetic Relaxation Dispersion (NMRD) profiles in the frequency range $10\text{ kHz} \leq \nu \leq 400\text{ MHz}$ for a colloidal suspension of the Zn-Gd-DOTA-4AmP nanoparticles in saline solution (Figure 5.17). NMRD profiles showed a maximum of relaxivity at intermediate magnetic fields, with a maximum value of r_1 at 10 MHz and 25°C ($r_1 = 16\text{ mM}^{-1}\text{s}^{-1}$). This local maximum is characteristic of the slowly rotating species as it has been commented in Section 5.2.4.3. Actually Zn-Gd-DOTA-4AmP nanoparticles reached a value of r_1 two times higher than the Gd-DOTA-4AmP complex at the same field and temperature ($r_1 = 7.4\text{ mM}^{-1}\text{s}^{-1}$).

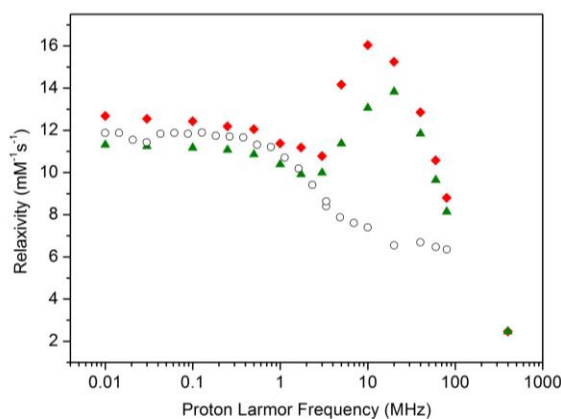


Figure 5.17. NMRD profiles of a colloidal suspension of Zn-Gd-DOTA-4AmP nanoparticles in saline solution (NaCl 0.9 %) at pH 7.4 at 25 °C (red diamond) and at 50 °C (green triangle) and Gd-DOTA-4AmP complex in saline solution (NaCl 0.9 %) at pH 7.4 at 25 °C (empty circle).

Interestingly, NMRD profiles also showed that relaxivity r_1 decreases with temperature, conversely to what was observed in the example previously reported by our group.²⁹ This temperature-dependence indicates that the relaxivity is not limited by proton exchange.

5.3.4.3. Relaxivity r_1 pH-dependence study.

Relaxivity pH dependence of Zn-Gd-DOTA-4AmP nanoparticles was studied at 20 MHz in the pH range between 4 and 10. Indeed, at this pH range, leaching of Gd-DOTA-4AmP is less than 3.0% in weight. However, a burst release is observed at $\text{pH} < 4$, indicating a fast degradation of the nanoparticles below pH 4 (Figure 5.18 or Figure 5b of the Publication 3).

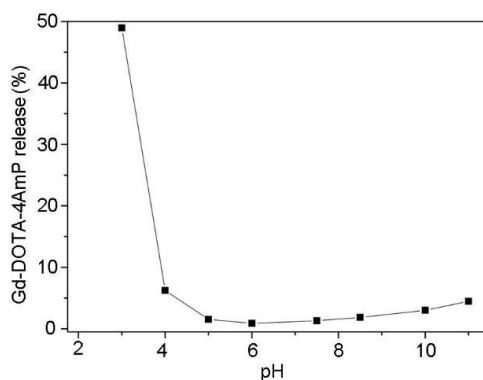


Figure 5.18. Gd-DOTA-4AmP release (wt. %) for Zn-Gd-DOTA-4AmP nanoparticles at the pH range of study.

In consequence, relaxometric data were collected in the pH range 4-10 by starting with a colloidal suspension of Zn-Gd-DOTA-4AmP nanoparticles in saline solution at pH 7.4. The pH was modified by addition of small amounts of concentrated hydrochloric acid or sodium hydroxide. Figure 5.19 (or Figure 5a of the Publication 3) plots relaxivities r_1 of Zn-Gd-DOTA-4AmP nanoparticles and Gd-DOTA-4AmP complex at different pH values (pH=4-10). Plotted data of both samples had the shape of an inverted parabola. For Zn-Gd-DOTA-4AmP Nanoparticles, r_1 increased from pH=4 ($r_1=7.9 \text{ mM}^{-1}\text{s}^{-1}$) to pH=6 (maximum $r_1=16.4 \text{ mM}^{-1}\text{s}^{-1}$), and then steadily decreased to reach a value of $r_1=8 \text{ mM}^{-1}\text{s}^{-1}$ at pH=10. For Gd-DOTA-4AmP complex, the maximum of r_1 was also reached at pH=6, but the value was much lower ($r_1=5.8 \text{ mM}^{-1}\text{s}^{-1}$).

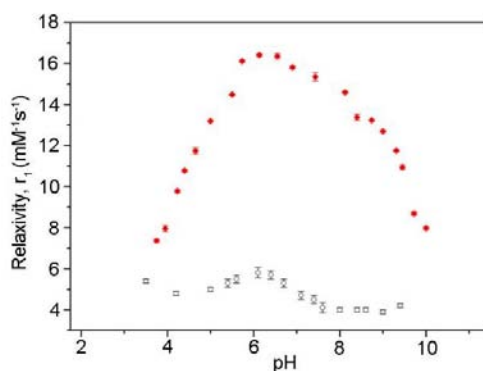


Figure 5.19. pH dependence of the relaxivity of a colloidal suspension of Zn-Gd-DOTA-4AmP nanoparticles (red diamond) and Gd-DOTA-4AmP complex (empty circle) measured at 20 MHz (25 °C).

It is clear from the results, that the nanostructuration of Gd-DOTA-4AmP complex amplified r_1 pH-dependence. Indeed, while for the difference between the maximum ($16.4 \text{ mM}^{-1}\text{s}^{-1}$; pH=6) and the minimum ($7.9 \text{ mM}^{-1}\text{s}^{-1}$; pH=4) corresponded to a factor of two ($\Delta r_1=108 \%$) for the Nanoparticles, the difference between the maximum ($r_1=5.8 \text{ mM}^{-1}\text{s}^{-1}$) and the minimum ($r_1=3.9 \text{ mM}^{-1}\text{s}^{-1}$) was reduced to a factor of 1.5 for the Gd-DOTA-4AmP complex.

5.4. Conclusions

To summarize, we have synthesised a CP using the Gd-DOTA-4AmP complex as the bridging ligand and Zn(II) ions as the connecting nodes. The CP of formula $\text{Zn}_{6.5}[\text{Gd}_3(\text{H-DOTA-4AmP})_2(\text{DOTA-4AmP})(\text{H}_2\text{O})_3] \cdot 18\text{H}_2\text{O}$ presented an interesting 3-D structure that can be rationalized in terms of its inorganic $\cdots\text{Zn(II)-PO}_3\text{-Zn(II)-PO}_3\cdots$ linkages. Although this CP could not be miniaturised without loss of crystallinity, we successfully obtained colloidal suspensions formed by analogous amorphous nanoparticles. A series of chemical characterization techniques (*e.g.* NMR, FT-IR, Elemental Analysis, etc.) together with the innovative PDF analysis were used to confirm that the main structural features of the crystalline material were maintained in the amorphous sample. Furthermore, colloidal suspension of the amorphous nanoparticles was stable enough to conduct studies of its relaxometric properties. Remarkably, nanoparticles showed an improved relaxivity r_1 compared to the molecular CA ($16 \text{ mM}^{-1} \text{ s}^{-1}$ compared to $7.4 \text{ mM}^{-1} \text{ s}^{-1}$), without losing the characteristic pH-dependence of Gd-DOTA-4AmP.

5.5. References

1. Aime, S., Botta, M. & Terreno, E. Gd(III)-based contrast agents for MRI. *Adv. Inorg. Chem.* **57**, 173–237 (2005).
2. Hajela, S. *et al.* A Tris-hydroxymethyl-substituted derivative of Gd-TREN-Me-3,2-HOPO: An MRI relaxation agent with improved efficiency. *J. Am. Chem. Soc.* **122**, 11228–11229 (2000).
3. Aime, S. *et al.* NMR relaxometric studies of Gd(III) complexes with heptadentate macrocyclic ligands. *Magn. Reson. Chem.* **36**, S200–S208 (1998).
4. Parker, D., Dickins, R. S., Puschmann, H., Crossland, C. & Howard, J. A. K. Being excited by lanthanide coordination complexes: aqua species, chirality, excited-state chemistry, and exchange dynamics. *Chem. Rev.* **102**, 1977–2010 (2002).
5. Woods, M. *et al.* Correlation of water exchange rate with isomeric composition in diastereoisomeric gadolinium complexes of tetra(carboxyethyl)dota and related macrocyclic ligands. *J. Am. Chem. Soc.* **122**, 9781–9792 (2000).
6. Aime, S. *et al.* NMR, Relaxometric, and structural studies of the hydration and exchange dynamics of cationic lanthanide complexes of macrocyclic tetraamide ligands. *J. Am. Chem. Soc.* **121**, 5762–5771 (1999).
7. Aime, S. *et al.* Controlling the variation of axial water exchange rates in macrocyclic lanthanide(III) complexes. *Chem. Commun.* **37**, 1120–1121 (2002).
8. Song, Y. *et al.* Multimodal gadolinium-enriched DNA-gold nanoparticle conjugates for cellular imaging. *Angew. Chem. Int. Ed. Engl.* **48**, 9143–9147 (2009).
9. Datta, A. *et al.* High relaxivity gadolinium hydroxypyridonate-viral capsid conjugates: nanosized MRI contrast agents. *J. Am. Chem. Soc.* **130**, 2546–52 (2008).
10. Liepold, L. O. *et al.* Supramolecular protein cage composite MR contrast agents with extremely efficient relaxivity properties. *Nano Lett.* **9**, 4520–6 (2009).
11. Tse, N. M. K. *et al.* Mesoporous europo-gadoliniosilicate nanoparticles as bimodal medical imaging agents and a potential theranostic platform. *Adv. Healthc. Mater.* **2**, 836–45 (2013).
12. Moghaddam, M. J. *et al.* Chelating oleyl-EDTA amphiphiles: self-assembly, colloidal particles, complexation with paramagnetic metal ions and promise as magnetic resonance imaging contrast agents. *Soft Matter* **7**, 10994 (2011).
13. Tsotsalas, M., Busby, M., Gianolio, E., Aime, S. & De Cola, L. Functionalized nanocontainers as dual magnetic and optical probes for molecular imaging applications. *Chem. Mater.* **20**, 5888–5893 (2008).
14. Richard, C. *et al.* Noncovalent functionalization of carbon nanotubes with amphiphilic gd3+ chelates: toward powerful t1 and t2 MRI contrast agents. *Nano Lett.* **8**, 232–6 (2008).

15. Tóth, É. *et al.* water-soluble gadofullerenes: toward high-relaxivity, pH-responsive MRI contrast agents. *J. Am. Chem. Soc.* **127**, 799–805 (2005).
16. Caravan, P. Strategies for increasing the sensitivity of gadolinium based MRI contrast agents. *Chem. Soc. Rev.* **35**, 512–523 (2006).
17. Hifumi, H., Yamaoka, S., Tanimoto, A., Citterio, D. & Suzuki, K. Gadolinium-based hybrid nanoparticles as a positive MR contrast agent. *J. Am. Chem. Soc.* **128**, 15090–1 (2006).
18. Bridot, J.-L. *et al.* Hybrid gadolinium oxide nanoparticles: multimodal contrast agents for in vivo imaging. *J. Am. Chem. Soc.* **129**, 5076–84 (2007).
19. Ju, Q. *et al.* Amine-functionalized lanthanide-doped KGdF₄ nanocrystals as potential optical/magnetic multimodal bioprobes. *J. Am. Chem. Soc.* **134**, 1323–30 (2012).
20. Rieter, W. J., Taylor, K. M. L., An, H., Lin, W. & Lin, W. Nanoscale metal-organic frameworks as potential multimodal contrast enhancing agents. *J. Am. Chem. Soc.* **128**, 9024–9025 (2006).
21. Taylor, K. M. L., Jin, A. & Lin, W. Surfactant-assisted synthesis of nanoscale gadolinium metal-organic frameworks for potential multimodal imaging. *Angew. Chem. Int. Ed.* **47**, 7722–7725 (2008).
22. Coxall, R. A. *et al.* Inter-ligand reactions: in situ formation of new polydentate ligands. *J. Chem. Soc. Dalton Trans.* 2349–2356 (2000). doi:10.1039/b001404o
23. Clearfield, A. Recent advances in metal phosphonate chemistry. *Curr. Opin. solid state Mater. Sci.* **1**, 268–278 (1996).
24. Clearfield, A. Recent advances in metal phosphonate chemistry II. *Curr. Opin. Solid State Mater. Sci.* **6**, 495–506 (2002).
25. Fu, R., Huang, X., Hu, S., Xiang, S. & Wu, X. Rational design of new bright luminescent zinc diphosphonates with 12-member ring channels. *Inorg. Chem.* **45**, 5254–5256 (2006).
26. Drumel, S., Janvier, P., Barboux, P., Bujoli-Doeuff, M. & Bujoli, B. Synthesis, structure and reactivity of some functionalized zinc and copper(II) phosphonates. *Inorg. Chem.* **34**, 148–156 (1995).
27. Allan, P. K. *et al.* Pair distribution function-derived mechanism of a single-crystal to disordered to single-crystal transformation in a hemilabile metal–organic framework. *Chem. Sci.* **3**, 2559–2564 (2012).
28. Mohideen, M. I., Allan, P. K., Chapman, K. W., Hriljac, J. A. & Morris, R. E. Ultrasound-driven preparation and pair distribution function-assisted structure solution of a copper-based layered coordination polymer. *Dalton Trans.* **43**, 10438–10442 (2014).
29. Carné-Sánchez, A. *et al.* Relaxometry studies of a highly stable nanoscale metal-organic framework made of Cu(II), Gd(III), and the macrocyclic DOTP. *J. Am. Chem. Soc.* **135**, 17711–

17714 (2013).

Conclusions

The efforts of this Thesis have been focused on the development of new diagnostic systems based on CPs for MRI-CA applications. Polyazamacrocyclic ligands have been used as linkers of the coordination networks to avoid the release of toxic Gd(III) ions.

In Publication 1 (Chapter 3), the synthesis and use of a new carboxylic-based polyazamacrocyclic ligand has demonstrated to be a successful general strategy for the fabrication of heterometallic CPs. Indeed, two new heterometallic, and one homometallic CPs have been synthesised. However, this new ligand have not proved useful for producing CPs containing the relevant Gd(III) ion.

In Publication 2 (Chapter 4), the use of the phosphonate-based polyazamacrocyclic ligand DOTA-4AmP has been postulated as an alternative to synthesise coordination networks that contain Gd(III) inside the macrocyclic cavity. Indeed, a new CP containing the unit Gd(III)-DOTA-4AmP as linker has been produced. Interestingly, this new CP presented a phase transformation upon adsorption/desorption of water vapours. This phase transformation has been completely characterized thanks to the combination of different XRD techniques operated under humidity-controlled environment. Unfortunately, due to the difficulties in the miniaturisation together with the lack of stability under mild acidic environments, this CP could not be used for the study of the MRI relaxometric properties.

In Publication 3 (Chapter 5), the Gd(III)-DOTA-4AmP unit has been combined with Zn(II) ions to produce a new CP that has been successfully miniaturised yielding nanoparticles that form a stable colloid appropriate for the study of the MRI relaxometric properties. This new CP has demonstrated to be stable in a wide range of pH (pH=4-10) and to have no cytotoxicity thanks to the release of the safe Gd(III)-DOTA-4AmP unit during degradation instead of the toxic Gd(III). Finally, the relaxometric study has shown that the CP particles have a maximum of relaxivity of around $16 \text{ mM}^{-1}\text{s}^{-1}$, which is more than two times higher than that of the discrete Gd(III)-DOTA-4AmP complex ($7.4 \text{ mM}^{-1}\text{s}^{-1}$). Furthermore, the CP particles retain the pH dependence profile of the monomer but doubling the relaxivity response to pH change.

In conclusion, in this Thesis we have demonstrated that the versatile CPs can also be used to produce MRI-CAs with improved relaxivity and that the risk of toxicity can be avoided when polyazamacrocyclic ligands are employed as the linkers of the coordination network and the toxic Gd(III) ions are placed in the interior of their macrocyclic cavities.

Appendix

The Appendix of this Thesis contains the following three publications:

- **Publication 1:**

Aríñez-Soriano, J., Albalad, J., Pérez-Carvajal, J., Imaz, I., Busqué, F., Juanhuix, J., Two-step synthesis of heterometallic coordination polymers using a polyazamacrocyclic linker. *CrystEngComm*. **18**, 4196–4204 (2016).

- **Publication 2:**

Aríñez-Soriano, J., Albalad, J., Vila-Parrondo, C., Pérez-Carvajal, J., Rodríguez-Hermida, S., Cabeza, A., Juanhuix, J., Imaz, I., Maspoch, D., Single-crystal and humidity-controlled powder diffraction study of the breathing effect in a metal–organic framework upon water adsorption/desorption. *Chem. Commun.* **52**, 7229–7232 (2016).

- **Publication 3:**

Aríñez-Soriano, J., Albalad, J., Carné-Sánchez, A., Bonnet, C. S., Busqué, F., Lorenzo, J., Juanhuix, J., Terban, M. W., Imaz, I., Tóth, E., Maspoch, D., pH-Responsive Relaxometric Behaviour of Coordination Polymer Nanoparticles Made of a Stable Macrocyclic Gadolinium Chelate. *Chem. - A Eur. J.* **22**, 13162–13170 (2016).

Publication 1: “Two-step synthesis of heterometallic coordination polymers using polyazamacrocyclic linker.”



Cite this: *CrystEngComm*, 2016, 18, 4196

Two-step synthesis of heterometallic coordination polymers using a polyazamacrocyclic linker†

J. Aríñez-Soriano,^a J. Albalad,^a J. Pérez-Carvajal,^a I. Imaz,^{*a} F. Busqué,^b J. Juanhuix^c and D. Maspoch^{*ad}

A new macrocyclic linker 1,4,7,10-tetraazacyclododecane-1,7-bis(4-acetamidobenzoic)-4,10-diacetic acid (**H₄L1**) was synthesized and characterized. This linker was used to create two heterometallic coordination polymers following a two-step synthesis. This synthesis consisted of first combining this polyazamacrocyclic linker with Ni(II) or Mn(II) ions to obtain the corresponding metallomacrocyclic complexes showing non-coordinated carboxylic groups. In a second step, these metallated macrocycles were used as building units to construct two heterometallic Ni(II)–Zn(II) and Mn(II)–Zn(II) coordination polymers when combined with Zn(II) ions. In addition, a third Zn(II)–Zn(II) coordination polymer could also be synthesized by direct mixing of **H₄L1** with Zn(II) ions. Interestingly, the Mn(II)–Zn(II) coordination polymer exhibits a reversible type-I “crystal-to-amorphous transformation” upon water sorption/desorption.

Received 22nd December 2015,
Accepted 11th February 2016

DOI: 10.1039/c5ce02520f

www.rsc.org/crystengcomm

Introduction

Coordination polymers have become an in-depth thread of study during the past few decades mainly because of their myriad potential properties and applications.^{1–3} In this field, the strategic design of the organic linkers to be used (known as the *linker design approach*) has proven critical for tuning the composition and structure of coordination polymers and, thus, for achieving the desired functionality for a target application.^{4–6} For example, Kitagawa *et al.* designed a luminescent porous coordination polymer-based sensor by using a dipyrrolyl derivative of the photoactive 1,4,5,8-naphthalenediimide.⁷ The material showed strong shifting on the emitted wavelength when different volatile organic compounds were adsorbed on the framework. In a similar way, Zhou *et al.* designed a porous coordination polymer with light-controlled reversible alteration of its adsorbing properties through the design of a photosensitive linker.⁸ The continuous investigation of new organic linkers is thus essential for accessing novel coordination polymers with enhanced

performances in numerous applications such as in catalysis, gas sorption, separation, sensors, pollutant removal, and antibacterials.

Polyazamacrocycles (cyclen and cyclam derivatives) are a family of heteromolecules with high affinity to chelate metal ions in their cavities due to the preorganization of their binding sites and their kinetic and thermodynamic stability induced by the macrocyclic effect.^{9,10} Because of this affinity, these macrocyclic ligands have already shown promise in different fields ranging from contrast agents¹¹ and catalysis^{12,13} to sensors.¹⁴ Recently, the functionalization of the reactive amine positions of polyazamacrocycles with pendant arms incorporating functional groups (*e.g.* carboxylates, amides, and phosphonates)^{15–18} has opened the possibility of using them as multitopic organic linkers. These organic linkers have the potential to coordinate a metal ion inside the inner cavity and different ones through these pendant arms, extending the framework and thus forming heterometallic coordination polymers. However, their use as linkers for the synthesis of coordination polymers is to date limited; only a few examples of homometallic^{19–26} and even less heterometallic²⁷ coordination polymers are found in the literature. This scarcity of structures can be attributed to their high degree of flexibility that makes it difficult to obtain suitable crystals for single-crystal X-ray diffraction, to their sensitivity to harsh reaction media, and to the tendency of their pendant arms to coordinate the metal ions within the macrocyclic cavity,²⁸ thereby promoting the generation of mononuclear compounds rather than coordination polymers.

Herein, we present the stepwise synthesis of heterometallic coordination polymers using polyazamacrocycles as

^a Catalan Institute of Nanoscience and Nanotechnology (ICN2), CSIC and The Barcelona Institute of Science and Technology, Campus UAB, Bellaterra, 08193 Barcelona, Spain. E-mail: inhar.imaz@icn.cat, daniel.maspoch@icn.cat

^b Universitat Autònoma de Barcelona, Departament de Química, 08193 Bellaterra, Spain

^c ALBA Synchrotron, 08290 Cerdanyola del Vallès, Barcelona, Catalonia, Spain

^d Institució Catalana de Recerca i Estudis Avançats (ICREA), 08100 Barcelona, Spain

† Electronic supplementary information (ESI) available: Characterization details and crystallographic views. CCDC 1443836–1443841. For ESI and crystallographic data in CIF or other electronic format see DOI: 10.1039/c5ce02520f

organic linkers. Our strategy consists of first preparing complexes of the polyazamacrocyclic 1,4,7,10-tetraazacyclododecane-1,7-bis(4-acetamidobenzoic)-4,10-diacetic acid (**H₄L1**) with Mn(II) and Ni(II) ions and then using these metallated macrocycles as building units to create heterometallic coordination polymers. We show that the coordination of these Mn(II)/Ni(II) building units showing free carboxylic groups with Zn(II) ions allows the synthesis of two bimetallic Zn(II)–Mn(II) and Zn(II)–Ni(II) coordination polymers (Scheme 1). We also show that a Zn(II)–Zn(II) coordination polymer could be synthesized by direct mixing of **H₄L1** with Zn(II) ions. Interestingly, the Mn(II)–Zn(II) coordination polymer shows a reversible type-I “crystal-to-amorphous transformation” upon water sorption/desorption.²⁹

Experimental

General considerations

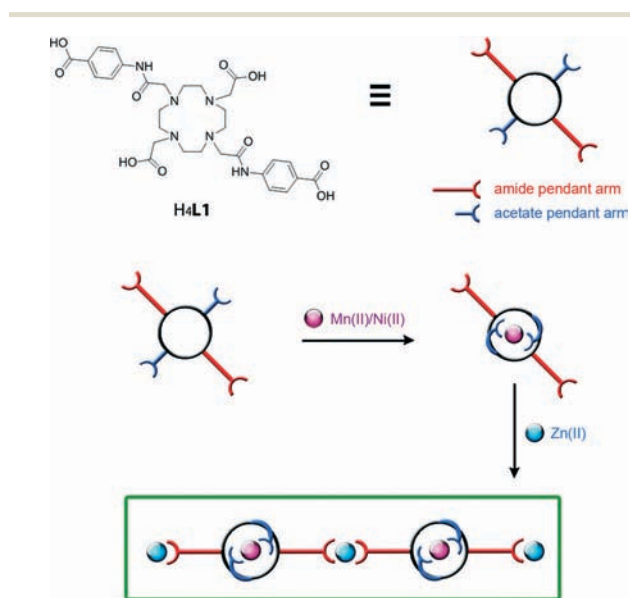
tert-Butyl-4-aminobenzoate, bromoacetyl bromide, potassium carbonate and trifluoroacetic acid were purchased from Sigma-Aldrich. DO2AtBu (a.k.a. di-*tert*-butyl-2,2'-(1,4,7,10-tetraazacyclododecane-1,7-diyl)diacetate) was purchased from CheMatech. All solvents were purchased from Fisher Scientific and Scharlab. Solvents and reagents were used as received unless otherwise stated. ¹H and ¹³C NMR spectra of intermediates **1** and **2** were recorded on a Bruker Avance DPX-360 spectrometer operating at 360 and 90 MHz, respectively. ¹H and ¹³C NMR spectra of **H₄L1** were recorded on a Bruker Avance III 400 SB operating at 400 and 100 MHz, respectively. Samples were dissolved in CDCl₃ or D₂O after purification. Mass spectra were acquired using a microTOF-QII ESI-MS instrument. The purity of all bulk material batches was confirmed by X-ray powder diffraction (XRPD) patterns collected using an X'Pert PRO MPD analytical diffractometer

(Panalytical) at 45 kV and 40 mA with Cu Kα radiation ($\lambda = 1.5419 \text{ \AA}$) and compared with single crystal simulated patterns. Thermogravimetric analyses were performed under nitrogen flow using an STA 449 F1 Jupiter-Simultaneous TGA-DSC from NETZSCH with a heating rate of $5 \text{ }^\circ\text{C min}^{-1}$. IR spectra were recorded in transmission mode on a Bruker Tensor 27FTIR equipped with a Golden Gate diamond ATR cell. Gravimetric water sorption measurements were performed at 298 K using a flow of nitrogen, up to a relative humidity of 90%, using a DVS-Advantage-1 (Surface Measurements Systems). Elemental analysis measurements were performed using a Flash EA 2000 CHNS, Thermo Fisher Scientific analyser.

Synthesis of the linker

Synthesis of 4-*tert*-butyl(2-bromoacetamido)benzoate (1). **1** was synthesized by adapting a literature procedure.¹⁵ Potassium carbonate (4.0 g, 28.8 mmol) was added to a solution of *tert*-butyl-4-aminobenzoate (5.0 g, 26.2 mmol) in dichloromethane (100 mL). The reaction mixture was stirred vigorously and cooled to $0 \text{ }^\circ\text{C}$ in an ice bath. Bromoacetyl bromide (2.5 mL, 28.8 mmol) was added dropwise afterwards. The reaction mixture was allowed to warm to room temperature and then stirred for 12 h. The resulting mixture was then filtered over Celite®, the solids were discarded and the filtrate was concentrated by evaporation of the solvents under vacuum. Yield: 6.64 g (21.2 mmol, 65%). Found: C 49.8%, H 4.9%, N 4.7%; C₁₃H₁₆NO₃Br requires: C 49.7%, H 5.1%, N 4.5%. ¹H NMR (360 MHz, CDCl₃): $\delta = 8.26$ (1H, s br, NH), 8.02 (2H, d, $^3J_{\text{H-H}} = 7.5 \text{ Hz}$, Ar), 7.63 (2H, d, $^3J_{\text{H-H}} = 7.5 \text{ Hz}$, Ar), 4.07 (2H, s, BrCH₂), 1.61 (9H, s, C(CH₃)₃). ¹³C NMR (90 MHz, CDCl₃): $\delta = 164.8$ (C=O), 163.1 (C=O), 140.2 (Ar), 130.4 (Ar), 128.3 (Ar), 118.6 (Ar), 80.8 (C(CH₃)₃), 29.1 (C(CH₃)₃), 27.9 (BrCH₂). *m/z* (ESI-TOF): 336.02 (100%, [M + Na]⁺), an appropriate isotopic pattern was observed.

Synthesis of 1,4,7,10-tetraazacyclododecane-1,7-bis(4-*tert*-butylacetamidobenzoate)-4,10-bis(*tert*-butylacetate) (2). DO2AtBu (1.09 g, 2.71 mmol) and potassium carbonate (0.94 g, 6.78 mmol) were added to a solution of bromoacetamide **1** (1.78 g, 5.70 mmol) in acetonitrile (50 mL). The reaction mixture was heated under reflux at $85 \text{ }^\circ\text{C}$ for 72 h. The resulting mixture was then filtered over Celite® to remove the inorganic salts, and the filtrate was concentrated by evaporation of the solvents under vacuum. Finally, the title compound was purified by column chromatography over silica gel, eluting with 13% methanol in dichloromethane, to obtain an analytical sample. Yield: 1.41 g (1.63 mmol, 60%). Found: C 59.2%, H 7.7%, N 9.1%; C₄₆H₇₀N₆O₁₀Br requires: C 58.3%, H 7.6%, N 8.9%. ¹H NMR (360 MHz, CDCl₃): $\delta = 7.96$ (4H, d, $^3J_{\text{H-H}} = 7.5 \text{ Hz}$, Ar), 7.65 (2H, d, $^3J_{\text{H-H}} = 7.5 \text{ Hz}$, Ar), 3.30 (4H, s, –NCH₂–CONH–), 3.11 (4H, s, –NCH₂COO–), 2.96 (8H, s, –NCH₂CH₂N–), 2.80 (8H, s, –NCH₂CH₂N–), 1.57 (18H, s, C(CH₃)₃), 1.38 (18H, s, C(CH₃)₃). ¹³C NMR (90 MHz, CDCl₃): $\delta = 170.4$ (CH₂COO^{*t*}Bu), 169.5 (CH₂CONH), 165.2 (ArCOO^{*t*}Bu), 141.5 (NH–Ar) 130.6 (Ar),



Scheme 1 Illustration showing the two-step strategy used to synthesize heterometallic coordination polymers **6** and **7**.

126.9 (*Ar*-COO), 117.4 (*Ar*), 81.0 ($C(CH_3)_3$), 80.6 ($C(CH_3)_3$), 56.8 (NCH_2CONH), 52.4 (NCH_2COO), 51.8 (NCH_2CH_2N), 48.1 (NCH_2CH_2N), 28.0 ($C(CH_3)_3$), 27.8 ($C(CH_3)_3$). m/z (ESI-TOF): 889.50 (100%, $[M + Na]^+$), an appropriate isotope pattern was observed.

Synthesis of 1,4,7,10-tetraazacyclododecane-1,7-bis(4-acetamidobenzoic)-4,10-diacetic acid (H_4L1). Trifluoroacetic acid (15 mL) was added to a solution of **2** (0.96 mmol) in dichloromethane (15 mL). The reaction mixture was stirred at room temperature for 16 h to promote the cleavage of the *tert*-butyl groups. The resulting mixture was evaporated under vacuum at low temperature (30 °C) until dryness. The residue was taken up in methanol, and the solvent was evaporated again. Finally, the residue was dissolved in the minimum amount of methanol and precipitated by addition of diethyl ether to properly recover a pale white solid. To further purify the compound, H_4L1 (1 g) was dissolved in deionized water (100 mL) and the pH was set to 2.5 by adding concentrated hydrochloric acid to recrystallize the compound. Yield: 1.23 g (2.0 mmol, 91%). Found: C 44.4%, H 7.0%, N 10.3%; $C_{30}H_{38}N_6O_{10} \cdot 8H_2O$ requires: C 45.7%, H 7.2%, N 10.6%. 1H NMR (400 MHz, $CDCl_3$): δ = 7.72 (4H, d, $^3J_{H-H}$ = 7.5 Hz, *Ar*), 7.37 (4H, d, $^3J_{H-H}$ = 7.5 Hz, *Ar*), 3.24 (4H, s, NCH_2COO), 2.88 (4H, s, NCH_2CONH), 2.43 (16H, mult., NCH_2CH_2N). ^{13}C NMR (100 MHz, $CDCl_3$): δ = 179.9 (CH_2COO), 174.9 (CH_2CONH), 172.3 (*Ar*COO), 140.6 (*NH*-*Ar*), 132.0 (*Ar*), 129.8 (*Ar*-COO), 120.6 (*Ar*), 58.7 (NCH_2CONH), 57.8 (NCH_2COO), 50.5 (NCH_2CH_2N). m/z (ESI-TOF): 665.25 (100%, $[H_4L1 + Na]^+$), an appropriate isotope pattern was observed. ν_{max} (FTIR, cm^{-1}): 3222m, 2995w, 2366s, 2341s, 1686s, 1598s, 1535s, 1409s, 1258s, 1170s, 1094s (Scheme 2).

Synthesis of discrete complexes

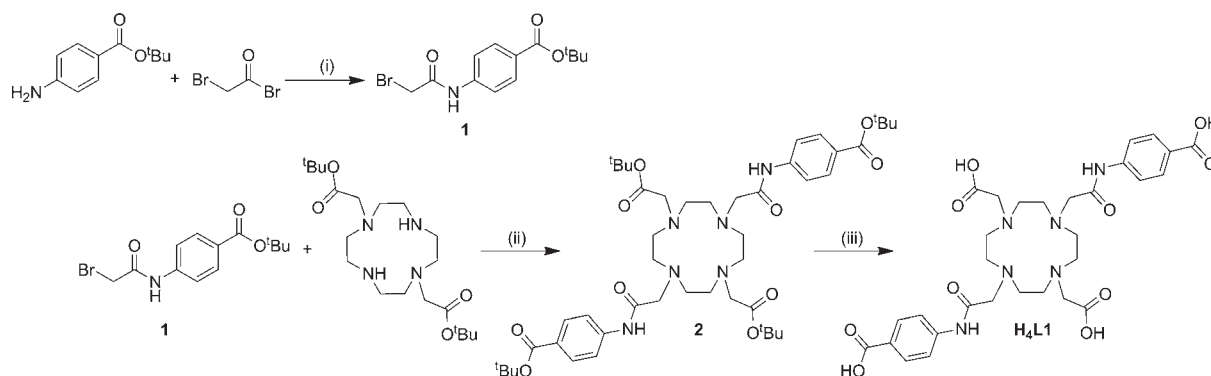
Synthesis of $[Mn(H_4L1)] \cdot [Na(H_2O)_6] \cdot 4H_2O$ (3**).** A stirred mixture of H_4L1 (1.0 g, 1.56 mmol) in water (100 mL) was basified to pH = 8.0 with 1 M sodium hydroxide. Then, manganese chloride (195.8 mg, 1.56 mmol) in water (2 mL) was added dropwise into the previous solution. After this, the pH of the stirred mixture was readjusted again to 8.0, and the mixture was left at room temperature under stirring for 18 h.

The pH of the suspension was again adjusted to pH = 12 to precipitate the excess of manganese chloride in the form of insoluble manganese hydroxides. The mixture was filtered, and the solids were discarded. The filtrate was then acidified to pH = 3 with 1 M hydrochloric acid to precipitate **3**. The precipitated complex was centrifuged, the solvent was replaced with fresh deionized water, and the solid was resuspended. This process was repeated twice. Finally, the suspension was filtered, and the pale yellow solid was air-dried. Yield: 1.1 g (1.36 mmol, 87%). Found: C, 45.4%, H 5.7%, N 10.4%; $C_{30}H_{47}N_6O_{16}MnNa$ requires: C 43.6%, H 5.7%, N 10.2%. m/z (ESI $^-$): 694.18 ($[Mn(HL1)]^-$, 100%), an appropriate isotope pattern was observed. ν_{max} (ATR, cm^{-1}): 3222m, 2968w, 2366s, 2341s, 1686s, 1598s, 1535s, 1409s, 1258s, 1170s, 1094s.

Synthesis of $[Ni(H_2L1)] \cdot 2H_2O$ (4**).** **4** was prepared following the same procedure as for **3**, except that nickel acetate (388 mg, 1.56 mmol) was used as the metal ion precursor, obtaining **4** as a light pink powder. Yield: 352 mg (0.50 mmol, 35%). Found: C 48.0%, H 5.3%, N 11.1%; $C_{30}H_{37}N_6O_{10}Ni \cdot 2H_2O$ requires: C 49.0%, H 5.5%, N 11.4%. m/z (ESI $^+$): 699.19 ($[Ni(H_3L1)]^+$, 100%), an appropriate isotope pattern was observed. ν_{max} (FTIR, cm^{-1}): 3222m, 2995w, 2366s, 2341s, 1686s, 1598s, 1535s, 1409s, 1258s, 1170s, 1094s.

Synthesis of coordination polymers

Synthesis of $[Zn(ZnL1)H_2O] \cdot 3H_2O$ (5**).** A solution of zinc acetate (85.6 mg, 390 μ mol) in distilled water (2 mL) was added dropwise to a solution of H_4L1 (100 mg, 156 μ mol) in 10 mL of pure water, adjusted to pH = 6.7. After 10 minutes, the solution became cloudy leading to the precipitation of a white crystalline powder of **5**. The powder was then collected by centrifugation, washed several times in pure water and maintained on the same solvent. Yield: 47 mg (68 μ mol, 47%). Found: C 42.5%, H 5.1%, N 10.1%; $C_{30}H_{36}N_6O_{11}Zn_2 \cdot 3H_2O$ requires: C 42.8%, H 5.0%, N 10.0%. ν_{max} (FTIR, cm^{-1}): 3453w, 2927m, 2871m, 1673s, 1595vs, 1550s, 1472w, 1416m, 1371m, 1304s, 1259s, 1203m, 1158s, 1091s, 923s. The experimental vs. simulated PXRD pattern can be found in the ESI. †



Scheme 2 Synthetic route for the synthesis of H_4L1 . Reagents and conditions: (i) K_2CO_3 , CH_2Cl_2 , 0 °C to RT, 12 h; (ii) K_2CO_3 , CH_3CN , reflux 85 °C, 72 h + column chromatography, 13% MeOH in CH_2Cl_2 ; (iii) trifluoroacetic acid, CH_2Cl_2 , 16 h.

Synthesis of $[\text{Zn}(\text{NiL1})\text{H}_2\text{O}]\cdot 8\text{H}_2\text{O}$ (6). A mixture of **4** (133 mg, 154 μmol) and zinc acetate (67.6 mg, 308 μmol) in pure distilled water was basified to pH = 6.5 with 1 M NaOH. The solution was allowed to react for 12 h at 85 °C. After this period, plate-shaped crystals of **4** were collected by filtration, washed several times in pure water, and air-dried. Yield: 52.0 mg (74 μmol , 52%). Found: C 39.1%, H 5.8%, N 8.8%; $\text{C}_{30}\text{H}_{36}\text{N}_6\text{O}_{11}\text{NiZn}\cdot 8\text{H}_2\text{O}$ requires: C 39.0%, H 5.7%, N 9.0%. ν_{max} (FTIR, cm^{-1}): 3342m, 2860w, 1600s, 1529m, 1372s, 1305m, 1260m, 1182m, 1092m, 924m. The experimental vs. simulated PXRD pattern can be found in the ESI.†

Synthesis of $[\text{Zn}(\text{MnL1})\text{H}_2\text{O}]\cdot 9\text{H}_2\text{O}$ (7). A solution of zinc acetate (75 mg, 340 μmol) in distilled water (10 mL) was added dropwise to a solution of **3** (10 mL, 136 μmol) in water at room temperature and pH = 8.5. After 10 min, white crystals of **7** were collected by filtration, washed several times in pure water, and air-dried. Yield: 68.6 mg (97 μmol , 68%). Found: C 37.5%, H 5.6%, N 8.6%; $\text{C}_{30}\text{H}_{36}\text{N}_6\text{O}_{11}\text{MnZn}\cdot 9\text{H}_2\text{O}$ requires: C 38.4%, H 5.8%, N 8.9%. ν_{max} (FTIR, cm^{-1}): 3275m, 2972w, 2872w, 1663w, 1585s, 1540s, 1372s, 1316s, 1260s, 1170m, 1092s, 1003w, 969m. The experimental vs. simulated PXRD pattern can be found in the ESI.†

X-Ray crystallography

Refinement and structural information is shown in Table 1. Crystallographic data for **3**–**5** were collected at 293 K at the I19 beamline at Diamond Synchrotron ($\lambda = 0.6889 \text{ \AA}$). These data were indexed, integrated and scaled using CrystalClear software from Rigaku group programs. Absorption correction was performed by using the Multi-Scan method giving max./

min. transmission factors of 1.000/0.923 (**3**), 1.000/0.654 (**4**), and 1.000/0.448 (**5**). Crystallographic data for **6** and **7** were collected at 100 K at the XALOC beamline at ALBA Synchrotron ($\lambda = 0.71049 \text{ \AA}$). These data were indexed, integrated and scaled using the XDS and IMOSFLM programs.³⁰ Absorption correction was not applied. Crystallographic data for **H₄L1** was collected at 293 K using a Bruker AXS SMART Apex diffractometer with graphite monochromated Mo- $K\alpha$ radiation ($\lambda = 0.71073 \text{ \AA}$), and it was corrected for Lorentz and polarisation effects. The frames were integrated with the Bruker SAINT software package. Absorption corrections were applied using SADABS giving max./min. transmission factors of 1.000/0.270. The structures were solved by direct methods and subsequently refined by correction of F^2 against all reflections using SHELXS2013 and SHELXL2013 within the WinGX package.³¹ All non-hydrogen atoms were refined with anisotropic thermal parameters by full-matrix least-squares calculations on F^2 using SHELXL2013, except for **3**, where the oxygen atoms bound to the disordered sodium atom were refined with isotropic thermal parameters. Hydrogen atoms were inserted at calculated positions and constrained with isotropic thermal parameters. The hydrogen atoms of the different hydration water molecules present in all six structures were not located on the Fourier map but were added in the empirical formula to allow accurate determination of the density and absorption coefficient. The structure of **3** contains disordered $[\text{Na}(\text{H}_2\text{O})_6]^+$. Two sites were identified corresponding to disordered partially occupied sodium atoms (one in a special position) and were refined with occupancy factors of 0.75/0.25. Due to this disorder, the oxygen atoms coordinated to these sodium ions were located and refined

Table 1 Crystallographic data of **H₄L1**, discrete complexes **3** and **4**, and coordination polymers **5**, **6** and **7**

Compound reference	H₄L1	3	4	5	6	7
Chemical formula	$\text{C}_{30}\text{H}_{38}\text{N}_6\text{O}_{10}\cdot 7\text{H}_2\text{O}$	$\text{C}_{30}\text{H}_{35}\text{MnN}_6\text{O}_{10}\text{Na}(\text{H}_2\text{O})_6\cdot 5\text{H}_2\text{O}$	$\text{C}_{30}\text{H}_{36}\text{N}_6\text{NiO}_{10}\cdot \text{H}_2\text{O}$	$\text{C}_{30}\text{H}_{34}\text{N}_6\text{O}_{11}\text{Zn}_2\cdot 3\text{H}_2\text{O}$	$\text{C}_{30}\text{H}_{34}\text{N}_6\text{NiO}_{11}\text{Zn}\cdot 8\text{H}_2\text{O}$	$\text{C}_{30}\text{H}_{34}\text{N}_6\text{MnO}_{11}\text{Zn}\cdot 9\text{H}_2\text{O}$
Formula mass	768.66	915.3	717.36	845.37	922.71	918.94
Crystal system	Monoclinic	Monoclinic	Monoclinic	Monoclinic	Monoclinic	Monoclinic
$a/\text{\AA}$	13.691(4)	11.730(4)	18.780(4)	10.830(3)	11.360(3)	37.000(4)
$b/\text{\AA}$	22.544(4)	19.810(4)	18.110(4)	18.480(3)	22.080(3)	12.500(4)
$c/\text{\AA}$	11.572(4)	17.130(4)	9.200(4)	16.550(3)	15.560(3)	18.680(4)
α	90	90	90	90	90	90
β	96.98(4)	105.77(4)	106.22(4)	103.90(4)	90.20(3)	111.40(3)
γ	90	90	90	90	90	90
Unit cell volume	3545.2	3830.7(17)	3004.4(17)	3215.3(13)	3902(14)	8044(4)
Temperature	150	150	150	150	150	150
Space group	$C2/c$	$P21/c$	$C2/c$	$P21/n$	$P21/n$	$C2/c$
Z	4	4	4	4	4	8
Reflections measured	23 208	17 623	5619	8378	111 901	29 802
Independent reflections	3632	8623	2984	3420	5038	4738
Reflections ($I > 2\sigma(I)$)	2885	7786	2077	1497	4415	3765
R_{int}	0.0402	0.0267	0.042	0.117	0.099	0.057
R_1 ($I > 2\sigma(I)$)	0.1019	0.1048	0.0841	0.0951	0.1057	0.1041
$wR(F^2)$ ($I > 2\sigma(I)$)	0.2711	0.2944	0.2394	0.2204	0.3426	0.1171
R_1 (all data)	0.1222	0.1105	0.1095	0.1989	0.1127	0.3237
$wR(F^2)$ (all data)	0.2549	0.3013	0.2671	0.2896	0.3522	0.3450

with different occupancy factors to correlate the different occupancies to the presence of this $[\text{Na}(\text{H}_2\text{O})_6]^+$ (CCDC 1443836–1443841).

Results and discussion

Crystal structures of $\text{H}_4\text{L1}$ and complexes 3 and 4

$\text{H}_4\text{L1} \cdot 7\text{H}_2\text{O}$. Suitable crystals of $\text{H}_4\text{L1}$ for single-crystal X-ray diffraction were obtained by diffusion of acidic vapours into a solution of $\text{H}_4\text{L1}$ (5 mg mL^{-1}) in water placed in the fridge at 5°C for one week. The structure was solved and refined in the monoclinic space group $C2/c$. The asymmetric unit was found to contain one half of the macrocyclic $\text{H}_4\text{L1}$ lying about a twofold axis, one half of a water molecule (O1W) on another twofold axis and three water molecules in general positions (Fig. 1a), resulting in the overall formula $\text{H}_4\text{L1} \cdot 7\text{H}_2\text{O}$. Charge balance considerations and the location of residual Fourier peaks suggest that $\text{H}_4\text{L1}$ is protonated on two of the four central nitrogen atoms (N2 and N2\#) and on two of the four carboxylic moieties (O2 and O2\#). The macrocycles $\text{H}_4\text{L1}$ are linked by hydrogen-bonded interactions between them and water molecules to form 1D chains extending along the ac plane (Fig. S9, ESI†). Water molecules act as connectors between two N–H of the amide groups ($\text{N3} \cdots \text{O1W}$, 2.16 \AA ; $\text{N3} \cdots \text{O1W}$, 169°) and between two deprotonated C–O of the acetate pendant arms ($\text{O1W} \cdots \text{O5}$, $2.813(0) \text{ \AA}$; $\text{O1W} \cdots \text{O5}$, $116.84(6)^\circ$). In these chains, a deprotonated C–O of the acetate pendant arms also forms hydrogen bonds with a benzene carboxylic acid group (O–H) of the amide pendant arms ($\text{O2} \cdots \text{O4}$, 1.67 \AA ; $\text{O2} \cdots \text{O4}$, 174°).

$[\text{Mn}(\text{H}_4\text{L1})] \cdot [\text{Na}(\text{H}_2\text{O})_6] \cdot 4\text{H}_2\text{O}$ (3). Suitable crystals for single-crystal X-ray diffraction were obtained by slow diffusion of acid vapours into a basic solution of 3 in water (5 mg

mL^{-1} , $\text{pH} = 8.5$) at 5°C for one week. Analysis of these crystals by single crystal X-ray diffraction gave a structure model in the monoclinic space group $P2_1/c$, where the asymmetric unit was found to contain one L1 macrocycle coordinated to a single Mn(II) ion (Fig. 1b) and one disordered $[\text{Na}(\text{H}_2\text{O})_6]^+$ counterion. The Mn(II) ion is placed within the macrocyclic cavity in a square antiprismatic molecular geometry. The square antiprism has one plane defined by the four aza nitrogen atoms from the macrocyclic core and the other plane defined by O1 and O6 of the amide groups and O4 and O9 of the acetate pendant arms. Mn(II) ion lies $1.324(0) \text{ \AA}$ above the plane formed by the four aza nitrogen atoms and $1.219(3) \text{ \AA}$ below the plane defined by the four oxygen atoms. The presence of a Na cation means that 3 must be negatively charged. By comparing the C–O distances of both benzene carboxylic acid groups, it can be noted that the $\text{C28} \cdots \text{O7}$ distance ($1.319(7) \text{ \AA}$) is longer compared to $\text{C28} \cdots \text{O8}$ ($1.227(5) \text{ \AA}$), $\text{C17} \cdots \text{O2}$ ($1.272(3) \text{ \AA}$) and $\text{C17} \cdots \text{O3}$ ($1.241(1) \text{ \AA}$) distances. These differences indicate that O7 is protonated, while the others are not. In the structure, this benzene carboxylic acid group is participating in a hydrogen bond with an acetate pendant arm ($\text{O7} \cdots \text{O4}$, 1.71 \AA ; $\text{O7} \cdots \text{O4}$, 163°) of another complex, while the amide group of the same amide pendant arm is H-bonded with the benzene carboxylic acid group of the non-equivalent amide pendant arm ($\text{N6} \cdots \text{O2}$, 2.03 \AA ; $\text{N6} \cdots \text{O2}$, 162°). Both types of hydrogen bonds define the formation of an H-bonded layer (Fig. S10, ESI†). In these layers, two equivalent protonated benzene carboxylic aromatic rings also form an offset face-to-face π – π interaction with a distance of $3.701(6) \text{ \AA}$ from centroid to centroid.

$[\text{Ni}(\text{H}_4\text{L1})] \cdot 2\text{H}_2\text{O}$ (4). Crystals of 4 suitable for single-crystal X-ray diffraction were obtained by slow diffusion of acid vapours into a basic solution of 4 in water (5 mg mL^{-1} , $\text{pH} = 8.5$) at 5°C for one week. The structure was solved and refined in the monoclinic space group $C2/c$, where the asymmetric unit was found to contain one half of the complex with the Ni(II) ion lying on a twofold axis. L1 coordinates to a single Ni(II) ion within the macrocyclic cavity in a highly distorted octahedral geometry (Fig. 1c). In this case, the four nitrogen atoms are far from being coplanar, lying at $0.397(4) \text{ \AA}$ from the average plane. The coordination sphere of Ni(II) is formed by the four aza nitrogen atoms and two equivalent O4 atoms of the acetate pendant arms. Contrary to 3, the oxygen atoms of the amide groups are not involved on any coordination bond, leaving both pendant arms free to rotate. The absence of any counterion and the symmetry equivalence between the two amide pendant arms indicate that both benzene carboxylic acid groups are protonated. These complexes are linked by hydrogen bonds to form layers along the ac plane (Fig. S11, ESI†). These layers are created by the typical $\text{R}_2^2(8)$ H-bonded dimers formed through the two benzene carboxylic acid groups ($\text{O3} \cdots \text{O2}$, 1.82 \AA ; $\text{O3} \cdots \text{O2}$, 168°) and hydrogen bonds involving N–H of the amide groups and C=O of the acetate pendant arms ($\text{N3} \cdots \text{O5}$, 1.93 \AA ; $\text{N3} \cdots \text{O5}$, 176°). These interactions formed a very compact structure in which only a hydrogen-bonded water molecule

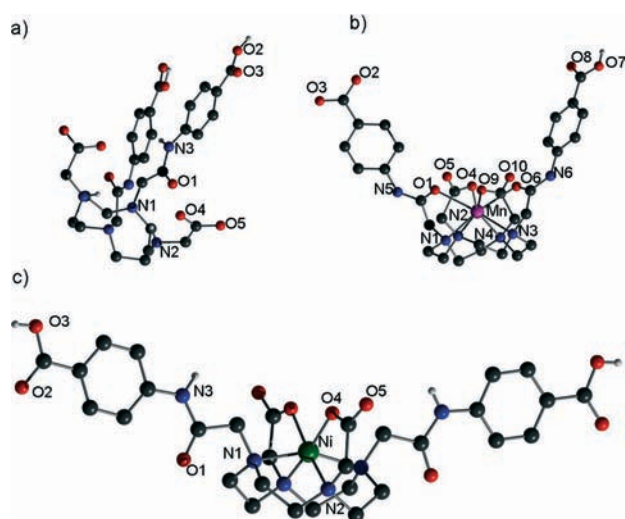


Fig. 1 Ball and stick representation of the crystal structures of (a) $\text{H}_4\text{L1}$, (b) 3 and (c) 4. The structures are represented with unique heteroatom labelling. Hydrogen atoms describing the protonation state have been included, and the rest have been omitted for clarity.

(O1W...O4, 3.022(1) Å; O1W-O4-C15, 132.22(2)°) fits in the asymmetric unit.

Crystal structures of coordination polymers

[Zn(ZnL1)H₂O]·3H₂O (5). 5 crystallises in the monoclinic space group $P2_1/n$ forming a one-dimensional coordination polymer. Its asymmetric unit contains two Zn(II) ions exhibiting two different coordination environments. Zn1 is chelated within the macrocyclic cavity through the four aza nitrogen atoms, two acetate (O4 and O9) pendant arms and O1 of the amide pendant arm in a capped trigonal prism molecular geometry (Fig. 2a). Zn2 adopts a distorted square pyramidal geometry coordinated to two benzene carboxylate groups in a bidentate (O7 and O8) and monodentate (O2) fashion, one acetate group (O5) that bridges Zn1 and Zn2, and one water molecule (Fig. 2b). The structure of 5 is constructed by the connection of Zn2 ions through three different L1 linkers, forming a double-strand chain in a zigzag conformation that extends along the *b* axis (Fig. 2c and d). The double-strand chains are then connected to each other along the *a* direction through hydrogen bonds (Fig. 2d). These hydrogen bonds (Fig. S12, ESI†) are defined between the uncoordinated amide and the non-bridging acetate group (N6-H...O10, 2.03 Å; N6-H...O10, 160°) and between a water molecule that acts as a connector between the coordinated amide group (N5-H...O2W, 1.91 Å; N5-H...O2W, 169°) and the bidentate benzene carboxylic acid group (O2W...O8, 2.852(1) Å; O2W-O8-C28, 149.13(5)°).

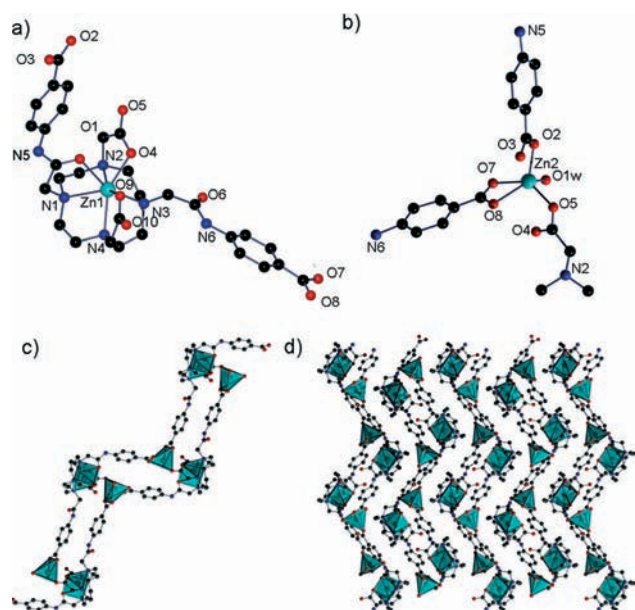


Fig. 2 Ball and stick representation of the crystal structure of 5. (a) Zn1-L1 unit. (b) Zn2 unit. (c) Double strand chain extending along the *b* axis. (d) Packing of the double strand chains viewed along the *b* axis. The sky blue capped trigonal prisms and square pyramids represent the coordination environment of Zn(II) in (c) and (d). H atoms have been omitted for clarity. Atom colour code: Zn, sky blue; C, black-grey; N, blue; O, red.

[Zn(NiL1)H₂O]·8H₂O (6). 6 also crystallises in the monoclinic space group $P2_1/n$, forming a one-dimensional coordination polymer. Its asymmetric unit contains a slightly modified building unit 4 (only the benzene rings are slightly rotated) and one Zn(II) ion connecting these units. As in 4, the Ni(II) ion shows a distorted octahedral geometry coordinated by the four aza nitrogen atoms and O4 and O9 of two acetate pendant arms (Fig. 3a). On the other hand, the Zn(II) ion is tetrahedrally coordinated to two benzene carboxylate groups (O3 and O7) acting both in a monodentate fashion, one O5 of the acetate pendant arm and one water molecule (Fig. 3b). In this structure, each Zn(II) ion connects three different nickelated L1 units creating a double strand chain extending along the [110] and [-110] directions (Fig. 3c and d). The different chains form a cross-linked structure in which the water molecule O2W acts as the connector between two different double-strand chains, forming hydrogen bonds (Fig. S13, ESI†) with one of the amide groups (N6-H...O2W, 2.02 Å; N6-H...O2W, 170°) and one oxygen atom from the benzene carboxylate moiety (O2W...O2, 2.818(1) Å; O2W-O2-C17, 105.58(0)°). In addition, the coordinated water molecule forms a hydrogen bond with the acetate pendant arm (O1W...O10, 2.591(0) Å; O1W-O10-C30, 140.07(4)°).

[Zn(MnL1)H₂O]·9H₂O (7). 7 crystallises in the monoclinic space group $C2/c$, forming a two-dimensional coordination polymer. The structural model shows a modified building unit 3 and one Zn(II) connecting these units. Indeed, if we compare the initial conformation of the building unit 3 with

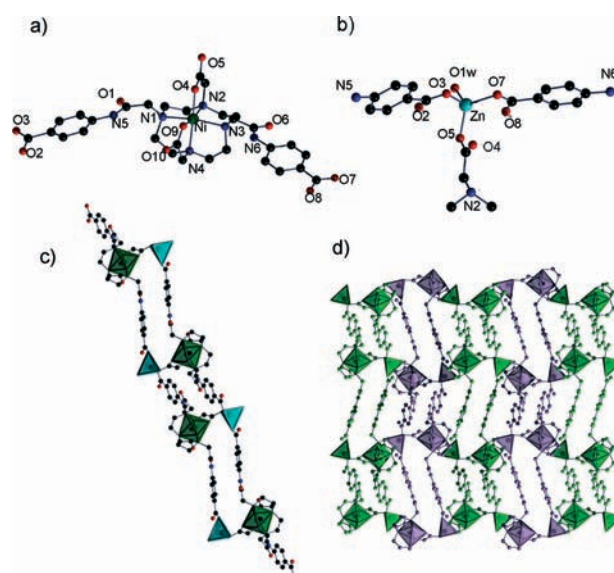


Fig. 3 Ball and stick representation of the crystal structure of 6. (a) Ni-L1 unit. (b) Zn unit. (c) Double strand chain extending along the [110] or [-110] direction. (d) Neighbouring double strand chains viewed along the *a* axis. The green octahedra and sky blue tetrahedra represent the coordination environment of Ni(II) and Zn(II), respectively, in (c). Different chains have been differently coloured in (d). H atoms have been omitted for clarity. Atom colour code: Zn, sky blue; Ni, green; C, black-grey; N, blue; O, red.

that found in 7, a clear difference is that the Mn(II) ion has changed its coordination number from eight to seven. This change leaves one amide pendant arm free to be accommodated in an extended position and, thus, facilitates the coordination of Zn(II) ions with the two benzene carboxylic acid groups. In 7, the Mn(II) ion adopts a capped trigonal prismatic geometry coordinated to the four aza nitrogen atoms, O4 and O9 atoms of two acetate pendant arms and O1 of the amide pendant arm (Fig. 4a). Similar to 6, the Zn(II) ion is tetrahedrally coordinated to two benzene carboxylate groups (O2 and O7) acting both in a monodentate fashion, one O5 of the acetate pendant arm and one water molecule (Fig. 4b). The coordination structure is built up from connecting each Mn(II)-L1 unit through three different Zn2 ions (Fig. 4c), forming corrugated layers that grow along the (-101) plane. The different layers are packed in an ABAB sequence connected *via* a water molecule, which directly connects

these layers through two hydrogen bond interactions (Fig. S14, ESI†) involving one amide pendant arm (N5-H...O4W, 2.13 Å; N5-H...O4W, 157°) and one benzene carboxylate moiety (O4W...O2, 2.962(4) Å; O4W-O2-C17, 132.79(2)°) and weak contacts through their aliphatic moieties (Fig. 4d and e and Fig. S14, ESI†). As shown in Fig. 4e, the remaining water molecules form independent H-bonded networks that run parallel to the (-101) plane.

Structural integrity and water adsorption of 7

The high content of water molecules in the framework of 7 prompted us to investigate its behaviour upon water sorption/desorption. Initially, we performed a thermogravimetric analysis (TGA) on 7, showing a first weight loss of 21.2% from 20 to 120 °C. This loss was attributed to the loss of all water molecules (19.2%) according to the molecular formula [Zn(MnL1)H₂O]·9H₂O (Fig. 5a). A second weight loss was found in the temperature range of 340–470 °C corresponding to the decomposition of the framework.

To evaluate the water-vapour sorption properties, 7 was first activated at 120 °C overnight under vacuum, and the activated sample (7') was characterized by TGA and PXRD (Fig. 5a and b). TGA revealed the absence of any weight loss from 20 to 340 °C, confirming that 7' was free of guest water molecules. On the other hand, the experimental PXRD showed that 7' becomes an amorphous material after evacuating the water molecules. This behaviour is not unexpected as layers of 7 are three-dimensionally packed *via* hydrogen-bonded water molecules, so that their removal is likely inducing their disordering and loss of crystallinity. Remarkably, the framework of 7 was recovered when 7' was re-immersed in water or exposed to water vapors (Fig. 5b), as confirmed by

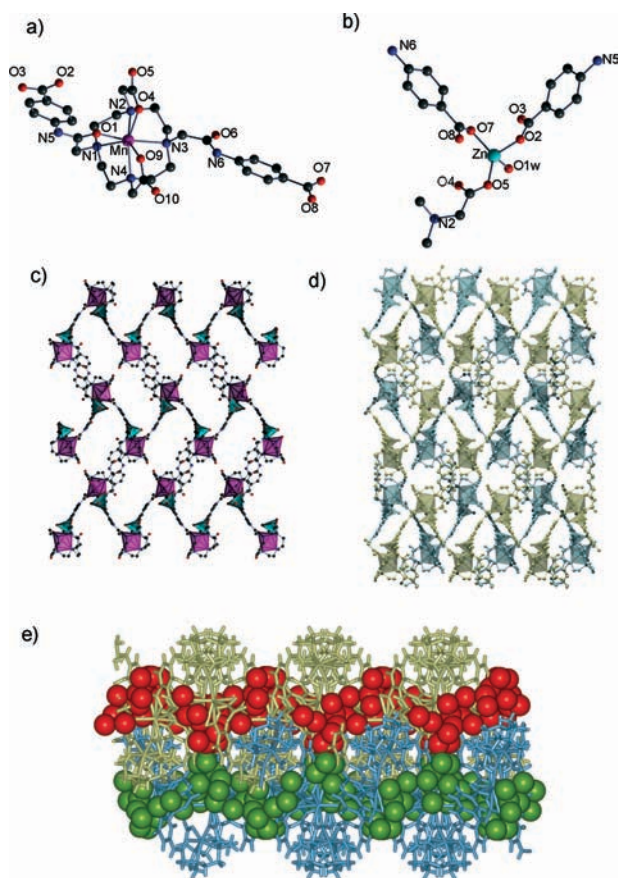


Fig. 4 Ball and stick representation of the crystal structure of 7. (a) Mn-L1 unit. (b) Zn unit. (c) Single coordination layer viewed along the *c* axis. (d) Two neighbouring corrugated layers viewed along the [101] axis. (e) Two neighbouring corrugated layers showing the independent H-bonded network of guest water molecules. The violet capped trigonal prisms and the sky blue tetrahedra represent the coordination environment of Mn(II) and Zn(II) in (c). The two layers in (d) and (e) and the two H-bonded networks of water molecules in (e) have been differently coloured. H atoms have been omitted for clarity. Atom colour code: Zn, sky blue; Mn, violet; C, black-grey; N, blue; O, red.

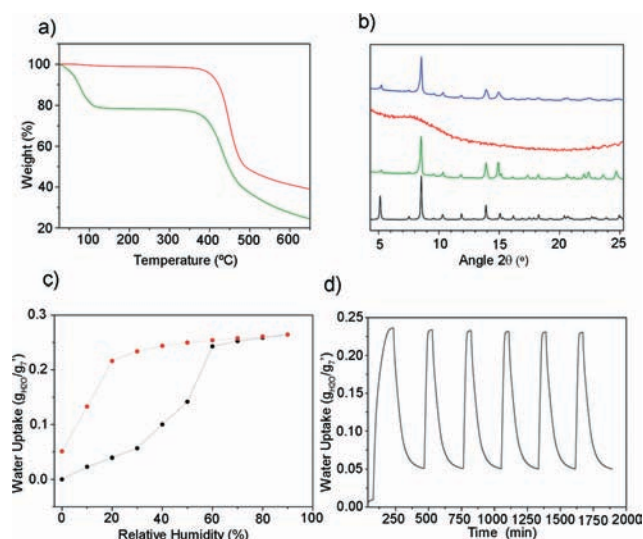


Fig. 5 (a) TGA of 7 (green) and 7' (red). (b) PXRD patterns of 7: simulated (black), as made (green), activated under vacuum at 120 °C (red), and activated and immersed in water for 48 h (blue). (c) Water isotherm of 7 at 25 °C. (d) Water sorption/desorption cycles at 60% and 2% RH.

X-ray powder diffraction (XRPD) patterns. This reversible behavior is typical of a type-I “crystal-to-amorphous transformation” as described by Kitagawa *et al.*²⁹

Dynamic water sorption measurements performed on 7' showed an adsorption branch with a sigmoidal shape representative of a type II trend.³² The water uptake reaches a plateau at a relative humidity (RH) of 60%, achieving an uptake of 0.23 g of H₂O per g of 7'. The maximum water uptake was 0.26 g of H₂O per g of 7' at a RH of 90%. This weight increase can be attributed to 10 water molecules (calculated on the basis of the dehydrated formula, theoretical = 24%), in agreement with TGA results and the initial hydrated crystal structure. In addition, we observed a hysteresis loop between the adsorption and desorption branches, from which 5.1% in weight was found to be not desorbed. This percentage can be attributed to two water molecules (calculated on the basis of the dehydrated formula, theoretical = 4.7%) that cannot be desorbed without heating this material. We can tentatively ascribe these two water molecules to those that are more strongly bonded in the framework of 7, that is, O1W that is coordinated to the Zn(II) ions (Fig. 4b) and O4W that is responsible for three-dimensionally connecting the coordination layers through several hydrogen bond interactions (Fig. S14, ESI†). In fact, when performing an XRPD of the sample resulting from the desorption process, we could observe a certain degree of crystallinity, thus confirming that this sample shows a certain ordering between layers (Fig. S15, ESI†).

We then performed six water sorption/desorption cycles by alternately exposing the outgassed material to humid (60% RH) and dry (2% RH) environments (Fig. 5d). Remarkably, the maximum uptake at 60% RH (*ca.* 23%) was not significantly modified with the number of cycles, confirming the stability of the material to water sorption/desorption processes. Furthermore, it should be noted that the 5% in weight of water molecules that remains in the material after desorption reduces its working capacity. However, as a counterpart, it makes the cycles narrower, which means that this slightly crystalline material shows a faster response to water sorption than its amorphous analogue 7'.

Conclusions

In conclusion, we have synthesised a tetraazacyclododecane-based linker H₄L1 and demonstrated its versatility in the formation of two discrete Mn(II) and Ni(II) chelates showing free carboxylic groups. These complexes were further used, in a second step, as metallated building units to create two heterometallic Zn(II)–Ni(II) (6) and Zn(II)–Mn(II) (7) coordination polymers. In addition, a third homometallic Zn(II)-based coordination polymer (5) was synthesized by direct mixing of H₄L1 with Zn(II) ions. 5 and 6 show extended double strand chains stacked to each other through hydrogen bonds, whereas 7 forms corrugated layers packed in an ABAB fashion also containing independent H-bonded networks of water molecules. Interestingly, this coordination polymer exhibits a reversible type-I “crystal-to-amorphous transformation” upon

water sorption/desorption and a plateau uptake of 23% in weight at 60% RH and is stable up to at least six water sorption/desorption cycles.

Acknowledgements

This work was supported by MINECO-Spain through project PN MAT2012-30994. I. I. and J. A. thank MINECO for an RyC contract (RYC-2010-06530) and an FPU predoctoral grant (AP-2010-5934), respectively. ICN2 acknowledges the support of the Spanish MINECO through the Severo Ochoa Centers of Excellence Program, under Grant SEV-2013-0295.

Notes and references

- 1 G. Férey, *Chem. Soc. Rev.*, 2008, 37, 191–214.
- 2 C. Janiak, *Dalton Trans.*, 2003, 2781–2804.
- 3 S. Kitagawa, R. Kitaura and S. Noro, *Angew. Chem., Int. Ed.*, 2004, 43, 2334–2375.
- 4 F. A. Almeida Paz, J. Klinowski, S. M. F. Vilela, J. P. C. Tomé, J. A. S. Cavaleiro and J. Rocha, *Chem. Soc. Rev.*, 2012, 41, 1088–1110.
- 5 D. Zhao, D. J. Timmons, D. Yuan and H. C. Zhou, *Acc. Chem. Res.*, 2011, 44, 123–133.
- 6 W. Lu, Z. Wei, Z.-Y. Gu, T.-F. Liu, J. Park, J. Park, J. Tian, M. Zhang, Q. Zhang, T. Gentle III, M. Bosch and H.-C. Zhou, *Chem. Soc. Rev.*, 2014, 43, 5561–5593.
- 7 Y. Takashima, V. M. Martínez, S. Furukawa, M. Kondo, S. Shimomura, H. Uehara, M. Nakahama, K. Sugimoto and S. Kitagawa, *Nat. Commun.*, 2011, 2, 168.
- 8 J. Park, D. Yuan, K. T. Pham, J.-R. Li, A. Yakovenko and H.-C. Zhou, *J. Am. Chem. Soc.*, 2012, 134, 99–102.
- 9 D. H. Busch, *Acc. Chem. Res.*, 1978, 11, 392–400.
- 10 T. Hubin, *Coord. Chem. Rev.*, 2003, 241, 27–46.
- 11 F. Benetollo, G. Bombieri, L. Calabi, S. Aime and M. Botta, *Inorg. Chem.*, 2003, 42, 148–157.
- 12 R. Cibulka, R. Vasold and B. König, *Chem. – Eur. J.*, 2004, 10, 6224–6231.
- 13 C.-S. Jeung, J. B. Song, Y.-H. Kim and J. Suh, *Bioorg. Med. Chem. Lett.*, 2001, 11, 3061–3064.
- 14 E. Tamanini, A. Katewa, L. M. Sedger, M. H. Todd and M. Watkinson, *Inorg. Chem.*, 2009, 48, 319–324.
- 15 S. J. Ratnakar, M. Woods, A. J. M. Lubag, Z. Kovacs and A. D. Sherry, *J. Am. Chem. Soc.*, 2008, 130, 6–7.
- 16 L. M. De León-Rodríguez, S. Viswanathan and A. D. Sherry, *Contrast Media Mol. Imaging*, 2010, 5, 121–125.
- 17 J. M. Taylor, R. K. Mah, I. L. Moudrakovski, C. I. Ratcliffe, R. Vaidhyanathan and G. K. H. Shimizu, *J. Am. Chem. Soc.*, 2010, 132, 14055–14057.
- 18 D. A. Knight, J. B. Delehanty, E. R. Goldman, J. Bongard, F. Streich, L. W. Edwards and E. L. Chang, *Dalton Trans.*, 2004, 2006–2011.
- 19 G. Ortiz, S. Brandès, Y. Rousselin and R. Guillard, *Chem. – Eur. J.*, 2011, 17, 6689–6695.
- 20 E. Y. Lee and M. P. Suh, *Angew. Chem., Int. Ed.*, 2004, 43, 2798–2801.

- 21 C. S. Hawes, S. R. Batten and D. R. Turner, *CrystEngComm*, 2014, **16**, 3737–3748.
- 22 H.-M. Zhang, H. Wu, Y.-Y. Liu, J. Yang, D.-W. Kang and J.-F. Ma, *CrystEngComm*, 2015, **17**, 1583–1590.
- 23 C. S. Hawes, Y. Nolvachai, C. Kulsing, G. P. Knowles, A. L. Chaffee, P. J. Marriott, S. R. Batten and D. R. Turner, *Chem. Commun.*, 2014, **50**, 3735–3737.
- 24 D. Kong, D. G. Medvedev and A. Clearfield, *Inorg. Chem.*, 2004, **43**, 7308–7314.
- 25 L. V. Tsymbal, Y. D. Lampeka, V. I. Boyko, V. I. Kalchenko, S. V. Shishkina and O. V. Shishkin, *CrystEngComm*, 2014, **16**, 3707–3711.
- 26 W.-Y. Gao, Y. Niu, Y. Chen, L. Wojtas, J. Cai, Y.-S. Chen and S. Ma, *CrystEngComm*, 2012, **14**, 6115–6117.
- 27 A. Carné-Sánchez, C. S. Bonnet, I. Imaz, J. Lorenzo, E. Tóth and D. Maspoch, *J. Am. Chem. Soc.*, 2013, **135**, 17711–17714.
- 28 J. Zagal, M. Páez and J. F. Silva, in *N4-Macrocyclic Metal Complexes*, ed. J. Zagal, F. Bedioui and J.-P. Dodelet, Springer, New York, 2006.
- 29 S. Kitagawa and K. Uemura, *Chem. Soc. Rev.*, 2005, **34**, 109–119.
- 30 W. J. Kabsch, *J. Appl. Crystallogr.*, 1993, **26**, 795–800.
- 31 G. M. Sheldrick, *Acta Crystallogr., Sect. A: Found. Crystallogr.*, 2008, **64**, 112–122.
- 32 S. Brunauer, *The Adsorption of Gases and Vapors, Vol. 1, Physical Adsorption*, Princeton University Press, Princeton, NJ, 1945.

Publication 1: Supporting Information

Figure S1. Characterization of **1**: (a) ^1H -NMR (CDCl_3 , 298 K, 360 MHz), and (b) ^{13}C -NMR (CDCl_3 , 298 K, 90 MHz).

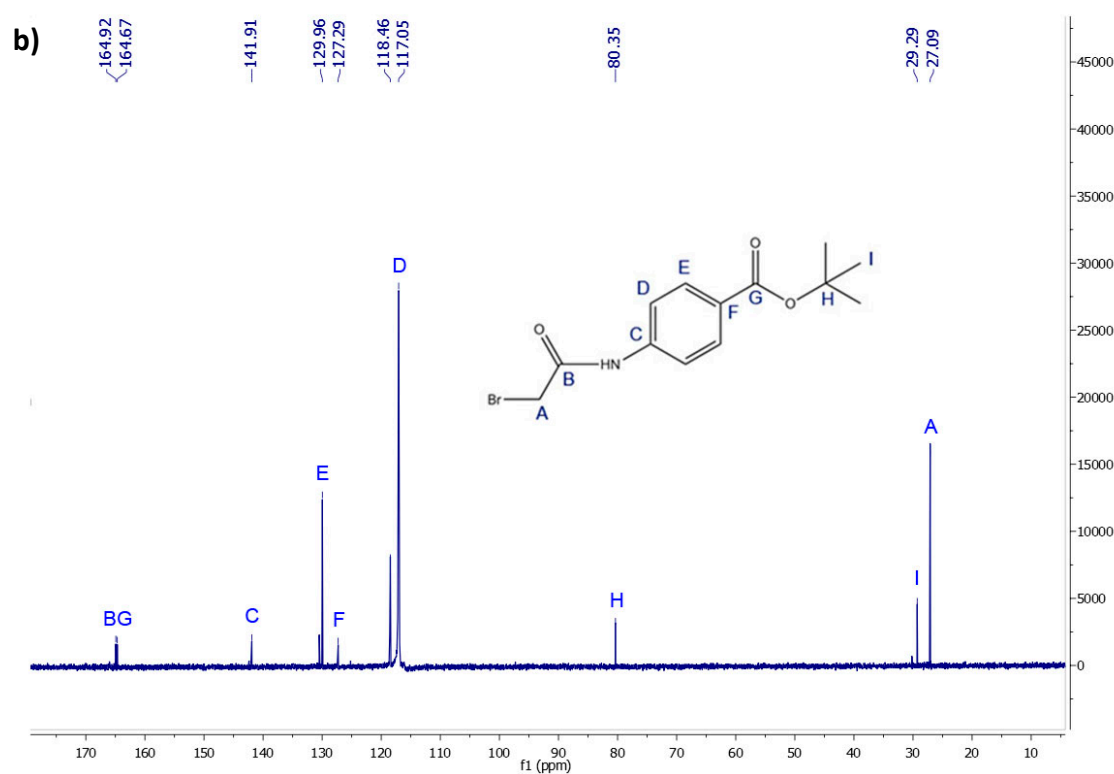
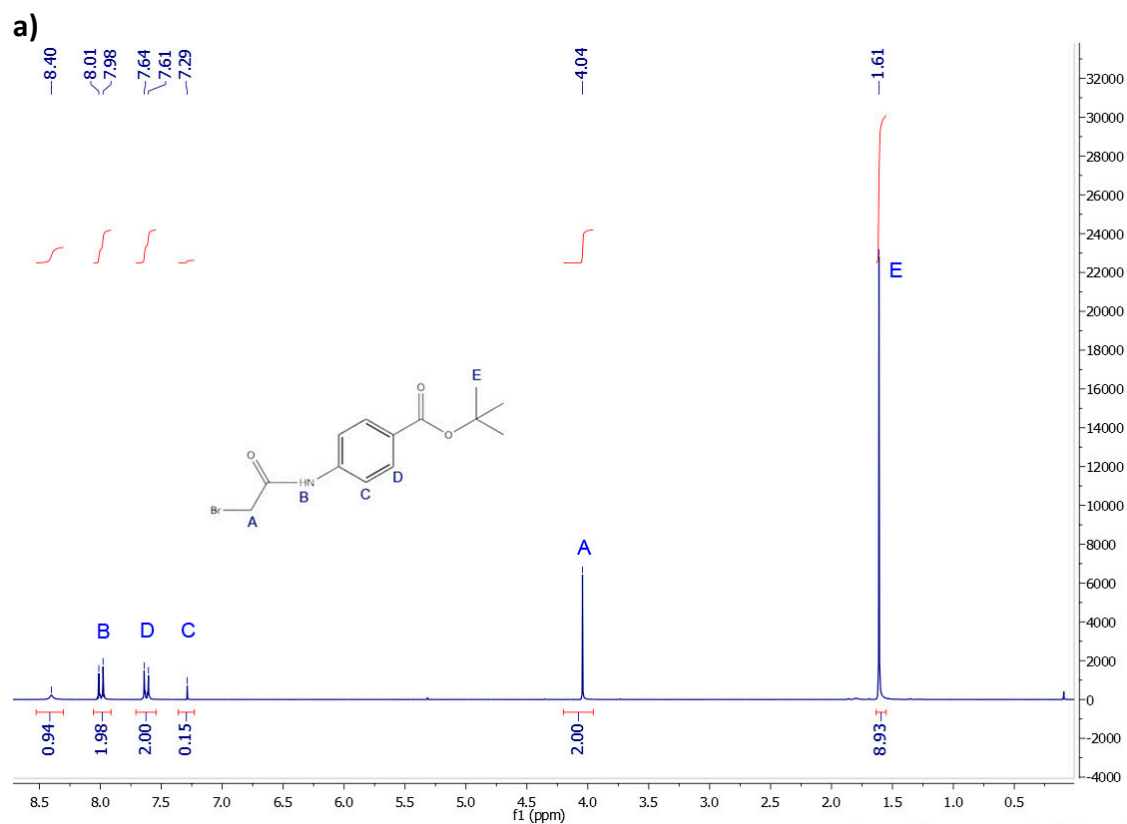
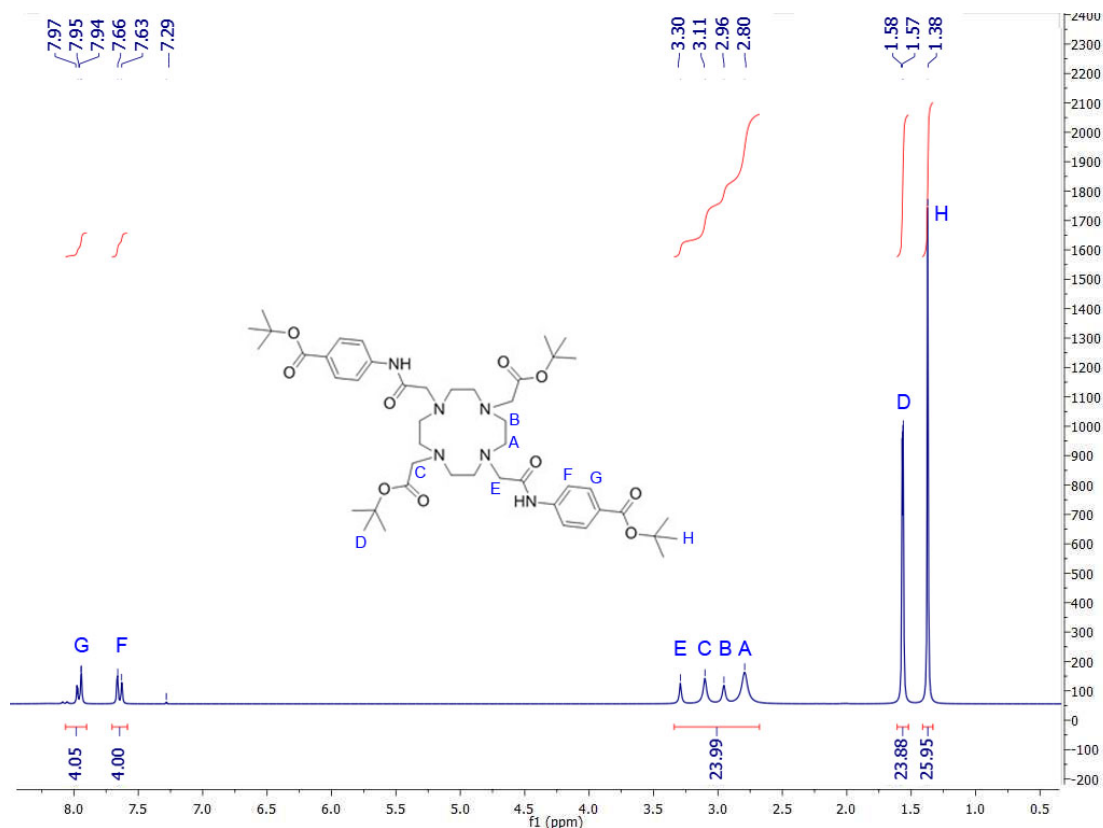
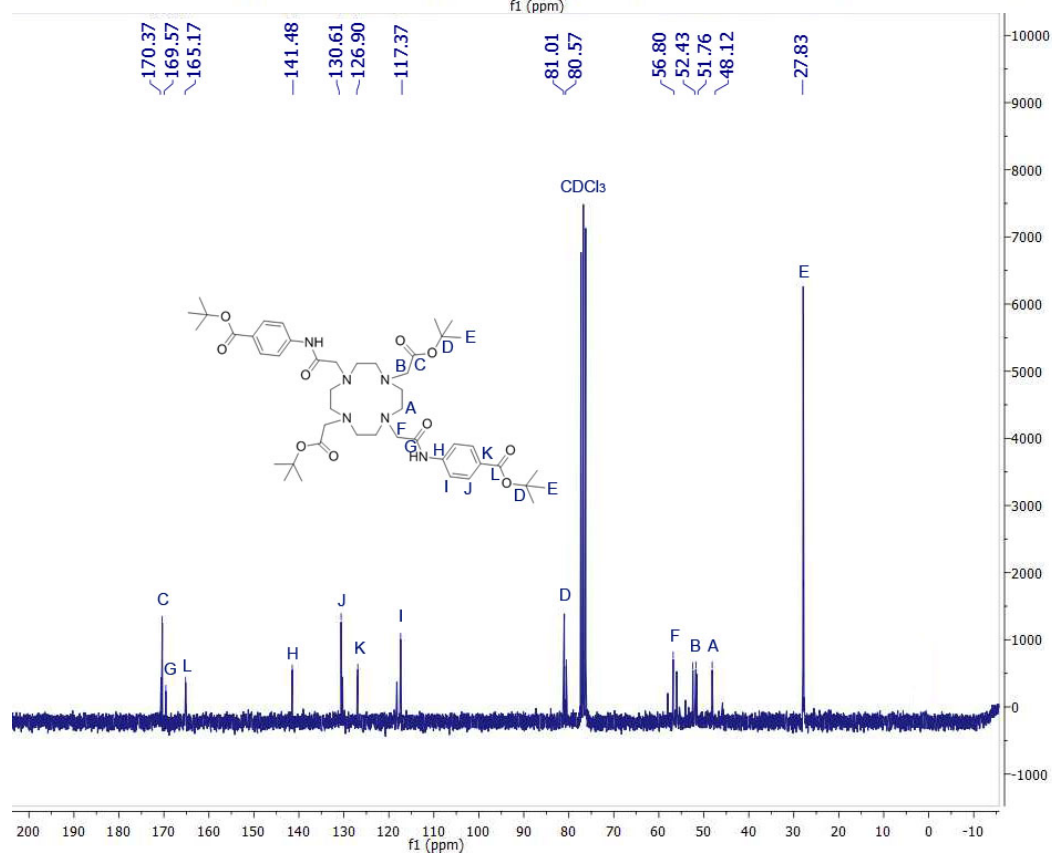


Figure S2. Characterization of **2**: (a) ^1H -NMR (CDCl_3 , 298 K, 360 MHz), (b) ^{13}C -NMR (CDCl_3 , 298 K, 90 MHz), and (c) ESI-TOF/MS spectrum.

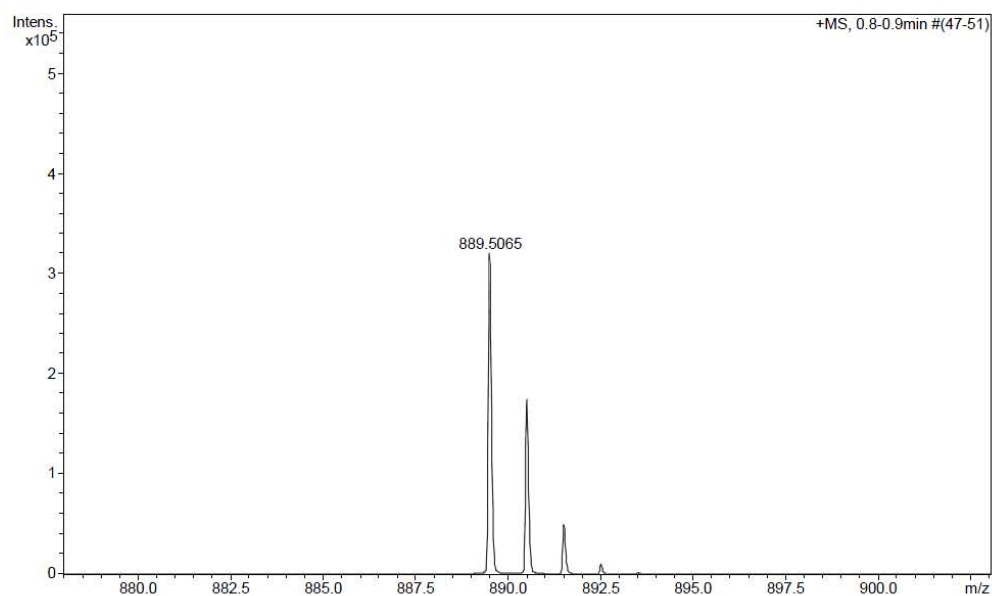
a)



b)



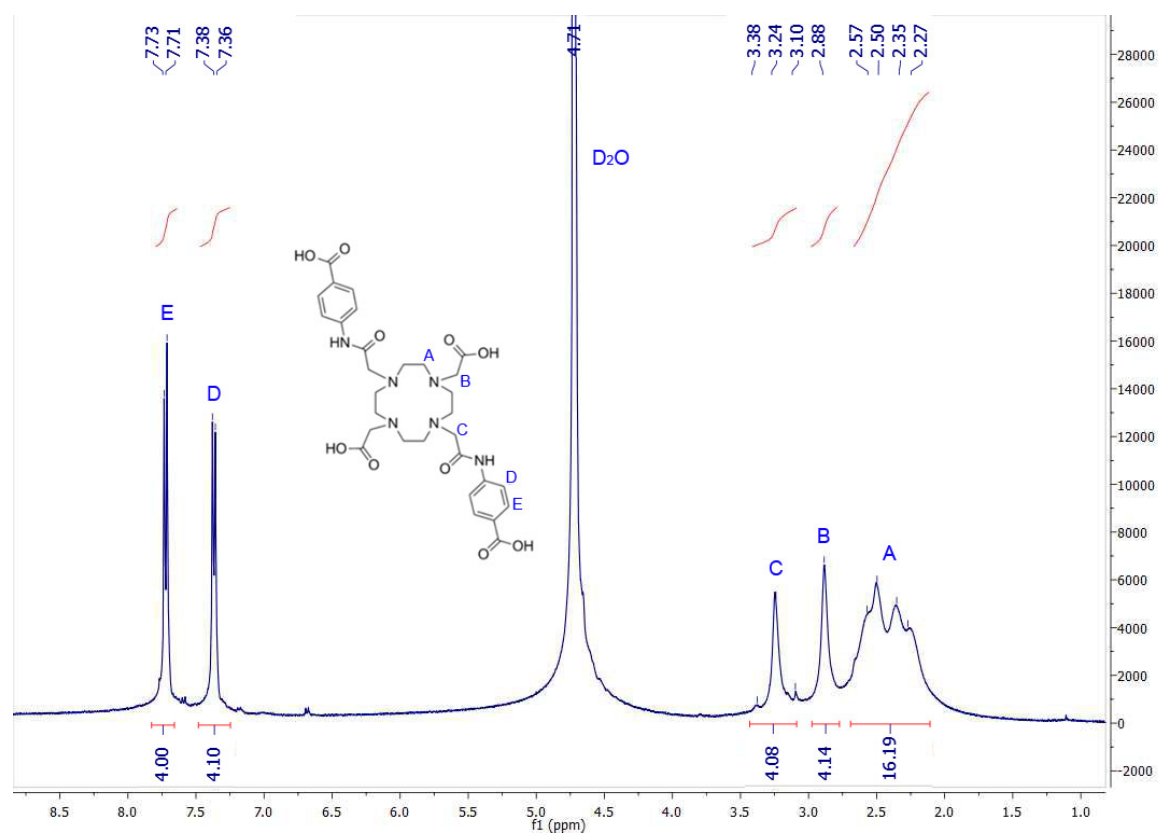
c)



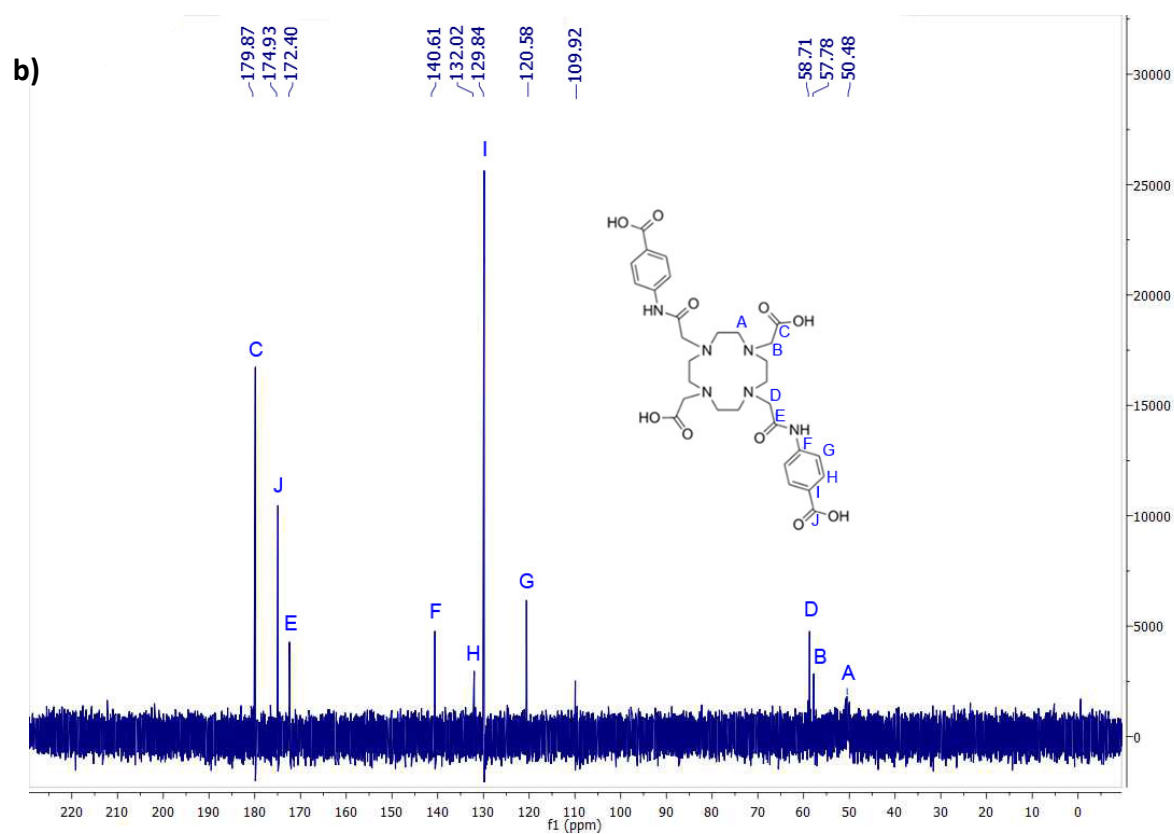
#	m/z	I	I %
1	889.5065	320137	100.0
2	890.5093	174966	54.7
3	891.5109	49802	15.6
4	892.5131	10089	3.2

Figure S3. Characterization of H₄L1: (a) ¹H-NMR (D₂O, 298 K, 400 MHz), (b) ¹³C-NMR (D₂O, 298 K, 100 MHz), (c) ESI-TOF/MS spectrum, and (d) FT-IR spectrum.

a)



H Label	δ (ppm)	Integration	Mult ($^3J_{H-H}$ (Hz))	Assignment
H _A	2.43	16H	mult	NCH ₂ CH ₂ N
H _B	2.88	4H	s	NCH ₂ CONH
H _C	3.38	4H	s	NCH ₂ COO
H _D	7.37	4H	d (7.5 Hz)	Ar
H _E	7.72	4H	d (7.5 Hz)	Ar



C Label	δ (ppm)	Assignment
C_A	50.5	NCH ₂ CH ₂ N
C_B	55.8	NCH ₂ COO
C_C	179.9	CH ₂ COO
C_D	58.7	NCH ₂ CONH
C_E	172.3	Ar-COO
C_F	140.6	NH-Ar
C_G	120.6	Ar
C_H	132.0	Ar
C_I	129.8	Ar-COO
C_J	174.9	CH ₂ CONH

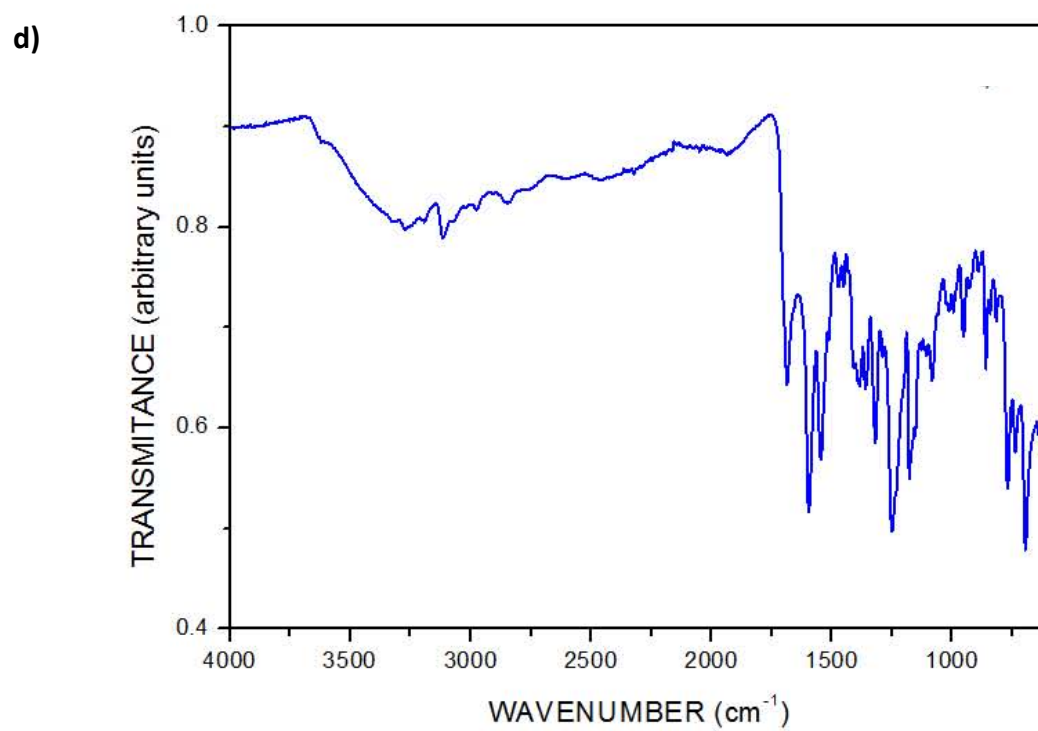
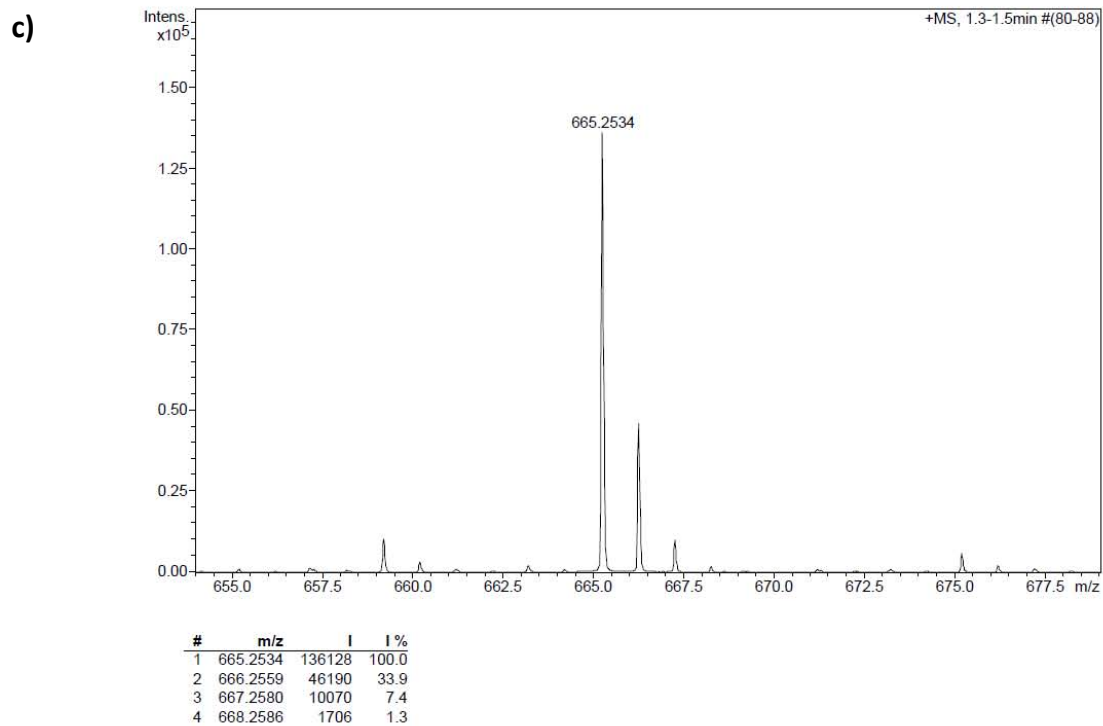


Figure S4. Characterization of **3**: (a) ESI-TOF/MS spectrum, and (b) FT-IR spectrum.

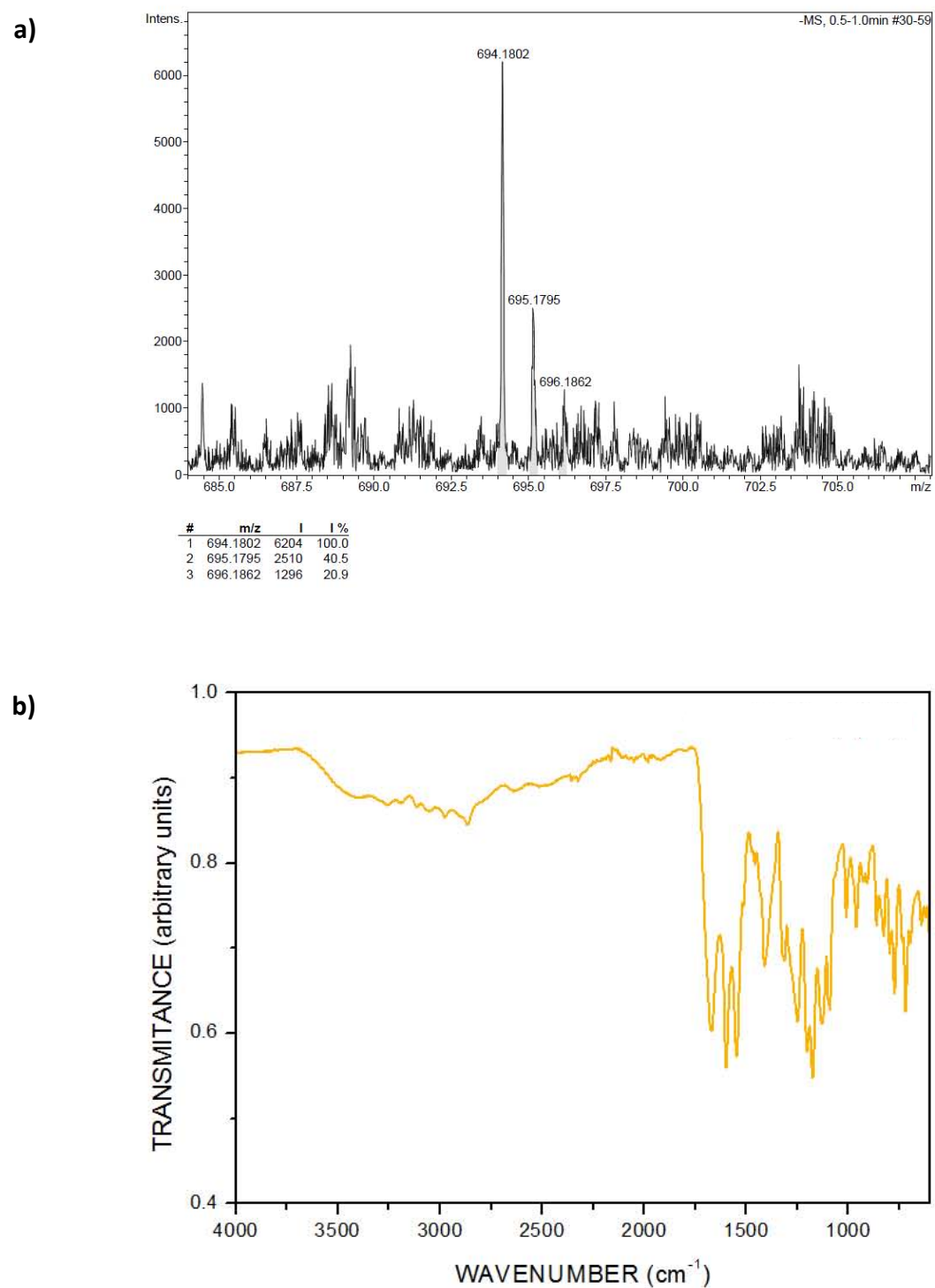


Figure S5. Characterization of **4**: (a) ESI-TOF/MS spectrum, and (b) FT-IR spectrum.

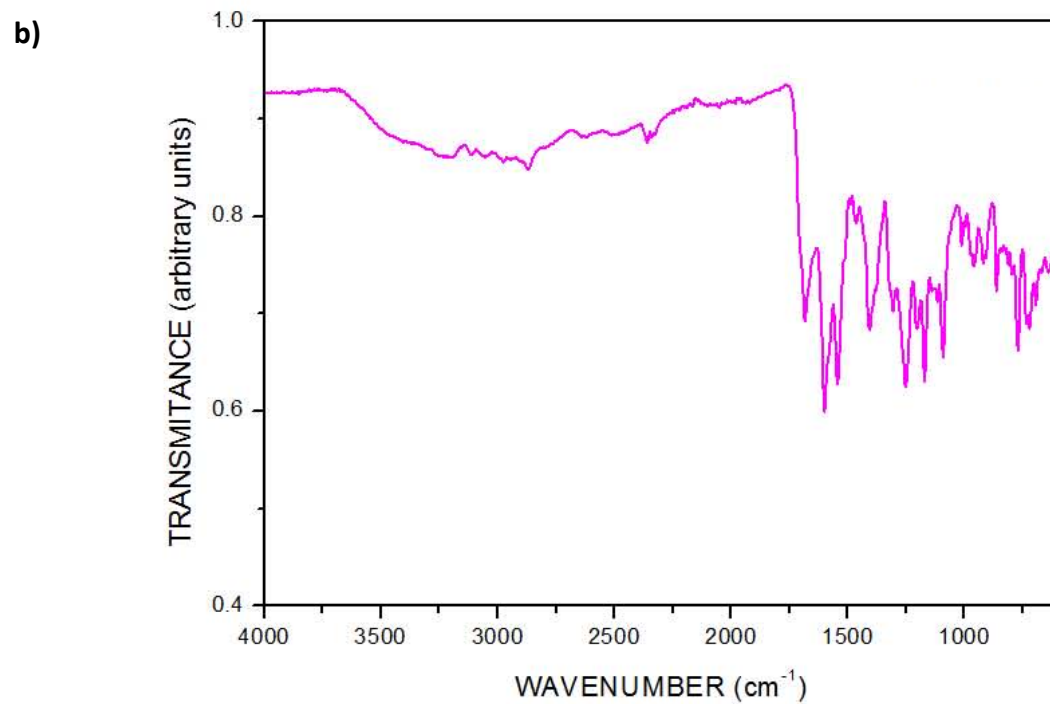
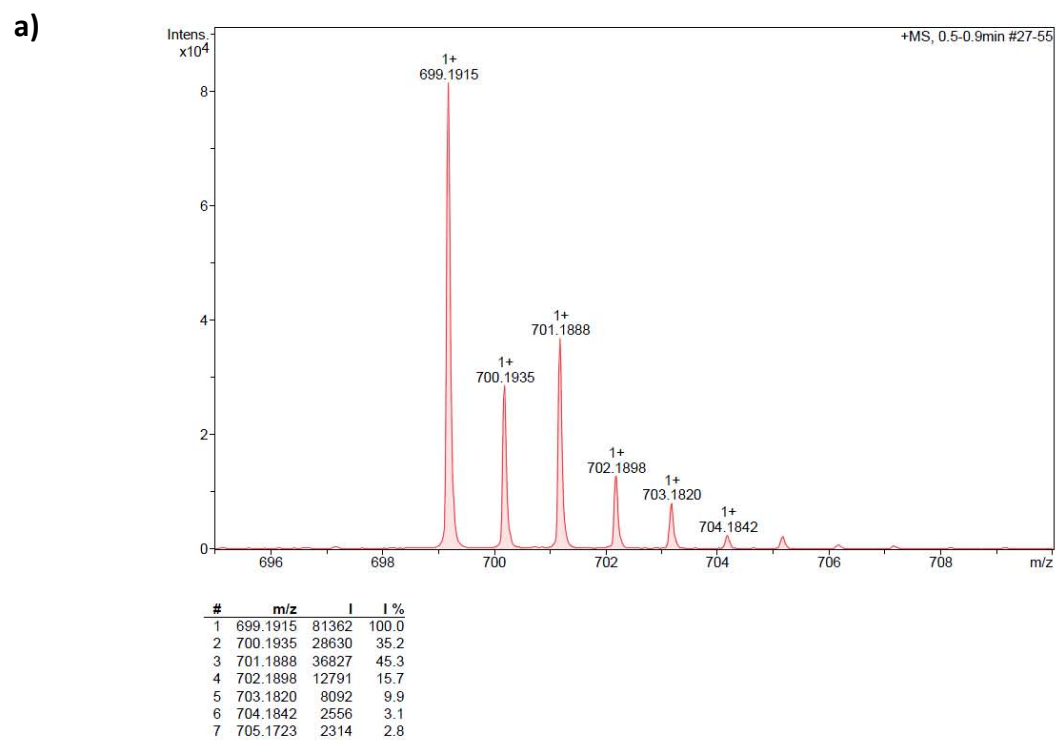
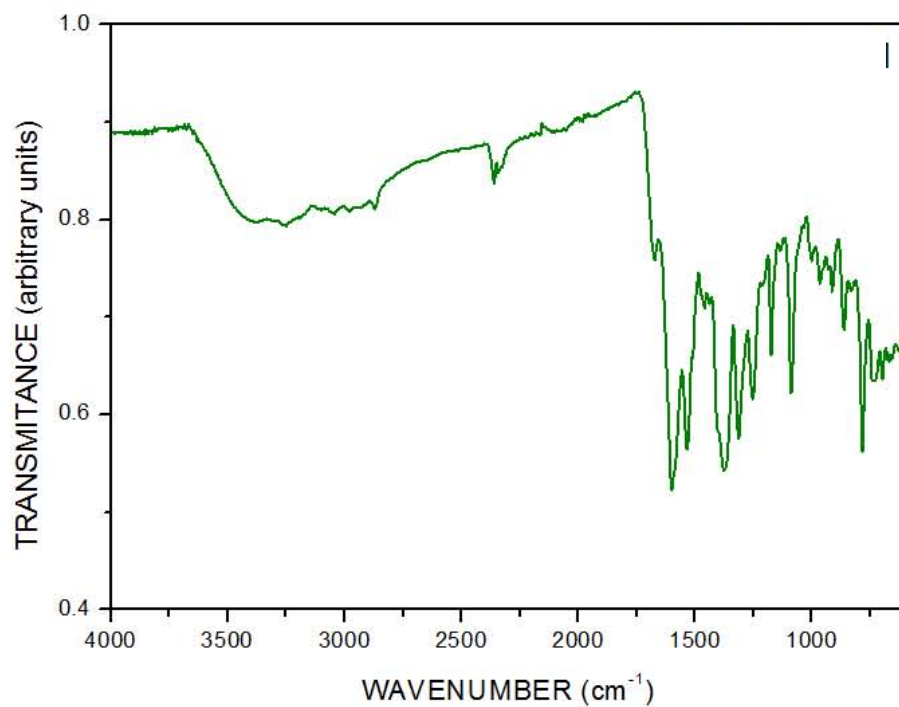


Figure S6. Characterization of **5**: (a) FT-IR spectrum, and (b) Powder X-Ray diffraction pattern of **5** (green), in comparison to the simulated pattern (black).

a)



b)

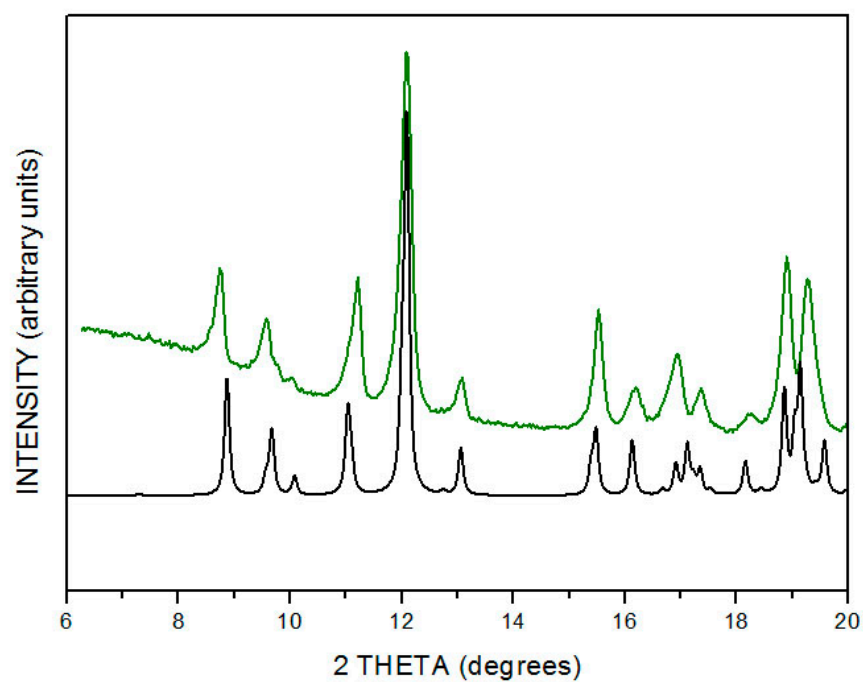


Figure S7. Characterization of **6**: (a) FT-IR spectrum, and (b) Powder X-Ray diffraction pattern of **6** (red), in comparison to the simulated pattern (black).

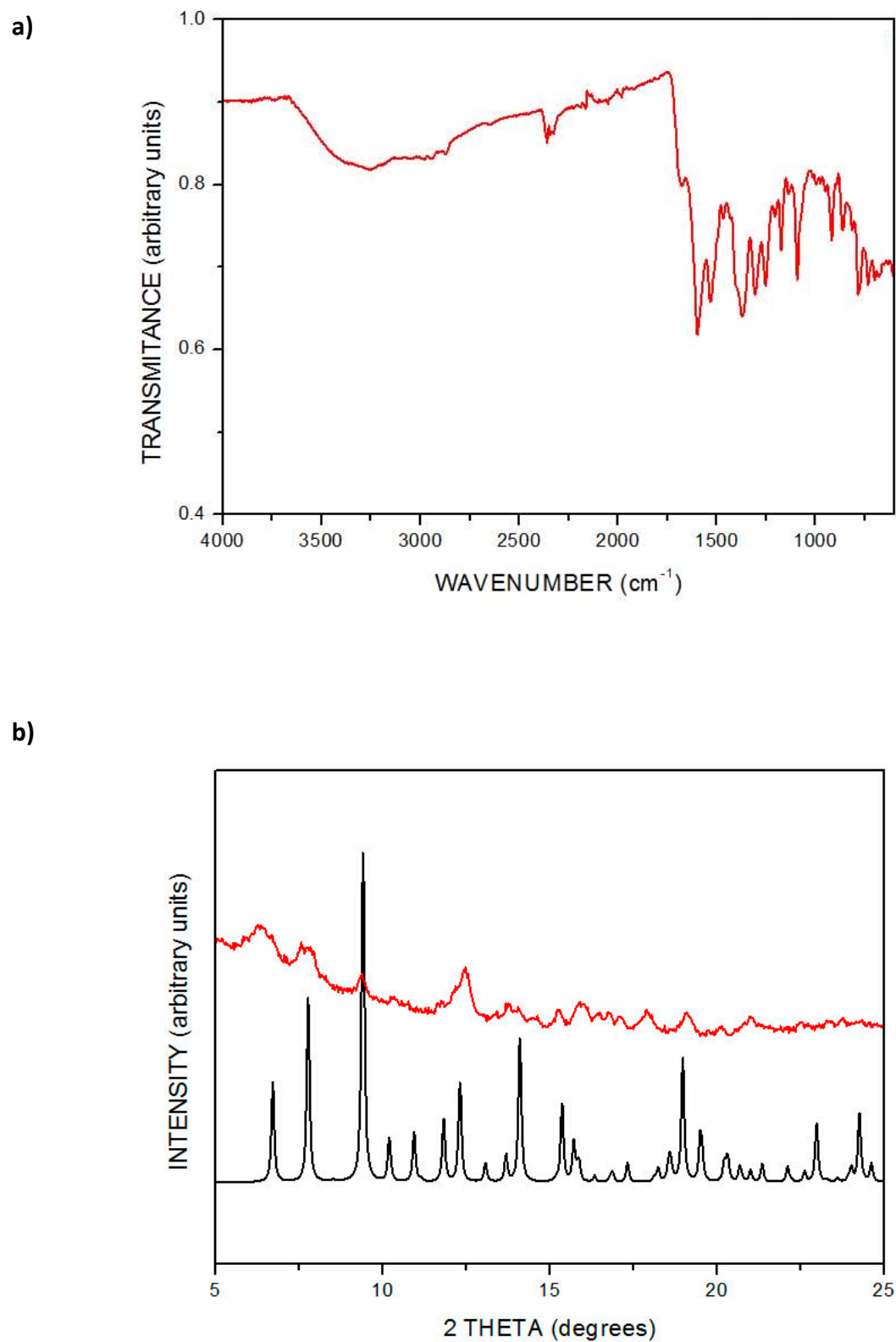


Figure S8. Characterization of **7**: (a) FT-IR spectrum, and (b) Powder X-Ray diffraction pattern of **7** (orange), in comparison to the simulated pattern (black).

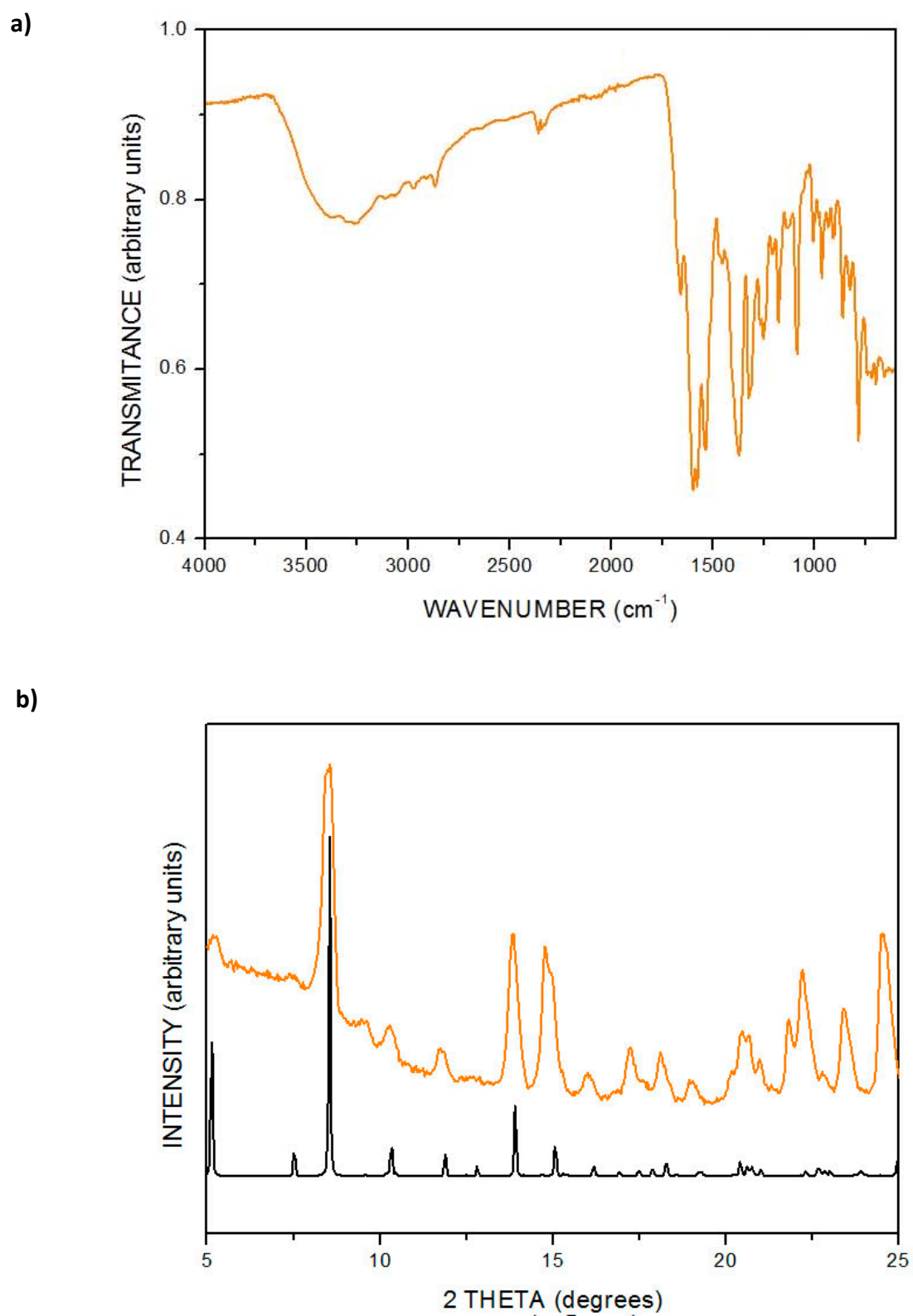
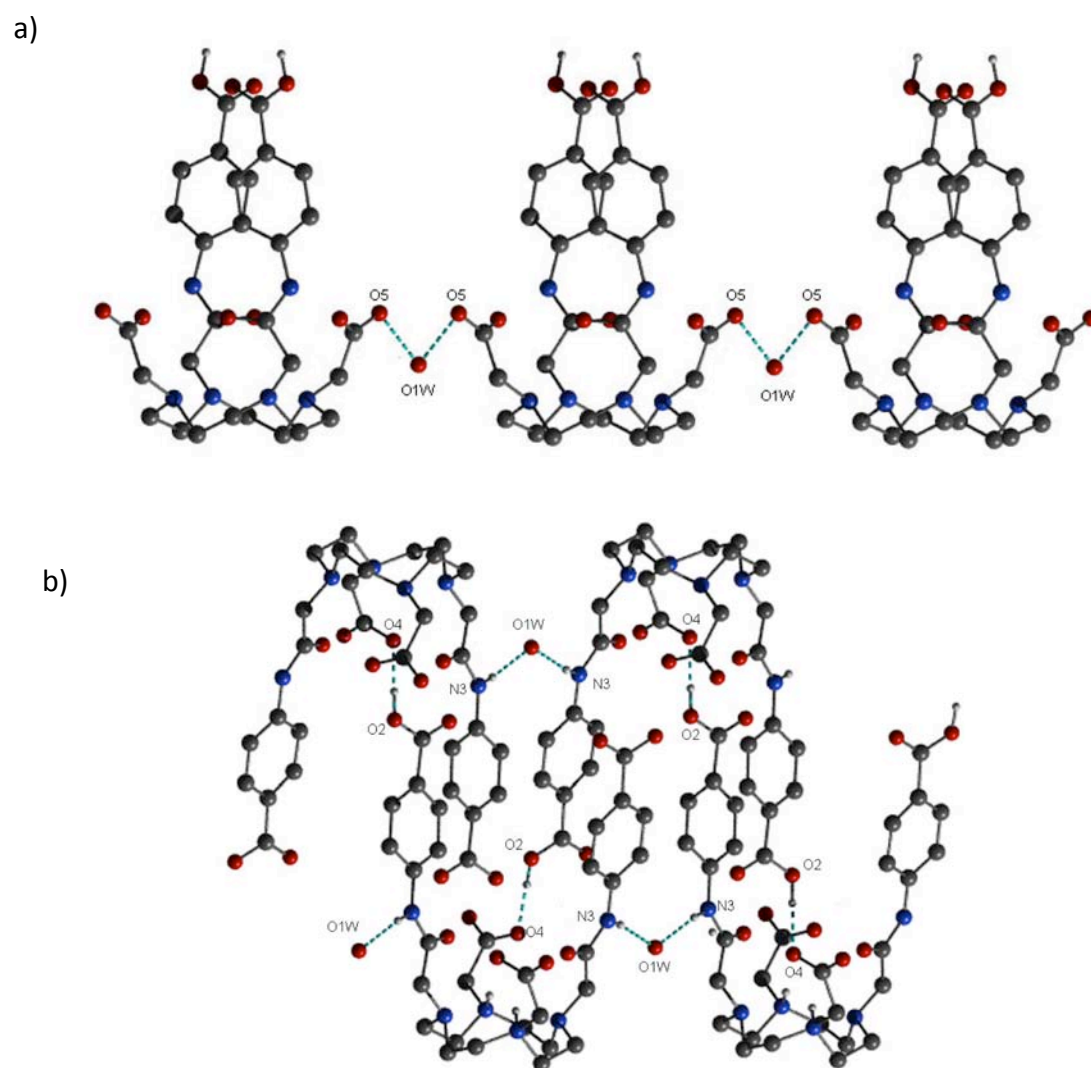


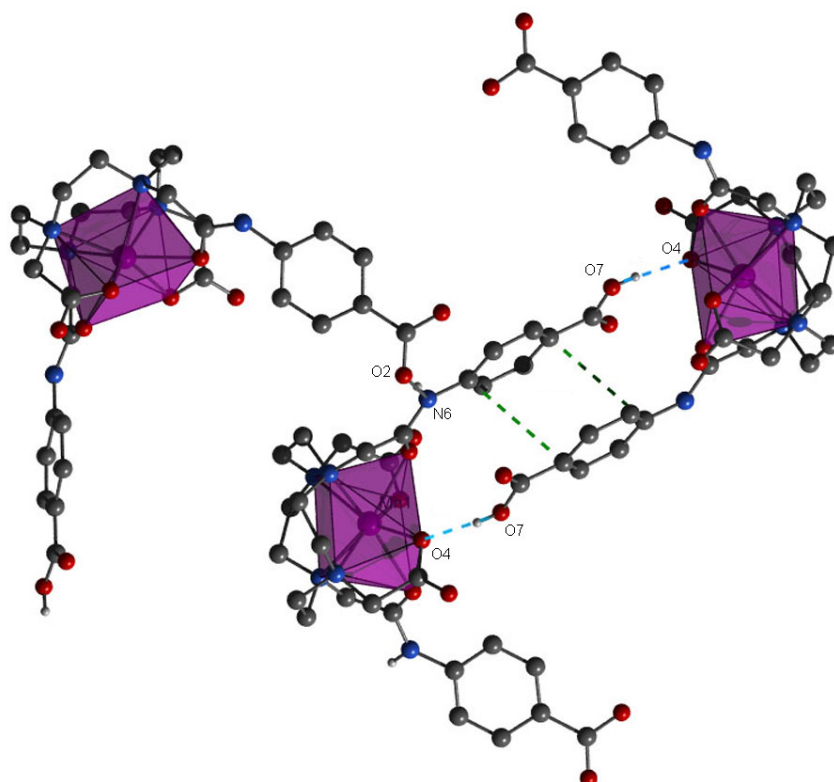
Figure S9. Views of the H-bonded packing of H₄L1. Hydrogen bonds are marked as sky blue dash lines. Hydrogen-bond geometry (Å, °) data is shown below.



<i>D</i> —H... <i>A</i>	<i>D</i> —H	H... <i>A</i>	<i>D</i> ... <i>A</i>	<i>D</i> —H... <i>A</i>
N3—H...O1W ⁱ	0.86	2.16	3.004(8)	169
O1W—H...O5 ^{ii, iii}	--	--	2.813(0)	--
O2—H...O4 ^{iv}	0.92	1.67	2.592(0)	174

Symmetry codes: (i) *x*, *y*, 1+*z*; (ii) 1/2-*x*, 1/2-*y*, 1-*z*; (iii) -1/2+*x*, 1/2-*y*, -1/2+*z* (iv) *x*, -*y*, 1/2+*z*

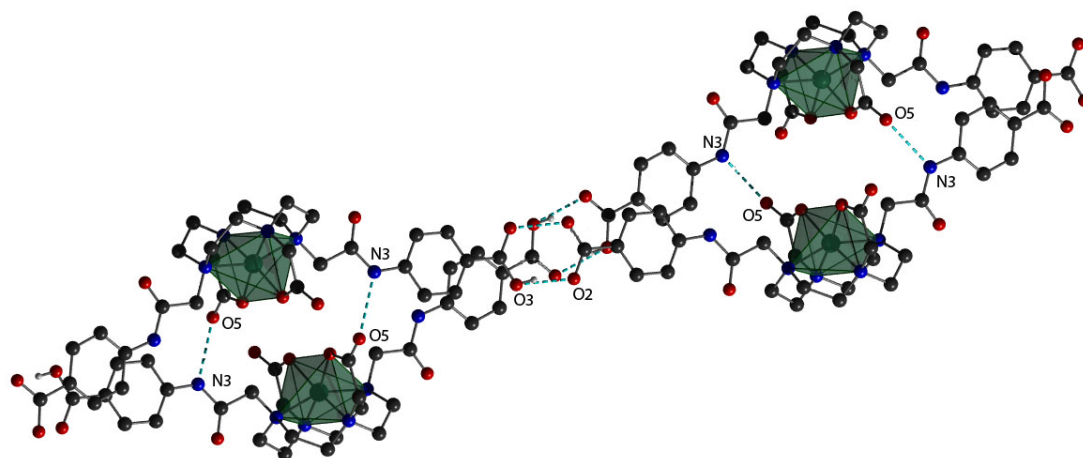
Figure S10. View of the H-bonded packing of **3**. Hydrogen bonds are marked as sky blue dash lines, and π - π stacking interactions are marked as green dash lines. Hydrogen-bond geometry (\AA , $^\circ$) data is shown below.



$D-H\cdots A$	$D-H$	$H\cdots A$	$D\cdots A$	$D-H\cdots A$
$O7-H\cdots O4^i$	0.82	1.71	2.510(8)	163
$N6-H\cdots O2^{ii}$	0.86	2.04	2.879(6)	164

Symmetry codes: (i) $2-x, 1-y, 3-z$; (ii) $2-x, -1/2+y, 5/2-z$

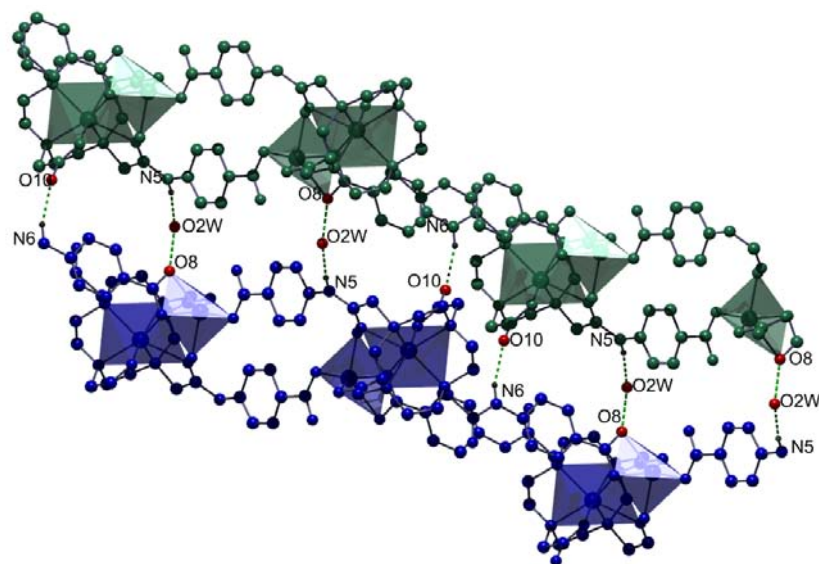
Figure S11. View of the H-bonded packing of **4**. Hydrogen bonds are marked as sky blue dash lines. Hydrogen-bond geometry (Å, °) data is shown below.



<i>D</i> —H... <i>A</i>	<i>D</i> —H	H... <i>A</i>	<i>D</i> ... <i>A</i>	<i>D</i> —H... <i>A</i>
O3—H...O2 ⁱ	0.82	1.82	2.628(7)	168
N3—H... O5 ⁱⁱ	0.86	1.93	2.791(5)	176
O1W—H...O4 ^{iii, iv}	--	--	3.022(4)	--

Symmetry codes: (i) -x, -y, -2-z; (ii) 1-x, -y, -z; (iii) x, -y, -1/2+z; (iv) 1-x, -y, -z

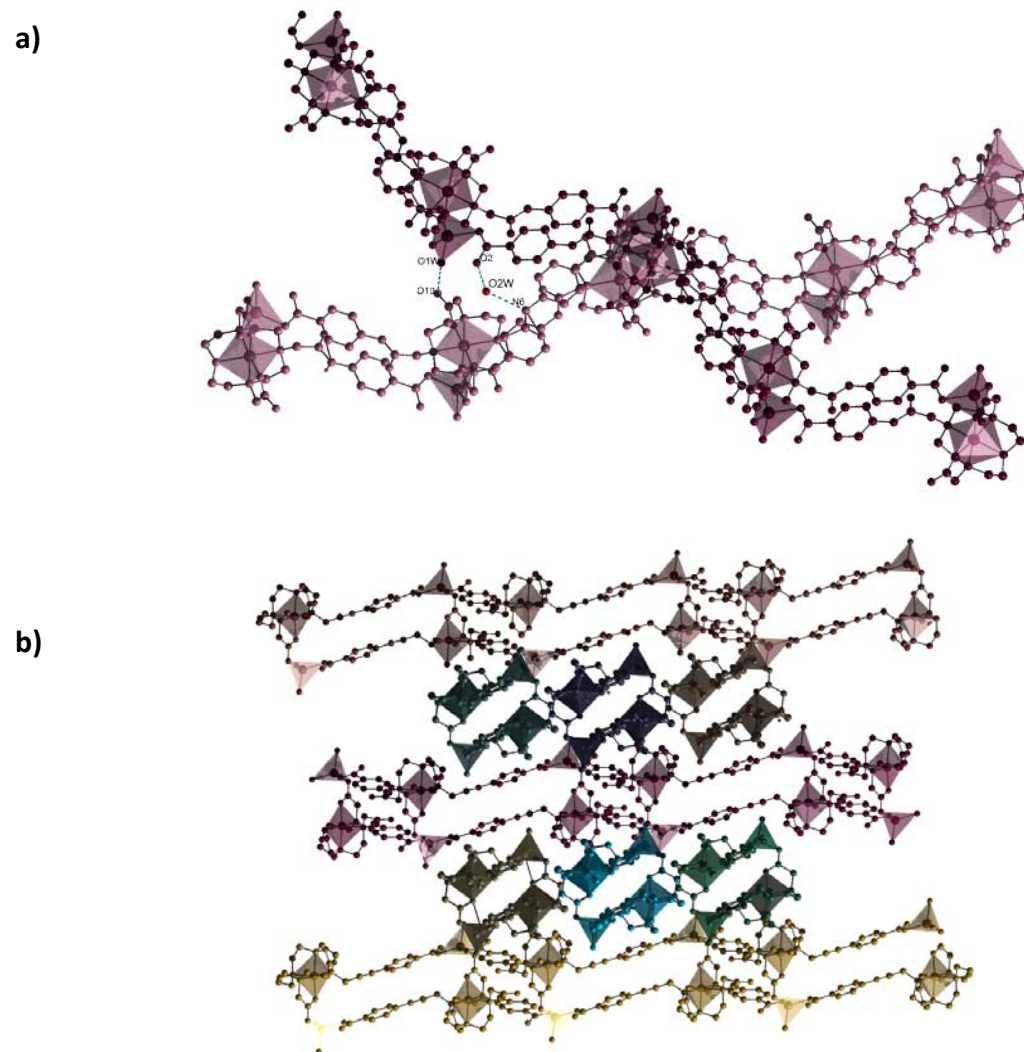
Figure S12. View of the H-bonded packing of the double-strand chains in **5**. Hydrogen bonds are marked as green dash lines. Hydrogen-bond geometry (Å, °) data is shown below.



<i>D</i> —H... <i>A</i>	<i>D</i> —H	H... <i>A</i>	<i>D</i> ... <i>A</i>	<i>D</i> —H... <i>A</i>
N6—H...O10 ⁱ	0.86	2.03	2.852(6)	160
N5—H... O2W	0.86	1.92	2.765(2)	169
O2W—H...O8 ⁱ	--	--	2.850(3)	--

Symmetry codes: (i) 1-x, 1-y, -z

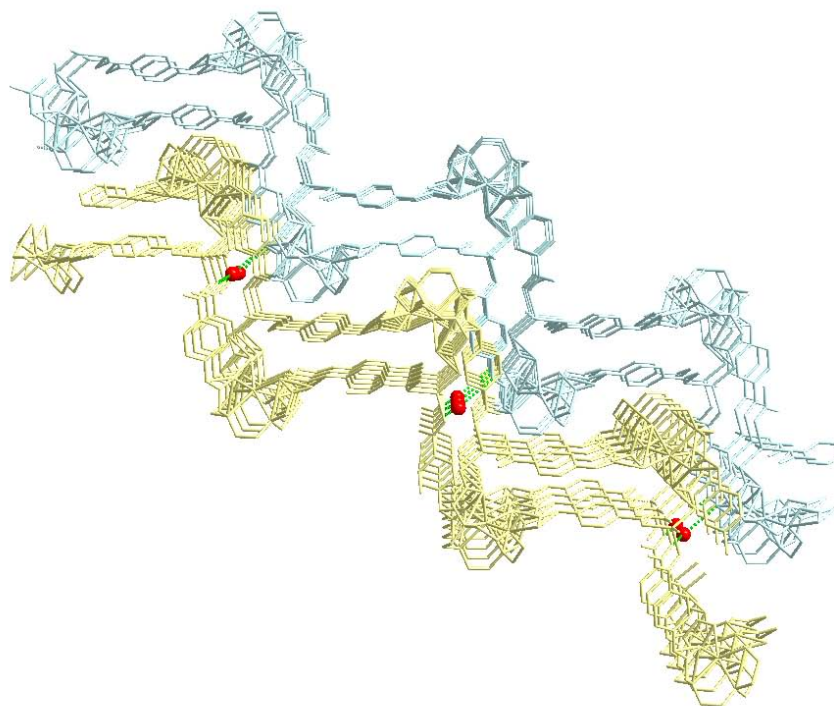
Figure S13. Views of a) the hydrogen bonds between double-strand chains in **6** and b) the packing of these double-strand chains along the [110] direction. Hydrogen bonds are marked as sky blue dash lines. Hydrogen-bond geometry (Å, °) data is shown below.



$D-H\cdots A$	$D-H$	$H\cdots A$	$D\cdots A$	$D-H\cdots A$
N6—H \cdots O2W	0.86	2.02	2.874(5)	170
O2W—H \cdots O2 ⁱ	--	--	2.818(1)	--
O1W—H \cdots O10 ⁱⁱ	--	--	2.591(0)	--

Symmetry codes: (i) $1/2-x, -1/2+y, 3/2-z$; (ii) $1/2+x, 1/2-y, 1/2+z$

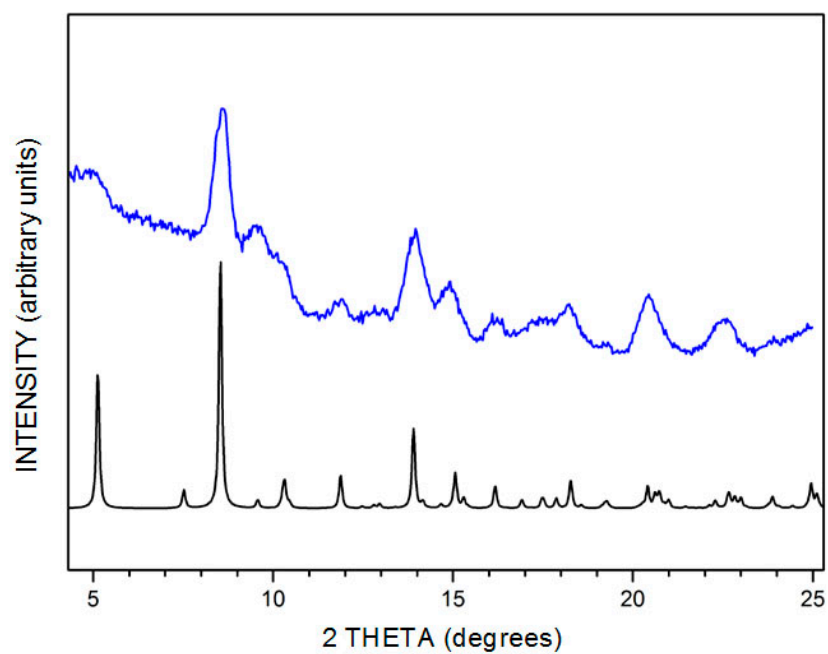
Figure S14. View of the H-bonded packing of the layers of **7** via O4W water molecule along the *b* axis. Hydrogen bonds are marked as sky blue dash lines. Hydrogen-bond geometry (Å, °) data is shown below.



<i>D</i> —H... <i>A</i>	<i>D</i> —H	H... <i>A</i>	<i>D</i> ... <i>A</i>	<i>D</i> —H... <i>A</i>
N5—H...O4W ⁱ	0.86	2.13	2.941(7)	157
O4W—H... O2	--	--	2.962(4)	--

Symmetry codes: (i) *x*, 2-*y*, -1/2+*z*

Figure S15. Powder X-Ray diffraction pattern resulting from the activated, amorphous 7' once it has been exposed to a water sorption/desorption cycle (blue), in comparison to the simulated pattern (black).



Publication 2: “Single-crystal and humidity-controlled powder diffraction study of the breathing effect in a metal-organic framework upon water adsorption /desorption.”



Cite this: *Chem. Commun.*, 2016,
52, 7229

Received 7th April 2016,
Accepted 4th May 2016

DOI: 10.1039/c6cc02908f

www.rsc.org/chemcomm

Single-crystal and humidity-controlled powder diffraction study of the breathing effect in a metal–organic framework upon water adsorption/desorption†

Javier Ariñez-Soriano,^a Jorge Albalad,^a Christian Vila-Parrondo,^a
Javier Pérez-Carvajal,^a Sabina Rodríguez-Hermida,^a Aurelio Cabeza,^b
Jordi Juanhuix,^c Inhar Imaz^{*a} and Daniel MasPOCH^{*ad}

Herein we report a study on water adsorption/desorption-triggered single-crystal to single-crystal transformations in a MOF, by single-crystal and humidity-controlled powder X-ray diffraction and water-sorption measurements. We identified a gate-opening effect at a relative humidity of 85% upon water adsorption, and a gate-closure effect at a relative humidity of 55 to 77% upon water desorption. This reversible breathing effect between the “open” and the “closed” structures of the MOF involves the cleavage and formation of several coordination bonds.

Research on metal–organic frameworks (MOFs), also known as porous coordination polymers (PCPs), has recently put the spotlight on applications that rely on water-sorption properties. These applications include heat transformation,^{1–4} enhancement of CO₂ capture,^{5–7} proton conductivity,^{8–11} air dehumidification,¹² and water delivery in remote areas.¹³ Among the various MOFs that have shown promising water-sorption capabilities,^{2,14} the flexible “third-generation” MOFs^{15–17} are very interesting because, upon exposure to water at a very specific gate pressure, they can undergo a reversible change from a “closed” structure to an “open” one. Consequently, these MOFs can exhibit stepwise adsorption of water (usually reflected by an S-shape water-sorption isotherm) or behave as water-induced switching materials, which are useful for applications such as heat transformation,¹⁸ sensors¹⁹ and proton conductivity.^{20–22} A clear example of this

type of flexible MOF is Al-MIL-53-OH,^{14,23} which abruptly takes up water at a relative humidity (RH) of roughly 80%, due to a phase transition from its “closed” structure to its “open” one.

To date, very few studies on the breathing effects induced by water sorption in MOFs have been done, and even fewer studies have explored the single crystal-to-single crystal (SC–SC) transformations between the “closed” and “open” structures during water sorption.^{24,25} Knowledge on these phase transitions is important for understanding the pertinent water-sorption mechanisms and for developing more efficient MOFs. Much of the work done so far has focused on investigating SC–SC transformations induced by water in dense MOFs—namely, to study the reversible transitions between crystalline states with different proton conductivities.^{20–22} Importantly, a case showing a water-induced SC–SC transformation between “closed” and “open” structures was reported by Chen *et al.*, who found a transition between a 5-fold interpenetrated network (the “open” or hydrated structure) and a 6-fold interpenetrated network (the “closed” or dehydrated structure). They proved that these reversible transformations involved coordination bond cleavages and formation in which water molecules intervened.²⁵ More recently, Morris *et al.* studied the SC–SC transformation of a flexible MOF by using *in situ* temperature-controlled single-crystal diffraction studies. They found that the transition between the hydrated porous phase (which is porous to NO) and the dehydrated non-porous phase involved the reversible breaking and formation of several bonds.²⁶ Importantly, neither of these two examples has been investigated in terms of water sorption.

Herein, we report a study on water adsorption/desorption-triggered SC–SC transformations in a MOF, by single-crystal and humidity-controlled powder X-ray diffraction and water-sorption measurements. Specifically, we describe the synthesis of a new flexible MOF, of formula [Mn₂(Gd-H-DOTA-4AmP)(H₂O)₇]·21H₂O (**1**) [where Gd-H₈-DOTA-4AmP is Gd(III)-1,4,7,10-tetraazacyclododecane-1,4,7,10-tetraacetamidomethylene phosphonic acid (Fig. 1a)],²⁷ which exhibits an S-shape (Type V)^{28,29} water isotherm. It abruptly takes up water at a RH of 85%, reaching

^a Catalan Institute of Nanoscience and Nanotechnology (ICN2), CSIC and The Barcelona Institute of Science and Technology, Campus UAB, Bellaterra, 08193 Barcelona, Spain. E-mail: inhar.imaz@icn2.cat, daniel.masPOCH@icn2.cat

^b Dpto Química Inorgánica, Cristalografía y Mineralogía, Universidad de Málaga, Campus de Teatinos s/n, 29071 Málaga, Spain

^c ALBA Synchrotron, 08290 Cerdanyola del Vallès, Barcelona, Catalonia, Spain

^d Institució Catalana de Recerca i Estudis Avançats (ICREA), 08100 Barcelona, Spain

† Electronic supplementary information (ESI) available: Experimental section, TGA, PXRD, and water sorption measurements. 1471149 (**1-op**) and 1471150 (**1-cp**). For ESI and crystallographic data in CIF or other electronic format see DOI: 10.1039/c6cc02908f

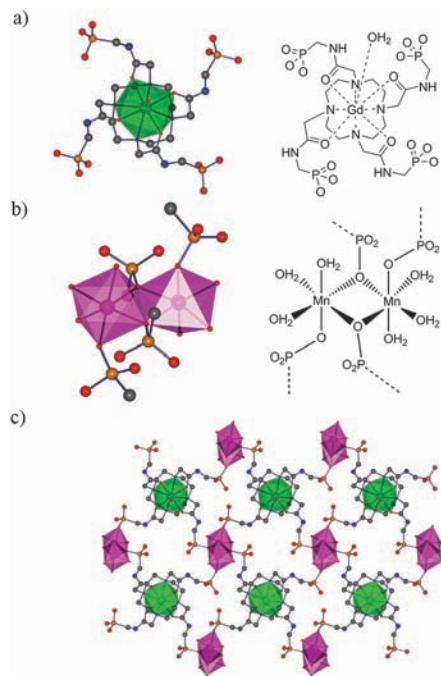


Fig. 1 Crystal structure of **1-op**. (a) Coordination environment of Gd-H-DOTA-4AmP. (b) Representations of the $[\text{Mn}_2(\text{PO}_3\text{R})_4(\text{H}_2\text{O})_6]$ binuclear building unit. (c) View of a coordination layer along the *b*-axis. Colour code: Gd, green; Mn, pink; P, orange; O, red; N, blue; and C, grey. H atoms have been omitted for clarity.

its total water uptake of $0.4 \text{ g}_{\text{water}} \text{ g}_1^{-1}$ at a RH of 95%. We used single-crystal X-ray diffraction (SCXRD) and humidity controlled powder X-ray diffraction (PXRD) measurements to determine that the water adsorption/desorption mechanism in **1** involves an SC–SC transition between two different phases: **1-op** (1-open pore) and **1-cp** (1-closed pore). To our knowledge, this is the first-ever reported use of humidity-controlled PXRD measurements on a flexible MOF to understand its water-sorption behaviour in terms of SC–SC transition.

Crystals of **1-op** suitable for SCXRD were obtained by the reaction of Gd-H₈-DOTA-4AmP with manganese acetate tetrahydrate in water at room temperature for 10 days (yield: 80%). The structure of **1-op** was resolved and refined in the monoclinic space group $P2_1/c$, revealing the formation of a 2-D network of formula $[\text{Mn}_2(\text{Gd-H-DOTA-4AmP})(\text{H}_2\text{O})_7] \cdot 21\text{H}_2\text{O}$. The basic unit of **1-op** is a binuclear unit of formula $[\text{Mn}_2(\text{PO}_3\text{R})_4(\text{H}_2\text{O})_6]$, in which the two Mn(II) ions are bridged by two O atoms of two phosphonate groups (Fig. 1b). Both Mn(II) centres adopt a distorted octahedral geometry coordinated to three O atoms of phosphonate groups and to three water molecules. In this structure, each binuclear unit is connected to four Gd-H-DOTA-4AmP linkers and each Gd-H-DOTA-4AmP linker is connected to four binuclear Mn(II) units, creating layers extending along the *ac* plane (Fig. 1c). These layers show a corrugated conformation and stack up along the *b*-axis, forming 1-D channels that run along the *a*-axis (Fig. 2). The channels have dimensions of approximately $14.8 \text{ \AA} \times 9.5 \text{ \AA}$, affording an estimated solvent-accessible void volume of 2657 \AA^3 , which represents 45% of the total cell volume (5958 \AA^3) of **1-op**. These channels are filled with 21 guest water molecules per formula unit, as confirmed by elemental analysis and thermogravimetric (TGA) analysis (Table S2 and Fig. S1, ESI†).

Interestingly, single crystals of **1-op** underwent structural transformations when they were exposed to a dry environment (RH < 40%) for 8 hours. SCXRD performed on the resulting crystals revealed the formation of a new phase, of formula $[\text{Mn}_2(\text{Gd-H-DOTA-4AmP})(\text{H}_2\text{O})_7] \cdot 5\text{H}_2\text{O}$ (**1-cp**), which crystallises in the monoclinic space group $C2/c$. **1-cp** is also formed by coordination layers made of binuclear Mn(II) units bridged by Gd-H-DOTA-4AmP linkers. However, compared to **1-op**, **1-cp** showed drastically reduced cell volume (compare 5958 \AA^3 (**1-op**) to 4335 \AA^3 (**1-cp**); 27% reduction), and especially, reduced solvent-accessible volume (from 2657 \AA^3 (**1-op**) to 682 \AA^3 (**1-cp**); 74% reduction). As expected, this reduction makes **1-cp** almost non-porous to N₂ ($S_{\text{BET}} = 30 \text{ m}^2 \text{ g}^{-1}$) and CO₂ (Fig. S3, ESI†). This reduction is a direct consequence of the transition from the

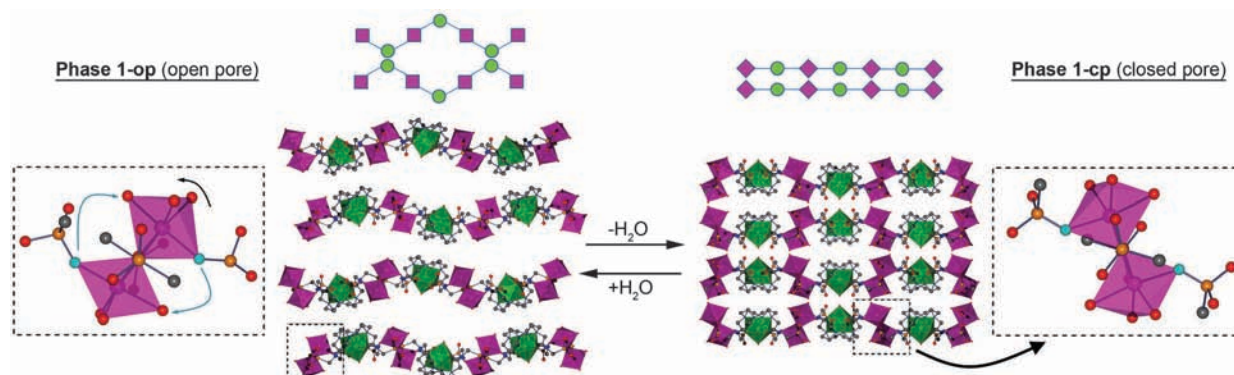


Fig. 2 Schematic representations and views of (top, left) the corrugated coordination layers of **1-op** and (top, right) the flatter coordination layers of **1-cp** along the *a*-axis. Note that the corrugated layers define the 1D channels, whereas the flat layers close them. (bottom, left) Details of the Mn(II) binuclear subunit in **1-op** showing the cleavage/formation of coordination bonds (blue arrows) and the rotation of the subunit (black arrow) during the phase transition. (bottom, right) View of the resulting binuclear subunit in **1-cp**. Colour code: Gd, green; Mn, pink; P, orange; O, red; N, blue; and C, grey. H atoms have been omitted for clarity.

corrugated conformation of the coordination layers in **1-op** to a flatter conformation in **1-cp**. This change leads to closer packing between the coordination layers along the *b*-axis [*b*-axis is reduced from 19.8 Å (**1-op**) to 14.5 Å (**1-cp**)], thereby closing the 1D channels (Fig. 2). This dense packing means that, whilst there is no direct hydrogen bonding between the corrugated layers of **1-op**, the closest layers in **1-cp** form two direct hydrogen bonds between the O3 atom of the phosphonate group and the Mn(II)-bound water molecule O3W (O3W...O3, 2.83 Å) and the O7 atom of the phosphonate group and Gd(III)-bound water molecule O1W (O1W...O7, 2.65 Å; Fig. S4, ESI†). Interestingly, it also involves the removal of sixteen guest water molecules, such that only five guest water molecules remain between the layers of **1-cp**, as confirmed by elemental analysis and TGA (Table S3 and Fig. S1, ESI†).

A more detailed analysis of the **1-op** → **1-cp** transformation shows that the transition from the corrugated layers to the flatter layers is promoted by the rotation of the Mn(II) binuclear building unit around the *a* axis (Fig. 2). As illustrated in Fig. 2, this rotation requires the cleavage and formation of two phosphonate–Mn(II) and two water–Mn(II) coordination bonds per binuclear Mn(II) unit. Here, we hypothesise that guest water molecules may participate in this ligand exchange mechanism by coordinating to the Mn(II) ions and forming intermediate species such that two coordinated water molecules would ultimately be replaced with two guest water molecules.^{25,30}

To verify the reversibility of this SC–SC transformation, we incubated crystals of **1-cp** in water overnight. PXRD analysis of the resulting crystals revealed that the **1-op** phase is recovered (Fig. S5, ESI†), demonstrating that the transition **1-op** ↔ **1-cp** is reversible. As **1-op** ↔ **1-cp** involves the loss and gain of many water molecules, we then investigated whether **1** shows a gate-opening effect upon water sorption. To this end, we combined water-sorption measurements with PXRD analysis in a humidity-controlled environment (Fig. 3 and 4).^{31,32} The collected water isotherm showed different paths between the adsorption and desorption branches. In this isotherm, the water adsorption branch follows a representative type II trend up to a RH of 85%, in which the water uptake is 0.28 g_{water} g₁^{−1} or 19 H₂O per formula unit. At this RH, a step appears, changing the trend of the isotherm from type II to type V; behaviour that is characteristic of a gate-opening effect in flexible MOFs (Fig. 3a).³³ This event increases the water uptake up to 0.40 g_{water} g₁^{−1} or 28 H₂O per formula unit at a RH of 95%. The presence of this step is in agreement with the transition phase **1-cp** → **1-op** recorded using humidity-controlled PXRD measurements (Fig. 3b). Indeed, while the characteristic PXRD pattern of **1-cp** was observed up to an RH of 80%, the PXRD pattern at a RH of 90% (corresponding to the middle of the step) showed the coexistence of peaks characteristic of both phases. The transition was completed at a RH of 95%, in which the PXRD pattern showed the characteristic pattern of **1-op**.

The desorption branch also shows a step in the RH range from 70% to 55% (Fig. 4a). This abrupt desorption of water molecules correlates well with humidity-controlled PXRD measurements of the transition **1-op** → **1-cp** (Fig. 4b).³⁴ Hence, the PXRD

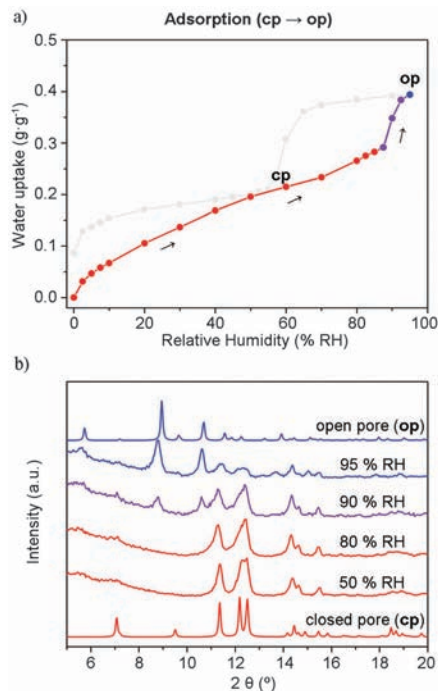


Fig. 3 (a) Adsorption branch of the water isotherm of **1** showing the presence of **1-cp** (red), **1-op** (blue) and mixed (purple) phases. (b) Humidity-controlled PXRD measurements of **1** at different RH values, showing the presence of **1-cp** (red), **1-op** (blue) and mixed (purple) phases.

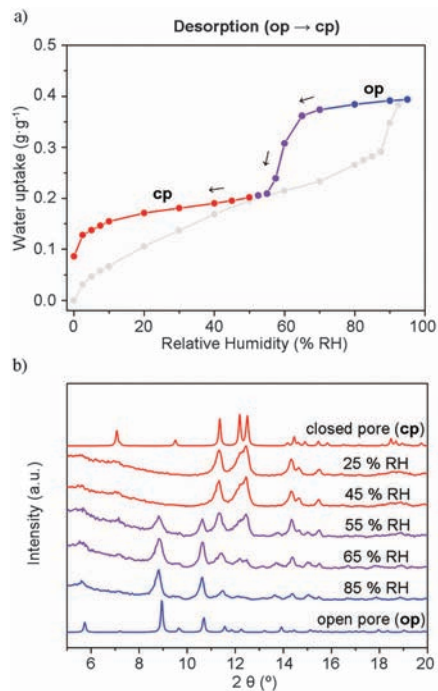


Fig. 4 (a) Desorption branch of the water isotherm of **1** showing the presence of **1-cp** (red), **1-op** (blue) and mixed (purple) phases. (b) Humidity-controlled PXRD measurements of **1** at different RH values, showing the presence of **1-cp** (red), **1-op** (blue) and mixed (purple) phases.

pattern at a RH of 85% is identical to that of **1-op**, whereas those patterns collected at RHs of 65% and 55% showed the coexistence

of peaks characteristic of both phases. Below a RH of 45%, the PXRD pattern is characteristic of **1-cp**, as confirmed by the lack of all characteristic peaks of **1-op** (e.g. $2\theta = 9.0^\circ$ and 10.7°).

We then performed four consecutive cycles of water adsorption/desorption to further analyse the reversibility of the water sorption process (Fig. S6, ESI†). Remarkably, the stepwise trend in the isotherm remained and the maximum uptake ($0.40 \text{ g}_{\text{water}} \text{ g}_1^{-1}$) was not significantly different among the cycles, confirming the stability of the material to water sorption/desorption processes. The kinetic study of the phase transition **1-cp** \rightarrow **1-op**, whereby the **1-cp** phase was exposed to an environment having a RH of 95% (Fig. S7, ESI†), revealed that the first peaks of the porous phase appeared in the first 15 minutes, whilst the transition could be considered complete after 2.5 hours.

In conclusion, we have described the water-induced reversible SC-SC transformation of a MOF from a “closed” structure to an “open” one. This reversible transformation involves the rupture and formation of several coordination bonds. We have shown that combining water sorption measurements with single-crystal and humidity-controlled powder X-ray diffraction can provide valuable information on any breathing effects that occur during the water adsorption/desorption processes. It is clear that **1** shows gate opening at a RH of 85%, achieving a total water uptake of $0.40 \text{ g}_{\text{water}} \text{ g}_1^{-1}$. It also shows a large hysteresis, in which the gate closure occurs at an RH range of 55–70%. Furthermore, we have performed kinetics and recyclability studies, showing a total reversibility between the transition **1-op** \leftrightarrow **1-cp** for at least four cycles.

This work was supported by the Spanish MINECO through project PN MAT2015-65354-C2-1-R and by EU FP7 through ERC-Co grant agreement no. 615954. I. I. and J. A. thank the MINECO for a RyC grant (RYC-2010-06530) and a FPU predoctoral grant (AP2010-5934), respectively. J. A. also thanks the Chemistry PhD programme of the Universitat Autònoma de Barcelona. A. C. thanks MINECO and Junta de Andalucía through research projects MAT2013-41836-R and P12-FQM-1656, respectively. ICN2 acknowledges the support from the Spanish MINECO through the Severo Ochoa Centres of Excellence Programme, under Grant SEV-2013-0295.

Notes and references

- J. Ehrenmann, S. K. Henninger and C. Janiak, *Eur. J. Inorg. Chem.*, 2011, 471–474.
- S. K. Henninger, F. Jeremias, H. Kummer and C. Janiak, *Eur. J. Inorg. Chem.*, 2012, 2625–2634.
- F. Jeremias, A. Khutia, S. K. Henninger and C. Janiak, *J. Mater. Chem.*, 2012, 22, 10148–10151.
- M. F. de Lange, K. J. F. M. Verouden, T. J. H. Vlucht, J. Gascon and F. Kapteijn, *Chem. Rev.*, 2015, 115, 12205–12250.
- E. Soubeyrand-Lenoir, C. Vagner, J. W. Yoon, P. Bazin, F. Ragon, Y. K. Hwang, C. Serre, J.-S. Chang and P. L. Llewellyn, *J. Am. Chem. Soc.*, 2012, 134, 10174–10181.
- A. O. Yazaydin, A. I. Benin, S. A. Faheem, P. Jakubczak, J. J. Low, R. R. Willis and R. Q. Snurr, *Chem. Mater.*, 2009, 21, 1425–1430.
- Y. F. Chen, R. Babarao, S. I. Sandler and J. W. Jiang, *Langmuir*, 2010, 26, 8743–8750.
- A. Mallick, T. Kundu and R. Banerjee, *Chem. Commun.*, 2012, 48, 8829–8831.
- S. C. Sahoo, T. Kundu and R. Banerjee, *J. Am. Chem. Soc.*, 2011, 133, 17950–17958.
- R. M. P. Colodrero, P. Olivera-Pastor, E. R. Losilla, M. A. G. Aranda, L. Leon-Reina, M. Papadaki, A. C. McKinlay, R. E. Morris, K. D. Demadis and A. Cabeza, *Dalton Trans.*, 2012, 41, 4045–4051.
- R. M. P. Colodrero, P. Olivera-Pastor, E. R. Losilla, D. Hernández-Alonso, M. A. G. Aranda, L. Leon-Reina, J. Rius, K. D. Demadis, B. Moreau, D. Villemin, M. Palomino, F. Rey and A. Cabeza, *Inorg. Chem.*, 2012, 51, 7689–7698.
- P. Guo, A. G. Wong-Foy and A. J. Matzger, *Langmuir*, 2014, 30, 1921–1925.
- H. Furukawa, F. Gándara, Y.-B. Zhang, J. Jiang, W. L. Queen, M. R. Hudson and O. M. Yaghi, *J. Am. Chem. Soc.*, 2014, 136, 4369–4381.
- J. Canivet, A. Fateeva, Y. Guo, B. Coasne and D. Farrusseng, *Chem. Soc. Rev.*, 2014, 43, 5594–5617.
- S. Kitagawa and K. Uemura, *Chem. Soc. Rev.*, 2005, 34, 109–119.
- A. Schneemann, V. Bon, I. Schwedler, I. Senkovska, S. Kaskel and R. A. Fischer, *Chem. Soc. Rev.*, 2014, 43, 6062–6096.
- S. Horike, S. Shimomura and S. Kitagawa, *Nat. Chem.*, 2009, 1, 695–704.
- C. J. S. K. Henninger, F. Jeremias, J. Ehrenmann, in *International Sorption Heat Pump Conference (ISHPC11)*, Padua, 2011, pp. 415–423.
- Y. Takashima, V. M. Martinez, S. Furukawa, M. Kondo, S. Shimomura, H. Uehara, M. Nakahama, K. Sugimoto and S. Kitagawa, *Nat. Commun.*, 2011, 2, 168.
- S.-S. Bao, N.-Z. Li, J. M. Taylor, Y. Shen, H. Kitagawa and L.-M. Zheng, *Chem. Mater.*, 2015, 27, 8116–8125.
- M. Sadakiyo, T. Yamada, K. Honda, H. Matsui and H. Kitagawa, *J. Am. Chem. Soc.*, 2014, 136, 7701–7707.
- S. Tominaka, F.-X. Coudert, T. D. Dao, T. Nagao and A. K. Cheetham, *J. Am. Chem. Soc.*, 2015, 137, 6428–6431.
- A. Shigematsu, T. Yamada and H. Kitagawa, *J. Am. Chem. Soc.*, 2011, 133, 2034–2036.
- T. Zheng, J. M. Clemente-Juan, J. Ma, L. Dong, S.-S. Bao, J. Huang, E. Coronado and L.-M. Zheng, *Chem. – Eur. J.*, 2013, 19, 16394–16402.
- J.-P. Zhang, Y.-Y. Lin, W.-X. Zhang and X.-M. Chen, *J. Am. Chem. Soc.*, 2005, 127, 14162–14163.
- P. K. Allan, B. Xiao, S. J. Teat, J. W. Knight and R. E. Morris, *J. Am. Chem. Soc.*, 2010, 132, 3605–3611.
- F. K. Kalman, M. Woods, P. Caravan, P. Jurek, M. Spiller, G. Tircsó, R. Kiraly, E. Brücher and A. D. Sherry, *Inorg. Chem.*, 2007, 46, 5260–5270.
- N. C. Burtch, H. Jasuja and K. S. Walton, *Chem. Rev.*, 2014, 114, 10575–10612.
- D. Fairen-Jimenez, N. A. Seaton and T. Duren, *Langmuir*, 2010, 26, 14694–14699.
- M. C. Bernini, F. Gándara, M. Iglesias, N. Snejkó, E. Gutiérrez-Puebla, E. V. Brusau, G. E. Narda and M. A. Monge, *Chem. – Eur. J.*, 2009, 15, 4896–4905.
- D. Fröhlich, S. K. Henninger and C. Janiak, *Dalton Trans.*, 2014, 43, 15300–15304.
- F. Jeremias, D. Fröhlich, C. Janiak and S. K. Henninger, *RSC Adv.*, 2014, 4, 24073–24082.
- S. Brunauer, *The Adsorption of Gases and Vapors Vol I – Physical Adsorption*, Princeton University Press, 1943.
- T. K. Maji, G. Mostafa, R. Matsuda and S. Kitagawa, *J. Am. Chem. Soc.*, 2005, 127, 17152–17153.

Publication 2: Supporting Information

S1. Experimental section

S1.1. General considerations

All chemical reagents and solvents were purchased from commercial sources and used as received without further purification. Purity of all bulk material batches was confirmed by X-ray powder diffraction (PXRD) patterns collected on an X'Pert PRO MPD analytical diffractometer (Panalytical) at 45 kV, 40 mA using Cu K α radiation ($\lambda = 1.5419 \text{ \AA}$), and compared with single crystal simulated patterns. Thermogravimetric analyses were performed under nitrogen flow using an STA 449 F1 Jupiter–Simultaneous TGA-DSC (NETZSCH) at a heating rate of 5 °C/min. Elemental Analysis measurements were performed on a Flash EA 2000 CHNS (Thermo Fisher Scientific) analyser. Water vapor adsorption–desorption isotherms were measured using a gravimetric instrument DVS Advantage-1 (Surface Measurement Systems Ltd). The weight of the dry powder was constantly monitored and recorded at 25 °C and different relative humidity values. The relative humidity inside the chamber was adjusted by bubbling a carrier gas (N₂) in pure water until stream saturated in water (95% Relative Humidity). The adsorbed moisture was expressed as $\frac{g_{\text{water}}}{g_{\text{dry sample}}}$. Prior to the water adsorption measurements, samples were outgassed each cycle at 110 °C during 3 hours using a heating rate of 0.5 °C/min.

S1.2. Synthesis of Gd-H₈-DOTA-4AmP

A solution of DOTA-4AmP (354 mg, 396 μmol) in water (8 mL) was basified to pH = 10 with 1M sodium hydroxide. Then, a solution of gadolinium chloride hexahydrate (147 mg, 396 μmol) in water (2 mL) was added dropwise into the DOTA-4AmP solution warmed at 70 °C under continuous stirring. The pH of the stirring mixture was kept at 10 by addition of concentrated NaOH during the addition process. Note that, after each addition of gadolinium chloride into the DOTA-4AmP solution, a white precipitate initially appeared, but dissolved into solution after a few minutes, indicating that Gd-DOTA-4AmP was successfully formed. In this reaction, the absence of free Gd(III) in the reaction mixture was monitored by the xylenol orange test.¹ Thus, the addition of gadolinium chloride was stopped after the xylenol test showed the persistent presence of free gadolinium. Then, the mixture was left at 70 °C under stirring for 18 hours. Finally, the pH was adjusted to pH = 8 by the addition of concentrated HCl (1M). The exact concentration of Gd(III) ions was determined by ICP-MS, and the final concentration of the Gd-H₈-DOTA-4AmP solution was adjusted to 20 mM by the addition of water to yield an approximate volume of 20 mL.

S1.3. Synthesis of 1

Twenty mL of an aqueous solution of manganese acetate tetrahydrate (196.07 mg, 0.8 mmol) were mixed with 20 mL of the synthesized Gd-H₈-DOTA-4AmP (0.4 mmol) solution, which had previously been adjusted to pH = 6. Immediately after mixing, a white precipitate appeared. Then, the pH of the mixture was adjusted to pH = 5.36 by cautious addition of concentrated HCl (1M), at which point the precipitate disappeared. Then, the aqueous mixture was placed in a conical flask and left undisturbed for 10 days, after which time, a white crystalline precipitate appeared at the bottom of the flask. The resulting crystals were washed several times with deionized water and finally, filtered and dried at room temperature.

S1.4. X-Ray Crystallography

Crystallographic data for **1-op** and **1-cp** were collected at 100 K in the XALOC beamline at the ALBA synchrotron ($\lambda = 0.88557 \text{ \AA}$).² Due to crystal degradation during the dehydration process, different crystals of the **1-cp** phase were collected. The best data set enabled us to resolve the structure, but the crystal degradation led to poor crystal data and consequently, to high R_{int} . These data were indexed, integrated and scaled using the XDS program.³ Absorption correction was not applied. The structures were solved by direct methods and subsequently, refined by correction of F₂ against all reflections using SHELXS2013 and SHELXL2013 within the WinGX package.⁴ All non-hydrogen atoms were refined with anisotropic thermal parameters by full-matrix least-squares calculations on F² using SHELXL2013. Hydrogen atoms were inserted at calculated positions and constrained with isotropic thermal parameters. The hydrogen of the crystal-lattice water molecules present in the structure were not located on the Fourier map, but were added into the empirical formula to enable accurate determination of the density. CCDC 1471149 (**1-op**) and CCDC 1471150 (**1-cp**).

S1.5. Humidity-controlled PXRD measurements

Thermodiffractometric studies at different relative humidity values were collected on a D8 ADVANCE (Bruker AXS) diffractometer equipped with a Johansson Ge(111) primary monochromator, which gives a monochromatic Mo radiation ($\lambda = 0.7093 \text{ \AA}$), and an Anton Paar MHC-trans chamber. The X-ray tube was operating at 50 kV and 50 mA. The energy-dispersive linear detector LYNXEYE XE 500 μm , optimized for high-energy radiation, was used with the maximum opening angle. Data were collected at 25 °C and relative humidity (RH) values ranged between 5% and 95%. Samples were held at each relative humidity at least for 30 min, before recording any pattern, giving sufficient time for any transformation to occur. For the experiment carried out at 25 °C and at a constant relative humidity of 95%, powder X-ray diffraction patterns

were collected every 15 min. All patterns were measured between 2° and 27° (2θ) with a step size of 0.017° and counting time of 96 s/step. All PXRD patterns were converted from Mo-K alpha to Cu-K alpha.

Table S1. Crystallographic Table

Compound reference	1- <i>op</i>	1- <i>cp</i>
Chemical Formula	C ₂₀ H ₅₁ GdMn ₂ N ₈ O ₂₃ P ₄ ·21(H ₂ O)	C ₂₀ H ₅₁ GdMn ₂ N ₈ O ₂₃ P ₄ ·5(H ₂ O)
Formula Mass	1541.00	1252.76
Crystal System	Monoclinic	Monoclinic
Space group	P 21/c	C 2/c
a/ Å	12.300(4)	26.090(5)
b/ Å	19.750(4)	14.510(5)
c/ Å	24.630(4)	12.200(5)
α/ °	90	90
β/ °	95.30(4)	110.19(4)
γ/ °	90	90
Unit Cell Volume / Å ³	5957.7(17)	4335(2)
Temperature/ K	100	100
Z	4	4
Reflections Measured	31272	24777
Independent Reflections	8782	4318
Reflections (<i>I</i> > 2σ(<i>I</i>))	8049	1874
R _{int}	0.0876	0.4237
R ₁ (<i>I</i> > 2σ(<i>I</i>))	0.2453	0.1361
wR(<i>F</i> ²) (<i>I</i> > 2σ(<i>I</i>))	0.2481	0.2856
R ₁ (all data)	0.0909	0.1812
wR(<i>F</i> ²) (all data)	0.2481	0.3219

Table S2. Elemental analysis of 1-*op*

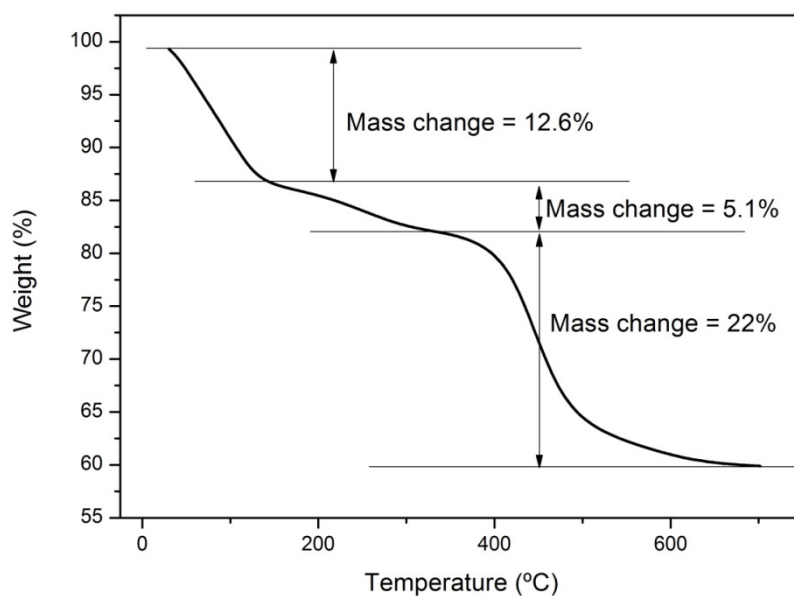
	1-<i>op</i> (calc. wt.%) C ₂₀ H ₅₁ GdMn ₂ N ₈ O ₂₃ P ₄ ·21(H ₂ O)	1-<i>op</i> (exp. wt.%)
C	15.6	16.0 ± 1.2
N	7.3	8.1 ± 1.1
H	6.1	5.4 ± 1.4

Table S3. Elemental analysis of 1-*cp*

	1-<i>cp</i> (calc. wt.%) C ₂₀ H ₅₁ GdMn ₂ N ₈ O ₂₃ P ₄ ·5(H ₂ O)	1-<i>op</i> (exp. wt.%)
C	19.2	18.1 ± 1.2
N	8.9	8.3 ± 1.1
H	4.9	5.2 ± 1.4

Figure S1. Thermogravimetric (TGA) analysis

(a) TGA analysis of **1-op** shows three weight-loss steps. The first step shows a weight loss of 12.6%, corresponding to the loss of 21 guest water molecules (calculated = 13.2%). The second step shows a weight loss of 5.1%, which is attributed to the loss of seven coordinated water molecules (calculated = 4.4%). Finally, the third step corresponds to the decomposition of the framework itself.



(b) TGA analysis of **1-cp** shows two weight loss steps. The first step shows a weight loss of 9.7%, corresponding to the loss of all 12 water molecules (calculated = 8.5%). The second step corresponds to the decomposition of the framework itself.

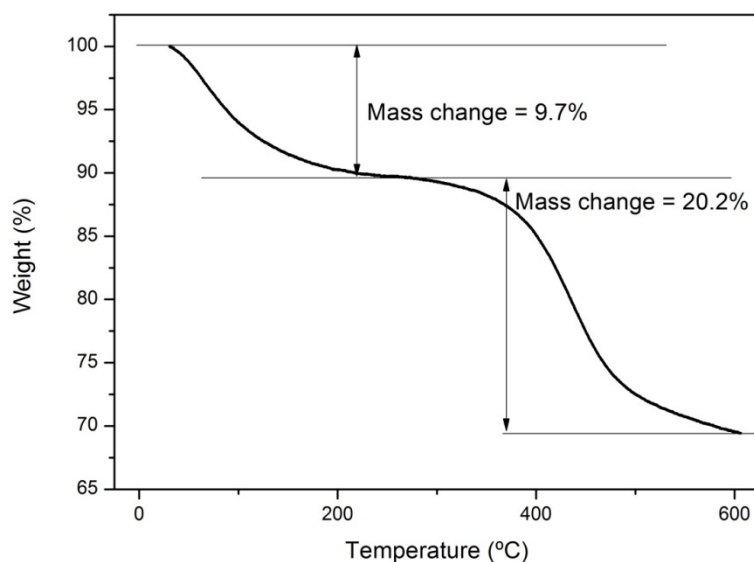
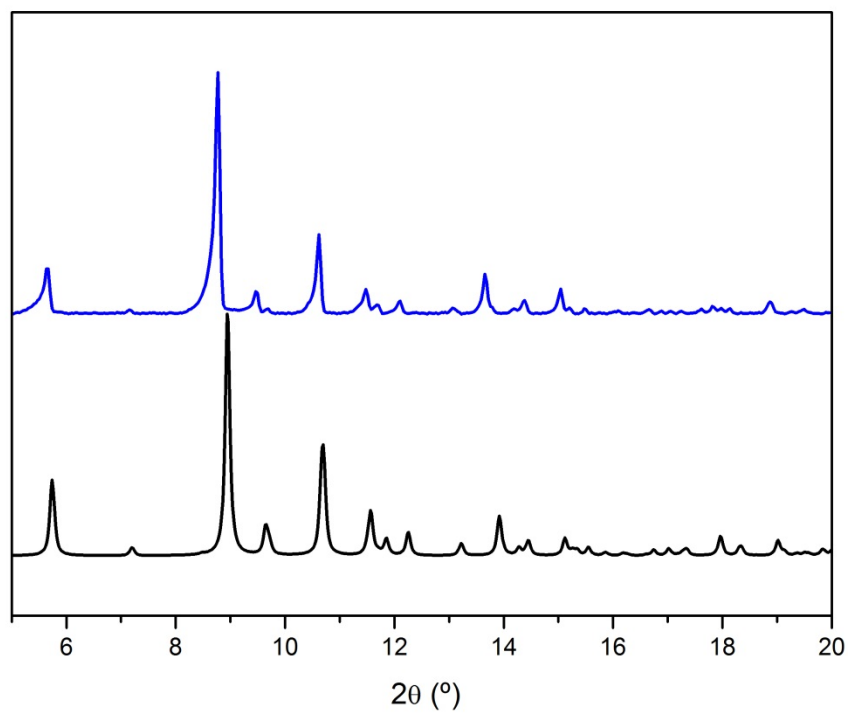


Figure S2. Powder X-ray diffraction patterns

(a) Experimental pattern (blue) for **1-*op*** as compared to the simulated pattern (black)



(b) Experimental pattern (red) for **1-*cp*** as compared to the simulated pattern (black)

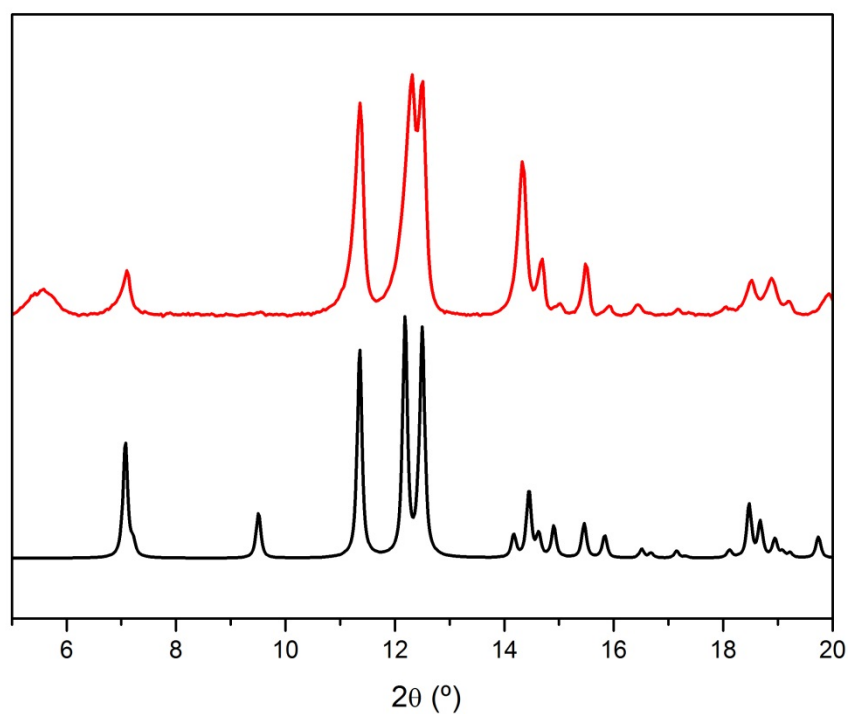


Figure S3. N₂ (77 K, top) and CO₂ (194 K, bottom) adsorption-desorption isotherms for 1-*cp*. The data were collected using an AutosorbIQ (Quantachrome Instruments). Prior to the measurement, samples were activated at 30°C under vacuum.

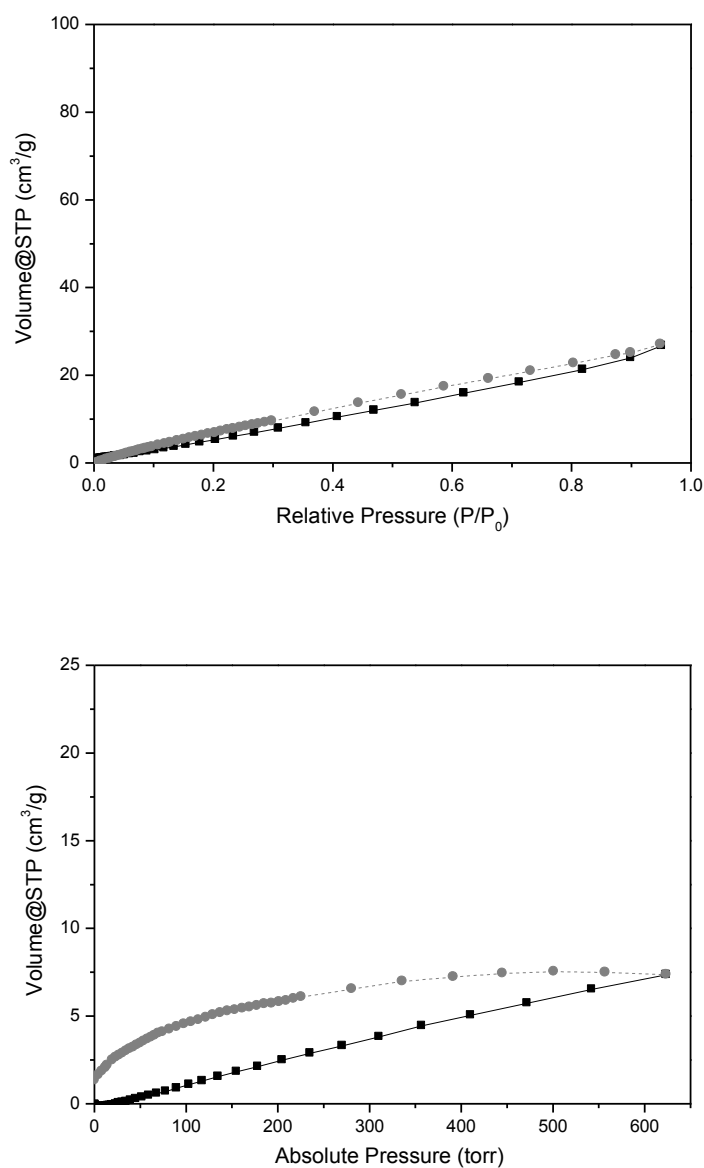
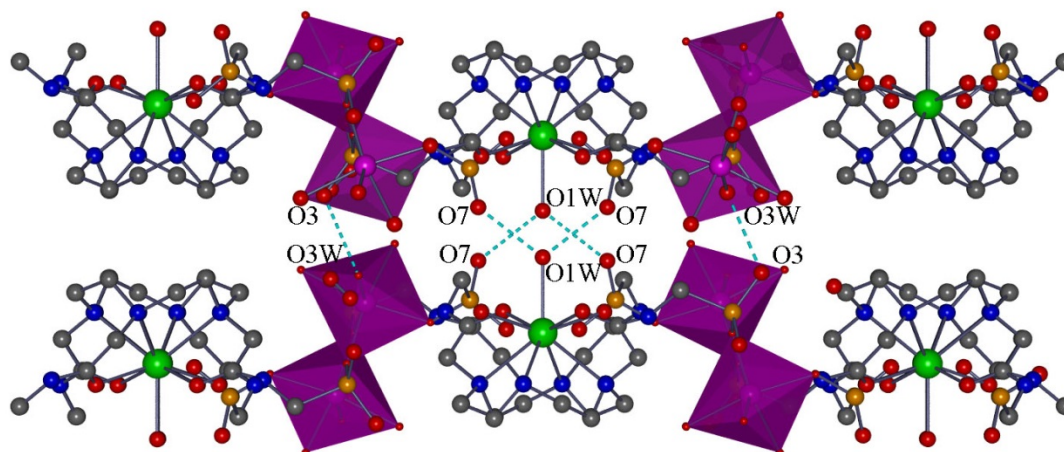


Figure S4. Hydrogen-bonding contacts

- a) In **1-*cp***, direct hydrogen bonds are established between the coordination layers: (O3W \cdots O3, 2.83 Å) and (O1W \cdots O7, 2.65 Å).



- b) In **1-*op***, direct hydrogen bonds are not established between layers. O3W-O3 and O1W-O7 are separated by distances of 15 Å and 8.6 Å, respectively.

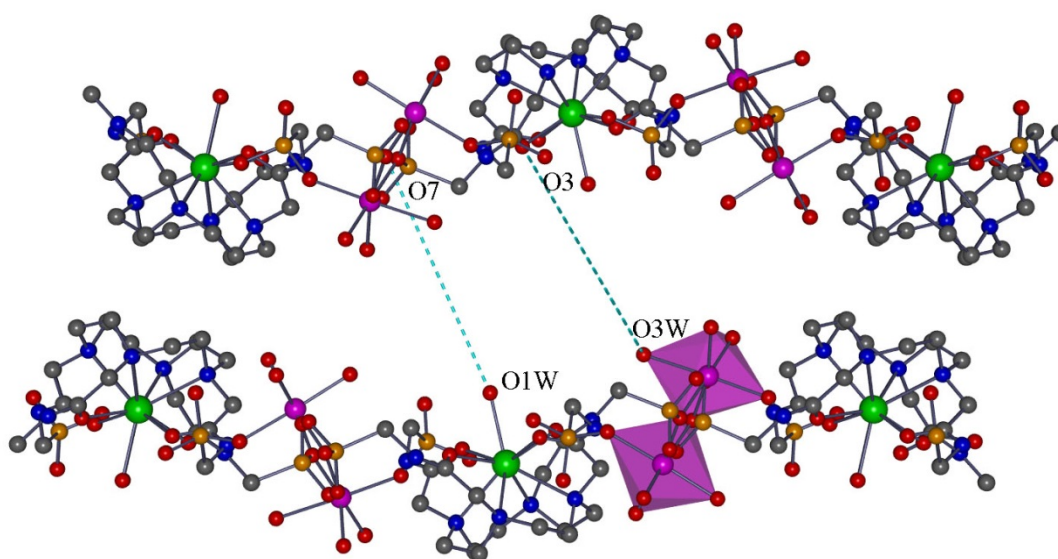


Figure S5. PXRD measurements confirming the reversibility of the SC-SC $1\text{-op} \leftrightarrow 1\text{-cp}$ transformation. PXRD patterns for (a) synthesized 1-op , (b) 1-cp obtained by drying 1-op at room temperature, and (c) 1-op obtained by incubating 1-cp in water overnight.

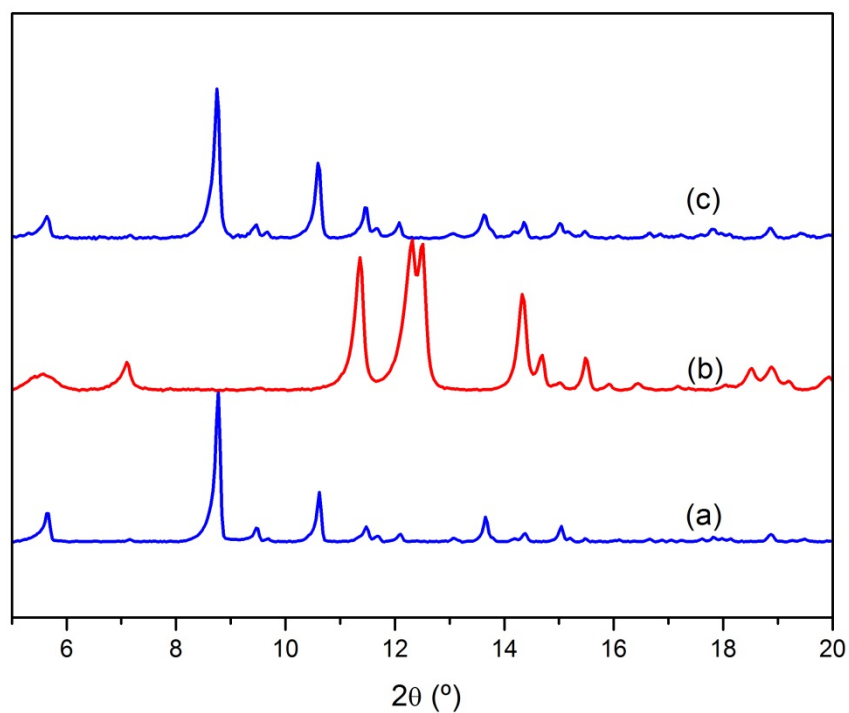


Figure S6. Study on water-sorption recyclability. Four consecutive cycles of water adsorption/desorption were performed to analyse the reversibility of the water sorption process. Before each cycle, the samples were activated by exposing the crystals to an environment at 110 °C for 2 hours.

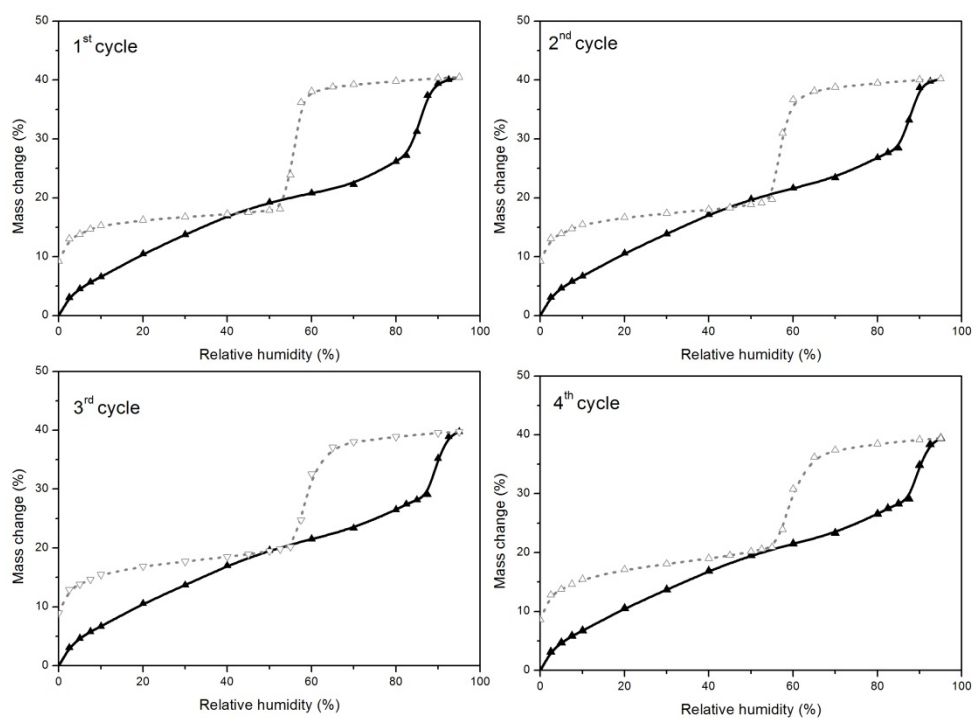
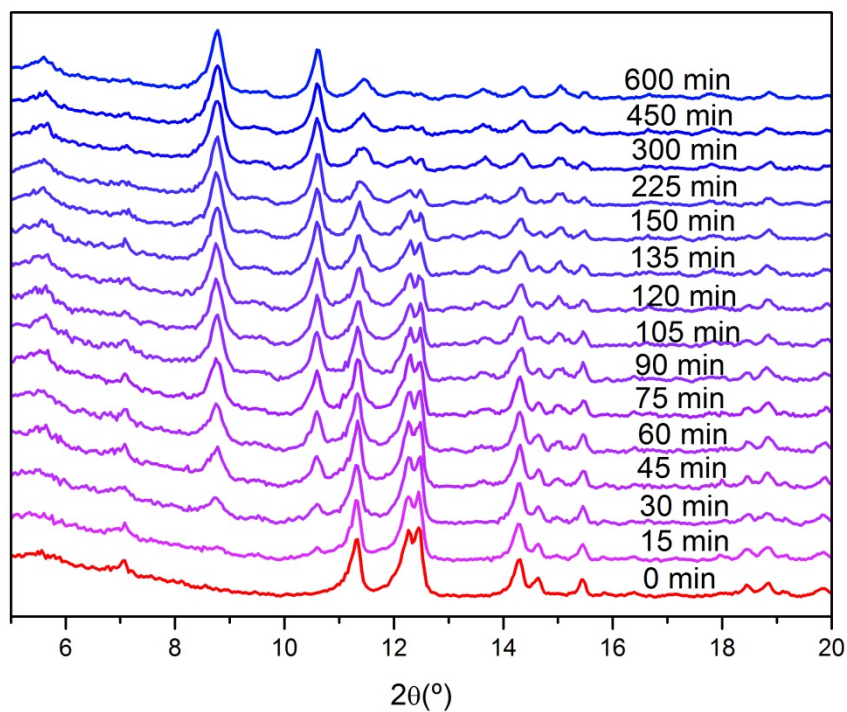


Figure S7. Kinetics study on the transition 1-*cp*→1-*op*. In this study, 1-*cp* crystals were exposed to an environment at 25 °C and a constant RH of 95%. PXRD patterns were collected every 15 minutes.



References

- 1 A. Barge, G. Cravotto, E. Gianolio and F. Fedeli, *Contrast Media Mol. Imaging*, **1**, 184–8.
- 2 J. Juanhuix, F. Gil-Ortiz, G. Cuní, C. Colldelram, J. Nicolás, J. Lidón, E. Boter, C. Ruget, S. Ferrer and J. Benach. *J. Synchr. Rad.*, 2014, **21**, 679–689
- 3 W. Kabsch, *J. Appl. Crystallogr.*, 1993, **26**, 795–800.
- 4 G. M. Sheldrick, *Acta Crystallogr. A.*, 2008, **64**, 112–22.

Publication 3: “pH-Responsive relaxometric behaviour of coordination polymer nanoparticles made of a stable macrocyclic gadolinium chelate”.

■ Supramolecular Chemistry

pH-Responsive Relaxometric Behaviour of Coordination Polymer Nanoparticles Made of a Stable Macrocyclic Gadolinium Chelate

Javier Arriñez-Soriano,^[a] Jorge Albalad,^[a] Arnau Carné-Sánchez,^[a] Célia S. Bonnet,^[b] Félix Busqué,^[c] Julia Lorenzo,^[d] Jordi Juanhuix,^[e] Maxwell W. Terban,^[f] Inhar Imaz,^[a] Éva Tóth,^{*,[b]} and Daniel Maspoch^{*,[a, g]}

Abstract: Lanthanide-containing nanoscale particles have been widely explored for various biomedical purposes, however, they are often prone to metal leaching. Here we have created a new coordination polymer (CP) by applying, for the first time, a stable Gd^{III} chelate as building block in order to prevent any fortuitous release of free lanthanide(III) ion. The use of the Gd-DOTA-4AmP complex as a design element in the CP allows not only for enhanced relaxometric proper-

ties (maximum $r_1 = 16.4 \text{ mM}^{-1} \text{ s}^{-1}$ at 10 MHz), but also for a pH responsiveness ($\Delta r_1 = 108\%$ between pH 4 and 6.5), beyond the values obtained for the low molecular weight Gd-DOTA-4AmP itself. The CP can be miniaturised to the nanoscale to form colloids that are stable in physiological saline solution and in cell culture media and does not show cytotoxicity.

Introduction

Magnetic resonance imaging (MRI) is a powerful diagnostic tool in medical science thanks to its non-invasive character and sub-millimetre spatial resolution. This success would not have been possible without the parallel development of contrast agents (CAs), which are substances capable of enhancing the intrinsic contrast of the technique and improve its anatomical resolution.^[1] From the 1980s, paramagnetic Gd^{III} chelates have stood out for their excellent properties as CAs and their

safe use in comparison to the toxic, free Gd^{III} ions.^[2,3] Some of these Gd^{III} chelates (e.g., Dotarem[®] and Prohance[®]) are currently commercially available and widely used in clinics. However, these substances are still affected by low sensitivity, lack of selectivity and low retention times, meaning that they are only effective in areas of high bioaccumulation. For this reason, there has been much interest in developing strategies to enhance the performance of this class of CAs.^[4] Among the different strategies, a promising one is their nanostructuration, either by using them as building units to make new nanostructured materials or by attaching them onto pre-synthesised nanomaterials.^[5] This approach provides the potential advantages of lowering the rotational tumbling of the Gd^{III} chelates, enhancing the payload of Gd^{III} ions per nanoparticle, and increasing the in vivo circulation time. To date, excellent results have been obtained by structuring Gd^{III} chelates in dendrimers,^[6] viral capsids,^[7] proteins,^[8] mesoporous silica,^[9] polymeric self-assembled nanoparticles,^[10,11] and liposomes.^[12]

Nanoscale coordination polymers (CPs) and metal-organic frameworks (MOFs) are an alternative class of materials to be explored for nanostructuring these CAs. Prior to this work, some advances have been done in developing MRI CAs from CPs/MOFs.^[13–15] These CAs have mainly been synthesised by the assembly of individual Gd^{III} ions and polycarboxylic organic linkers.^[16,17] However, since lanthanide-carboxylate-based CPs/MOFs typically lack stability in water and especially in body fluids, they would degrade when exposed to these media releasing the Gd^{III} ions in their free toxic form. In addition, this lack of stability also prevents detailed relaxometry studies because of the interference of the leached free paramagnetic Gd^{III} ions.

Herein, we present for the first time the incorporation of a Gd^{III} macrocyclic chelate in the structure of a CP by connect-

[a] J. Arriñez-Soriano, J. Albalad, A. Carné-Sánchez, I. Imaz, Prof. D. Maspoch
Catalan Institute of Nanoscience and Nanotechnology (ICN2)
CSIC and The Barcelona Institute of Science and Technology
Campus UAB, Bellaterra, 08193 Barcelona (Spain)
E-mail: daniel.maspoch@icn2.cat

[b] C. S. Bonnet, Prof. É. Tóth
Centre de Biophysique Moléculaire, CNRS, Université d'Orléans
Rue Charles Sadron, 45071, Orléans (France)
E-mail: eva.jakabtoth@cnrs-orleans.fr

[c] Prof. F. Busqué
Departament de Química, Universitat Autònoma de Barcelona
Campus UAB, Bellaterra, 08193 Barcelona (Spain)

[d] Prof. J. Lorenzo
Departament de Bioquímica i Biologia Molecular
Institut de Biotecnologia i Biomedicina (IBB)
Campus UAB, 08193 Bellaterra (Spain)

[e] J. Juanhuix
ALBA Synchrotron, Cerdanyola del Vallès, 08290 Barcelona (Spain)

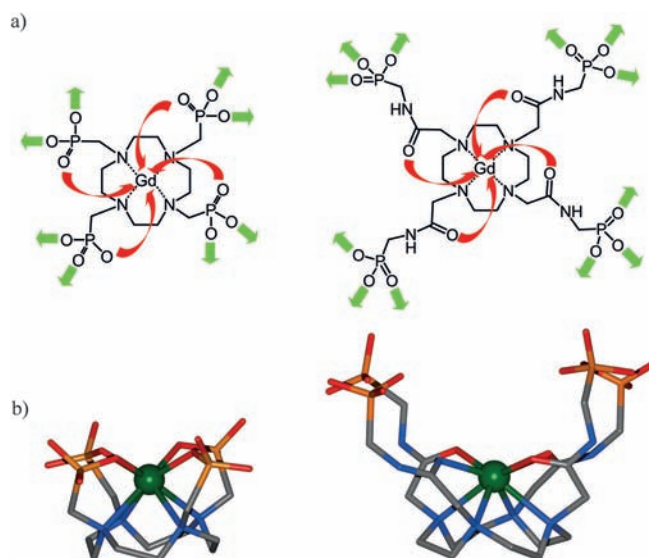
[f] M. W. Terban
Department of Applied Physics and Applied Mathematics
Columbia University, New York (USA)

[g] Prof. D. Maspoch
ICREA, Pg. Lluís Companys 23, 08010 Barcelona (Spain)

Supporting information for this article is available on the WWW under <http://dx.doi.org/10.1002/chem.201602356>.

ing it through Zn^{II} ions. Previous attempts made in our group to build up a CP using a Gd^{III} macrocyclic chelate were focused on using the 1,4,7,10-tetraazacyclododecane-1,4,7,10-tetraethylenephosphonic acid (DOTP).^[18] However, we found that the corresponding Gd-DOTP chelate did not react with most of metal ions (e.g., Zn^{II} , Ni^{II} , Co^{II} , Mn^{II} , Fe^{III} and Mg^{II}), presumably because the four phosphonate groups were coordinating the Gd^{III} ions (Scheme 1).^[19] In fact, the Gd-DOTP chelate reacted only with Cu^{II} ions,^[20] but through a mechanism that involved the replacement of the Gd^{III} by the Cu^{II} inside the DOTP macrocyclic cavity leaving the phosphonate groups free to coordinate to the replaced Gd^{III} ions. In this work, we hypothesize that the introduction of a second functionality in the pendant arms of the macrocyclic ligand applied as linker should ensure the coordination of the Gd^{III} inside the macrocyclic cavity while leaving the phosphonate groups free to coordinate to second metal ions and thus form the CP. For this reason, we have selected 1,4,7,10-tetraazacyclododecane-1,4,7,10-tetraacetamidomethylene phosphonic acid (DOTA-4AmP).^[21] In contrast to DOTP, this macrocyclic ligand has two functionalities (amide and phosphonate groups) in each one of the four pendant arms. The four oxygen atoms of the amide groups along with the four ring nitrogen atoms chelate the Gd^{III} ions inside the macrocyclic cavity, thereby allowing the Gd-DOTA-4AmP to have the four phosphonate groups free to coordinate with other metal ions forming CPs (Scheme 1). Importantly, the resultant CPs should also show more stability under aqueous conditions since phosphonates form stronger bonds with metals than carboxylates do.^[22] Finally, another potential feature to be considered when using this macrocyclic linker is that, since the Gd-DOTA-4AmP chelate has been already proved to be endowed with pH dependent relaxivities,^[21,23] its use could pave the way for the synthesis of nanostructured CPs that, in addition to enhanced CA properties, could behave as a pH-responsive contrast agent.

We demonstrate that bulk crystals of a three-dimensional CP with formula $\text{Zn}_{6.5}[\text{Gd}_3(\text{H-DOTA-4AmP})_2(\text{DOTA-4AmP})(\text{H}_2\text{O})_3] \cdot 18\text{H}_2\text{O}$ (**1**) are formed when the preformed Gd-DOTA-4AmP chelate is diffused slowly with Zn^{II} ions, whereas increasing the rate of this reaction produced amorphous $90(\pm 30)$ nm in diameter CP nanoparticles. Here, Zn^{II} ion was selected as the secondary metal ion for a series of key considerations: 1) its stability constant with macrocyclic ligands^[24,25] is much lower than that of Gd^{III} ^[26,27] and lower than those of other metals (e.g., Fe^{III} ,^[28] Cu^{II} ,^[24,25] etc.), preventing a competition with Gd^{III} to occupy the macrocyclic cavity; 2) its toxicity^[29] is lower than other metals (e.g., Co^{II} ,^[30,31] Cu^{II} ,^[32,33] etc.), avoiding health risks in the case of disassembly of the structure inside the body; and 3) it is a diamagnetic metal, so the performed relaxivity studies can be interpreted only in terms of the nanostructuration of its building block, the Gd-DOTA-4AmP chelate.^[21] Importantly, the colloidal CP nanoparticles we have designed feature a high stability in physiological saline solution and in cell culture media, while they showed an increased r_1 relaxivity of $16 \text{ mM}^{-1} \text{ s}^{-1}$ at 10 MHz (25 °C, pH 7.4) when compared with that of the original Gd-DOTA-4AmP chelate. In addition, they amplify the relaxivity pH response ($\Delta r_1 = 108\%$) that, at inter-



Scheme 1. a) Gd-DOTP (left) and Gd-DOTA-4AmP (right) showing the coordination with Gd^{III} (red arrows) and their potential coordination to a second metal ion (green arrows). b) Three-dimensional conformation of Gd-DOTP (left) and Gd-DOTA-4AmP (right). Colour code: C (grey), N (blue), O (red), P (orange), Gd (green).

mediate fields (20–40 MHz), doubles the one of the Gd-DOTA-4AmP chelate.

Results and Discussion

Synthesis and crystal structure of **1**

The macrocyclic ligand DOTA-4AmP was synthesised adapting a procedure reported in the literature.^[21] This was then used as a linker to create the crystals of **1** following a two-step synthesis.^[34] This synthesis consisted of first combining DOTA-4AmP with Gd^{III} ions to obtain the corresponding metallomacrocyclic complex Gd-DOTA-4AmP showing non-coordinated phosphonic groups. Here, the Gd-DOTA-4AmP was prepared by adding dropwise a solution of gadolinium chloride hexahydrate in water into an aqueous solution of DOTA-4AmP adjusted to pH 10 (using 1 M NaOH) while being stirred at 70 °C. The pH of the mixture was kept at 10 using 1 M NaOH throughout the addition. Then, the mixture was left at 70 °C under stirring for 18 h. Finally, the pH was adjusted to pH 8 by the addition of concentrated HCl. The exact concentration of Gd^{III} ions was determined by ICP-MS, and the final concentration of the GdDOTA-4AmP solution was adjusted to 20 mM by the addition of water. In a second step, an ethanolic solution of zinc acetate was layered onto the aqueous solution of Gd-(DOTA-4AmP). After two weeks, transparent octahedral crystals of **1** suitable for single crystal X-ray diffraction were collected.

Crystal structure of **1** was solved and refined in the tetragonal $P4_2/n$ group (Table S1, in the Supporting Information). The asymmetric unit was found to contain three Gd-DOTA-4AmP units, in which the Gd^{III} ion was confirmed to be chelated inside the macrocyclic cavity. These Gd^{III} ions adopt a capped square antiprismatic geometry coordinated to the four ring ni-

trogen atoms, the four oxygen atoms of the amide functionalities and one water molecule at the capping position (Figure 1a). On the other hand, Zn^{II} ions adopt a tetrahedral geometry coordinated to four O atoms of the phosphonate groups of the macrocyclic Gd-DOTA-4AmP units. In this structure, the three Gd-DOTA-4AmP of the asymmetric unit have differences in their geometry and coordination modes. According to the notation introduced by Harris et al.^[35] (Figure S1a in the Supporting Information), the phosphonate groups of Gd1-DOTA-4AmP and Gd2-DOTA-4AmP show the binding mode [3.111] in one pendant arm and the binding mode [2.110] in the other three arms (Figure 1a and Figure S1b in the Supporting Information). The phosphonate groups of the Gd3-DOTA-4AmP unit adopt the binding mode [3.111] in one arm, [1.100] in another arm, and [2.110] in the two remaining arms (Figure S1b in the Supporting Information).

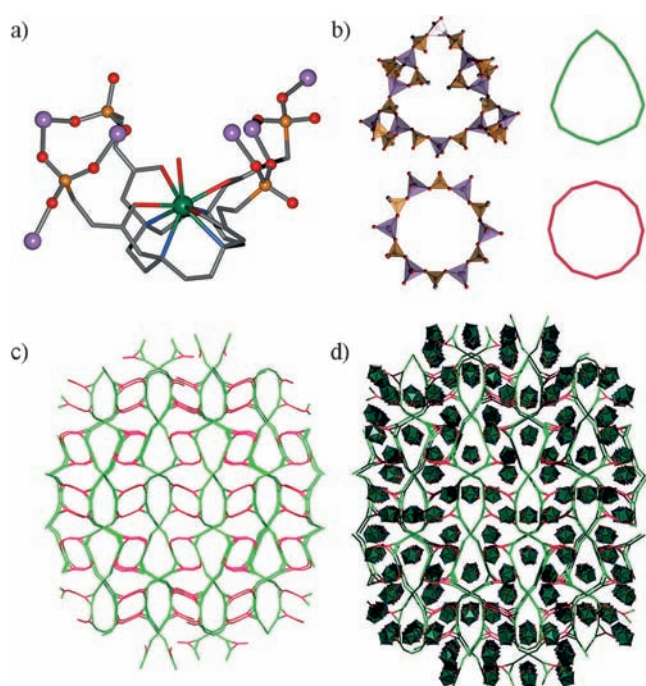


Figure 1. a) Gd-DOTA-4AmP unit found in **1**. b) Egg-shaped 32-membered ring and circular 24-membered ring found in **1**. c) View of the three-dimensional $\text{Zn}^{\text{II}}\text{-PO}_3$ network resulting from the assembly of the two types of rings along *a* axis. d) Identical view of **1** including the Gd-DOTA-4AmP units. Colour code: C (grey), N (blue), O (red), P (orange), Gd (green), Zn (purple).

Overall, it is very interesting to note that the resulting structure can be analysed in terms of an inorganic framework since the $\cdots\text{Zn}^{\text{II}}\text{-PO}_3\text{-Zn}^{\text{II}}\text{-PO}_3\cdots$ linkages extend along the three dimensions. In this framework, the basic units are tri-winged paddle wheel Zn^{II} units, which are formed by two Zn^{II} ions bridged by three phosphonate groups (Figure S2 in the Supporting Information). The assembly of these Zn^{II} units generates two types of $\text{Zn}_x\text{P}_x\text{O}_{2x}$ rings (Figure 1b), one circular 24-membered ring ($\text{Zn}_6\text{P}_6\text{O}_{12}$, 10.9×10.3 Å) and one egg-shaped 32-membered ring ($\text{Zn}_8\text{P}_8\text{O}_{16}$, 16.3×5.6 Å). The size of these rings is relatively larger than other $\text{Zn}_x\text{P}_x\text{O}_{2x}$ rings previously reported.^[36] Figure 1c shows the three-dimensional $\text{Zn}^{\text{II}}\text{-PO}_3$ network resulting

from the assembly of these two types of rings. Importantly, the Gd-DOTA-4AmP units are enclosed in the “hypothetical” channel system of this framework, resulting in a more compact structure (Figure 1d) in which guest water molecules are hydrogen-bonded with the oxygen atoms of the different phosphonate groups.

Synthesis and characterisation of the Zn-Gd-DOTA-4AmP nanoparticles

Any attempt to miniaturize **1** and form colloidal crystalline nanoparticles by means of different techniques (e.g., hydrothermal synthesis, fast mixing of reactants, emulsions, etc.) failed. Here, all trials led to the formation of amorphous Zn-Gd-DOTA-4AmP nanoparticles. In fact, by reproducing exactly the same synthesis, but instead of a slow diffusion of both solutions we rapidly mixed them, amorphous Zn-Gd-DOTA-4AmP nanoparticles were immediately formed. These nanoparticles were then purified by centrifugation and washed several times with ethanol and water, and finally redispersed in water. The resulting white colloid showed a good stability (Figure 2a), and the first reversible flocculation traces only appeared after one day. Field-emission scanning (FESEM) and transmission (TEM) electron microscopy images of the colloid demonstrated the formation of rounded nanoparticles (Figure 2b–d and Figure S4 in the Supporting Information) with a size of $90(\pm 30)$ nm (calculated from TEM images by averaging the diameter of at least 150 particles from images of different areas of the same sample).

To gain more information about the structural–chemical correspondence between Zn-Gd-DOTA-4AmP nanoparticles and

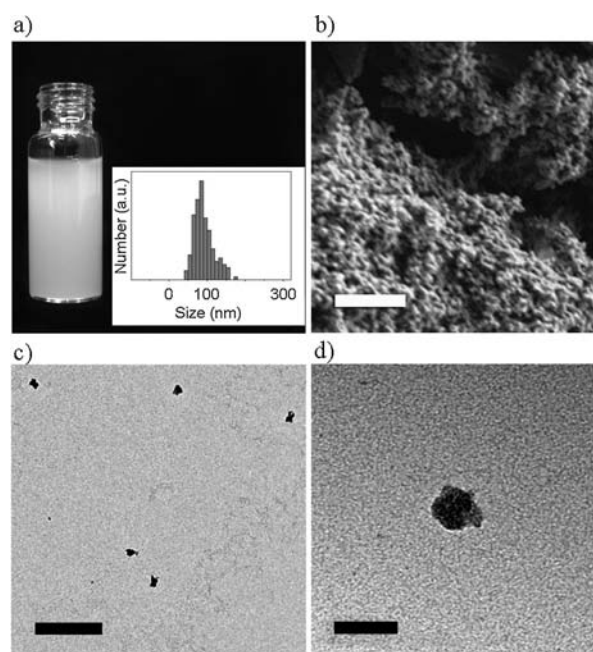


Figure 2. a) Photograph of the colloidal suspension of Zn-Gd-DOTA-4AmP nanoparticles and the size distribution (inset). b) SEM, and c, d) TEM images of Zn-Gd-DOTA-4AmP nanoparticles. Scale bars: b) 1 µm, c) 500 nm, and d) 100 nm.

the crystalline structure of **1**, we compared the results obtained using different characterisation techniques. First, ICP-MS analysis performed on the nanoparticles showed a Zn/Gd proportion of 2.07, which is consistent with that of the crystalline structure (Zn/Gd = 2.16). This result confirms that the proportion between both metal ions is analogous in both materials. Second, elemental analysis performed on the nanoparticles agreed with the formula $\text{Zn}_{6.5}[\text{Gd}_3(\text{H-DOTA-4AmP})_2(\text{DOTA-4AmP})(\text{H}_2\text{O})_3] \cdot 18\text{H}_2\text{O}$ (Table S2 in the Supporting Information). Third, both infrared (FT-IR) spectra (Figure S5 in the Supporting Information) and thermogravimetric analysis (TGA; Figure S6, in the Supporting Information) carried out with the nanoparticles and **1** matched. Here, the IR spectra confirm the coordination of the phosphonate groups of Gd-DOTA-4AmP to the Zn^{II} metal ions, as evidenced by the presence of two strong peaks at 1070 and 992 cm^{-1} .^[37] TGA showed a first weight loss of 9.1% for **1** and 10.6% for Zn-Gd-DOTA-4AmP nanoparticles in the range 35–275 °C, which was attributed to the loss of all guest water molecules (theoretical = 10.5% considering molecular formula of **1**). Decomposition of **1** and Zn-Gd-DOTA-4AmP nanoparticles occurs in the range of 275–740 °C in a single step (Figure S6 in the Supporting Information). Finally, ^{31}P MAS NMR solid-state measurements using Eu^{III} instead of Gd^{III} (**1** and **1-Eu** are isostructural; see Figure S3 and Figure S5 in the Supporting Information)^[38,39] confirmed that the peak shift to higher fields and its widening due to the inclusion of Eu^{III} in the DOTA-4AmP ligand was maintained in the case of Zn-Eu-DOTA-4AmP nanoparticles and in crystals of **1-Eu**. This result confirmed the presence of the lanthanide(III)-DOTA-4AmP unit in both materials (Figure S7 in the Supporting Information).

We also collected X-ray total scattering pair distribution function (PDF) data for both samples. PDF analysis is an excellent technique to access structural information about materials in which disorder or crystallite size broadening effects limit the use of conventional Bragg crystallographic techniques.^[40] Because of this, PDF analysis has recently been applied in CP/MOFs to study conformational changes^[41] or to identify the correct structural features in MOF nanocrystals.^[42] Figure 3 shows the results of these measurements as the PDF, $G(r)$ function of each sample. $G(r)$ provides the real-space probability of finding a pair of atoms at a distance r relative to the average atomic density in an isotropic sample; that is, it is a weighted

histogram of atom-atom distances in a structure. The presence of peaks in the case of **1** at $r > 5\text{ Å}$ (Figure 3a and Figure S8 in the Supporting Information) indicates long-range order and agrees with the Bragg diffraction observed in the PXRD measurements (Figure S3 in the Supporting Information). On the other hand, Zn-Gd-DOTA-4AmP nanoparticles appear diffuse for $r > 5\text{ Å}$, demonstrating the loss of long-range order as a consequence of the miniaturisation process. However, careful analysis (using PDFgui software, Figure S9 in the Supporting Information)^[43] of the peaks at low distances (r) revealed that **1** and Zn-Gd-DOTA-4AmP nanoparticles present a very similar pattern (Figure 3a). Figure 3 correlates the peak positions of $G(r)$ for both materials with the average atomic distances extracted from the crystalline structure of **1**. Their similarity confirms that the main building blocks forming the crystal structure of **1** are also present in the nanoparticles. The loss of the peak at 5.43 Å shows that disordering may develop between the Gd^{III} ion and the Zn^{II} ion distance upon miniaturisation. Additionally, the presence of two broader features beyond 5 Å (Figure S8 in the Supporting Information) show that a small degree of structural coherence remains up to about 10 Å.

To this end, altogether these techniques confirmed that even though the Zn-Gd-DOTA-4AmP nanoparticles do not show a long-range structural ordering, their composition and chemical connectivity at a short range is comparable to those found in the structure of **1**.

Relaxometric measurements

Reliable relaxometry studies of any material need to be done in a stable nanoparticle colloid. Thus, we first studied the stability of these nanoparticles in physiological saline solution (NaCl, 0.9%). For this, as-synthesised Zn-DOTA-4AmP nanoparticles were first centrifuged and redispersed in water three times and finally redispersed in the medium of study to form a stable colloid. Exposure of this sample to saline solution at pH 5.5, 7.4, and 8.5 and at $T = 37.5\text{ °C}$ led to negligible leaching of total Gd^{III} : 1.7, 1.2 and 1.8% in the first 10 min, and 3.6, 1.3 and 1.8% after 10 h, as determined by ICP-MS (Figure S10 in the Supporting Information).

The form in which the small amount of Gd^{III} is released during this degradation was studied by mass spectrometry

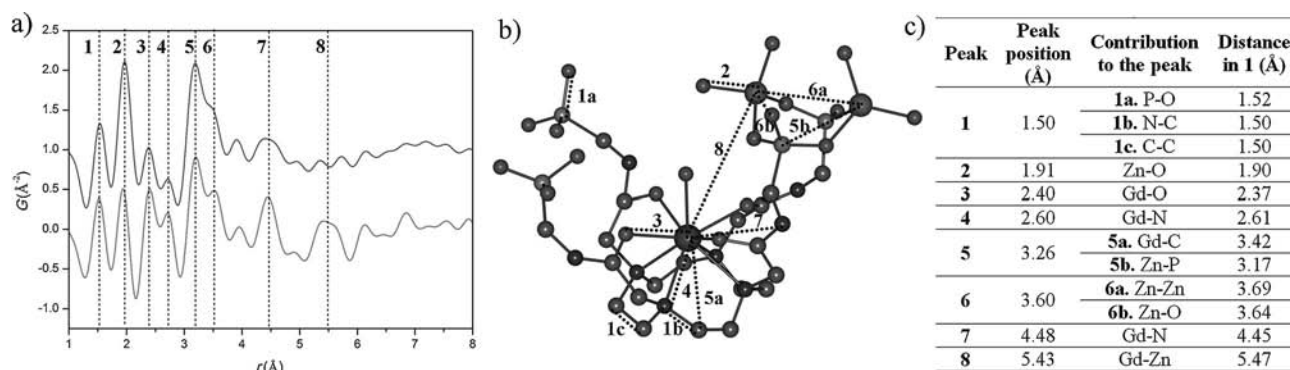


Figure 3. a) Pair distribution function $G(r)$ of **1** (bottom) and Zn-Gd-DOTA-4AmP nanoparticles (top). b) Characteristic distances indicated in the PDF. c) Pair atom correlations contributing to the peaks in the PDF with their corresponding average crystallographic distance in **1**.

(ESI-TOF) and ^1H NMR spectroscopy. To study the former, we analysed the supernatants resulting from the degradation experiments using ESI-TOF. From this analysis, we found species corresponding to $[\text{Gd-4H-DOTA-4AmP}]^- = 930.1$, $[\text{Gd-4H-DOTA-4AmP}]^- = 932.1$, $[\text{Gd-4H-DOTA-4AmP}]^- = 929.1$, $[\text{Gd-4H-DOTA-4AmP}]^- = 928.1$ and $[\text{Gd-4H-DOTA-4AmP}]^- = 927.1$ (Figure S11 in the Supporting Information), confirming that Gd^{III} ions are still chelated when they are leached. In addition, studying the supernatant resulting from incubating a colloid of Zn-Eu-DOTA-4AmP nanoparticles (strongly relaxing Gd^{III} ions were replaced by Eu^{III} ions that allow for NMR observations; vide supra) to acidic D_2O conditions by ^1H NMR further corroborated that lanthanide ions are still chelated during the degradation of the nanoparticles. Indeed, the ^1H NMR spectrum showed the presence of the characteristic eight resonances of equal intensity corresponding to the chelate Eu-DOTA-4AmP (Figure S12 in the Supporting Information), but not those signals corresponding to free DOTA-4AmP. These results are in agreement with cytotoxicity assays conducted with two cell lines, Hep G2 and MCF-7. Both cells showed good viability (75% for Hep G2 and for MCF-7) when incubated for 24 h with Zn-Gd-DOTA-4AmP nanoparticles, even at $[\text{Gd}] = 200 \mu\text{M}$. This lack of cytotoxicity for the nanoparticles is attributed to the eventual release of the Gd-DOTA-4AmP species nontoxic to cells instead of the free Gd^{III} ion. Indeed, identical toxicity experiments performed on the Gd-DOTA-4AmP chelate showed that Gd-DOTA-4AmP exhibits similar viabilities (69% for Hep G2 and 67% for MCF-7). Clearly, the lack of cytotoxicity does not guarantee in vivo nontoxicity. Also, the presence of phosphonate groups often drives to bone accumulation of such agents.^[44] Nevertheless, they still might be helpful in small animal studies without causing acute toxicity, as it has been evidenced by the successful use of Gd-DOTA-4AmP for pH-mapping of mouse kidney^[45] or rat glioma.^[46]

Relaxometry properties were investigated by ^1H nuclear magnetic relaxation dispersion (NMRD) profiles in the frequency range $10 \text{ kHz} \leq \nu \leq 400 \text{ MHz}$ using a colloidal suspension of the Zn-Gd-DOTA-4AmP nanoparticles in saline solution. The suspension was stable throughout the measurement without addition of surfactants or thickeners that can interfere. The relaxivity r_1 profiles as a function of the magnetic field at pH 7.4 at 25°C and 50°C show an increase at intermediate magnetic fields, reaching a maximum of r_1 at 10 MHz and 25°C ($r_1 = 16 \text{ mM}^{-1} \text{ s}^{-1}$; Figure 4). This is characteristic of slowly rotating species and enables to reach more than two times higher relaxivities than that of the discrete Gd-DOTA-4AmP complex at the same field and temperature ($r_1 = 7.4 \text{ mM}^{-1} \text{ s}^{-1}$). Figure 4 also shows that the relaxivity slightly decreases with temperature, conversely to what was observed for the previously reported CAMOF-1,^[18] where mean proton exchange was the limiting factor. The temperature-dependence of the relaxivities of Zn-Gd-DOTA-4AmP nanoparticles indicates that the relaxivity is not limited by proton exchange.

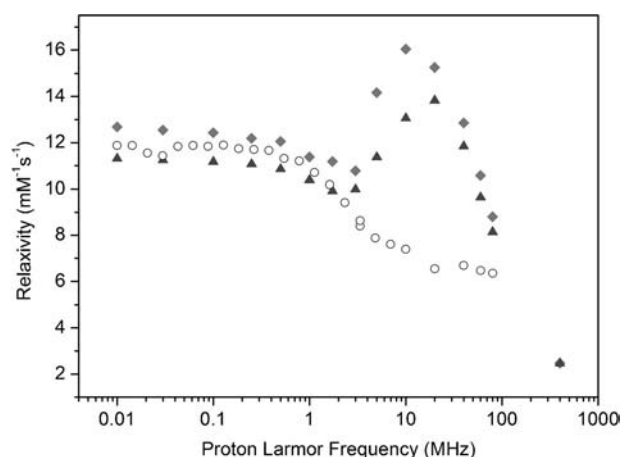


Figure 4. NMRD profiles of a colloidal suspension of Zn-Gd-DOTA-4AmP nanoparticles in saline solution (NaCl 0.9%) at pH 7.4 at 25°C (light grey diamond) and at 50°C (dark grey triangle) and Gd-DOTA-4AmP complex in saline solution (NaCl 0.9%) at pH 7.4 at 25°C (empty circle).

pH-dependent relaxometric study

The pH dependence of r_1 of Zn-Gd-DOTA-4AmP nanoparticles was studied at 20 MHz in the pH range between 4 and 10 (Figure 5a). This pH range was selected to avoid leaching of either Gd-DOTA-4AmP or Zn^{II} ions. Indeed, the release is less than 3.0% in weight at $4 < \text{pH} < 10$, however a burst release of the complex was observed at $\text{pH} \leq 4$, indicating a fast degradation of the nanoparticles below pH 4 (Figure 5b). In consequence, relaxometric data were collected in the pH range 4–10 by starting with a colloidal suspension of these nanoparticles in saline solution at pH 7.4 and with a Gd^{III} concentration of 5.4 mM. The pH was stepwise lowered to 4 and then increased to 10 by the addition of small quantities of hydrochloric acid and sodium hydroxide, respectively, after which the pH and T_1 were immediately measured. The concentration of Gd^{III} was corrected after each addition of concentrated acid/base to calculate r_1 . Identical r_1 values were obtained when starting the measurements from a colloidal suspension with a pH initially set at 4 and raising it with sodium hydroxide, confirming the reversibility of the pH dependence of Zn-Gd-DOTA-4AmP nanoparticles. The plotted data have the shape of an asymmetric inverted parabola (Figure 5a). The r_1 values steeply increase from pH 4 ($r_1 = 7.9 \text{ mM}^{-1} \text{ s}^{-1}$) to pH 6 (maximum $r_1 = 16.4 \text{ mM}^{-1} \text{ s}^{-1}$), then steadily decrease reaching a value of $r_1 = 8 \text{ mM}^{-1} \text{ s}^{-1}$ at pH 10. For direct comparison, we also repeated the pH dependence study for the Gd-DOTA-4AmP complex.^[21] The r_1 values increase from pH 4 ($r_1 = 4.8 \text{ mM}^{-1} \text{ s}^{-1}$) up to pH 6 (maximum $r_1 = 5.8 \text{ mM}^{-1} \text{ s}^{-1}$), followed by a decrease to reach a minimum at pH 9 ($r_1 = 3.9 \text{ mM}^{-1} \text{ s}^{-1}$). As Figure 5a evidences, the use of the nanoparticle amplifies the pH-dependent relaxivity changes at this frequency. Indeed, for Zn-Gd-DOTA-4AmP nanoparticles, the difference between the maximum ($r_1 = 16.4 \text{ mM}^{-1} \text{ s}^{-1}$; pH 6) and the minimum ($7.9 \text{ mM}^{-1} \text{ s}^{-1}$; pH 4) relaxivity values corresponds to a factor of two ($\Delta r_1 = 108\%$), while for Gd-DOTA-4AmP, the difference between the maximum ($r_1 = 5.8 \text{ mM}^{-1} \text{ s}^{-1}$) and the minimum ($r_1 = 3.9 \text{ mM}^{-1} \text{ s}^{-1}$) is a factor of 1.5. This is nevertheless a slightly smaller amplifica-

tion than what has been observed for Gd-DOTA-4AmP conjugated to a G5-PAMAM dendrimer ($\Delta r_1 = -122\%$ between pH 6 and 9).^[47] Evidently, the amplification of the pH response by nanoscale systems such as our CP or the G5-PAMAM dendrimer operates only at intermediate fields, where the effect of slow rotation on proton relaxivity is observable.

Sherry and co-workers showed with potentiometric and relaxometric studies that the phosphonates of the pendant arms were responsible of the unique pH-responsive behaviour of Gd-DOTA-4AmP.^[21] They concluded that the protons of the Gd^{III}-bound water molecule undergo a prototropic exchange with the bulk solvent which is catalysed by the phosphonate

groups located close enough to the coordinated water. In particular, they could derive that the diprotonated complex has the maximal effect on the measured relaxivity and was responsible for the relaxivity peak at pH 6.3. They have also shown that converting these phosphonate groups to phosphonate esters eliminates the pH responsive behaviour.^[48]

It is remarkable that the pH dependence profile of the relaxivity is preserved when Gd-DOTA-4AmP is part of a coordination polymer framework, despite the fact that most of the phosphonate oxygens are involved in coordination bonds to the Zn^{II} cations. We have proved that the coordination polymer is not destroyed in the pH range 4–10 (see above). We can thus hypothesize that three possible mechanisms could account for the pH responsiveness of the nanoparticles, which can take place simultaneously. First, the pH dependence in the nanoparticles can be attributed to non-coordinating phosphonate groups on the surface of the nanoparticles. Second, intrinsic defects of any framework could also assure the presence of a number of non-coordinating phosphonate groups also in the interior of the nanoparticles. Finally, it has been described that coordinated oxygen atoms of the phosphonate groups can also accept protons,^[49] making possible their protonation and the catalysis of the prototropic water exchange on the Gd^{III} centres as formulated by Sherry.

By potentiometry, Sherry et al. determined four protonation constants for the monomer Gd-DOTA-4AmP complex, which are $\log K_{H1-4} = 7.20, 6.47, 6.03$ and 5.36 , respectively.^[21] In order to gain some information about the protonation scheme of the Zn-Gd-DOTA-4AmP nanoparticles, we have titrated a solution of the nanoparticles (5.4 mM in Gd^{III}) by adding increasing amounts of 1 M NaOH. The titration curve shows that protonation occurs in a larger range (pH 4 to 10, Figure 5c) than what was observed for the monomer, which is not surprising as many protonation sites are in close proximity, and the Zn-Gd-DOTA-4AmP nanoparticle is expected to behave as a polyelectrolyte. This implies that the protonation of one site strongly influences the protonation of neighbouring sites. As a result, the protonation steps extend on a larger pH range, instead of being characterised by discrete protonation constants. This site-binding model explains the characteristic broadening of the titration curve of polyelectrolytes with respect to the one of a corresponding monoprotic acid or base.^[50]

Although it is impossible to extract protonation constants from the titration curve, it unambiguously indicates that in average, there are several protonation sites per Gd-DOTA-4AmP unit in the nanoparticles. It implies that protonation occurs also within the interior of the framework. This is an interesting finding since it shows that these nanoparticles can accept a large quantity of protons without the destruction of the coordination polymeric network. We note that metal coordination of protonated phosphonate oxygens has been previously reported.^[49] Based on these results, we can conclude that the possibility to protonate the phosphonate oxygens even within the nanoparticles explains why the pH-dependent relaxivities are retained.

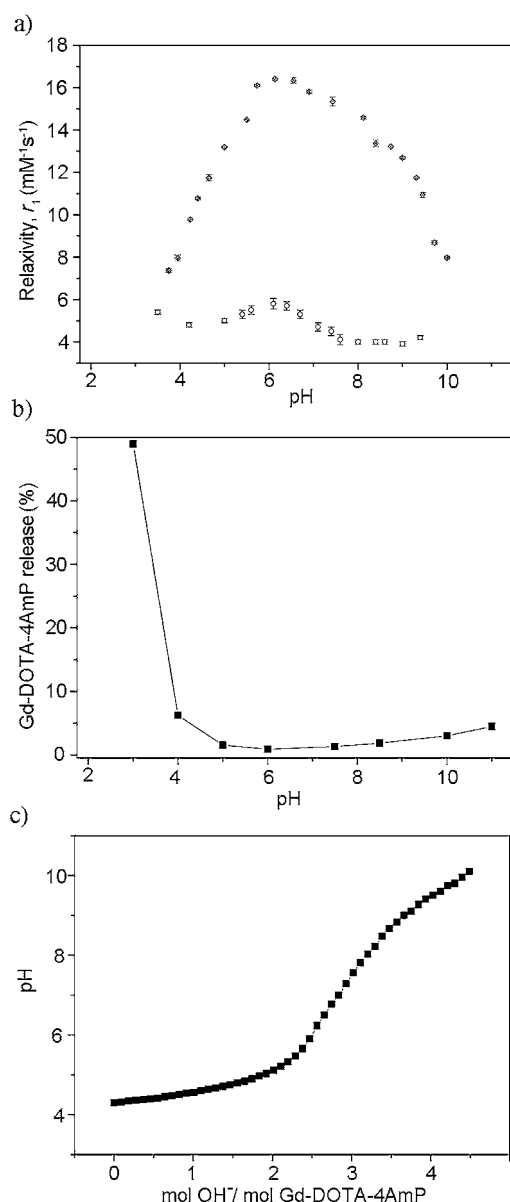


Figure 5. a) pH dependence of the relaxivity of a colloidal suspension of Zn-Gd-DOTA-4AmP nanoparticles (filled diamond) and Gd-DOTA-4AmP complex (empty circle) measured at 20 MHz (25 °C). b) Gd-DOTA-4AmP release (wt. %) for Zn-Gd-DOTA-4AmP nanoparticles at the pH range of study. c) Potentiometric titration of a colloidal suspension of Zn-Gd-DOTA-4AmP nanoparticles.

Conclusions

We have created a bimetallic Zn^{II}- and Gd^{III}-based coordination polymer (CP) by using, for the first time, a macrocyclic chelate (Gd-DOTA-4AmP) as building block. This design element warrants stable complexation of the lanthanide ion, even in case of partial disassembly of the polymeric network. This coordination polymer can be miniaturised to the nanometer scale (90(±30) nm) to form stable colloids, preserving its structural coherence up to about 10 Å. The colloid is stable in saline solution at physiological pH, in cell culture media; and it does not show cytotoxicity. The Zn-Gd-DOTA-4AmP nanoparticle has a maximum r_1 relaxivity of 16.4 mm^{−1}s^{−1} at pH 6 and 10 MHz. It retains the pH-dependence profile of the monomer in the pH range 4–10, with a double relaxivity response to pH change ($\Delta r_1 = 108\%$) as compared to the monomer Gd-DOTA-4AmP ($\Delta r_1 = 50\%$). Furthermore, we have demonstrated by potentiometric measurements that the Zn-Gd-DOTA-4AmP CP nanoparticles behave as a polyelectrolyte, accepting several protons per Gd-DOTA-4AmP unit without destroying the CP framework.

This proof-of-concept study shows that Gd^{III}-chelates can serve as building blocks to create stable MOFs/CP. Such systems can be explored to enhance the relaxivity or pH dependence properties in view of their potential use in MRI diagnostics.

Experimental Section

General considerations

All chemical reagents and solvents were purchased from commercial sources and used as received without further purification. NMR spectra were recorded on a Bruker Avance DPX-250 spectrometer and Bruker AMX-400 Wide Bore for liquid and solid-state samples, respectively. Mass spectra were acquired on a micrOTOF-QII ESI-MS instrument. Purity of all bulk material batches was confirmed by X-ray powder diffraction (XRPD) patterns collected on an X'Pert PRO MPD analytical diffractometer (Panalytical) at 45 kV, 40 mA by using Cu_{Kα} radiation ($\lambda = 1.5419$ Å), and compared with single-crystal simulated patterns. Thermogravimetric analyses were performed under nitrogen flow using a STA 449 F1 Jupiter-Simultaneous TGA-DSC from NETZSCH with a heat rate of 5 °C min^{−1}. IR spectra were recorded in transmission mode on a Bruker Tensor 27FTIR equipped with a Golden Gate diamond ATR cell. Elemental analysis measurements were performed on a Flash EA 2000 CHNS, Thermo Fisher Scientific analyser. Inorganic elemental analysis measurements were performed on an ICP-MS 7500ce, Agilent Technologies. Scanning electron microscope images were acquired on a FEI Quanta 650F working at an accelerating voltage of 2 kV and a beam current of 50 pA. Transmission electron microscope images were acquired on a JEOL JEM-1400 working at an accelerating voltage of 120 kV.

Synthesis of Gd-DOTA-4AmP and Eu-DOTA-4AmP

First, a solution of DOTA-4AmP (354 mg, 396 μmol) in water (8 mL) was prepared and the pH was adjusted to 10 by cautious addition of 1 M NaOH. Then, a solution of gadolinium chloride hexahydrate was prepared (147 mg, 396 μmol) in water (2 mL). Gadolinium

chloride solution was added dropwise into the stirring DOTA-4AmP solution which was warmed at 70 °C. The pH of the stirring mixture was kept at 10 by addition of concentrated NaOH (1 M) during the addition process. Note that, after each addition of gadolinium chloride into the DOTA-4AmP solution, a white precipitate appears at first, but it is dissolved after some minutes, indicating that Gd-DOTA-4AmP is being formed. The absence of free Gd^{III} in the stirring mixture was also monitored by xylenol orange test.^[51] The addition of gadolinium chloride was stopped after the xylenol test showed the persistent presence of free gadolinium. Then, the mixture was left at 70 °C under stirring for 18 h. Finally, the pH was adjusted to pH 8 by the addition of concentrate HCl. The exact concentration of Gd^{III} ions was determined by ICP-MS, and the final concentration of the Gd-DOTA-4AmP solution was adjusted to 20 mM by the addition of water. The same procedure was followed for the synthesis of Eu-DOTA-4AmP but using europium chloride hexahydrate instead of gadolinium chloride.

Synthesis of 1 and 1-Eu

A solution of zinc acetate dihydrate in ethanol (4 mL, 11.3 mM) was carefully layered onto a Gd-DOTA-4AmP aqueous solution (4 mL, 5.2 mM) in a 9 mL glass vial. This glass vial containing the liquid diffusion was capped and left undisturbed at room temperature for two weeks. After that, transparent octahedral crystals of **1** appeared on the walls and at the bottom of the vial. To recover crystals of **1**, the liquid phase was exchanged by fresh EtOH/water mixture (50:50) and the vials were sonicated in an ultrasounds bath at 0 °C to detach the crystals from the glass walls. The process was repeated two more times, and the crystals were finally kept under pure water. The same procedure was followed for the synthesis of 1-Eu but using an aqueous solution of Eu-DOTA-4AmP instead of Gd-DOTA-4AmP.

Synthesis of Zn-Gd-DOTA-4AmP and Zn-Eu-DOTA-4AmP nanoparticles

A solution of zinc acetate dihydrate in ethanol (4 mL, 11.3 mM) was rapidly added onto a Gd-DOTA-4AmP aqueous solution (4 mL, 5.2 mM) under stirring (900 rpm) at room temperature. Immediately after this addition, the appearance of a white solid was observed, and the mixture was left stirring for 12 h. To recover Zn-Gd-DOTA-4AmP nanoparticles, the solid was precipitated by centrifugation (44000 RCF, 10 min) and washed four times with EtOH/water mixture (50:50) and finally redispersed in pure water. The same procedure was followed for the synthesis of Zn-Eu-DOTA-4AmP nanoparticles but using an aqueous solution of Eu-DOTA-4AmP instead of Gd-DOTA-4AmP.

X-ray crystallography

Crystallographic data for **1** were collected at 100 K at XALOC beamline^[52] at ALBA synchrotron ($\lambda = 0.88557$ Å). These data were indexed, integrated and scaled using XDS program.^[53] Absorption correction was not applied. The structure was solved by direct methods^[54] and subsequently refined by correction of F^2 against all reflections using SHELXS2013 and SHELXL2013 within the WinGX package.^[55] All non-hydrogen atoms were refined with anisotropic thermal parameters by full-matrix least-squares calculations on F^2 using SHELXL2013. Hydrogen atoms were inserted at calculated positions and constrained with isotropic thermal parameters. The hydrogen of the crystal lattice water molecules present in the structure were not located on Fourier map, but were added in the empirical formula to allow accurate determination of density and

absorption coefficient. CCDC 1471203 contains the supplementary crystallographic data for this paper. These data are provided free of charge by The Cambridge Crystallographic Data Centre.

Total X-ray scattering PDF measurements

Total scattering X-ray PDF experiments were performed at the National Synchrotron Light Source II (NSLS-II) on beamline 28-ID at Brookhaven National Laboratory. The miniaturised sample (shown) was measured using the rapid acquisition pair distribution function (RaPDF) technique^[56] with an X-ray energy of 65.7107 keV ($= 0.188682 \text{ \AA}$). A Perkin-Elmer 2D at panel detector (2048×2048 pixels and $200 \times 200 \text{ \mu m}$ pixel size) was mounted orthogonal to the beam path with a sample-to-detector distances of 300.785 mm. The raw 2D data were azimuthally integrated and converted to 1D intensity versus the magnitude of the scattering vector Q ($Q = 2\pi \sin(\theta)/\lambda$) using xPDFsuite^[57] then corrected, normalised and Fourier transformed to obtain the PDF, $G(r)$, using PDFgetX3.^[58] A Ni standard was measured to calibrate the experimental setup with xPDF suite and fit with an FCC Ni model in PDFgui^[43] to determine the instrumental resolution effects on the PDF, $Q_{\text{damp}} = 0.033039 \text{ \AA}^{-1}$ and $Q_{\text{broad}} = 0.013760 \text{ \AA}^{-1}$. Both miniaturised and crystalline (shown) samples were measured on a subsequent date with an X-ray energy of 67.3910 keV ($= 0.183977 \text{ \AA}$) and a detector distance of 207.6170 mm, giving instrumental resolution effects $Q_{\text{damp}} = 0.043902 \text{ \AA}^{-1}$ and $Q_{\text{broad}} = 0.017594 \text{ \AA}^{-1}$. The separate measurements of the miniaturised samples were consistent, but with better statistics collected on the former.

Cytotoxicity assays

Human breast-cancer cells (MCF-7) and human hepatocellular carcinoma cells (HepG2) were obtained from the American Type Culture Collection (ATCC, Manassas, VA, USA). The cells were routinely cultured with DMEM F12 or DMEM (Invitrogen) containing 10% (v/v) heat-inactivated foetal bovine serum (FBS), at 37°C in a humidified 5% CO_2 atmosphere. Growth inhibitory effects on cell lines were measured by the XTT (sodium 2,3-bis(2-methoxy-4-nitro-5-sulphophenyl)-5-[(phenylamino)-carbonyl]-2H-tetrazolium inner salt) assay. Cells were plated at a density of 4×10^3 cells per well in 100 \mu L of culture medium in 96-well plates, and cultured. After 24 h incubation cells were treated with different concentrations of Gd-DOTA-4AmP and Zn-Gd-DOTA-4AmP nanoparticles during 24 h and then, 20 \mu L of XTT was added. After 2 h, the colour formed was quantified with a spectrophotometric plate reader at 490 nm by a microplate reader (Victor3). The percentage of cell viability was calculated by dividing the average absorbance of the cells treated with the complex by that of the control. Each sample was tested in quadruplicate.

Relaxometry measurements

Proton NMRD profiles were recorded on a Stelar SMARTracer fast field cycling relaxometer (0.01–10 MHz) and a Bruker WP80 NMR electromagnet adapted to variable field measurements (20–80 MHz) and controlled by a SMARTracer PC NMR console. The temperature was monitored by a VTC91 temperature control unit and maintained by a gas flow. The temperature was determined by previous calibration with a Pt resistance temperature probe. The longitudinal relaxation rates ($1/T_1$) were determined in physiological saline solution (NaCl, 0.9%) for colloidal suspensions of Zn-Gd-DOTA-4AmP nanoparticles ($[\text{Gd}] = 5.0\text{--}5.4 \text{ mM}$).

Acknowledgements

This work was supported by the MINECO-Spain through projects PN MAT2012-30994. I.I. and J.A.S. thank the MINECO for a RyC contract and a predoctoral FPU grant, respectively. J.A. is grateful to the Generalitat de Catalunya for a predoctoral FI grant. ICN2 is supported by the Spanish MINECO through the Severo Ochoa Centers of Excellence Program, under Grant SEV-2013-0295. M.T. acknowledges support from the US Department of Energy NEUP #DE-NE 0000746 and S. J. L. Billinge for helpful discussion. Use of the National Synchrotron Light Source II, Brookhaven National Laboratory, was supported by the US Department of Energy, Office of Science, Office of Basic Energy Sciences, under Contract No. DE-SC0012704. E.T. and C.S.B. acknowledge financial support of the Ligue contre le Cancer (France).

Keywords: chelates • contrast agents • coordination polymers • gadolinium • relaxometry

- [1] A. S. Merbach, L. Helm, É. Tóth, *The Chemistry of Contrast Agents in Medical Magnetic Resonance Imaging*, Wiley, 2013.
- [2] P. Caravan, J. J. Ellison, T. J. McMurry, R. B. Lauffer, *Chem. Rev.* **1999**, *99*, 2293–2352.
- [3] S. Aime, M. Botta, E. Terreno, *Adv. Inorg. Chem.* **2005**, *57*, 173–237.
- [4] E. Terreno, D. D. Castelli, A. Viale, S. Aime, *Chem. Rev.* **2010**, *110*, 3019–3042.
- [5] M. Botta, L. Tei, *Eur. J. Inorg. Chem.* **2012**, 1945–1960.
- [6] J. Zhu, Z. Xiong, M. Shen, X. Shi, *RSC Adv.* **2015**, *5*, 30286–30296.
- [7] J. Min, H. Jung, H.-H. Shin, G. Cho, H. Cho, S. Kang, *Biomacromolecules* **2013**, *14*, 2332–2339.
- [8] M. B. Winter, P. J. Klemm, C. M. Phillips-Piro, K. N. Raymond, M. A. Marletta, *Inorg. Chem.* **2013**, *52*, 2277–2279.
- [9] G. Zhang, J. Gao, J. Qian, L. Zhang, K. Zheng, K. Zhong, D. Cai, X. Zhang, Z. Wu, *ACS Appl. Mater. Interfaces* **2015**, *7*, 14192–14200.
- [10] C. Diaferia, E. Gianolio, P. Palladino, F. Arena, C. Boffa, G. Morelli, A. Accardo, *Adv. Funct. Mater.* **2015**, *25*, 7003–7016.
- [11] L. M. Randolph, C. L. M. LeGuyader, M. E. Hahn, C. M. Andolina, J. P. Patterson, R. F. Mattrey, J. E. Millstone, M. Botta, M. Scadeng, N. C. Gianneschi, *Chem. Sci.* **2016**, *7*, 4230–4236.
- [12] K. Zhang, M. Liu, X. Tong, N. Sun, L. Zhou, Y. Cao, J. Wang, H. Zhang, R. Pei, *Biomacromolecules* **2015**, *16*, 2618–2623.
- [13] J. Della Rocca, W. Lin, *Eur. J. Inorg. Chem.* **2010**, 3725–3734.
- [14] J. Della Rocca, D. Liu, W. Lin, *Acc. Chem. Res.* **2011**, *44*, 957–968.
- [15] P. Horcajada, T. Chalati, C. Serre, B. Gillet, C. Sebrie, T. Baati, J. F. Eubank, D. Heurtaux, P. Clayette, C. Kreuz, *Nat. Mater.* **2010**, *9*, 172–178.
- [16] W. J. Rieter, K. M. L. Taylor, H. An, W. Lin, W. Lin, *J. Am. Chem. Soc.* **2006**, *128*, 9024–9025.
- [17] K. M. L. Taylor, A. Jin, W. Lin, *Angew. Chem. Int. Ed.* **2008**, *47*, 7722–7725; *Angew. Chem.* **2008**, *120*, 7836–7839.
- [18] A. Carné-Sánchez, C. S. Bonnet, I. Imaz, J. Lorenzo, E. Tóth, D. Maspoch, *J. Am. Chem. Soc.* **2013**, *135*, 17711–17714.
- [19] F. Avecilla, J. A. Peters, C. F. G. C. Geraldes, *Eur. J. Inorg. Chem.* **2003**, 4179–4186.
- [20] C. F. G. C. Geraldes, M. P. M. Marques, B. de Castro, E. Pereira, *Eur. J. Inorg. Chem.* **2000**, 559–565.
- [21] F. K. Kalmán, M. Woods, P. Caravan, P. Jurek, M. Spiller, G. Tircsó, R. Kiraly, E. Brücher, A. D. Sherry, *Inorg. Chem.* **2007**, *46*, 5260–5270.
- [22] K. J. Gagnon, H. P. Perry, A. Clearfield, *Chem. Rev.* **2012**, *112*, 1034–1054.
- [23] G. V. Martinez, X. Zhang, M. L. García-Martín, D. L. Morse, M. Woods, A. D. Sherry, R. J. Gillies, *NMR Biomed.* **2011**, *24*, 1380–1391.
- [24] E. T. Clarke, A. E. Martell, *Inorg. Chim. Acta* **1991**, *190*, 27–36.
- [25] S. Chaves, R. Delgado, J. J. R. F. Da Silva, *Talanta* **1992**, *39*, 249–254.
- [26] X. Wang, T. Jin, V. Comblin, A. Lopez-Mut, E. Merciny, J. F. Desreux, *Inorg. Chem.* **1992**, *31*, 1095–1099.

- [27] K. Kumar, C. A. Chang, L. C. Francesconi, D. D. Dischino, M. F. Malley, J. Z. Gougoutas, M. F. Tweedle, *Inorg. Chem.* **1994**, *33*, 3567–3575.
- [28] E. T. Clarke, A. E. Martell, *Inorg. Chim. Acta* **1991**, *190*, 37–46.
- [29] G. J. Fosmire, *Am. J. Clin. Nutr.* **1990**, *51*, 225–227.
- [30] J. R. Curtis, G. C. Goode, J. Herrington, L. E. Urdaneta, *Clin. Nephrol.* **1976**, *5*, 61–65.
- [31] C. L. Evans, *Br. J. Pharmacol. Chemother.* **1964**, *23*, 455–475.
- [32] R. P. Singh, S. Kumar, R. Nada, R. Prasad, *Mol. Cell. Biochem.* **2006**, *282*, 13–21.
- [33] L. Gaetke, *Toxicology* **2003**, *189*, 147–163.
- [34] J. Ariñez-Soriano, J. Albalad, J. Pérez-Carvajal, I. Imaz, F. Busqué, J. Juanhuix, D. Maspoch, *CrystEngComm* **2016**, *18*, 4196–4204.
- [35] R. A. Coxall, S. G. Harris, D. K. Henderson, S. Parsons, P. A. Tasker, R. E. P. Winpenny, *J. Chem. Soc. Dalton Trans.* **2000**, 2349–2356.
- [36] R. Fu, X. Huang, S. Hu, S. Xiang, X. Wu, *Inorg. Chem.* **2006**, *45*, 5254–5256.
- [37] S. Drumel, P. Janvier, P. Barboux, M. Bujoli-Doeuff, B. Bujoli, *Inorg. Chem.* **1995**, *34*, 148–156.
- [38] L. Di Bari, G. Pescitelli, A. D. Sherry, M. Woods, *Inorg. Chem.* **2005**, *44*, 8391–8398.
- [39] R. S. Dickins, D. Parker, J. I. Bruce, D. J. Tozer, *Dalton Trans.* **2003**, 1264–1271.
- [40] S. J. L. Billinge, T. Egami, *Underneath the Bragg Peaks*, 2nd ed., Pergamon, **2012**.
- [41] P. K. Allan, K. W. Chapman, P. J. Chupas, J. A. Hriljac, C. L. Renouf, T. C. A. Lucas, R. E. Morris, *Chem. Sci.* **2012**, *3*, 2559–2564.
- [42] M. I. Mohideen, P. K. Allan, K. W. Chapman, J. A. Hriljac, R. E. Morris, *Dalton Trans.* **2014**, *43*, 10438–10442.
- [43] C. L. Farrow, P. Juhas, J. W. Liu, D. Bryndin, E. S. Božin, J. Bloch, T. Proffen, S. J. L. Billinge, *J. Phys. Condens. Matter* **2007**, *19*, 335219.
- [44] T. Vitha, V. Kubíček, P. Hermann, L. Vander Elst, R. N. Muller, Z. I. Kolar, H. T. Wolterbeek, W. A. P. Breeman, I. Lukes, J. A. Peters, *J. Med. Chem.* **2008**, *51*, 677–683.
- [45] N. Raghunand, C. Howison, A. D. Sherry, S. Zhang, R. J. Gillies, *Magn. Reson. Med.* **2003**, *49*, 249–257.
- [46] M. L. Garcia-Martin, G. V. Martinez, N. Raghunand, A. D. Sherry, S. Zhang, R. J. Gillies, *Magn. Reson. Med.* **2006**, *55*, 309–315.
- [47] M. M. Ali, M. Woods, P. Caravan, A. C. L. Opina, M. Spiller, J. C. Fetting, A. D. Sherry, *Chem. Eur. J.* **2008**, *14*, 7250–7258.
- [48] Z. Shanrong, W. Kuangcong, D. Sherry, *Invest. Radiol.* **2001**, *36*, 82–86.
- [49] G. Guerrero, J. G. Alauzun, M. Granier, D. Laurencin, P. H. Mutin, *Dalton Trans.* **2013**, *42*, 12569–12585.
- [50] G. J. M. Koper, M. Borkovec, *Polymer (Guildf)* **2010**, *51*, 5649–5662.
- [51] A. Barge, G. Cravotto, E. Gianolio, F. Fedeli, *Contrast Media Mol. Imaging* **2006**, *1*, 184–188.
- [52] J. Juanhuix, F. Gil-Ortiz, G. Cuní, C. Colldelram, J. Nicolás, J. Lidón, E. Boter, C. Ruget, S. Ferrer, J. Benach, *J. Synchrotron Radiat.* **2014**, *21*, 679–689.
- [53] W. Kabsch, *J. Appl. Crystallogr.* **1993**, *26*, 795–800.
- [54] L. Palatinus, G. Chapuis, *J. Appl. Crystallogr.* **2007**, *40*, 786–790.
- [55] G. M. Sheldrick, *Acta Crystallogr. Sect. A* **2008**, *64*, 112–122.
- [56] P. J. Chupas, X. Qiu, J. C. Hanson, P. L. Lee, C. P. Grey, S. J. L. Billinge, *J. Appl. Crystallogr.* **2003**, *36*, 1342–1347.
- [57] X. Yang, P. Juhas, C. L. Farrow, S. J. L. Billinge, *arXiv* **2015**, 1402.3163v3.
- [58] P. Juhás, T. Davis, C. L. Farrow, S. J. L. Billinge, *J. Appl. Crystallogr.* **2013**, *46*, 560–566.

Received: May 17, 2016

Published online on August 4, 2016

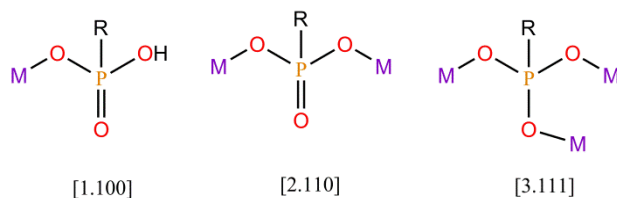
Publication 3: Supporting Information

Table S1. Crystallographic Table of 1.

Compound reference	1
Chemical Formula	Zn ₁₃ Gd ₆ C ₁₂₀ H ₁₈₄ O ₁₃₇ P ₂₄ , O ₃₅
Formula Mass	7028.1
Crystal System	Tetragonal
a/ Å	33.570(4)
b/ Å	33.570(4)
c/ Å	32.580(4)
α	90
β	90
γ	90
Unit Cell Volume	36715.9
Temperature	100
Space Group	P42/n
Z	4
Reflections Measured	152593
Independent Reflections	14855
Reflections ($I > 2\sigma(I)$)	11753
R _{int}	0.1120
R ₁ ($I > 2\sigma(I)$)	0.1351
wR(F ₂) ($I > 2\sigma(I)$)	0.4161
R ₁ (all data)	0.1568
wR(F ₂) (all data)	0.3859

Figure S1. Coordination modes of Gd-DOTA-4AmP units: a) Notation introduced by Harris *et al.*¹⁰ b) The three different Gd-DOTA-4AmP units found in the structure of **1** with the coordination mode of each arm indicated.

a)



b)

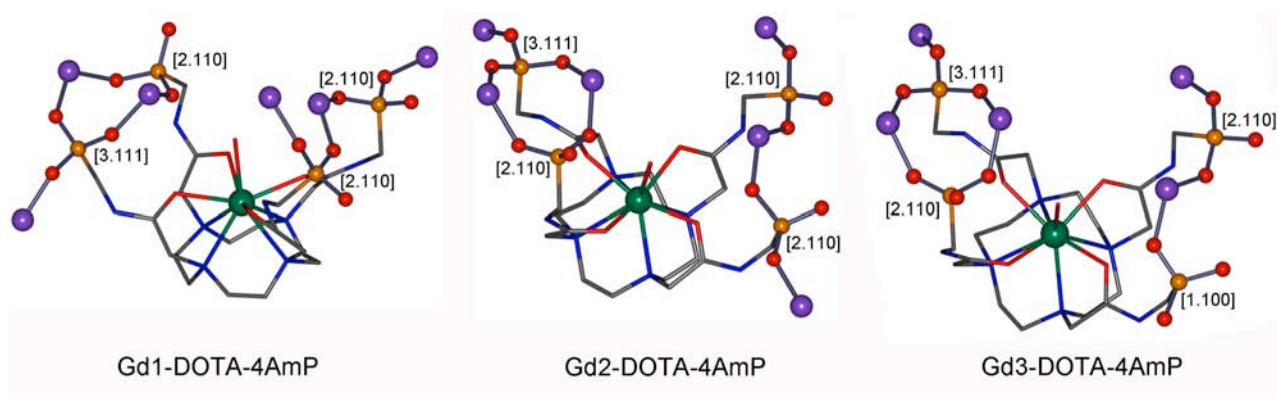


Figure S2. Paddle wheel-like Zn(II) units: these building units forming the structure of **1** are formed by two Zn(II) ions bridged by three phosphonate groups.

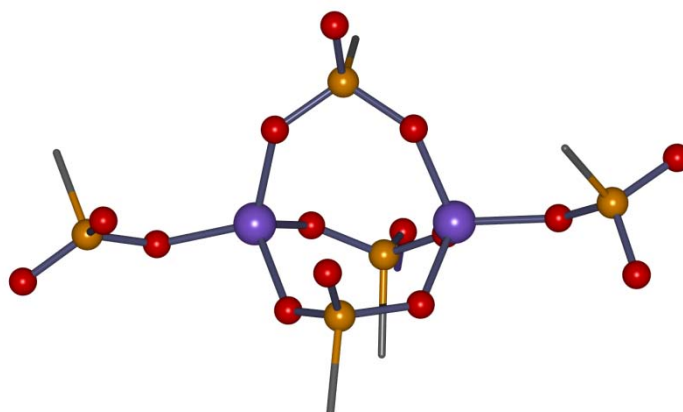


Figure S3. Powder X-ray diffraction measurements: **1** (red) and **1-Eu** (blue) as compared to the simulated powder pattern for **1** (black).

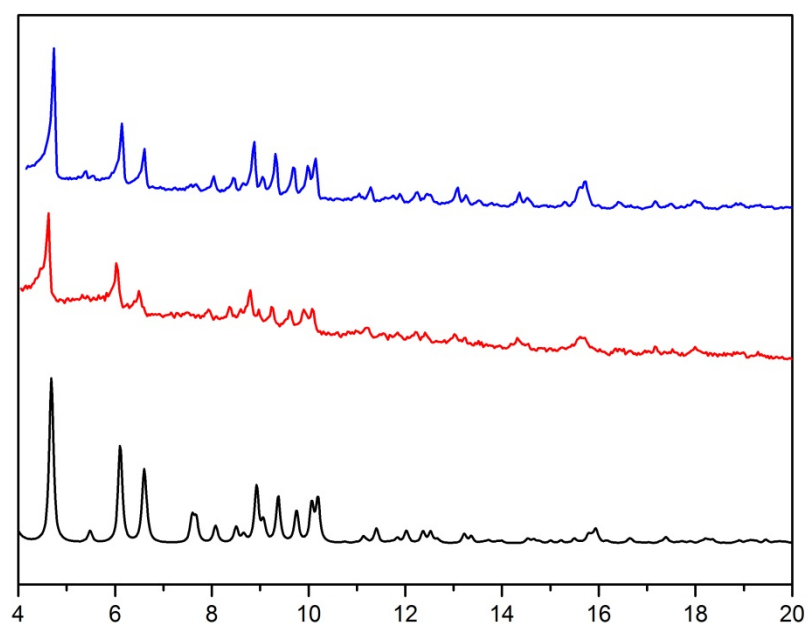


Figure S4. Zn-Gd-DOTA-4AmP nanoparticles: Field-Emission Scanning Electron Microscopy (FESEM) images of the colloid of Zn-Gd-DOTA-4AmP nanoparticles.

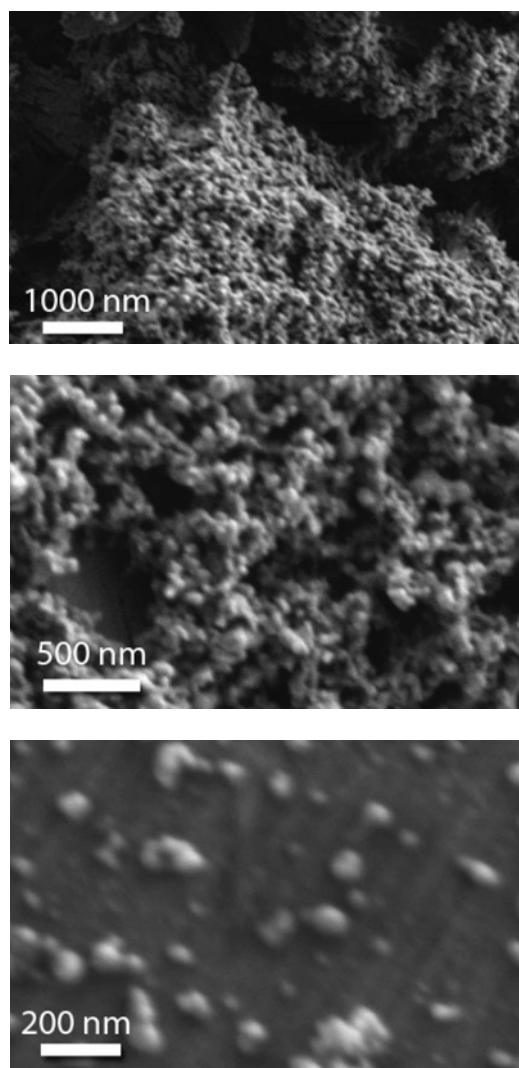


Table S2. Elemental analysis: The table shows the correspondence between the elemental analysis of Zn-Gd-DOTA-4AmP nanoparticles and **1**. C, H and N content have been obtained from CHN elemental microanalysis, while Zn and Gd content have been obtained from ICP-MS analysis.

	Calculated from 1 (wt. %) $\text{Zn}_{6.5}[\text{Gd}_3(\text{H-DOTA-4AmP})_2(\text{DOTA-4AmP})(\text{H}_2\text{O})_3] \cdot 18\text{H}_2\text{O}$	Zn-Gd-DOTA-4AmP nanoparticles (wt. %)
C	20.1	21.8 ± 1.2
N	9.4	9.8 ± 1.1
H	4.2	4.0 ± 1.4
Zn	11.9	12.2 ± 1.0
Gd	13.2	14.2 ± 1.0

Figure S5. FT-IR analysis: FT-IR spectra of **1** (red), Zn-Gd-DOTA-4AmP nanoparticles (green), **1**-Eu (blue) and Zn-Eu-DOTA-4AmP nanoparticles (black).

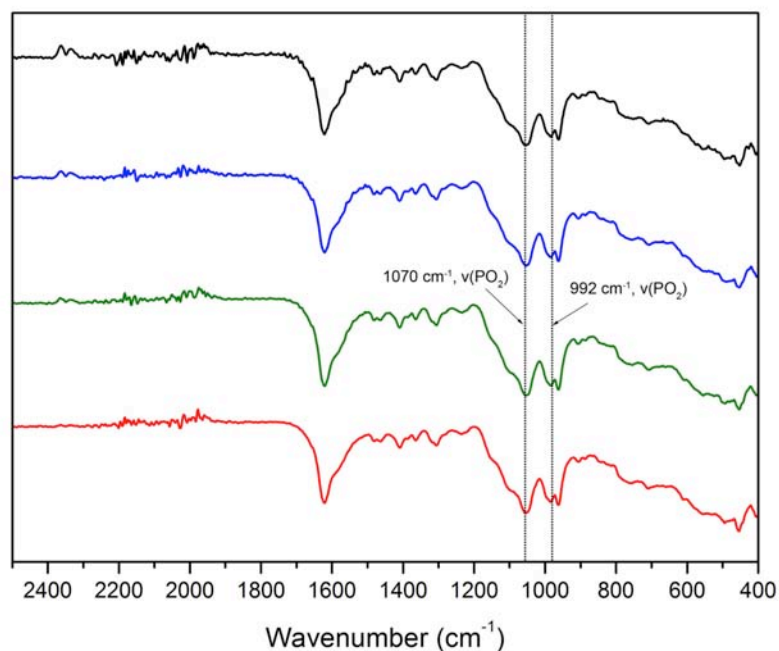
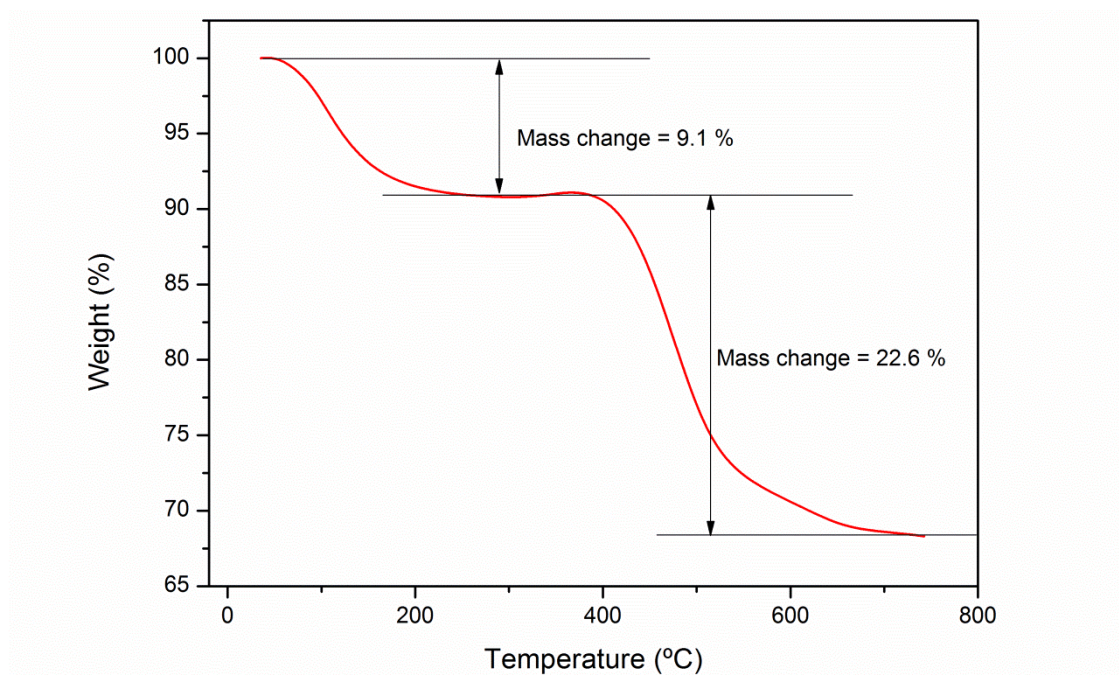


Figure S6. Thermogravimetric analysis: a) TGA analysis of **1**. b) TGA analysis of Zn-Gd-DOTA-4AmP nanoparticles

a)



b)

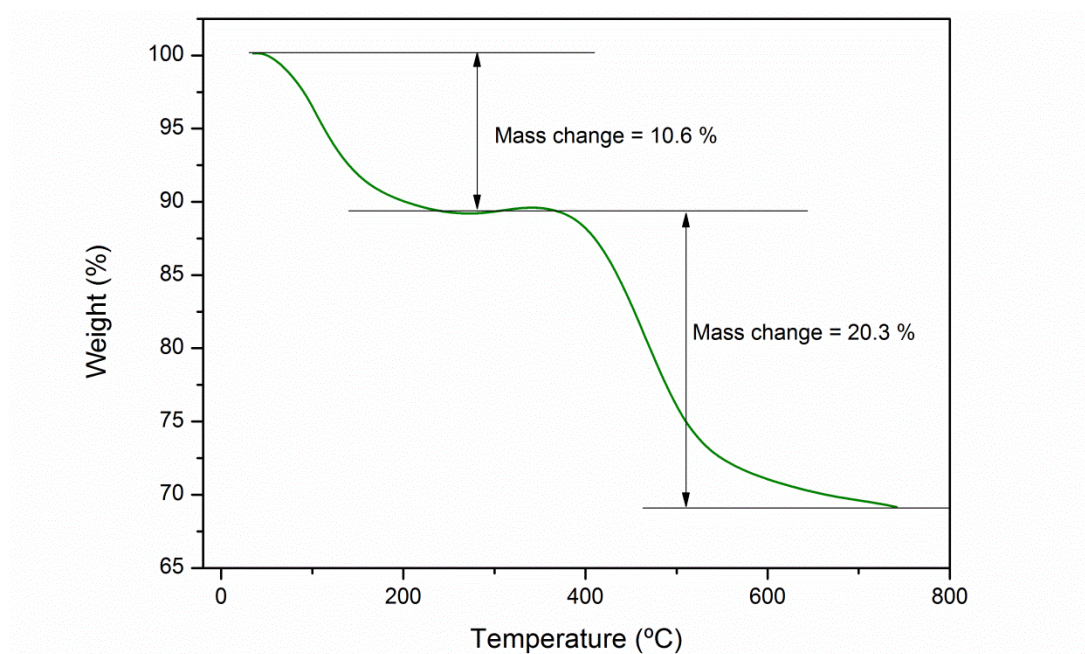
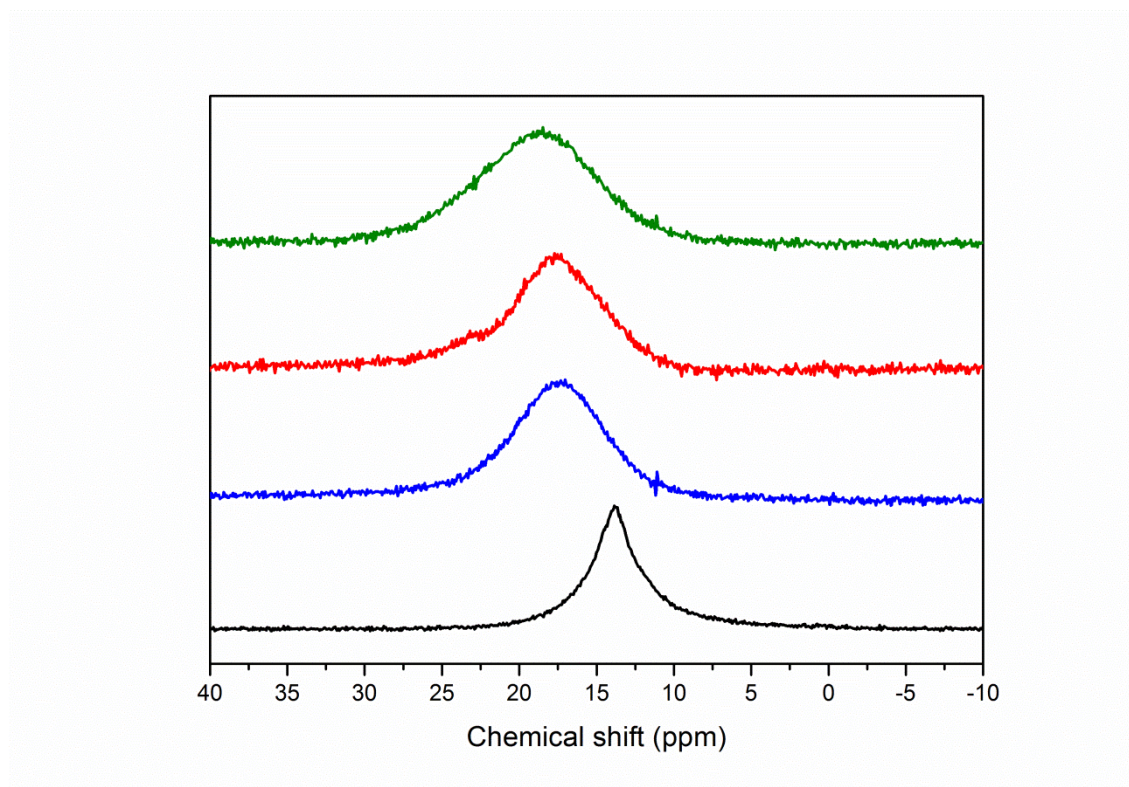


Figure S7. ^{31}P MAS NMR solid-state measurements: Figure and Table showing the solid-state NMR study performed for **1**-Eu and Zn-Eu-DOTA-4AmP nanoparticles.



Sample	δ (ppm)	$\Delta\delta$ at half height (ppm)
DOTA-4AmP (black)	13.8	3.0
Eu-DOTA-4AmP (blue)	17.3	6.6
1 -Eu crystals (red)	17.6	6.6
Zn-Eu-DOTA-4AmP nanoparticles (green)	18.6	8.8

Figure S8. PDF measurements: Total X-Ray Scattering Pair Distribution Function (PDF) data collected for **1** (red) and Zn-Gd-DOTA-4AmP nanoparticles (green).

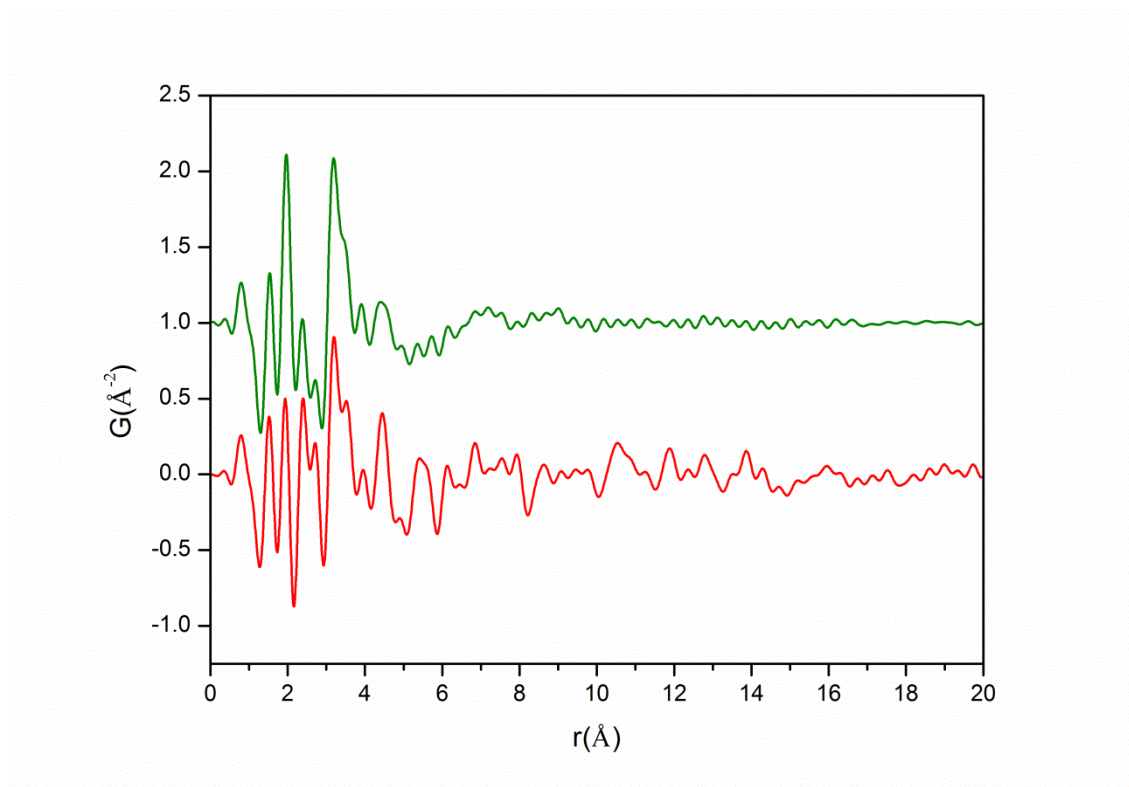


Figure S9. Atom-atom correlations: The figure shows the atom-atom correlations contributing to the first eight peaks of PDF spectra of the coordination polymer **1**, and the Zn-Gd-DOTA-4AmP nanoparticles, as well as the simulated spectrum of the CP **1** showing good correspondence with the experimental spectra. All the simulations were performed using PDFgui software.⁹

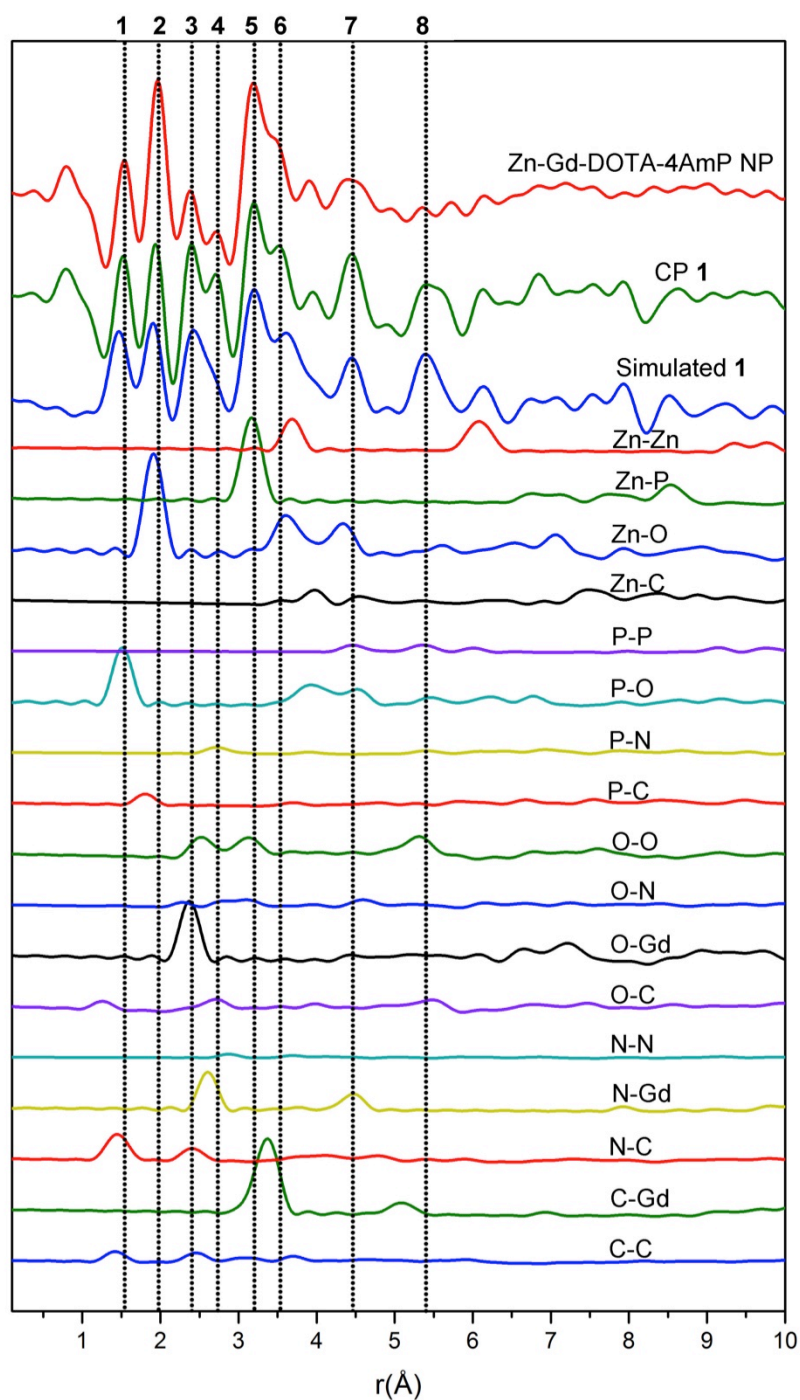


Figure S10. Stability study: Time dependence of the percentage of total (a) Gd(III) and (b) Zn(II) in Zn-Gd-DOTA-4AmP nanoparticles leached upon incubation in saline solution (NaCl 0.9%) at pH = 5.5, 7.4, and 8.5 and at T = 37.5°C.

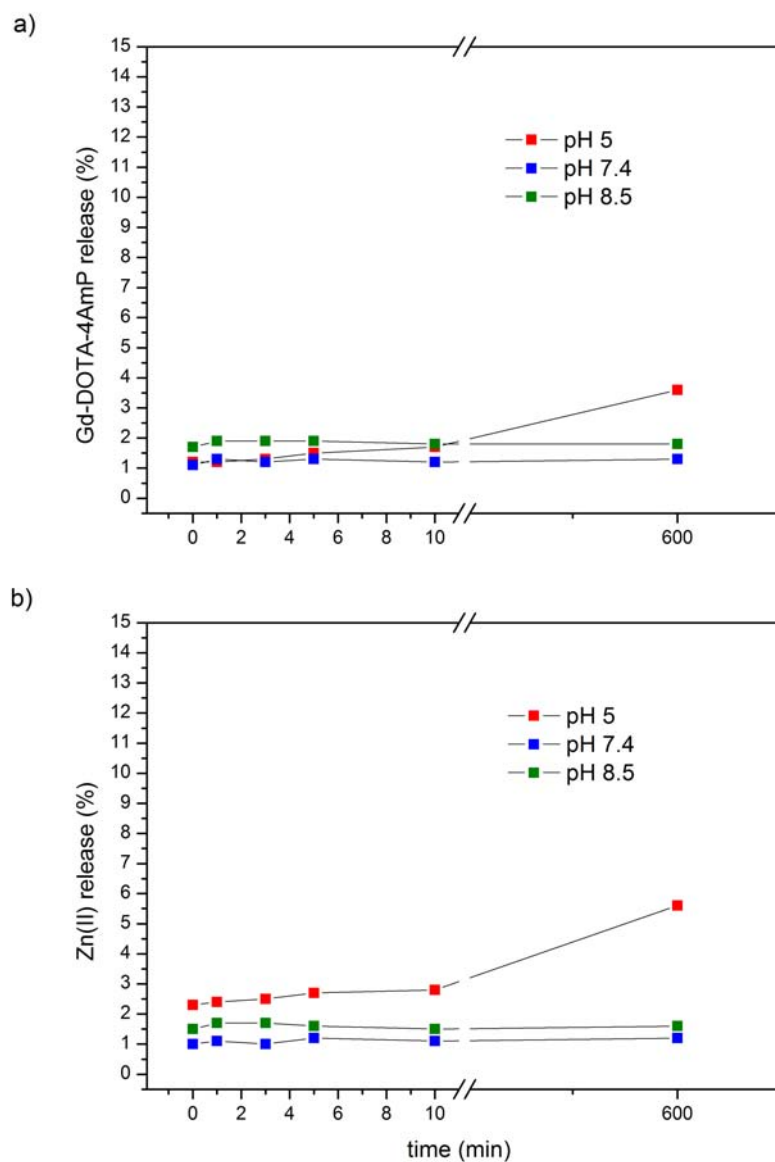


Figure S11. Mass spectrometry stability study: Mass spectrometry analysis (ESI-TOF) of the leached products of Zn-Gd-DOTA-4AmP nanoparticles at pH = 5, 7.4 and 8.5 compared with the products from the total degradation of the nanoparticles at pH = 3 and the building block Gd-DOTA-4AmP. The different spectra show that, in all the cases, we obtained the release of the Gd-DOTA-4AmP building block.

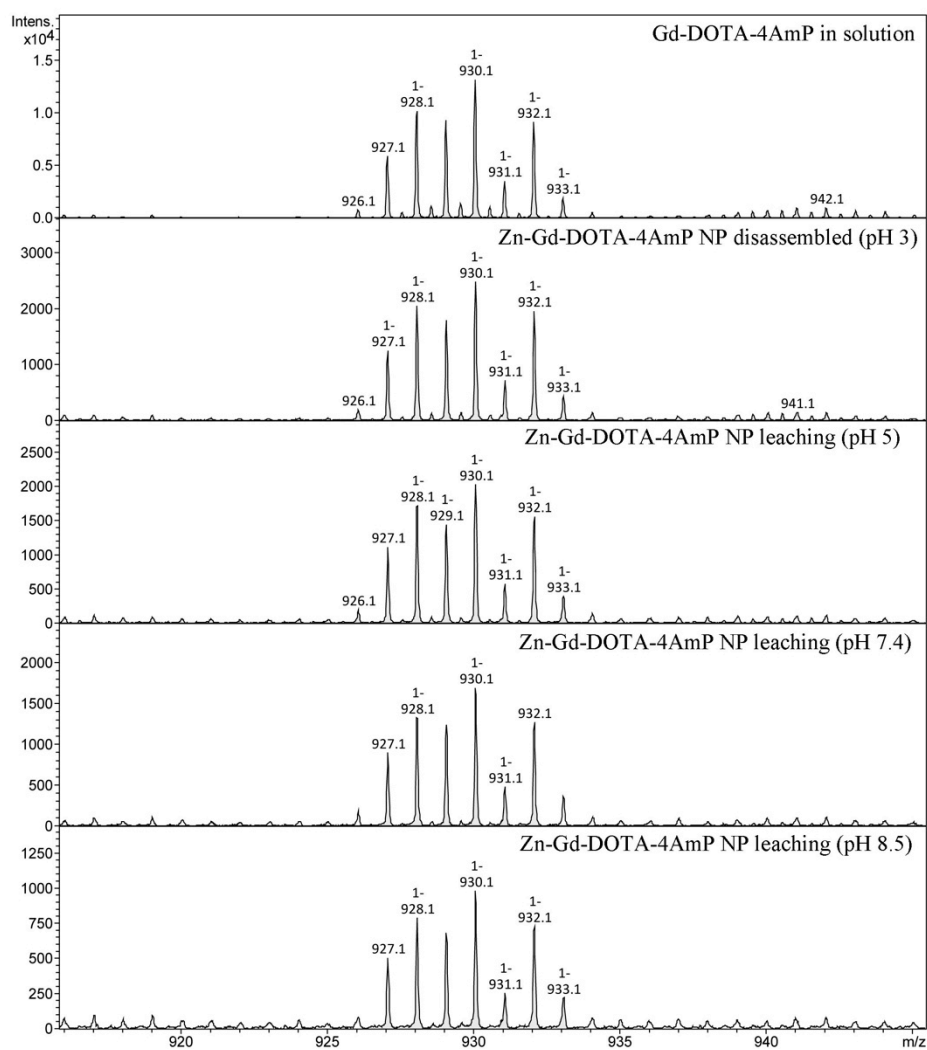


Figure S12. ^1H NMR stability study: ^1H NMR spectrum resulting from incubating a colloid of Zn-Eu-DOTA-4AmP nanoparticles in and acidic D_2O solution. The spectrum shows the presence of the characteristic eight resonances of equal intensity corresponding to the chelate Eu-DOTA-4AmP.

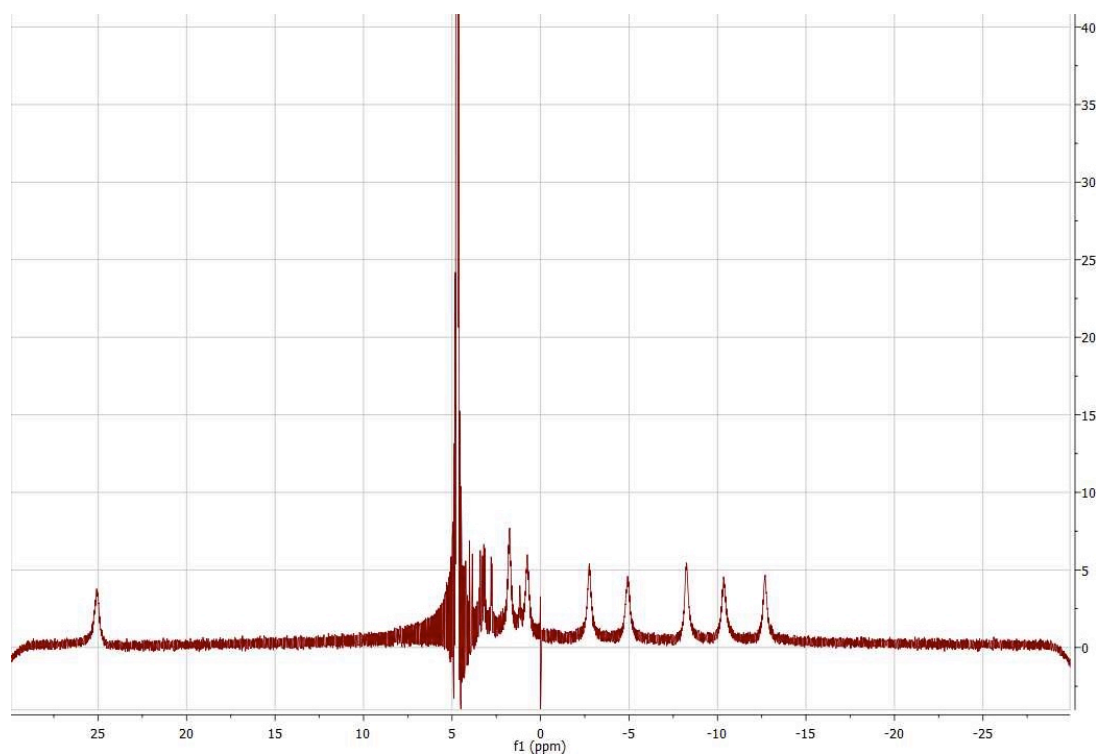
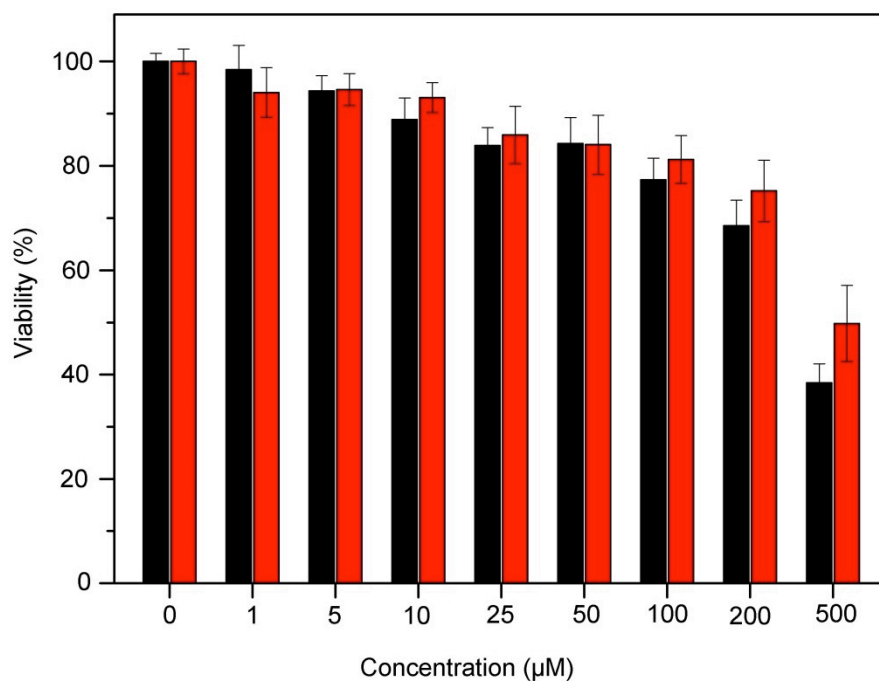
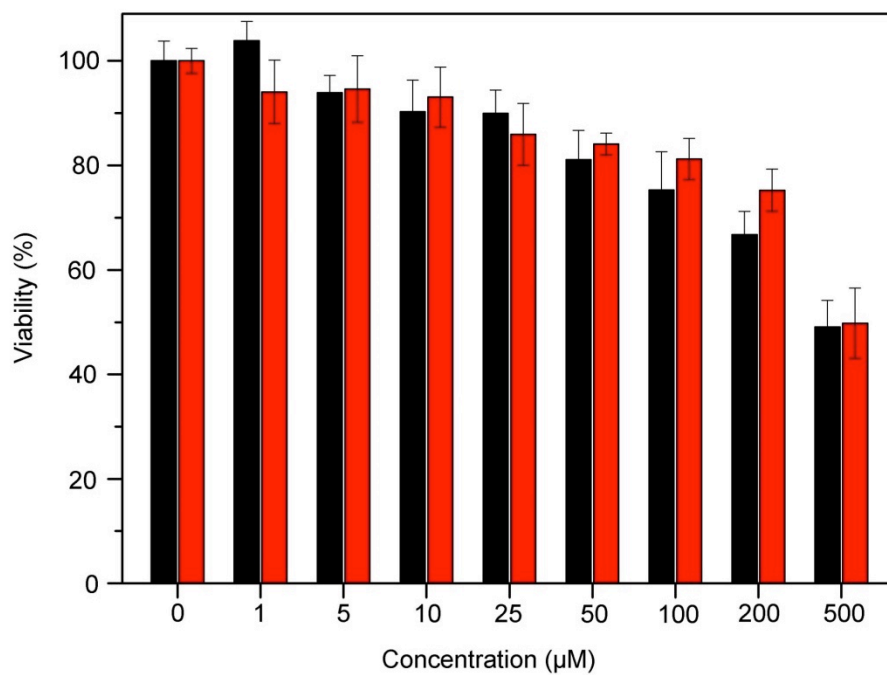


Figure S13. Cytotoxicity studies: Cell viability at different concentrations for Gd-DOTA-4AmP (black bars) and Zn-Gd-DOTA-4AmP nanoparticles (red bars) after 24 h. Viability assays were conducted in Hep G2 (a) and MCF-7 (b) cell lines.

a)



b)



References

- 1 A. Barge, G. Cravotto, E. Gianolio and F. Fedeli, *Contrast Media Mol. Imaging*, **1**, 184–8.
- 2 J. Juanhuix, F. Gil-Ortiz, G. Cuní, C. Colldelram, J. Nicolás, J. Lidón, E. Boter, C. Ruget, S. Ferrer and J. Benach, *J. Synchr. Rad.*, 2014, **21**, 679–689.
- 3 W. Kabsch, *J. Appl. Crystallogr.*, 1993, **26**, 795–800.
- 4 L. Palatinus and G. Chapuis, *J. Appl. Crystallogr.*, 2007, **40**, 786–790.
- 5 G. M. Sheldrick, *Acta Crystallogr. A.*, 2008, **64**, 112–22.
- 6 P. J. Chupas, X. Qiu, J. C. Hanson, P. L. Lee, C. P. Grey and S. J. L. Billinge, *J. Appl. Crystallogr.*, 2003, **36**, 1342–1347.
- 7 X. Yang, P. Juhas, C. L. Farrow and S. J. L. Billinge, arXiv, 2015, 1402.3163v3.
- 8 P. Juhás, T. Davis, C. L. Farrow and S. J. L. Billinge, *J. Appl. Crystallogr.*, 2013, **46**, 560–566.
- 9 C. L. Farrow, P. Juhas, J. W. Liu, D. Bryndin, E. S. Božin, J. Bloch, T. Proffen and S. J. L. Billinge, *J. Phys. Condens. Matter*, 2007, **19**, 335219.
- 10 R. A. Coxall, S. G. Harris, D. K. Henderson, S. Parsons, P. A. Tasker and R. E. P. Winpenny, *J. Chem. Soc. Dalt. Trans.*, 2000, 2349–2356.